DITEN

UNIVERSITA' DEGLI STUDI DI GENOVA

SCUOLA POLITECNICA - DITEN

DIPARTIMENTO DI INGEGNERIA NAVALE, ELETTRICA, ELETTRONICA E DELLE TELECOMUNICAZIONI

DOCTORAL THESIS IN
NAVAL ARCHITECTURE & MARINE ENGINEERING

THE EFFECT OF UNDERWATER EXPLOSION ON A MINE COUNTERMEASURES VESSEL: STRUCTURAL RESPONSE AND MATERIAL DESIGN

AUTHOR:
T.V. (GN) FRANCESCO MANNACIO

TUTORS:
PROF. CESARE MARIO RIZZO
PROF. MARCO GAIOTTI
C.V. (GN) SERGIO SIMONE

In memory of Admiral Davide Gabrielli

Summary

Index of figures

Index of tables

Acknowledgements

As the ship cannot accomplish the mission without the contribution of the crew, also this thesis could not have been completed without the valuable support of the people who contributed to its success. In particular, this endeavour would not have been possible without the enlightened guide of my supervisor Prof. Cesare Mario Rizzo, who always encouraged me to carry out the research, even when the topics of study seemed to be too hard to be approached. He has been a point of reference for me from the beginning, when I was in the dark about the difficulties of the PhD travel, conveying to me his passion for scientific investigation. In every circumstance, he was available for any kind of suggestions or support that I needed, being able to provide me with positive lessons even in case of failure. I consider myself lucky to have had him as a PhD guide. I'm extremely grateful to Captain Sergio Simone, who supported the research, helping me in the difficult task of carrying out the work integrating the needs of the academic and the military world. I also gratefully acknowledge Prof. Marco Gaiotti, who showed a special interest in the PhD topic, providing his valuable advice every time I needed it. I would like to express my deepest gratitude to Mr Marco Venturini who shared with me his wide experience in the shock field and supported me in each phase of the research, helping me to concretize my ideas. I also want to thank Mr Fabrizio Di Marzo and Mr Vincenzo Accardi, the qualified personnel of the Naval Support and Experimentation Centre (CSSN) who provided me with their knowledge in the theoretical and experimental field, contributing to the phases of setting, performing and post-processing of tests. Special thanks to Captain Cesare Ceccobelli, who believed in the quality of the research, and giving to me the opportunity of working until the last day with equipment and personnel of the Technical and Scientific Division in his employment. I would like to extend my sincere thanks to Mr Alfonso Barbato, who introduced me to the main topic of the PhD, providing me with bibliographical material, interesting notes and suggestions, which were particularly useful also for the performance of the whole work. I wish to acknowledge the help given by the company Brondi Srl, who provided materials and equipment to prepare the foundations' tests. Lastly, I'd like to mention Mr Massimo Guzzo, who provided me with his knowledge and expertise in the minesweepers' composite field.

I finally address my gratitude to my family, my parents, my brother, my sister and in particular my girlfriend Delia, who supported me every day during this troubled travel, accepting also that I had to sacrifice my free time for the purpose. This thesis is dedicated to all of you.

Abstract

In the modern geo-strategic scenario, characterized by the presence of sophisticated mines as well as rudimental and cheaper ones, the Italian Navy decided to design a New Generation Mine Countermeasures Vessel, in which the historical capabilities of minesweepers must be enhanced, considering the necessity of holding unmanned systems. In particular, they must survive in case of an **underwater explosion** event, according to some design criteria and corresponding limit states.

Nowadays, the continuous increase of using modern numerical methods, such as Finite Element (FE) methods, allowed by the evolution of the computational capabilities of computers, has strongly influenced the **shock** design against underwater explosions. However, the complete numerical simulation of the phenomena in issue is even nowadays a matter of research, and it requests the comparison of **numerical** results with **experimental** data and theoretical formulations for validation.

The main target of the thesis is to provide suitable methodologies for the ship design phase to assess the strength of naval structures in composite material against non-contact underwater explosions, thus reducing the **vulnerability** of the New Generation Mine Countermeasures Vessel. The experiments realized for this purpose were conducted in the Naval Support and Experimentation Centre's (CSSN) laboratory in La Spezia and allowed validation of a set of increasingly complex numerical models.

At first, the shock phenomenon involving ship structures only is analysed. Some reliable guidelines to perform a dynamic calculation using the finite element method, not yet available in the literature, are provided. Then, the dynamic response of New Generation Mine Countermeasures Vessel composite structure is studied. An experimental and numerical method to characterize the shock transient response of naval E-glass biaxial laminates is presented. This procedure opens for relatively straightforward material characterization, limiting the need for complex experimental shock trials to a few selected laminates. It can be applied in the design of minesweepers' structures to select the proper stacking sequences of laminates and to design adequate **composite** materials. Finally, the effectiveness of different numerical approaches to predict the effects of **Fluid-Structure Interaction** caused by non-contact underwater explosions on minesweepers hull structures is verified. In particular, a numerical methodology, in which the Volume of Fluid approach is pursued, provides the most realistic results when comparing analytical theory, numerical models and experiments. This modelling strategy includes the simulation of the complete phenomenon, in which structures, water and vapor of cavitation are included. Eventually, it can be considered a valuable and cost-effective tool for the design of composite structures subject to non-contact underwater explosions.

Keywords:
Underwater explosion, Shock, Vulnerability, Composites, Numerical, Experimental, Fluid-Structure Interaction

1 Introduction

1.1 Background

Naval vessels are subjected to dangerous threats when they are in an operational scenario, among which conventional and non-conventional mines play an important role even nowadays. The next decades will be characterized by the presence of sophisticated mines as well as rudimental and cheaper ones. The most dangerous will be the smart mines, which will become accessible and easier to obtain. In this contest, the technology of Maritime Warfare is in continuous development. Maritime Unmanned Systems are sometimes preferred by Navies to keep men safe from the dangers of a minefield. However, even if this technology has been the object of study by researchers for the last decades, it seems not to be fully reliable to substitute manned vessels. Conventional platforms, instead, such as minesweepers, have proved to be able to detect and counteract mines since 2nd World War. Therefore, the Italian Navy decided to combine old and new technologies by designing a New Generation Mine Countermeasures Vessel (NG-MCMV), in which the historical capabilities of minesweepers must be enhanced, considering the necessity of holding Unmanned Systems [1.3]. In the modern geo-strategic scenario, it is supposed that they can also operate far away from the homeland. Therefore, they should maintain strong offensive capabilities to carry out missions even in scenarios characterized by high levels of threat (radar-guided missiles, infrared, acoustically activated mines, magnetic, pressure mines, torpedoes, etc. all characterized by high destructive power). They must be able to continue the mission even after suffering damage. This capability of the naval vessel is called s*urvivability*, which can be defined, in other words, as the ability of a ship to remain operational in threatening situations and resist attacks [1.1].

Nowadays, for naval vessels, a *survivability* assessment is always included in a preliminary phase of design, to reduce costs in the attempt of designing ships that can survive in a hostile environment [1.5][1.1]. It is necessary to quantify this capability to verify if the ship satisfies the design requirements. However, the *survivability* is a wide concept which includes different thematic areas. In particular, the features of *recoverability*, *vulnerability* and *susceptibility* [1.4] are normally included in this *survivability* assessment, considering that their reduction leads to better skills of *survivability*. Therefore, it is necessary to focus separately on each of these concepts to produce an estimate of *survivability*.

In particular, the *susceptibility* is connected to the inability of the ship to avoid detection by threats. It refers to her stealthiness and self-defense capabilities. The *susceptibility* reduction is achieved, for example, by minimizing the ship's signatures that trigger or guide threats that are above or below the

surface. The composite materials of minesweepers provide a positive contribution to this reduction as they have non-magnetic characteristics. The *recoverability* is the vessel's inability to resume operation (fight, defend, move, survive) as a result of damage. It depends on the actions aimed at reducing damage effects. These actions include firefighting, leak prevention and security equipment. It should be noted that also the training of the crew plays a fundamental role in increasing the recovery capability of vessels. This feature is particularly difficult to quantify considering that depends also on human factors which are hardly predictable in a design phase. The comprehensive study of *susceptibility* and *recoverability* is beyond the aim of this thesis.

The *vulnerability*, instead, is the main area of research. It is linked to the capability of the ship to withstand a hit. It can be defined as the inability of the ship to continue the mission after being affected by any threats, such as anti-ship missiles, mines, cannon shots of various calibres, torpedoes or terrorist attacks. This is particularly critical for minesweepers, considering that the New Generation Mine Countermeasures Vessels must be able to operate in a minefield. The probability to be hit increases, but in any case, they must survive in case of the explosion of an underwater mine, according to some design criteria. Therefore, in an early design phase, particular attention must be given to the aspects of their *vulnerability* in an attempt of reducing it [1.2]. To understand which is the damage in case of impact, being able to predict it or obtain a good estimate is critical for the *vulnerability* assessment. And, this is crucial for composite materials, considering that it is possible to design the stacking sequence of laminates to modify the mechanical properties of the materials, influencing their structural response.

Nowadays, the continuous increase of using modern numerical methods, such as Finite Element (FE) methods, caused by the growth of the computational capabilities of personal computers, has strongly influenced the shock design against the UNDerwater EXplosion (UNDEX). However, the complete simulation of the non-linearities of the phenomena in issue is even now a matter of research, and it requests the comparison of numerical results with experimental data and theoretical formulations for validation. In addition, national rules, even if they allow the use of the FE methods, they do not provide precise guidelines for the designers.

The motivation for the research was born by the collaboration between the Naval Support and Experimentation Centre (CSSN) and the University of Genova, Department of Electrical, Electronics and Telecommunication Engineering and Naval Architecture (DITEN). The main goal of the laboratory is to jointly develop and manage research and experimentation activities of common interest in the field of marine structures with dual-use purposes, civilian and military. The CSSN's knowledge of the UNDEX phenomenon, generated by years of tests and experimentation realized in the past, and preserved by qualified personnel, is connected to the University's theoretical and

numerical expertise in the new technologies. National industries have been involved in this cooperation considering their experience in the shock design of naval vessels and in particular of minesweepers. The experiments and tests realized in this thesis were conducted in CSSN's laboratory using the Navy's facilities, while algorithms and theoretical knowledge were transferred from the university to military personnel.

1.2 Goal of the thesis and main contributions

The main target of the thesis is to provide some methodologies useful in the design phase to verify the resistance of naval structures in composite material to non-contact Underwater Explosions to reduce the *vulnerability* of the New Generation Mine Countermeasures Vessels.

Therefore, the first aim is to perform bibliographical research, providing a review of the state of the art of the shock phenomenon, including its effects on naval structures, the actual design approaches and the structural response to shock loads of minesweepers' composite materials.

The second goal is to provide some reliable guidelines, not available in the literature, to perform a dynamic calculation using the finite element method. These are useful to verify to shock loads machinery, foundations and naval structures in general, for which displacement, velocity or acceleration time histories are provided, as happens in the common practice of design. Therefore, the shock phenomenon in which only structures are considered is analysed, verifying the effects of the numerical choices in comparison to the experimental data, and evaluating the relative errors.

Third, the dynamic characterization of materials has proved to strongly influence the results of shock calculations. Therefore, an experimental and numerical method to characterize the shock transient response of naval E-glass biaxial laminates is presented, providing the mechanical inputs necessary to verify the shock response of minesweepers structures by calculation. This procedure can be used to design minesweepers' structures to select the proper stacking sequences and design materials.

Finally, once the shock of the composite materials structures has been analysed, the complete phenomenon, in which fluid and structure are involved, is studied. The last contribution of the thesis is to verify the effectiveness of different numerical approaches to predict the effects of Fluid-Structure Interaction (FSI) caused by non-contact UNDEX on minesweepers hull structures. In particular, a numerical methodology, in which FSI is simulated by combining Volume of Fluid (VOF) (a special Computational Fluid Dynamics approach) and Finite Element, is calibrated according to theory and experiments. This modelling strategy includes the simulation of the complete phenomenon, in which structures, water and vapor of cavitation are included. Eventually, it can be considered a valuable and

cost-effective tool for the design of composite structures subject to non-contact underwater explosions.
In this thesis, the main questions addressed include:

- What is the state of the art of shock design?
- How can we use Finite Elements to verify shock phenomenon effects on naval structures?
- How much Finite Elements are effective in predicting the dynamics of the shock phenomenon when only structures are simulated?
- What is the transient behaviour of naval E-glass composite materials to shock loads?
- How can we deal with composite materials in shock calculations?
- How much different numerical approaches are effective in predicting the effects of Fluid-Structure Interactions caused by non-contact UNDEX on composite hull structures?
- Are we able to conduct complete FSI calculations providing reliable results on minesweeper structures?

1.3 Thesis organization

The thesis is organized into nine chapters, including a general conclusion and a list of references for each chapter.
The first chapters, from no. 2 to 5, are devoted to the state of the art of the topics of study. In particular, in Chapter 2 a general description of the shock phenomenon is provided, concerning the shock wave and bubble pulse behaviour in the fluid. Chapter 3 investigates about the effects of underwater explosions on structures, introducing the air-backed and water-backed theoretical background. Chapter 4 explores the mechanical shock and its analytical descriptions, focusing on the design methodologies which are nowadays available for the shock assessment. Simplified approaches in which only structures are considered and more complete FSI methods are described highlighting their strengths and weaknesses. Chapter 5 describes the features of the naval composite materials, analysing the dynamic behaviour of the fiberglass laminates. The state of the art of the research on the topic, including the numerical approaches used to simulate the different failure modes, is reported. From Chapters 6 to 8 the validation of the methodologies proposed in the thesis to verify the shock effects on board of minesweepers are presented. In Chapter 6, the guidelines, useful in the design phase to assess the effects of mechanical shock by using Finite Element, are provided, verifying the results obtained from the comparison with experimental data. A reference configuration, in which the foundations and the related machinery are included, has been built and tested according to the rules. In Chapter 7, the dynamic characterization of composite materials is realized, performing a shock test

campaign on the naval E-Glass fiberglass laminates under study. Finally, Chapter 8 explores different FSI approaches in order to verify their effectiveness in predicting the effects on board of minesweepers.

1.4 Bibliography

[1.1] Atasaven K., Yilmaz Huseyin, “On the assessment of survivability of surface combatants”, *Journal of Naval Sciences and Engineering*, 24 Aprile 2019;

[1.2] Goodfriend D.B., “Exploration of system vulnerability in naval ship concept design”, Faculty of Virginia Polytechnic Institute and State University, 24 Settembre 2015;

[1.3] Guadalupi D., Maiorana F., Guzzo M., “New Generation Mine CounterMeasures Vessel (NG-MCMV)”, NAV 2022, Genova, 15-17 June 2022;

[1.4] OPNAVINST 9070.1B, *Survivability policy and standards for surface ships and craft of the U.S. Navy*, Department of the Navy, Washington D.C., 17 Novembre 2017;

[1.5] Piperakis A.S., “An Integrated Approach to Naval Ship Survivability in Preliminary Ship Design”, UCL, 2013.

2 The phenomena of underwater explosion

2.1 General properties of explosives

As reported in [2.21], an explosive can be defined as a chemical substance or a mixture of substances that produce an extremely fast, and able to self-sustain, exothermic redox reaction, when subjected to an adequate external input.
The energy involved is of the same order of magnitude of the redox reactions, but it is released in a very short time releasing high power.
Explosives are generally divided into three categories depending by how the chemical reaction takes place. They are:

- Deflagrating explosives, which normally produce a reaction propagating at an average speed in the air of 300 ÷ 400 m/s. They are used, for example, in the propulsion of rockets or projectiles
- Detonating explosives, which usually react at a speed of 2000 ÷ 9000 m/s. They are used for wartime munitions
- Triggering explosives, which almost always react in a detonation regime and require a weak impulse to start the reaction. This type of explosive is usually used to trigger particularly stable detonating explosives.

The effectiveness of an explosive depends by two factors:

- Amount of energy available in the explosive, which is related to the amount of heat and gases released during the reaction
- Speed of energy release.

2.2 Omnidirectional charges for underwater weapons

Naval mines generally can be considered as omnidirectional charges in the definition of D'Andrea [2.7]. They consist of three elements:

- Main charge
- Trigger device
- Booster

These charges of regular geometry, triggered at the center, generate explosive phenomena, which are almost equal in every direction (omnidirectional). A part of the explosive (25%) provides for the

formation of the jet, the rest (75%) is responsible for the occurrence of the shock wave and the phenomena related to the gas bubble.

Different configurations of mines exist, depending on their positioning in the sea as shown in **Figure 2.1**. Modern mines can be smart devices, able to detonate in case of changing of pressure, magnetic and electric field and noise produced by their target, without being detected easily. More details about different features of mines are reported by Friedman in [2.13].

The entire sequence of the explosion can be summarized as:

- Shock wave propagation at great distances
- Oscillation of the gas bubble with the production of decreasing pressure peaks
- Rise of the bubble under the influence of gravity.

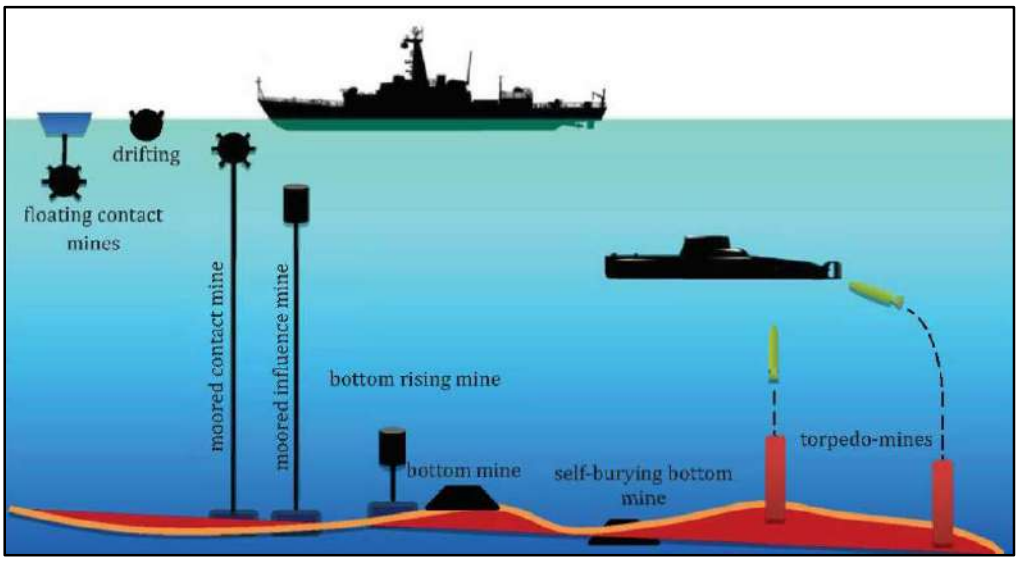

Figure 2.1 Sea mines configurations (Sztumoski [2.28])

2.3 Detonation in the underwater explosion

The phenomenon of detonation can be divided in three different phases:

- Intrinsic phase: it begins and ends within the explosive mass, causing its rapid increasing of energy
- Extrinsic phase: it determines the transport of energy through the fluid
- Working phase: it refers to the destructive effects on the target.

As soon as the intrinsic phase is finished, the particles of water in contact to the charge are immediately accelerated and compressed (at about 180000 bar of pressure). The local motion is transmitted to the continuous layers, resulting in the front of the shock wave. At the same time the very dense mass of- the gases, produced by the detonated explosive, begins to expand, resulting in a

reduction of the pressure in the surrounding water and in the occurrence of the so-called "pulsating bubble" phenomenon. Relations useful to characterize the physics of the detonation phenomenon are reported by Henrych in [2.17].

2.4 Shock wave

The shock wave differs from the sound wave by the following characteristics:

- The propagation speed (5000-8000 m/s) is several times higher than that of sound (1550 m/s) close to the charge. This limit value is reached at a distance of about seven times its radius
- The profile of the wave becomes gradually larger as it propagates
- The pressure of the shock wave decays with the distance faster than that of sound wave.

Close to the charge, at the high pressures generated by the explosion, the water behaves as a compressible fluid. For example, the volume of water decreases by 20% at a pressure of about 10000 kg/cm^2, as reported by Petralia in [2.21].

The value of the pressure decays exponentially in time according to the following laws, proposed by Cole in [2.4], reported by D'Andrea in [2.7], and shown in **Figure 2.2**:

$$P(t) = P_{max} e^{-\frac{t}{\vartheta}} \quad if\ t < \vartheta \tag{2.1}$$

and

$$P(t) = P_{max} \frac{e^{-1}}{t/\vartheta} \quad if\ \vartheta \leq t \leq 5\theta \tag{2.2}$$

where P_{max} is the pressure at time t=0 and ϑ is the constant of time, which corresponds to the time at which the pressure decreases to a value equal to P/e, considering e as the Nepero number.

The fundamental hydrodynamical relations related to the physic behaviour of the shock wave in fluids are reported by Cole [2.4] and Zamyshlyaev et al. [2.30]. However, the phenomenon of propagation of the shock wave in fluids and its interaction with surfaces have been a matter of research for many scientists. Sommerfeld and Müller [2.24] focused their analysis on plane shock waves and spherical shock waves in water, discussing the problem experimentally and numerically. Apazidis et al. [2.1] [2.2] [2.26] investigated their propagation in heterogeneous fluids, providing numerical simulations in good agreement with tests. Eliasson et al. [2.10] [2.11] [2.12] studied the effects of artificial disturbances on shock waves validating their numerical results with experimental data. Ghoshal and Mitra [2.15] [2.16] provided some guidelines to understand the shock wave reflection from submerged hydraulic structures and their behaviour in nonlinear compressible medium. In the following, the fundamental principles are discussed.

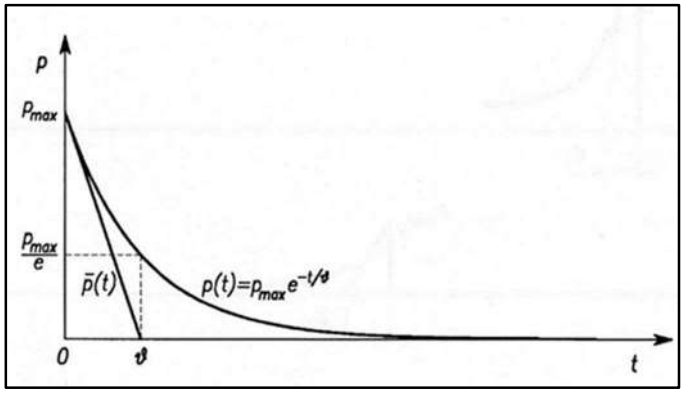

Figure 2.2 Exponential decay law of shock wave pressure (Marinò [2.19])

2.4.1 Impulse and energy

Once the trend of the pressures over time is known, it is possible to calculate the impulse and the energy per unit area using the following equations, in which ρ_0 and c_0 are respectively density and speed of shock wave:

$$I = \int_0^t P(t)dt \tag{2.3}$$

$$E = \frac{1}{\rho_0 c_0}\int_0^t P^2(t)dt \tag{2.4}$$

For a specific time of $t = 6{,}5\vartheta$ it is possible to calculate the impulse and energy as a function of the weight of the charge and the shock scenario using some formulas obtained experimentally and reported by Swisdak in [2.27].

2.4.2 Principle of similarity (or cubic root)

According to the principle of similarity explained by Petralia in [2.21], if the linear dimensions of two charges differ by a k factor, the shock wave remains unchanged if distances and times are corrected of the same k factor.

Now, since the volume (and therefore the weight) depends by the cube of the linear dimension, it can be said that two charges, which differ exclusively for their weight, produce similar shock waves at the same proportionally correct distance expressed by in which M is the mass of the charge.

Based on this principle, after a series of experimental tests of underwater explosions, a series of formulas were derived to calculate P_{max} and $\bar{\vartheta}$ as a function of the $\frac{R}{\sqrt[3]{W}}$ factor, in which W is the mass of the TNT charge.

Below some correlations proposed by Cole [2.4] are presented:

$$P_{max} = K\left(\frac{W^{1/3}}{R}\right)^{\alpha} \tag{2.5}$$

$$\theta = KW^{1/3}\left(\frac{W^{1/3}}{R}\right)^{\alpha} \tag{2.6}$$

in which, considering W in [kg], R in [m], the results will be P_{max} in [MPa] and θ in [ms]. For TNT charges the K and α coefficients proposed by Keil [2.18], adapted to the International System, are reported in **Table 2.1**.

This principle is valid in a certain range of distances. The lower limit of validity is about seven times the radius of the distance, below which the effects of energy dissipation on the front of the shock wave are of particular importance, while the upper limit is about nine hundred times the radius. After this point, the viscosity effects begin to influence the phenomenon. In **Figure 2.3** it is shown the trend of the pressures as a function of the distance and weight of the TNT charge, calculated by Szturomski [2.28].

In case of explosive different from TNT, the formulas set out above are still valid, but the weight of the charge must be expressed in terms of TNT equivalent, i.e. multiplying it by a coefficient which can be higher or lower than one depending by the effectiveness of the explosive (efficacy factor). Some of these experimental coefficients are reported by Swisdak [2.27] and Petralia [2.21].

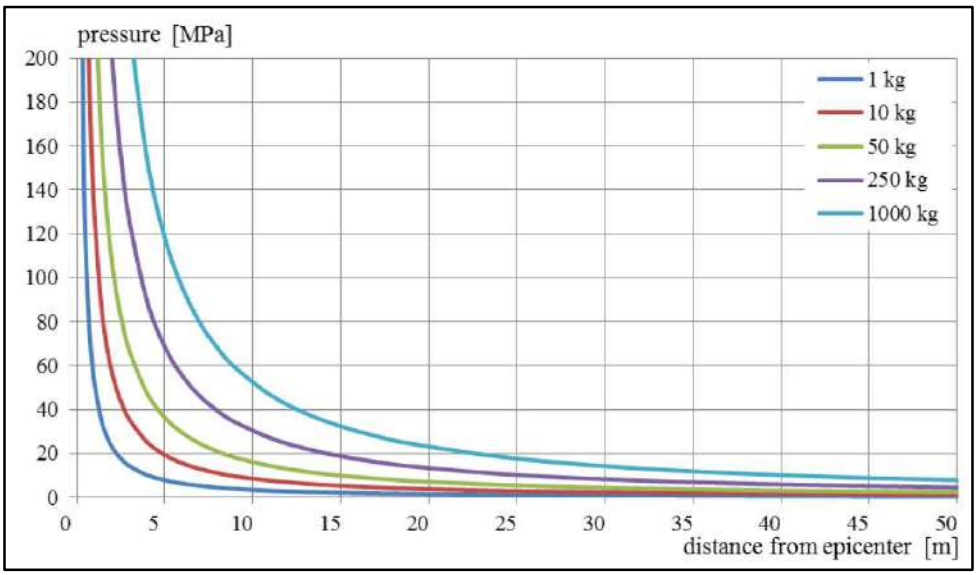

Figure 2.3 Pressure values as a function of distance and weight of the TNT charge (Szturomski [2.28])

Table 2.1 Coefficients in peak pressure and angle decay formulas

Equation	K	α
P_{max}	52.4	1.13
θ	92.5	-0.22

2.5 Reflection phenomena

The principles previously described are valid in case of explosion of a charge which happens in the open field. In the sea water it is necessary to refer to two phenomena: the reflection of the free surface, the so called "cut-off" phenomenon, and the one of the seabed.

According to the acoustic approximation, it is possible to consider the reflected wave as the light in a mirror, as it is represented in the **Figure 2.4**. The path of the reflected wave is equal to that of a direct wave generated by the same charge c', set in the virtual point which is symmetrical to the real one c.

In the case of the figure, the delay in which the wave reflected occurs at the measurement point M is equal to:

$$\Delta t = \frac{D_s - D}{c_0} \tag{2.6}$$

where c_0 represents the speed of sound in water.

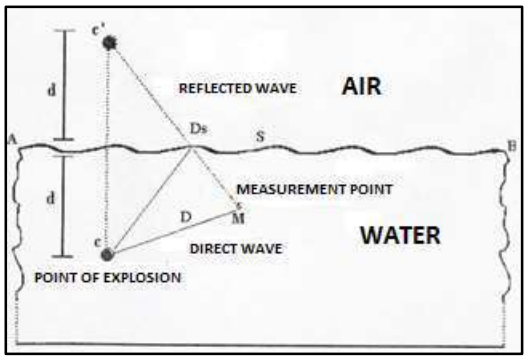

Figure 2.4 Shock wave paths (image adapted from D'Andrea [2.7])

2.5.1 Underwater explosion geometry

It is necessary to define a series of parameters to describe the UNDEX geometry, which are:

- The path of the direct shock wave D

- The paths of the shock wave reflected from free surface D_s and seabed D_f
- The vertical path of the charge until the occurrence of the first compression of the gas bubble
- The path of the direct wave generated by the peak pressure caused by the gas bubble
- The path of the reflected wave generated by the peak pressure caused by the gas bubble
- The angles of reflection β of the shock wave and the pressure wave caused by the gas bubble.

Considering as reference **Figure 2.5**, the distance between charge and measurement point (S) is calculated as follows:

$$D = \sqrt{D_0^2 + (Z - q)^2} \tag{2.7}$$

The path of the wave reflected from the free surface is calculated as:

$$D_s = \sqrt{D_0^2 + (Z + q)^2} \tag{2.8}$$

The path of the wave reflected from the seabed instead is obtained as:

$$D_f = \sqrt{D_0^2 + (Q - Z + Q - q)^2} \text{ if } Z - q \neq 0 \tag{2.9}$$

$$D_f = \sqrt{D_0^2 + 4(Q - Z)^2} \text{ if } Z - q = 0 \tag{2.10}$$

The angle of reflection β is given by:

$$\beta = \tan^{-1} \frac{Q - Z + Q - q}{D_0} \text{ if } D_0 \neq 0 \tag{2.11}$$

$$\beta = 90° \text{ if } D_0 = 0 \tag{2.12}$$

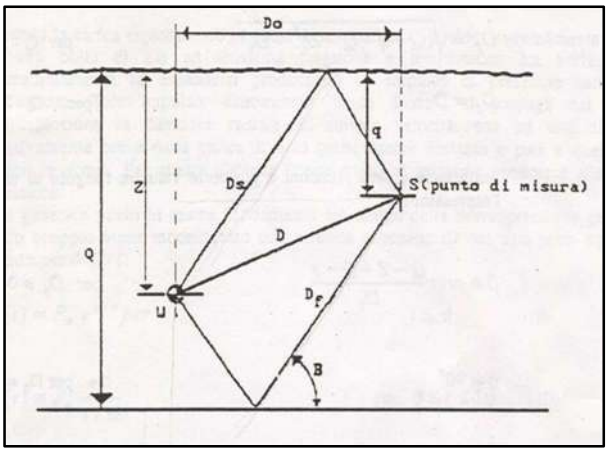

Figure 2.5 UNDEX geometry (D'Andrea [2.7])

2.5.2 Reflection caused by the free surface

When the shock wave reaches the interface between air and water, due to the large difference in density between the two fluids, it is reflected as a tensile wave, as defined by Costanzo in [2.5]. The velocity of the free surface's particles of water assumes an almost doubled value, while there is a

decrease in the density of the water layer: this leads to a pressure drop and to the generation of a tensile wave that propagates as a negative pressure.

If the explosion occurs close to the free surface, this tensile pressure reaches the measurement point with a short delay, which limits the effects of the direct wave, and, therefore, the resulting pressure curve appears as "cut-off", as shown in **Figure 2.6**.

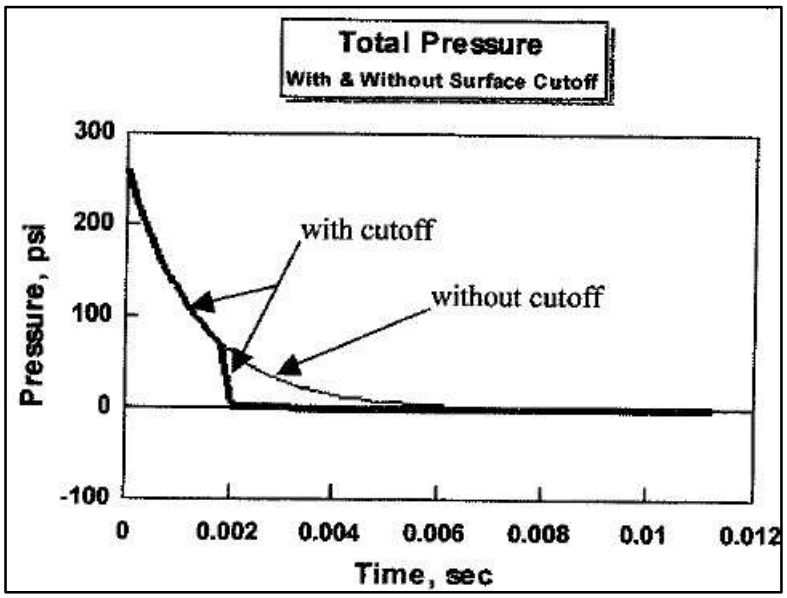

Figure 2.6 Change in pressure caused by free surface cut-off (Scavuzzo & Pusey [2.23])

2.5.3 Reflection caused by the seabed

In the case of the reflection caused by the seabed, the pressure wave that reaches the bottom of the sea, due to the different density of sea water and bottom, is partly transmitted to the ground (as a seismic wave) and partly reflected in the water above, with the consequence that one or more positive pressure peaks are added to the direct shock wave. See **Figure 2.7**.

For the purposes of the determination of the arrival delay Δt, it can be assumed that the wave reflected from the seabed is produced by a charge positioned symmetrically to the water-bottom demarcation line, as made for the previous case of the free-surface reflection.

Therefore, the reflection wave caused by the seabed produces a positive pressure on the measurement point which must be corrected for the effects of soil constituting the seabed. The pressure values relative to the reflected wave, which theoretically (in case of ideal bottoms of infinite density) should be double respect to the direct charge, must be multiplied by reflection coefficients K that depend by the structure of the seabed and the angle of incidence of the shock wave.

The impact of the wave with the seabed generates a movement of the particles both in the direction of the incident wave (longitudinal waves), and in the normal direction (transverse waves). These

propagation waves reach maximum values as a function of the critical angles of incidence β, above which a clear reduction is achieved. In **Figure 2.8** the paths of the reflected wave, the incident wave and the one dispersed in the ground are shown. Some formulas achieved by experimental tests are reported by D'Andrea in [2.8] in order to assess the reflection coefficient K. In addition, in **Figure 2.9**, some graphs in which for a different type of seabed (in order from left to right: mud, sand, rock, mixed mud and sand), this K value is reported in function of different angles of incidence. In summary, the reflection coefficient K results in the lowest values when the shock wave affects soft bottoms, acoustically similar to water, such as mud, while it assumes the maximum values in correspondence of rigid rocky bottoms. In the case of a charge placed on the seabed, the pressure peak can be calculated multiplying the value of the pressure that the charge would have in open water by the (1 + K) factor.

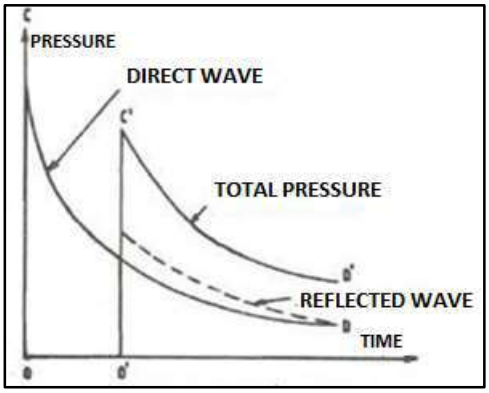

Figure 2.7 Representation of the effects of the reflection of the seabed on the total pressure (image adapted from D'Andrea [2.8])

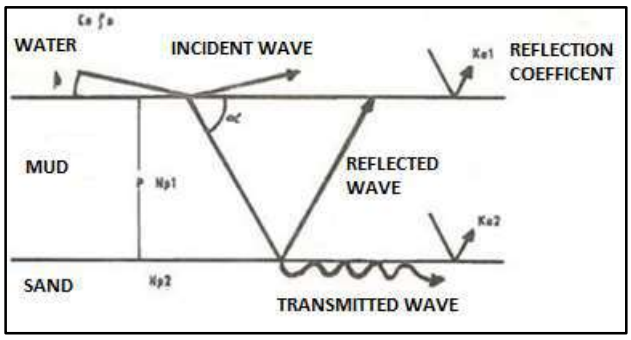

Figure 2.8 Path of the reflected wave on a seabed made by two different types of sedimentation (image adapted from D'Andrea [2.8])

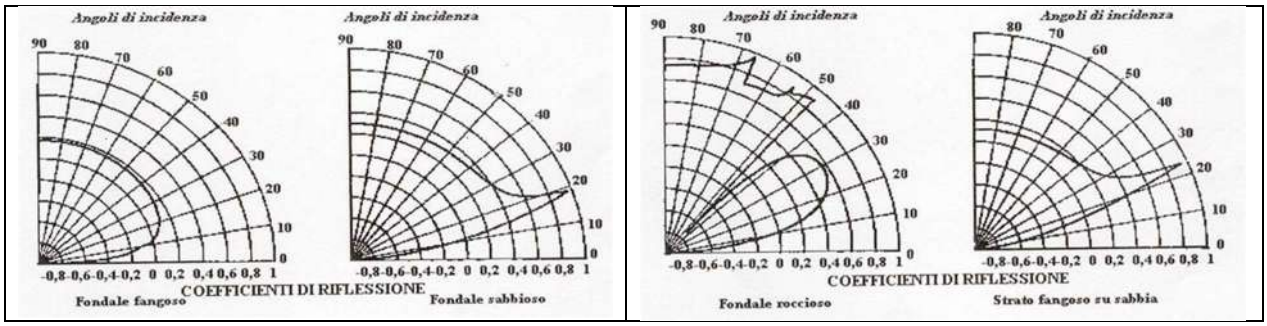

Figure 2.9 Values of the reflection coefficient K as a function of seabed type and angle of incidence (D'Andrea [2.8])

2.5.4 Total pressure at a measurement point in water

The total pressure $P(t)$ provided by the shock wave at a given measurement point is given by the algebraic sum of the direct wave pressure and of the pressure reflected by the free surface and by the bottom. Namely the pressure time history shown in **Figure 2.10** results:

$$P_{tot}(t) = P(t)_{\text{direct wave}} + P(t)_{\text{wave reflected from the free surface}} + P(t)_{\text{wave reflected from the bottom}} \quad (2.13)$$

From the mathematical point of view, it can be admitted that the $P(t)$ function has an almost exponential trend in the first 2/3 of the decay of the shock wave, after which, to consider a realistic phenomenon, it is necessary to employ a series of parameters and formulas, valid for TNT, available in the literature, and reported by D'Andrea [2.8].

The times, considering as a reference the instant of explosion, in which the shock waves arrive at the measurement point can be calculated as follows:

- Time between the detonation and the arrival of the shock wave in msec: $t_D = \frac{D}{c_0/_{1000}}$
- Time between the arrival of the shock wave and the reflection of the seabed in msec: $t_f = \frac{D_f}{c_0/_{1000}} - t_D$
- Time between the arrival of the shock wave and the reflection of the free surface in msec: $t_s = \frac{D_s}{c_0/_{1000}} - t_D$

where D is the path of the direct wave, while D_f and D_s are the distances travelled by the reflected wave from the free surface and from the bottom.

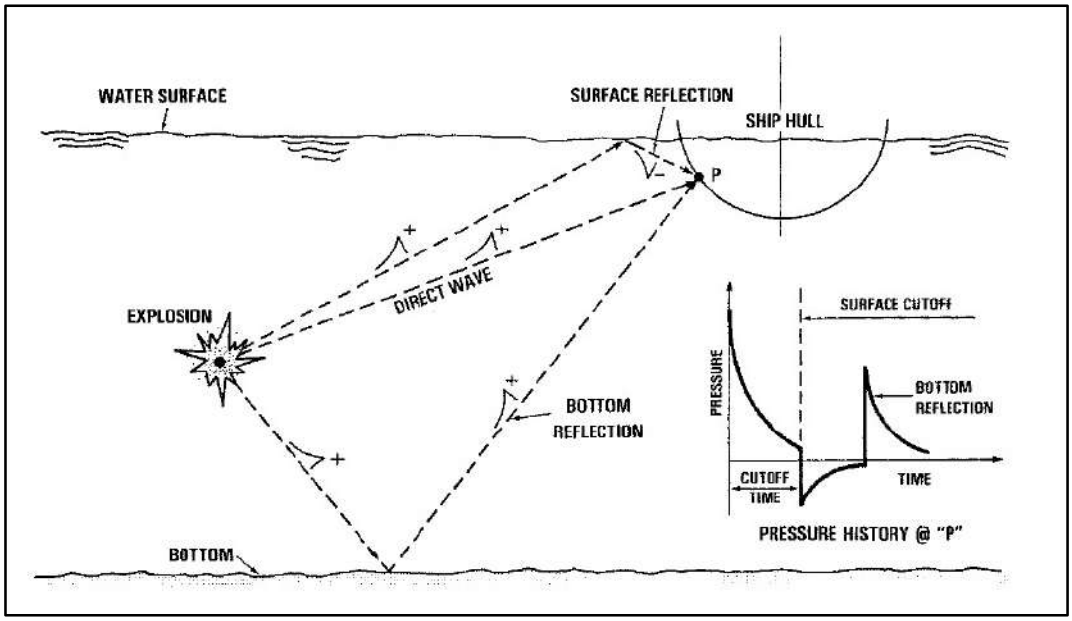

Figure 2.10 Pressure time history resulting curve (Costanzo [2.5])

2.6 The gas bubble

2.6.1 The phenomenon of the bubble pulse

Immediately after the formation of the shock wave front, the hyper compressed gases begin to expand rapidly, considering that the speed at the air/water interface is about 2500 m/s. The so-called "bubble" is formed, which expands at an early stage: the pressure of the gases inside decreases until it reaches the external hydrostatic pressure. However, due to the radial inertia forces of gases and water, the bubble continues to expand to a maximum radius, until the internal pressure will be much lower than the hydrostatic one and the friction forces will prevail over those of inertia. At this point, the hydrostatic pressure takes over, the inertial motion of the water reverses and the bubble compresses to a minimum radius, which is the result of the balance between internal gas pressure, hydrostatic pressure and inertial force of water. In this condition the internal pressure of the gases is much greater than the hydrostatic one, reaching even hundreds of atmospheres. A second "pneumatic" explosion occurs, with the emission of a second pressure pulse, which is about 15-20 % of the primary one. The sequence repeats in time, according to a series of expansion-contraction cycles, which is why it is said that the bubble begins to pulsate. A translation motion called "migration" is added to this oscillatory movement: it is the result of the force of gravity, buoyancy and surface effects, such as those of the seabed and any rigid surfaces. See **Figure 2.11**.

Due to the loss of energy that occurs at each cycle, the maximum radius gradually decreases, while the minimum one increase in size. In addition, the velocity of the gas bubble is not uniform, but it

grows, at first very slowly, then very quickly at the minimum radius: the bubble is subjected to a strong acceleration, and it moves rapidly in the direction of motion. Then, the average speed of this migration motion decreases as the average radius increases, as the resistance to motion increases. Therefore, this vertical motion reaches the maximum speeds when the bubble radii are smaller and the minimal velocities when the radii are larger.

Another important aspect of the bubble migration is the phenomenon of "jetting", which occurs as a result of the deformation of the bubble during its contraction. In the expansion phase the bubble is symmetrical, while in the contraction phase, the lower part moves vertically faster than the upper one, in such a way that it first becomes flat and then it takes the form of a " cap of a mushroom". A jet of water can infiltrate the lower part of the bubble and proceed until it breaks the upper part of the bubble and penetrates the layer of water above. This happens because small random distortions of the external layer of the bubble occur. They, which can be considered as "ripples", alter the pressure state of the surrounding water, changing its direction of flow. More details are reported by Petralia [2.21].

The characteristic parameters of the pulsating bubble phenomenon, which can be calculated by means of analytical expressions derived from experimental data on TNT from the studies of Taylor [2.29] and Cole [2.4], are the following:

- Oscillation period:

$$T = 2.1\frac{W^{1/3}}{(Z+10.3)^{5/6}}\ [s] \tag{2.14}$$

- Maximum radius:

$$R_{max} = 3.3\frac{W^{1/3}}{(Z+10.3)^{1/3}}\ [m] \tag{2.15}$$

- Minimum radius:

$$r_{min} = 8.24\frac{W^{5/9}}{(Z+10.3)^{11/9}} + 0.007W^{5/16}\ [m] \tag{2.16}$$

- Path of the charge to the minimum radius:

$$h = 13.2\frac{W^{11/24}}{(Z+10.3)^{5/6}}\ [m] \tag{2.17}$$

- Peak pressure at the minimum radius:

$$P_{rm} = 19.4\frac{3W}{4\pi D_b r_m^2}\left(1 - 0.1581\frac{W^{1/4}}{r_m^{3/4}}\right)\left[\frac{kg}{cm^2}\right] \tag{2.18}$$

These parameters are defined as a function of the mass of the explosive (W) in [kg], the depth of the charge (Z) in [m] and the distance of the measurement point from the center of the charge at the first minimum radius (D_b) in [m]. In **Figure 2.12** it is shown a graph in which the variation of the radius is reported as a function of the weight and the depth of the charge.

Some studies, made by the Explosion Research Departement U.S. Naval Laboratory, reported by Swisdak [2.27], correlated energy and impulse of the first bubble pulse as a function of the weight of the charge. Some examples of applications of these formulas are reported by Sulfredge et al. [2.25].

In addition, some studies have been performed in order to assess the dynamic behaviour in water. In particular, Geers and Hunter [2.14] provided an integrated model to predict the bubble-surface equation of motion in fluid, determining a theoretical law of the displacement time history of bubble radius, which is in agreement with experimental data.

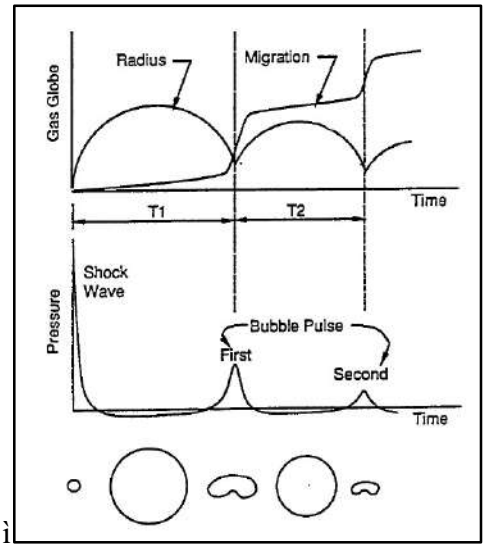

Figure 2.11 Oscillation and migration mechanism of the gas bubble (Reid [2.22])

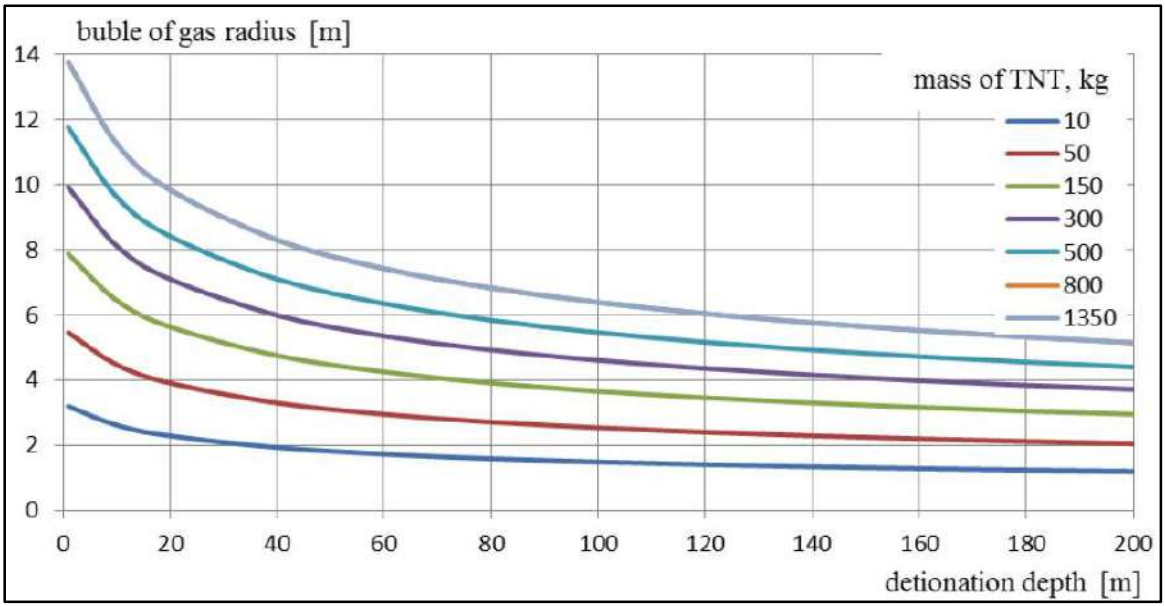

Figure 2.12 Radius of the gas bubble as a function of the mass of the charge and the detonation depth (Szturomski [2.28])

2.6.2 Effects of the interaction with surfaces

The bubble motion is influenced by the effects of the seabed and rigid surfaces according to an attractive component and by the effects of the air/water interface surface according to a repulsive component. A pressure gradient is created around the bubble: it is positive in the expansion phase, which involves a removal from the rigid surfaces, while in the compression phase it is negative. In particular, this difference of pressure is higher (more negative) on the bubble side close to the rigid surface where there is less possibility of compensation of the pressure field by the water flux. This is the reason why the bubble gets closer to the rigid surface in this phase. The predominant action is that of pushing towards the wall that occurs in the contraction phase, considering that this last phase has a longer duration than that of expansion and that the hydrostatic forces are less important on smaller bubbles than on larger bubbles. On the contrary, the effect of the free surface is always repulsive, as the pressure at the air/water interface is always constant, and the gradient of pressure around the bubble is always positive. Therefore, the bubble is always removed and pushed away from the free surface.

In summary, the bubble is attracted by the rigid surfaces and the seabed, increasing its period of oscillation, while it is moved away from the free surface, reducing its period of oscillation. In addition, a charge placed on the seabed tends to remain anchored to the bottom and to generate at its first compression a pressure peak higher than the charge in a free field. This phenomenon can be explained considering that there is a lower loss of energy than the charge in free field. Corrective formulas of

the oscillation period and the path of the charge that take into account the interactions with the surfaces are reported by Cole in [2.4].

2.6.3 Secondary pressure generated by the gas bubble

The trend of the secondary pressure curves caused by the gas bubble, shown in the **Figure 2.13**, follows different laws from those obtained by the shock wave. According to Cole [2.4], it has been experimentally detected that the pressure pulse generated by the first minimum of the gas bubble follows a Gaussian trend, the shapes and sizes of which depend on the physical characteristics of the charge and the explosion geometry. In addition, the resulting curve of the bubble pulse is influenced by the free surface and the seabed.

This shape can be obtained referring to a model provided by Bryant and Chambers [2.3] and described by D'Andrea [2.9]: if the explosion geometry and the weight of the charge are known, the pressure value for each instant can be obtained, using graphs obtained according to the theory.

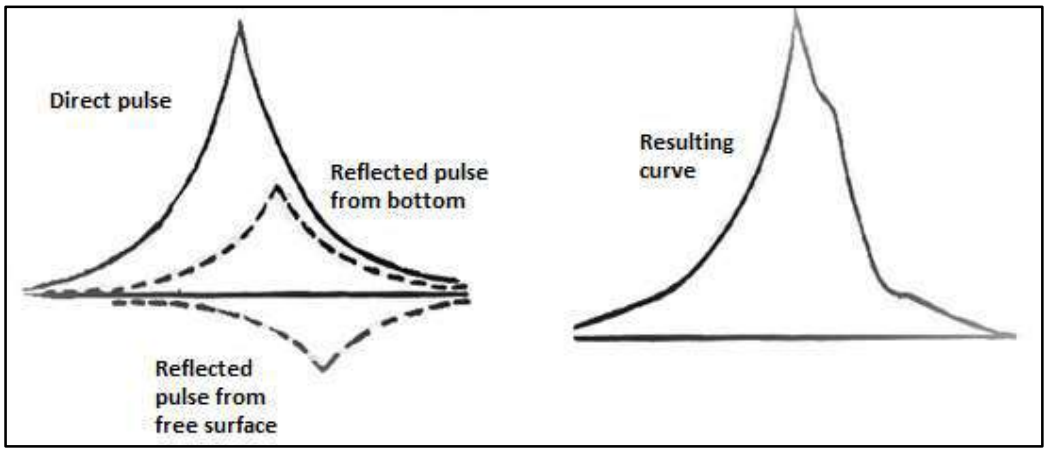

Figure 2.13 Trend of the secondary pressure generated by the shock bubble (image adapted from [2.4])

2.6.4 Effects on the free surface

When the shock wave reaches the free surface, the water particles are launched vertically upward to form a dome with an initial velocity which is about twice that of the shock wave, obtained by the sum of the velocities of the incident and the reflected front wave. On the free surface, sprays are formed that, nebulizing, give it a whitish appearance.

Petralia [2.21] presents some empirical formulas for calculating the raising velocity of the dome as a function of the weight and position of the explosive.

The passage of the negative tensile wave involves the boiling of the free surface, according to a phenomenon called "bulk cavitation", easily visible from above as a circular area that whitens very quickly until it reaches a diameter equal to the front of the incident wave. Once the gas bubble reaches the surface, however, "plumes" are formed, splashes of water that rise perpendicularly and radially to the surface. See **Figure 2.14**. If the bubble is near the free surface in the maximum compression phase, a violent spray called "piper" is generated, which could reach considerable heights. The formation of plumes depends on the weight, the depth of the charge, the seabed and the state of the sea and in principle it can be said that, for explosions which occur at high depth, the plumes are significantly smaller and less energetic.

In case of explosions which occur very close to the free surface, the layer of water in contact with the shock wave vaporizes and the products of the explosion emerge at high speed, transporting nebulized water and vapor: they move outwards "fan-like" forming a crown of smoke that progressively becomes almost spherical. A summary of the effects of underwater explosions is shown in **Figure 2.15**.

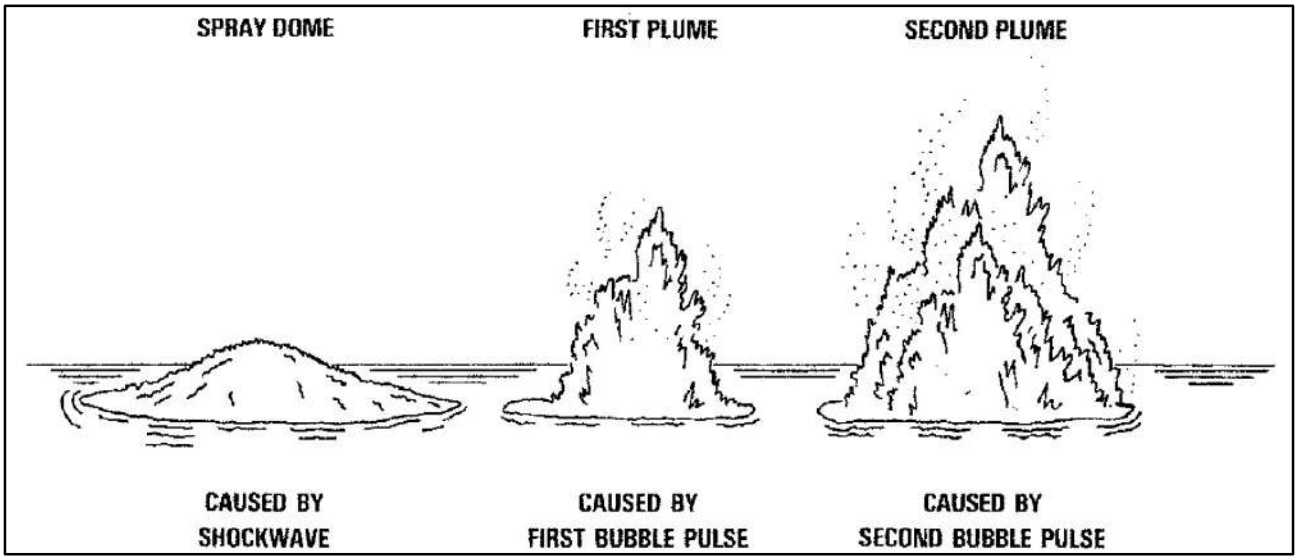

Figure 2.14 Effects on the free surface caused by shock wave and bubble pulses (Costanzo [2.5])

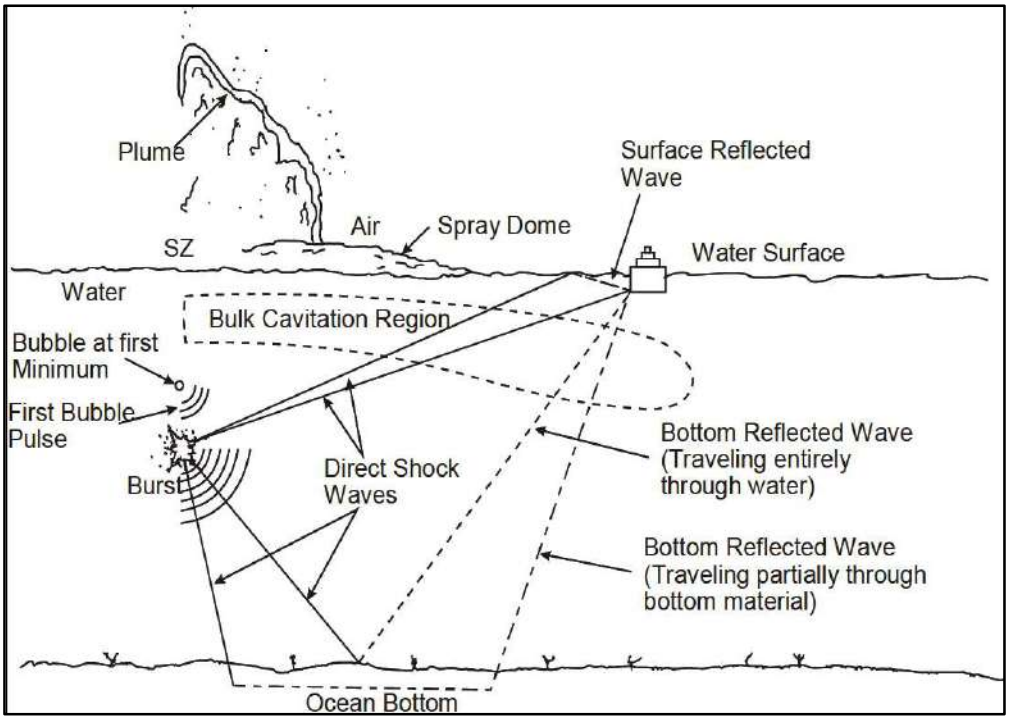

Figure 2.15 Summary of the effects of UNDEX (Costanzo [2.5])

2.7 Bulk cavitation

Bulk cavitation is the phenomenon that occurs when the shock wave reaches the surface and is reflected as a tensile wave. Water is not able to sustain this type of tension and it cavitates, transforming itself from homogeneous and continuous liquid to non-homogeneous and cavitating liquid. In this state the cavitation zone is not able to transmit any disturbance resulting from the shock. See **Figure 2.16**. The cavitation region is not fixed in time, but it expands as the front of the shock wave reflected from the free surface moves, following the movement of the shock wave. In Figure **2.17** it is shown in white the maximum extent of the bulk cavitation region in the fluid.

The phenomenon is particularly important, since, once the shock front and the wave reflected from the surface have passed, due to gravity and atmospheric pressure from above and the displacement of fluid due to the gas bubble from below, this cavitation zone closes, generating an additional pressure pulse, similar to a hammer impact. The initial point of collision between the two surfaces is located about a quarter of the cavitation region, as can be seen in **Figure 2.18**.

Therefore, this cavitation pulse produces an additional compression load on the target, resulting in a phenomenon that continues until the cavitation layer is completely closed. In most cases this pulse is smaller than the pressure of the shock wave and the pulses of the gas bubble. However, in certain explosion geometries it can be the cause of extensive damage to the hull of naval units. In **Figure 2.19** an example of the pressure pulse caused by the closure of bulk cavitation is shown.

An analytical model to determine the pressure and the duration in time of this further hammer is shown by Costanzo and Gordon in [2.6].

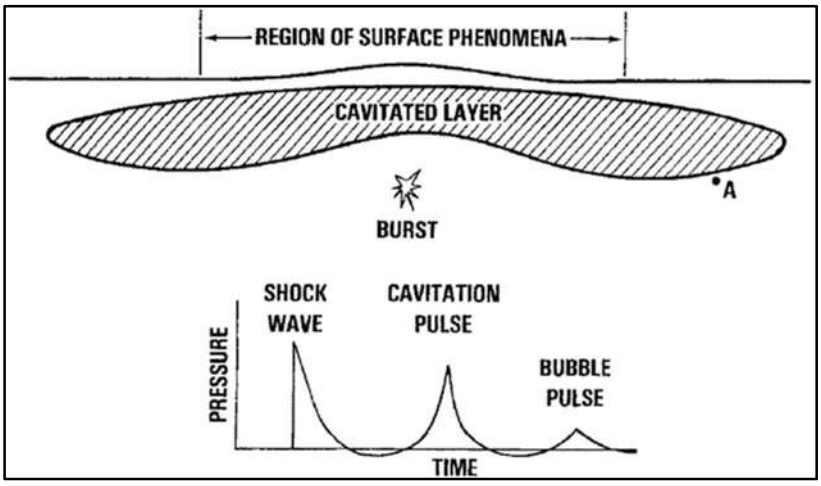

Figure 2.16 Effects of cavitated layer (Costanzo [2.5])

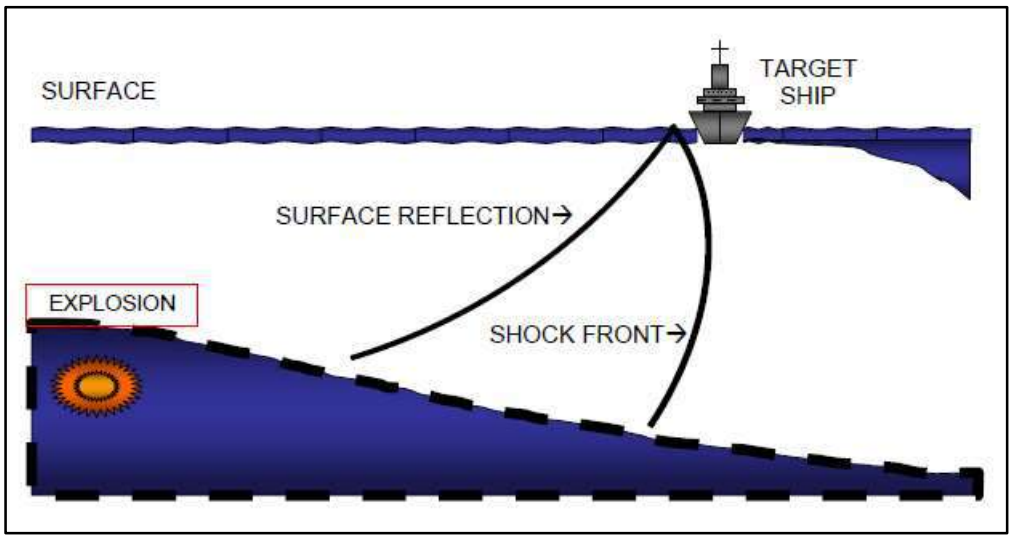

Figure 2.17 Formation of the region of bulk cavitation (Costanzo [2.5])

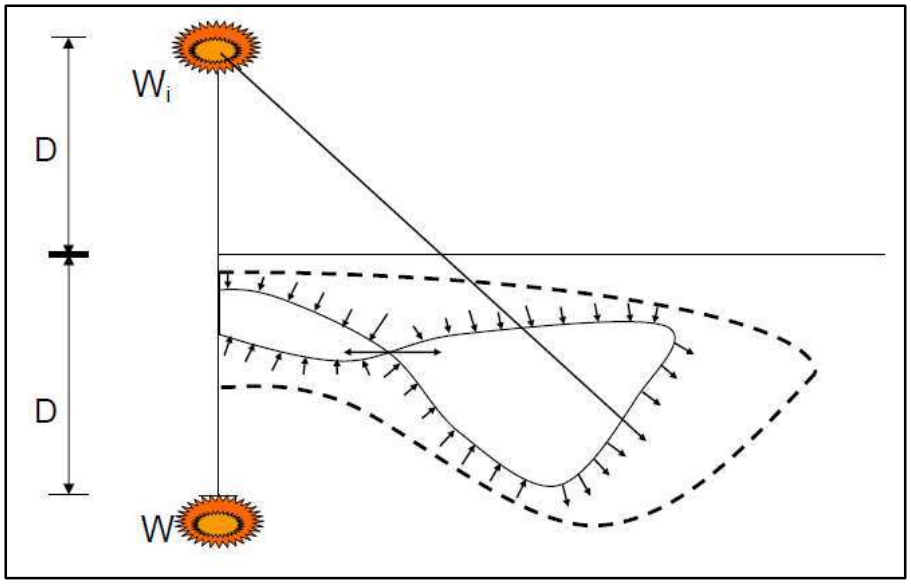

Figure 2.18 Closure of bulk cavitation zone (Costanzo [2.5])

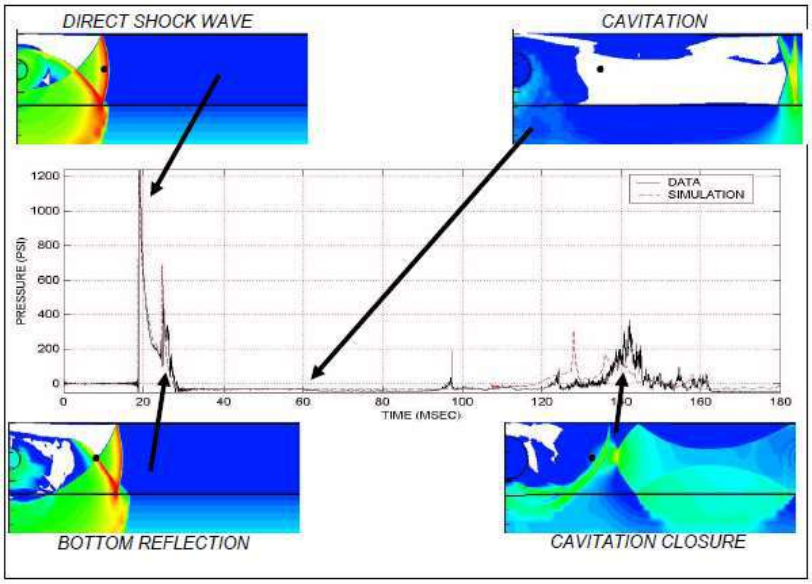

Figure 2.19 Cavitation pulse caused by the closure of the cavitation region (Costanzo [2.5])

2.8 Refraction

The refraction of shock waves is a phenomenon that has a certain relevance when dealing with large scenarios and when the water presents a consistent variation of the temperature gradient in depth. In this situation, the assumption of a linear propagation of shock waves such as the acoustic ones fails, as the temperature gradient leads to a variation in the wave speed causing refraction. Therefore, the shock wave is diverted from its original linear trajectory. This phenomenon can lead to the presence of blind spots that are not affected by the propagation of shock waves. In **Figure 2.20** several scenarios are shown, which differ from each other for the position of the charge and the speed gradient

in the water: for example, in the first explosion the shock waves pass below the position of the charge, therefore the transfer of energy on the target is less than that obtained considering the fluid where the sound velocity is constant. These effects must be considered when referring to scale effects on the resulting pressure loads or target response data.

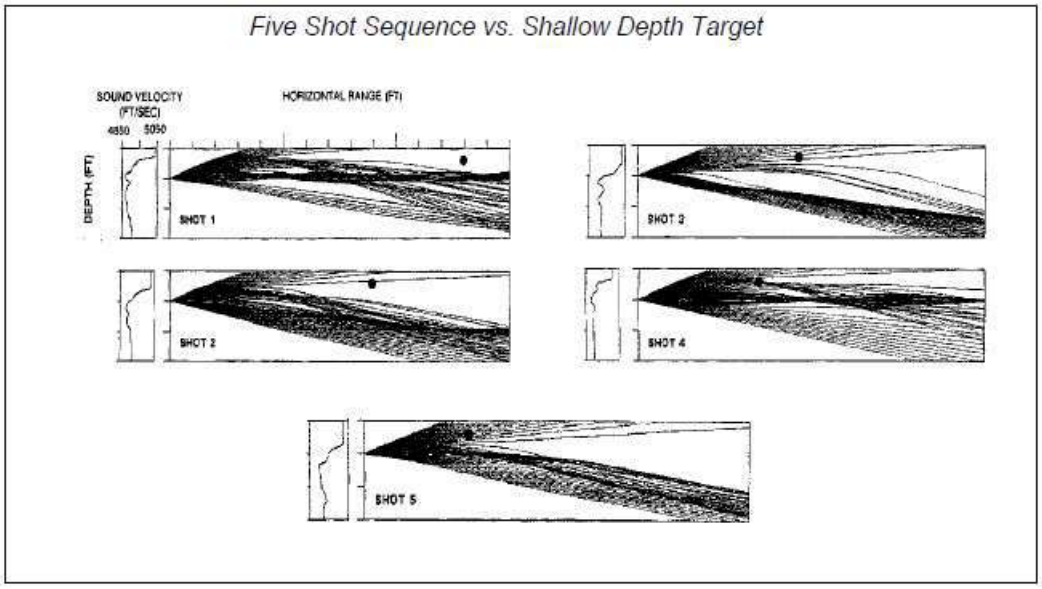

Figure 2.20 Effects of refraction on the shock waves (Costanzo [2.5])

2.9 Bibliography

[2.1] Apazidis N., "Numerical investigation of shock induced bubble collapse in water", Physics of Fluids 28 (4) 046101, 2016;

[2.2] Apazidis N., Lesser M., Tillmark N., Johansson B., "An experimental and theoretical study of converging polygonal shock waves", Shock Waves 12 (1), 39–58, 2002;

[2.3] Bryant A. R., Chambers Li. G., *The theoretical shape of the pressure pulse produced by an underwater explosion bubble*, Naval Construction Research Establishment, 1950;

[2.4] Cole R. H., *Underwater explosions*, Woods Hole Oceanographic Institution, 1914;

[2.5] Costanzo F. A., "Underwater Explosion Phenomena and Shock Physics", Society for Experimental Mechanics Inc, Jacksonville, Florida USA, 2010;

[2.6] Costanzo F. A, Gordon J. D., "A Solution to the Axisymmetric Bulk Cavitation Problem", The Shock and Vibration Bulletin, 53, Naval Research Laboratory, Washington D.C., 1983;

[2.7] D'Andrea A., *Studio per una valutazione di massima del comportamento di elementi strutturali semplici di scafi navali sottoposti ad esplosioni non a contatto*, MARIPERMAN, La Spezia, 1992;

[2.8] D'Andrea A., *La dinamica dell'esplosione subacquea*, MARIPERMAN, La Spezia, 1992;

[2.9] D'Andrea A., Scaini S., *Calcoli di dinamica dell'esplosione*, Nane Edizioni, Roma, Novembre 2015;

[2.10] Eliasson V., Apazidis N., Tillmark N., "Controlling the form of strong converging shocks by means of disturbances", Shock Waves 17, 29–42, 2007;

[2.11] Eliasson V., Henshaw W. D., Dimotakis P. E., "Simulations of converging shocks in water", The Journal of the Acoustical Society of America 125 (4) 2601, 2009;

[2.12] Eliasson V., Qiu S., "Interaction and coalescence of multiple simultaneous and non-simultaneous blast waves", Shock Waves 26 (3), 2015;

[2.13] Friedman N., *The Naval Institute Guide to World Naval Weapons Systems 1991/92*, Naval Institute Press, 1991;

[2.14] Geers, T. L., Hunter, K. S., 2002. An integrated wave-effects model for an underwater explosion bubble. Acoustical Society of America.

[2.15] Ghoshal R., Mitra N., "Non-contact near-field underwater explosion induced shock-wave loading of submerged rigid structures: nonlinear compressibility effects in fluid structure interaction", Journal of Applied Physics 112 024911, 2012;

[2.16] Ghoshal R., Mitra N., "Underwater oblique shock wave reflection from submerged hydraulic structures", Ocean Engineering 209 107324, 2020;

[2.17] Henrych J,, *The Dynamics of Explosion and its use*, Vol 1-2, Elsevier Scientific Publishing Company, Amsterdam Oxford New York, 1979;

[2.18] Keil A.H., "The Response of Ships to Underwater Explosions", Society of Naval Architects and Marine Engineers, New York, 16-17 Novembre 1961;

[2.19] Marinò A., Appunti di *"*Corso di Navi Militari e Sommergibili*"*, Università di Trieste, 2012;

[2.20] McGoldrick, R. T., Gleyzal, A. N., Hess, R. L., Gess Jr., G. K., "Recent Developments in the Theory of Ship Vibration", David Taylor Model Basin Report 1451, pp. 2-6 – 2-9, December 1960;

[2.21] Petralia S., *Compendio di esplosivistica*, MARIPERMAN, La Spezia, 2000;

[2.22] Reid W. D., *The Response of Surface Ships to Underwater Explosions*, Australian Department of Defence, 1996;

[2.23] Scavuzzo R.J., Pusey H.C., *Naval Shock Analysis and Design*, The Shock and Vibration Analysis Center, HI-TEST Laboratories, Inc., Second Printing 2002;

[2.24] Sommerfeld M., Müller H. M., "Experimental and numerical studies of shock wave focusing in water", Experiments in Fluids 6, 209-216, 1988;

[2.25] Sulfredge C. D., Morris R. H., Sanders R. L., *Calculating the Effect of Surface or Underwater Explosions on Submerged Equipment and Structures,* Oak Ridge National Laboratory, Tennessee, 2008*;*

[2.26] Sundarapandian S., Liverts M., Tillmark N., Apazidis N., "Plane shock wave interaction with a cylindrical water column", Physics of Fluids 28 (5) 056102, 2016;

[2.27] Swisdak M. M. Jr, *Explosion Effects and Properties: Part II – Explosion effects in water*, Naval Surface Weapon Center, 1978;

[2.28] Szturomski B., "The effect of an underwater explosion on a ship", scientific Journal of Polish Naval Academy, 2015;

[2.29] Taylor G.I., "The pressure and Impulse of Submarine Explosion Waves on Plates", Ministry of Home Security Report, FC 235, 1941;

[2.30] Zamyshlyaev B. V., Yakovlev Yu. S*., Dynamic loads in underwater explosion,* Naval Intelligence Support Center Washington, D. C., 1973.

3 The effects of underwater explosions on naval vessels

3.1 Contact and non-contact UNDEX explosions

Underwater explosions involving naval units can be divided into contact and non-contact explosions according to their distance from the ship. As reported by Szturomsky in [3.15], contact explosions are occur at a distance between 0 and 12 meters from the hull: in this case the explosive gases penetrate directly inside the hull, causing extensive damage. In the case of small naval units, with a single floodable compartment, this type of explosion generally leads to sinking, while in the case of larger ships, in which more floodable compartments are provided, this scenario can provide a severe impulse on the ship hull, but the vessel can maintain residual buoyancy and stability. However, the damage is extensive, and it takes several months for repairs. See **Figure 3.1**.

Non-contact explosions are considered if the explosive gases of the bubble do not directly affect the hull. They are divided into far or close explosions if they occur respectively at a distance of more or less than 30 meters from the ship. The damaged area generated by a close explosion is larger than the one obtained by a contact explosion: the shock wave impact can generate as a result hull breaking and severe damages to machinery and their foundations (**Figure 3.2**). In addition, experimental tests showed that the largest values of acceleration of the hull occur if an explosion of the same energy occurs in the middle of the ship, rather than at the bow or the stern of the vessel.

Non-contact explosions that occur relatively fat from the ship (more than 30 meters) usually do not lead to hull breakage, but they can provide plastic deformations (in the form of "indentation") (see **Figure 3.3**). In this case the longitudinal position of the explosion relative to the ship (bow, stern, center of the ship) has little influence on the effects of the explosion. The accelerations that are transmitted inside the hull can lead to considerable damage to the equipment; in addition, the area affected by the damage is extended throughout the ship.

Szturomsky in [3.15] provide a correlation between the distance, the weight of the charge and the effects on structures of naval vessels, as shown in **Figure 3.4**.

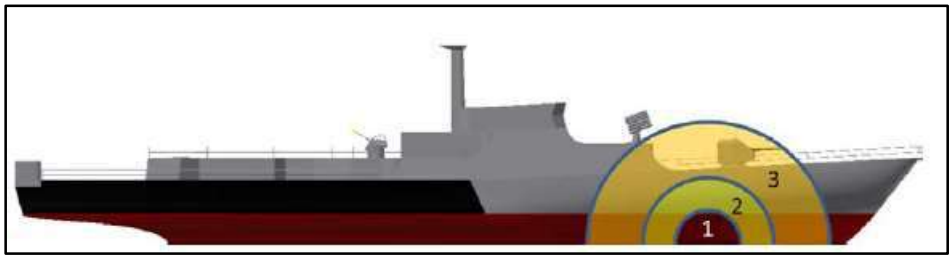

Figure 3.1 Effects of a contact UNDEX explosion: 1 - breach, 2 - melting of structures, 3 - zone of damage to structures and machinery (Szturomsky [3.15])

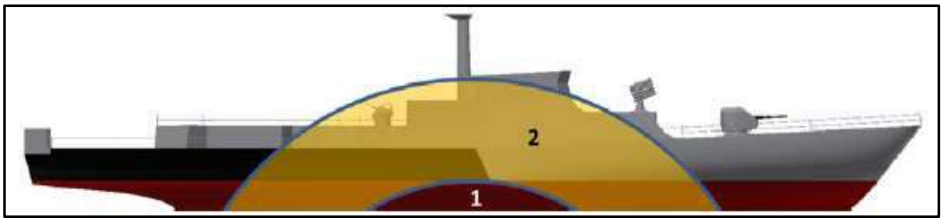

Figure 3.2 Effects of a non-contact UNDEX explosion in close field: 1 - hull breakage, 2 - zone of damage to structures and machinery (Szturomsky [3.15])

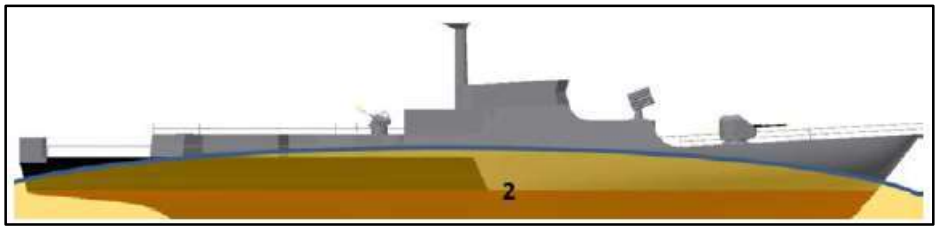

Figure 3.3 Effects of a non-contact explosion in far field: 2 - zone of damage to structures and machinery (Szturomsky [3.15])

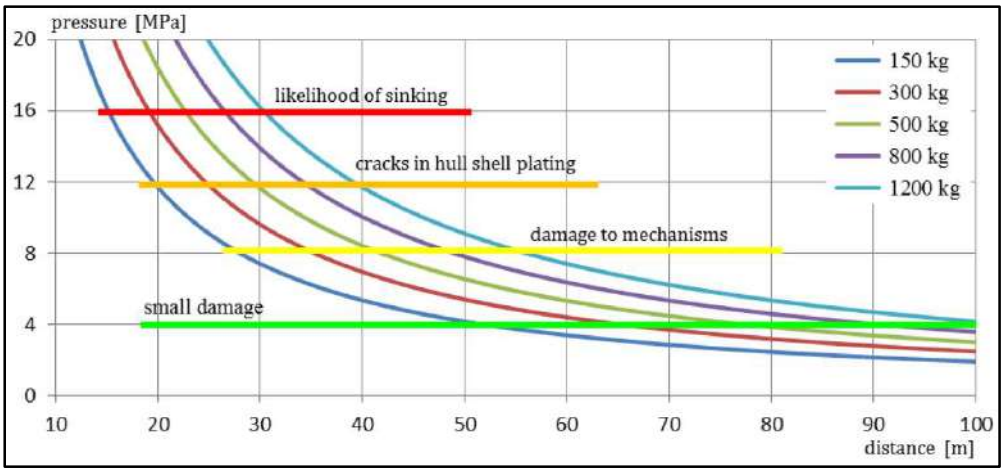

Figure 3.4 Effects of UNDEX on naval vessel as a function of TNT weight and distance from the hull (Szturomsky [3.15])

3.2 Keel Shock Factor

The damage mechanism of a ship involves two parameters: the peak of pressure of the shock wave and the maximum pressure resulting from the pulsation of the gas bubble. Even if the value of the latter is much lower than the shock wave one, it is characterized by a longer duration. Therefore, the respective impulses are comparable in terms of energy level. In case of contact explosions, when the distance of the charge from the keel is less than the maximum radius of the bubble, a non-negligible

importance is the projection of the flow against the target, caused by the deformation of the bubble affecting the rigid surface.

Hence, the needs of defining a factor to identify the severity of the explosion, in order to use it in a design phase, as reported for the first time by Shaw [3.13]. For naval vessels, considering explosions that happen close to the seabed, Keil [3.7] defined the Keel Shock Factor (KSF), as:

$$KSF = \frac{\sqrt{A\gamma W}}{R}\frac{(1+\cos\varphi)}{2} \tag{3.1}$$

where A is a coefficient that takes into account the type of seabed, γ refers to the correction for explosives which are different from TNT, W is the weight of the charge [kg], R represents the distance between charge and keel [m] and $\frac{(1+\cos\ )}{2}$ is a factor that takes into account the position of the explosion (considering φ the angle between the incident radius of the shock wave and the theorical line perpendicular to the keel).

In the case of explosion in deep water, where the seabed and the free surface are not taken into account, the expression is simplified as:

$$KSF = \frac{\sqrt{W}}{R} \tag{3.2}$$

3.3 Types of motions caused by an underwater explosion

As effect of UNDEX, the ship, which can be considered as a beam-hull, is subjected at first to a high acceleration, caused by the peak pressure of the shock wave. The effects of this phenomenon occur in time during the first milliseconds. Before the end of this effects, the ship is affected by the dynamic pressure generated by the first pulsation of the bubble, which remains over time and is about the same order of magnitude as the natural period of vibrating of the beam-hull. Therefore, the vessel begins to swing, according to a phenomenon known as whipping. The risk is that a resonance condition occurs, when the two periods (bubble and beam-hull) are coincident, which could lead to plastic deformations spread over the entire hull and superstructures up to breakage in some zones. The two phenomena (shock wave and bubble pulse) provide different effects on the ship, occurring in different time, as reported by Petralia [3.10] and Keil [3.7].

In summary, as reported by Marinò in [3.8], the interaction of the UNDEX generates the following motion phenomena on naval ship hulls:

- Rigid body motions, consisting of translations and rotations which depend by the characteristics of the charge, the distance and displacement of the vessel. The most important of the translational motions is that of heave, combined with the rotational motions of roll and

pitch depending by the position of the charge. They are also connected to other effects of the explosion, in particular to the wave motion generated by the discharge into the atmosphere of the gaseous products of the explosion and to the radial motion of the liquid that occurs during the expansion of the gas.

- Elastic motions (vibrations, flexural and torsional oscillations) of the elastic beam to which the naval vessel can be compared. While the primary shock wave causes high-frequency dynamic responses, affecting first the hull plating, then the reinforcements and the machinery installed on their foundations, the oscillations of the bubble provide low-frequency pulsating loads that can be dangerous if their frequency is close to the first natural frequency of the hull beam. In the latter circumstance, a resonance condition is created in which a global response of flexural oscillations in the longitudinal direction of low frequency and large amplitude (whipping) is excited, which can cause severe structural damage. On the contrary, the stresses imposed by this motion on the on-board equipment are generally low, thanks to the low level of acceleration to which it is affected. For particularly severe loads, whipping can cause permanent damage (failure due to instability of structures and cracks) to the hull. These loads can also cause extensive damage to personnel.
- Elastic or plastic deformation, depending on the severity of the explosion, of the hull area closest to the point where the explosion occurs.
- "Local" motions (not limited to the hull area adjacent to the explosion) transferred through the structures, inside the hull, reaching decks, bulkheads and superstructures. The structures of the ships, in fact, transmit the shock load with little damping, therefore the motions induced in areas which are far from the explosion zone can be severe and cannot be neglected.

3.4 Interaction between ship hull and pressure caused by explosions

There are two simplified models for studying the fluid-structure interaction between shock pressure and hull plating:

- Air-backed or water-backed flat plate of infinite extension
- Air-backed or water-backed flat plate of large extension of limited area fixed at the edges on a perfectly rigid and fixed support.

These theories are well-described by Taylor in works [3.9] [3.16]. The first method is suitable for naval hulls, the second is considered when the plate is fixed to particularly robust constraint or in case of small-scale targets.

3.4.1 Infinite air-backed plate theory

Referring to **Figure 3.5**, the equation of motion of a plate subjected to an underwater shock can be described as follows:

$$m\frac{d^2x}{dt^2} + kx = p_i + p_r \tag{3.3}$$

where x is the displacement of the plate, p_i and p_r are the pressure of the incident and reflected wave and m and k are the mass and the stiffness per unit area.

The pressures of the incident and reflected shock waves can be written as $p_i = \rho c u_i$ and $p_r = \rho c u_r$, where u_i and u_r are their velocities, ρ and c are respectively the density and the water velocity.

The resulting velocity of the plate is: $u = u_i - u_r$. It can be written in terms of pressures as:

$$P = \rho c\frac{dx}{dt} = \rho c u_i - \rho c u_r \tag{3.4}$$

from which it is possible to obtain:

$$p_r = p_i - \rho c\frac{dx}{dt} \tag{3.5}$$

This expression, replaced in the initial equation, provides the differential equation of motion:

$$m\frac{d^2x}{dt^2} + \rho c\frac{dx}{dt} + kx = 2p_i \tag{3.6}$$

In the initial phase of motion, up to the time when p = 0, the term kx (elastic) can be neglected, and, considering $p_i = P_m e^{-\frac{t}{\vartheta}}$, it is possible to integrate the previous expression, obtaining displacement, velocity and total pressure on the plate as a function of time.

The equations of velocity and total pressures are:

$$v = \frac{2P_m\vartheta}{m(1-\lambda)}\left[e^{-\frac{\lambda t}{\vartheta}} - e^{-\frac{t}{\vartheta}}\right] \tag{3.7}$$

$$p = p_i + p_r = 2p_i - \rho c v = \frac{2P_m}{\lambda - 1}\left[\lambda e^{-\frac{\lambda t}{\vartheta}} - e^{-\frac{t}{\vartheta}}\right] \tag{3.8}$$

in which there is the following dimensionless quantity:

$$\lambda = \frac{\rho c\vartheta}{m} \tag{3.9}$$

Through this equation of the plate motion, it is possible to obtain the maximum displacement. However, this value is not acceptable, as it does not take into account the presence of the plate, resulting in a double value compared to that it would be obtained without the presence of the target itself (case of water always in contact with the plate).

On the contrary, it is possible to solve the equation up to the time t_0 when p=0 and the velocity is at its maximum.

Considering p=0, it results that:

$$t_0 = \frac{\vartheta}{(\lambda - 1)} \ln \lambda \tag{3.10}$$

From here the maximum velocity of the plate is achieved, equal to:

$$v_m = \frac{2P_m}{\rho c} \lambda^{(\frac{1}{1-\lambda})} \tag{3.11}$$

Beyond time t_0, these solutions are no longer valid as it is no longer possible to neglect the term kx (elastic).

Using the expression of kinetic energy, it is possible to calculate the maximum displacement x_{max}:

$$E_c = \frac{1}{2} k x_{max}^2 = \frac{1}{2} m v_m^2 \tag{3.12}$$

However, this x_{max} value, calculated by this model, is lower than that measured by experimental data. This phenomenon can be explained by considering that after time t_0, a depression regime is created, in which cavitation occurs. The plate detaches from the water at v_m velocity and it is progressively slowed down by the elastic resistance kx and by the constraints to which it is fixed. This slowdown results in the reconstruction of a new mass of water and a further transfer of kinetic energy that involves a greater displacement than previously calculated.

A representation of the total pressure P_t and the velocity v shown by the plate is reported in **Figure 3.6.**

According to D'Andrea in [3.4], the ratio between the kinetic energy per unit area of the plate E_c and the kinetic energy the shock wave in the free field E_p calculated theoretically is much lower than that measured experimentally.

E_p can be obtained by using the following formula:

$$E_p = \frac{{P_m}^2 \theta}{2\rho c} \tag{3.13}$$

For naval hulls, where usually $\lambda > 5$, this ratio becomes $\frac{E_c}{E_p} \approx 0{,}9$, which is a higher value compared to the theoretical one of 0.5. The analysis of this ratios highlights that an appreciable amount of extra energy transmitted by cavitation phenomena occurs.

The previous formulas refer to a case in which the incident wave hits the target plate in the perpendicular direction. In the case of an oblique wave, in which an angle β is obtained between the surface of the plate and the direction of the wavefront, the above equations must be modified by considering $P_m cos\beta$ in place of P_m and $mcos\beta$ instead of m.

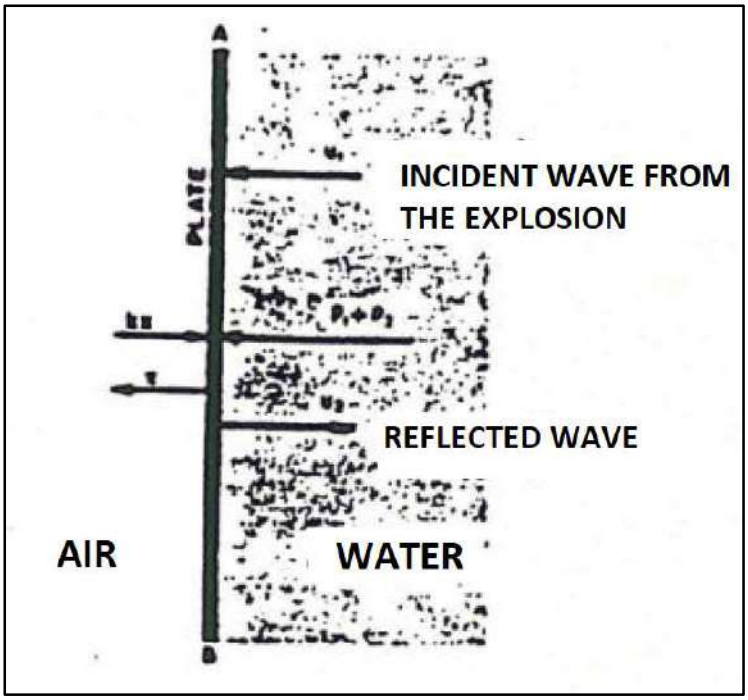

Figure 3.5 Incident and reflected shock waves on an infinite plate (image adapted from D'Andrea [3.4])

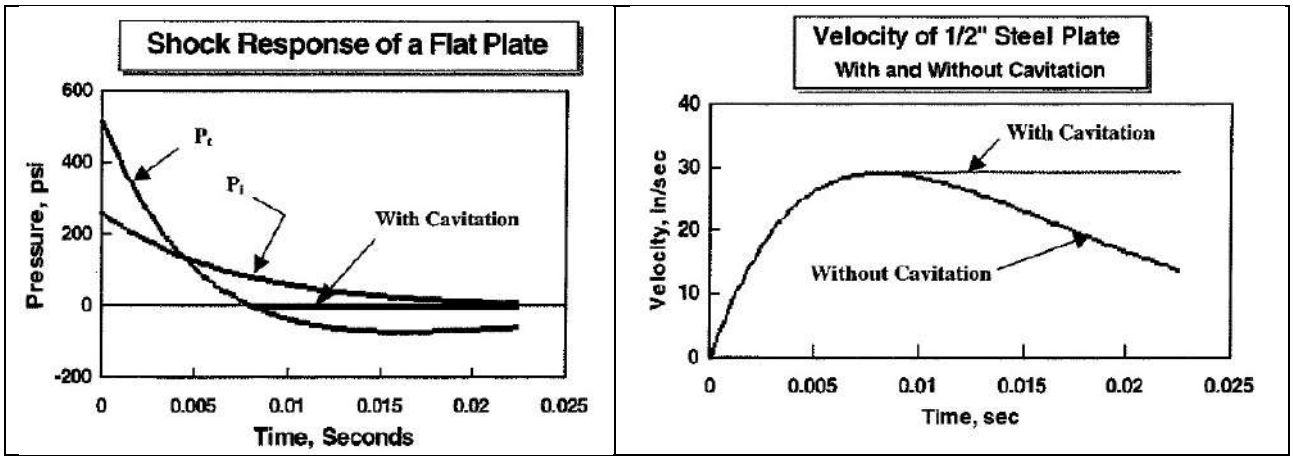

Figure 3.6 Total pressure P_t (on the left) and Velocity (on the right) resulting from the infinite air-backed plate theory (Scavuzzo & Pusey [3.12])

3.4.2 Infinite water-backed plate theory

The water-baked theory represents the case in which there are wing tanks or double hulls full of liquids. Such tanks, if properly realized, can significantly mitigate the effects of explosion.

In **Figure 3.7**, a scheme of a tank is shown, in which two plates of infinite size separate three different spaces in which there are respectively water, liquid and air.

As a result of the shock wave, the outer plate will move with a velocity v and transmit to the tank a pressure equal to $p_{int} = \rho c v$.

Taking into account the direction of the pressures, the total pressure on the outer plate is:

$$p = p_i + p_r + p_{int} = 2p_i - 2\rho c v \tag{3.14}$$

The equation of motion becomes:

$$m\frac{d^2x}{dt^2} + 2\rho c\frac{dx}{dt} + kx = 2p_i \tag{3.15}$$

The above equation can be integrated, making the same assumptions as in the case of the air backed plate theory, namely neglecting the elastic component (kx) and considering that the dimensionless coefficient λ becomes equal to $\lambda_w = \frac{2\rho c}{m}$.

Therefore, the velocity is maximum when the incident pressure (p_i) is equal to the hydrostatic one, which is behind the plate itself (p_{int}), and this condition occurs at the time t_w:

$$t_w = \frac{\vartheta}{(\lambda_w - 1)}\ln \lambda_w \tag{3.16}$$

The value of the maximum velocity is equal to about half that obtained in the air-backed condition. In addition, no cavitation is shown.

The maximum velocity v_{mw} results:

$$v_{mw} = \frac{P_m}{\rho c}\lambda_w^{\left(\frac{1}{1-\lambda_w}\right)} \tag{3.17}$$

In this condition (maximum velocity) the reflected pressure p_r is equal to zero. This can be demonstrated by substituting the values of v_{mw} and t_w in the expression $p_r = p_i - \rho c v_{mw}$. Instead, the pressure transmitted inside the tank, which is equal to the incident one, is obtained as:

$$p_{int} = \rho c v_{mw} = P_m \lambda_w^{\left(\frac{1}{1-\lambda_w}\right)} \tag{3.18}$$

Therefore, the shock wave passes over the outer plate and is transmitted inside the tank, reduced by a factor equal to $\lambda_w^{\left(\frac{1}{1-\lambda_w}\right)}$.

Finally, it is possible to calculate the maximum value of the pressure p_{maxI} transmitted to the inner plate.

Considering a fictitious charge W, placed at a distance D from the outer plate, such as it is able to generate an incident pressure p_{max} equal to $p_{int}(t_w)$.

From the empirical formulas for the peak of pressure generated by the shock wave, explained in Chapter 2, it results:

$$p_{max} = p_{int}(t_w) = 534.22\left(\frac{W^{1/3}}{D}\right)^{1.13} \tag{3.19}$$

from which it is obtained $W^{1/3}$, weight of the fictitious charge, as a function of $p_{int}(t_w)$.

At this point, it is possible to assess the value of p_{maxI} using the same empirical formula used above, substituting to $W^{1/3}$ the weight of the fictitious charge, function of $p_{int}(t_w)$, previously calculated, and placing to D the distance of the charge from the inner plate, which is defined as D + I.

It will then result:

$$p_{maxI} = p_{int}(t_w)\left(\frac{D}{D+I}\right)^{1.13} \tag{3.20}$$

At this point the knowledge of the pressure peak on the inner plate, the time constant ϑ, and the mass of the plate, lead the analysis of the shock effect on the inner plate back to that realized in the air-backed case previously described.

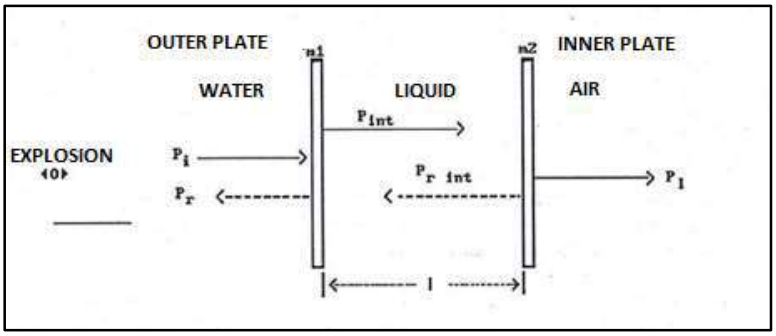

Figure 3.7 Scheme of shock wave propagation in a tank (image adapted from D'Andrea [3.4])

3.4.3 Finite plate constrained at the edges by a perfectly rigid and fixed support

In the case of a flat plate of finite size rigidly fixed to the edges, the transfer of energy between water and plate occurs in a different way than in the case of infinite plate.

This condition is realized when scale targets, used in experimental tests, and locally reinforced hull areas, such as under machinery foundations or at liquid tanks compartments, are considered.

According to D'Andrea [3.4], the finite plate can be schematized as a piston, as shown in **Figure 3.8**, which is deforming for the effect of the incompressible fluid, which is moving between the more rigid fixed supports. The equation of the motion is the same of the infinite plate, but the mass of the piston should be increased by a term of added mass, which depends by the shape of the finite plate.

The difference in stiffness between the surrounding fixed plane and the piston, the pressure on the contour is greater than that on the finite plate. Therefore, there is a tendency to have an "equalizer" effect of diffracted waves, which move from the edges towards the center at the speed of sound c, with consequent transfer of energy.

Comparing this time t_d in which the diffracted waves reach the center of the plate with the time t_0 of occurrence of cavitation in the infinite plate (which increases for severe charges), it may happen that

for charges of high weight the diffracted waves reach the center of the finite plate before the arise of cavitation.

Therefore, several cases are present:

- Small plates and severe charges: the diffracted waves reach the center before the arise of cavitation with consequent transfer of greater energy. The kinetic energy ratio ($\frac{E_c}{E_P}$) transmitted by the impact energy of the incident wave could also be greater than one.
- Large plates and small charges: diffracted waves do not reach the center before cavitation arises
- Intermediate case: finite plates are affected by both the presence of cavitation and diffracted waves.

The presence of diffracted waves entails an increase in the transmitted energy on the target compared to the case of the infinite plate.

In principle, according to this theory, it can be considered that the energy transferred to the plate is almost equal to that carried by the incident pressure wave $E_c \approx E_P$.

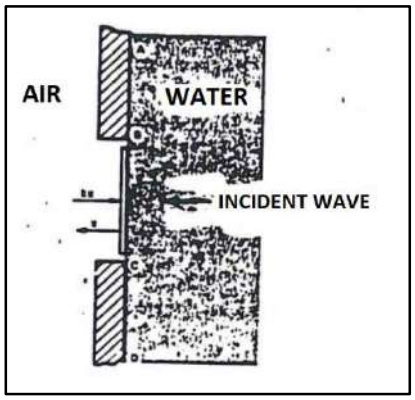

Figure 3.8 Finite plate constrained at the edges by a perfectly rigid and fixed support (image adapted from D'Andrea [3.4])

3.4.4 Deformation of a plate panel

Thin panels can be approximated as a flat plate. Its deformation can be evaluated if its final shape is known, as reported by D'Andrea in [3.4]. It follows that, for a rectangular plate of sides 2a and 2b, thickness h and fixed to the edges, as that shown in **Figure 3.9**, the displacement x(t) of the points can be calculated as:

$$x(t) = x_0(t) f(zy) \tag{3.21}$$

where:

- $x_0(t)$ is the deflection of the center of the plate

- $f(zy)$ is a function with a value of zero at the edges and the maximum at the center.

If the deformation of the plate is approximated to a paraboloid, it occurs:

$$f(zy) = (1 - \frac{z^2}{a^2})(1 - \frac{y^2}{b^2}) \tag{3.22}$$

Assuming that a plate of thickness h is subjected to a uniform yielding stress S_0, and that the displacements are small when compared with the smaller side of the plate, it is possible to assess the plastic energy of deformation E_s.

$$E_s = 4\int_0^a \int_0^b S_0(\varepsilon_y + \varepsilon_z)hdydz = \frac{64}{45}\left(\frac{a}{b} + \frac{b}{a}\right)S_0 h x_0^2 \tag{3.23}$$

where ε_y and ε_z are the strain according to the y and z axes.

It must be added to this E_s the energy necessary to overcome the atmospheric pressure that is on the inner side of the plate $E_{\Delta P}$, which is equal to:

$$E_{\Delta P} = \Delta p 4\int_0^a \int_0^b x dydz = \frac{4}{9}ab\Delta p x_0 \tag{3.24}$$

By equalizing the sum of the plastic energy of deformation and the energy necessary to overcome the atmospheric pressure to the equation of kinetic energy, it is possible to derive x_0, value of the maximum displacement of the flat plate. Therefore:

$$E_C = E_s + E_{\Delta P} \tag{3.25}$$

where:

$$E_C = \frac{1}{2}mAv_{max}^2 \tag{3.26}$$

where A=4ab is the area of the plate and v_{max} is the maximum velocity of the plate reached at the time t_0 of the arise of cavitation.

For damage assessments, in case the influence of the bubble pressure pulse is also considered to be of some importance, as it happens for explosions under the keel, this E_C value can be approximated as follows:

- $E_C = \frac{2}{3}E_P$ for infinite flat plate
- $E_C = E_P$ for plate fixed to the edges

in which E_P must be calculated considering both the energy of the shock wave in the free field and the one of the first pulsation of the bubble. Namely, E_P (in terms of energy per unit area) is obtained integrating the total pressure (shock wave + first bubble pulse) using the following equation:

$$E_P = \frac{1}{\rho c}\int_0^t P^2(t)dt \tag{3.27}$$

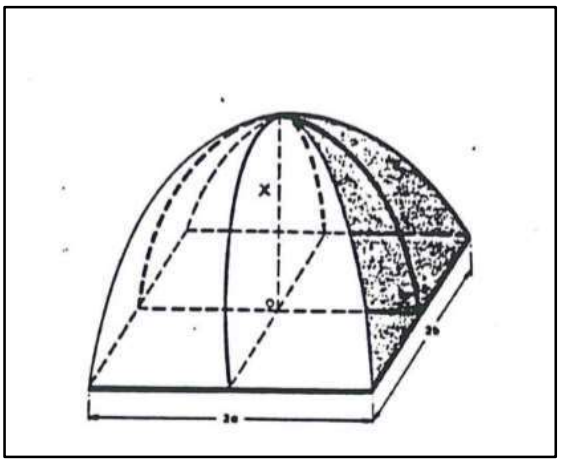

Figure 3.9 Empirical shape of a rectangular panel deformed by a shock wave (D'Andrea [3.4])

3.5 Considerations about the response of naval structures

The interaction of the shock wave with the flat plate involves a transfer of energy, which causes the deformation, in some cases up to breakage, of the target. In the same way, the naval ship hull is deformed, causing a decrease in the total pressure actinìg on the surface, until the phenomenon of cavitation arises with consequent separation between water and shell plates when they reach the maximum speed.

At first, stiffeners offer a certain resistance to inflection, however once accelerated they also reach the same velocity of the hull plates. This phenomenon is called "dishing". In this phase, multiple reflections are generated between the plates and the cavitation area with pressure peaks that determine an additional pressure load called "spray reloading". Subsequently, the closure of the cavitation space around the hull generates a further impulse similar to a hammer hit, called "reloading". In **Figure 3.10**, it can be noted the plate deflection depends mostly by the shock wave pressure, whose effects occur in the first milliseconds. The reload of cavitation, which happens in this time range, causes a further increasing in the maximum displacement. These phenomena occur in a time before the arrival of the first pulsation of the gas bubble, which can affect the ship after a time which can be in the order of seconds. This peak of pressure subsequently generates a further forcing action.

The deformation size is different if the damage is considered on the side shell or on the bottom.

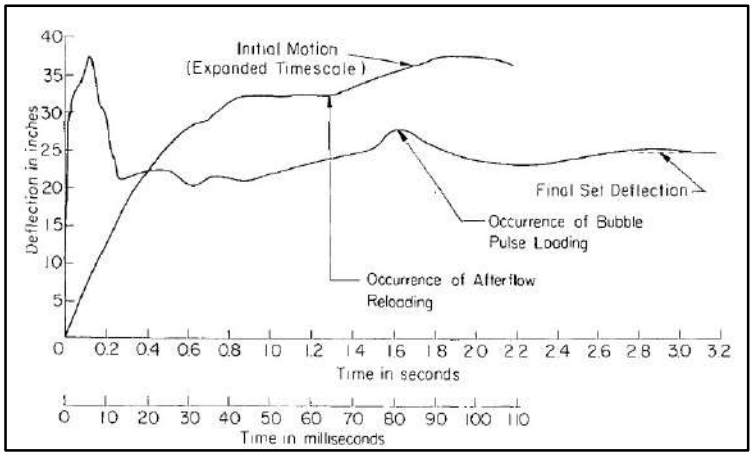

Figure 3.10 Deflection time history of the shell plating of a naval ship hull (Keil [3.7])

3.5.1 Damage on the side

According to Keil [3.7] and D'Andrea [3.5], experimental tests showed that, if the shell plating deflection is not very large, the stiffeners deflection is similar to that of the plates. Therefore, as an assumption, it can be considered that the structure is deformed as a unique plate of thickness, which is equal to that of the shell plating plus the additional one obtained by "spreading" the related stiffeners. See **Figure 3.11**.

On the other hand, if the reinforcing frames are particularly stiff, the sides can be deformed according to a phenomenon similar to *buckling* and if this occurs where there is a watertight bulkhead, it can cause the loss of their integrity. See **Figure 3.12**.

For the hull, in which there are wing tanks full of liquid, it has been noted that the plate in contact with the liquid on both sides is transparent to the shock wave, according to the water-backed theory, and the phenomena previously described are shown on the inner plate only.

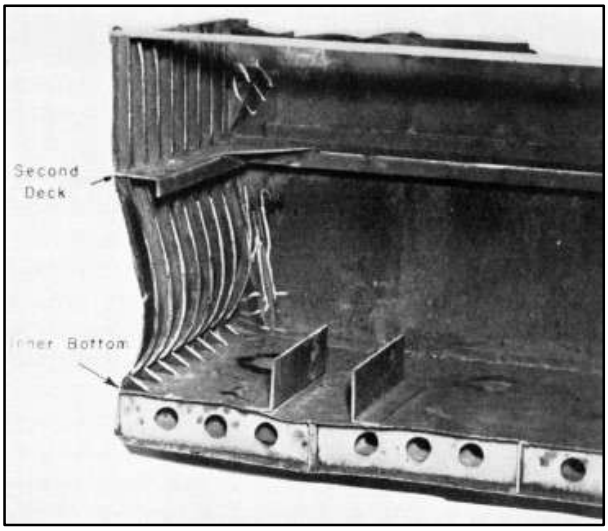

Figure 3.11 Damage on a merchant ship side caused by a non-contact UNDEX explosion (Keil [3.7])

Figure 3.12 Buckling of a bulkhead caused by a non-contact UNDEX explosion (Keil [3.7])

3.5.2 Damage on the bottom

An explosion that occurs under the keel provides different structural effects with respect to one which takes place on the side. In fact, the structures are reinforced and the arise of cavitation is hindered by the presence of diffracted waves. This happens in the case of small plates, fixed to robust stiffeners. The plates deflection occurs faster than the case in which the explosion happens on the side due to the presence of large masses such as those of longitudinal and transverse stiffeners.

The movement of the keel base, through the watertight bulkheads, transmits large forces to the upper decks, resulting in the displacement of the entire ship hull section.

The damage on the keel is also related to the pulsation and the migration of the gas bubble. Therefore, the deformation grows if the pulsation, during the migratory motion, take places closer to the keel.

For the purposes of dynamic calculations, the bottom of the ship can be compared to that of an unconstrained plate of uniform mass, the final inflection of which is usually less than that of the side.

Studies carried out by Zhang et al. in [3.17] showed that the most severe damage on the hulls occurs when the explosion occurs under the keel and the gas bubble collapses provides the occurrence of a high-speed jet of the type shown in **Figure 3.13**.

The destructive action is also increased by the ship oscillation, caused by the pulsations of the bubble (whipping motion), whose period is close to that of the hull resonance. In this case, therefore, the overall damage to the hull, with stresses that can cause the hull-beam breakage, are due to the load of the gas bubble pulsation.

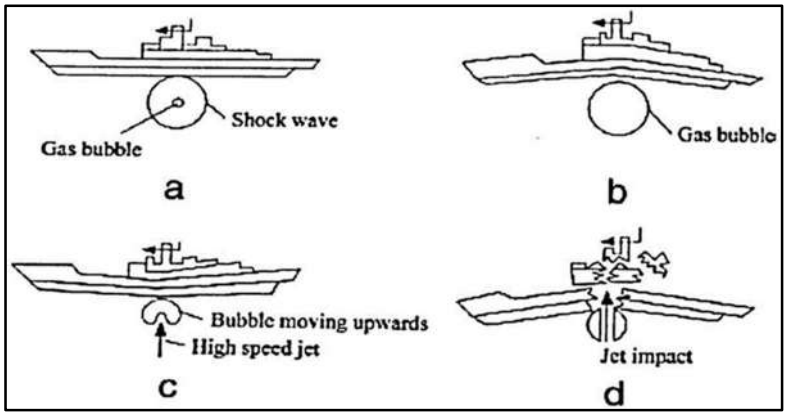

Figure 3.13 Damage to the hull due to an explosion: a) the shock wave causes the first shock to the ship, b) the bubble expands while the ship is rising, c) the bubble collapses and the jet is generated, d) the jet penetrates the hull and the ship breaks (Zhang et al. [3.17])

3.5.3 The times which influence the damage of naval structures

The behavior of the structures is regulated by the following time quantities:

- The constant of time of the shock wave (θ)
- The time in which the plate reaches the maximum translation speed and the phenomenon of cavitation occurs (t_0)
- The diffraction time in which pressure waves move at the speed of sound from the edge of the plate to the center of the soft structure (t_d)
- The time necessary to reach the maximum deformation of the structure (t_s)

- The time in which a sound wave passes through a thickness of water having a mass equal to that of the plate (t_p)

Usually, for thin plates the positive effect of the shock wave decreases quickly, as it results $t_p < t_0 < \theta$, while for thick plates t_p grows with t_0, as it results $\theta < t_0 < t_p$.

In principle, it can be said that for naval structures it happens that $t_s \gg \theta$. However, the times in question can be influenced by different factors, such as the construction criteria, the materials used, etc... Their knowledge is useful for classifying the type of action to which a hull is subjected as a result of an underwater explosion.

The factors that regulate the damage can be summarized as follows, according to D'Andrea in [3.4]:

- In the case that the shock wave effects finish before the diffraction phenomena arise and before the plate is completely deformed ($\theta \ll t_d, \theta \ll t_s$), it is possible to refer to a localized action. In practice, it can be considered as if each panel of the hull was deformed by the shock wave independently from the others. The impulse seems to be the predominant factor.
- If $\theta \gg t_d$, the pressures on the surface of the hull plates tend to readjust due to diffraction. Therefore, there is a non-localized action, and the determining element is the pressure field, similar to that determined by a compression realized hydraulically.
- In intermediate cases and when the cavitation occurs, the damage is proportional or equal to the energy produced by the shock wave.

3.6 Quick calculation methods to assess the hull damage

It is possible, making some assumptions, to perform simple calculations to determine the maximum deformation of the naval hulls, according to D'Andrea in [3.6].

The following cases are analyzed:

- Simple hull, the model of which is represented by an infinite flat plate;
- Double hull, for which reference is made to the double plate delimiting a tank filled with liquid;
- Naval vessel hull equipped by protection against underwater charges.

3.6.1 Simple hull

This model shall be used, for example, in case of a ship side between two watertight bulkheads in which the following assumptions are made:

- Diffraction phenomena must not occur, namely the t_d time must be higher than the constant of the shock wave ϑ
- The deformation must occur before the phenomena of reflection of the shock wave of the surface and the seabed affect the hull (t_s and t_f must be higher than t_0)
- The reinforcing stiffeners must be evenly distributed on the shell plates.

It is possible at this point to apply the Taylor air-backed plate theory to calculate the maximum x_0 deflection of the panel, as reported in the previous paragraphs.
This value is calculated by solving the following equality represented by a simple quadratic equation:

$$E_C = E_s + E_{\Delta P} \tag{3.28}$$

in which:

- the work necessary to plastically deform the plate (E_s) can be evaluated considering a rectangular plate on which the stiffeners are smeared along the thickness
- the additional energy ($E_{\Delta P}$) is connected to the fact that inside the hull the atmospheric pressure acts, while in the sea water a zero pressure acts, when cavitation occurs at t_0 time.

3.6.2 Double hull

In this case, the water-backed plate theory explained in the previous paragraphs can be applied.

3.6.3 Protected hull

A reference to this situation can be made in the case of naval or submarine vessels where a double-hull type is considered, but these structures are strongly reinforced by stiffeners, to the point of considering them as rigid. The effect of the explosion has the characteristics of the non-localized explosion, in which the diffraction time t_d is lower than the constant shock wave ϑ. Therefore, cavitation phenomena do not occur, and it can be assumed that a static pressure acts on the plating. This can be calculated by replacing the time pressure diagram to one with constant pressure, considering the same total energy. The problem is simplified, and it is possible to pass from a dynamic to a static analysis.

3.6.4 Translational velocity of the hull

The translational velocity of the hull is another important element, in addition to the shock factor, which allows us to evaluate the effects of an underwater explosion. In fact, from a functional point of

view, the rapid increase in velocity can provide to damage to the on-board equipment, as well as the shutdown of the electric motors. According to D'Andrea in [3.6], it has been experimentally found that velocities above 4 m/s can lead to stop of the vessel, velocity between 1.5 and 4 m/s the interruption of the mission and less than 1.5 m/s a minor damage.

This velocity can be calculated approximately by two methods: considering Taylor's flat plate theory and assimilating the hull to an equivalent flat plate [3.16], or referring to the "spar buoy" model explained by Costanzo in [3.2]. According to this method, it is possible to calculate the hull velocity referring to the velocity of vertical translation of a fluid particle, assuming that the speed of a point of the hull is comparable to the average velocity of a column of water in the free field as high as the average immersion of the hull itself.

According to the "spar buoy" model, this velocity (called Kick-off) is calculated by solving the following integral:

$$V_k = \int_0^d u(y)dy \tag{3.29}$$

where d is the mean immersion of the vessel and u(y) is the initial velocity of the fluid particle in free field. It is given by the following expression, in which δ angle represent the incidence of the shock wave:

$$u(y) = \frac{2P_m cos\delta}{\rho c} e^{\left(\frac{-2ycos\delta}{c\vartheta}\right)} \tag{3.30}$$

The integral results in the following expression of kick-off velocity:

$$V_k = \frac{P_m \vartheta}{\rho d}\left[1 - e^{\left(\frac{-2dcos\delta}{c\vartheta}\right)}\right] \tag{3.31}$$

On the contrary, the theory of the Taylor flat plate considers an equivalent plate of average unit mass m', whose surface is equal to that wet by the hull. The velocity is calculated by equaling the momentum of the plate to the rectangular pulse of the shock wave, which is equal to:

$$I = P_m t \tag{3.32}$$

where t represents the approximate duration of the load that can be determined by the following expression:

$$t = \frac{m' cos\delta}{\rho c} \tag{3.33}$$

In general, as reported by Reid in [3.11], it can be said that the velocities are transmitted between the decks of the ship, along the watertight bulkheads, without undergoing appreciable variations, while they show differences of up to 30% in the structures, like decks, which are between the bulkheads. Accelerations, on the other hand, vary significantly depending on the height of the ship and the flexibility of the decks, as shown in the **Figure 3.14**.

These models, even if they allow rapid calculations, have the defect of underestimating the translational speed of the structure, as they require the verification of the conditions of applicability, namely: the absence of cavitation, the presence of a plane shock wave and an explosion point far enough from the target.

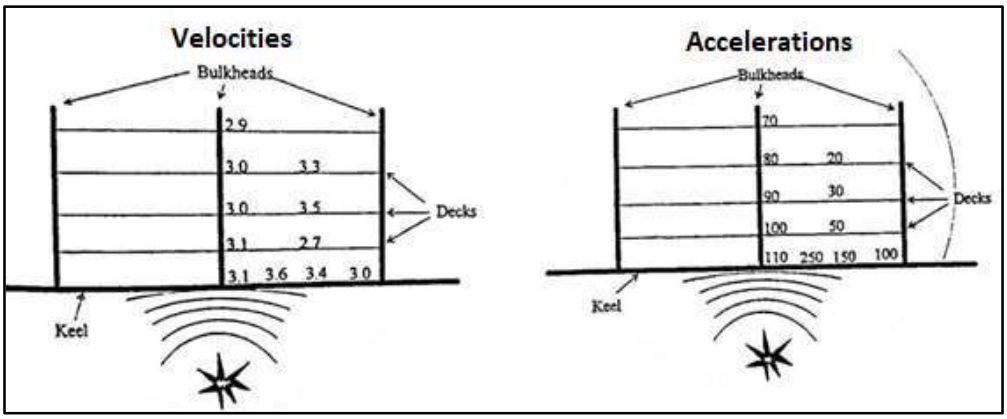

Figure 3.14 Schematic distribution of velocities (m/s) and accelerations (g) between two watertight bulkheads of a naval vessel (image adapted from Reid [3.11])

3.7 Bibliography

[3.1] Cole R. H., *Underwater explosions*, Woods Hole Oceanographic Institution, 1914;

[3.2] Costanzo F., "Spar Buoy Model," Shock and Vibration Symposium, Dayton, Ohio, October 1984;

[3.3] Costanzo F. A., "Underwater Explosion Phenomena and Shock Physics", Society for Experimental Mechanics Inc, Jacksonville, Florida USA, 2010;

[3.4] D'Andrea A., *Studio per una valutazione di massima del comportamento di elementi strutturali semplici di scafi navali sottoposti ad esplosioni non a contatto*, MARIPERMAN, La Spezia, 1992;

[3.5] D'Andrea A., *La dinamica dell'esplosione subacquea*, MARIPERMAN, La Spezia, 1992;

[3.6] D'Andrea A., Scaini S., *Calcoli di dinamica dell'esplosione*, Nane Edizioni, Roma, Novembre 2015;

[3.7] Keil A.H., "The Response of Ships to Underwater Explosions", Society of Naval Architects and Marine Engineers, New York, 16-17 Novembre 1961;

[3.8] Marinò A., Appunti di *"*Corso di Navi Militari e Sommergibili*"*, Università di Trieste, 2012;

[3.9] McGoldrick, R. T., Gleyzal, A. N., Hess, R. L., Gess Jr., G. K., "Recent Developments in the Theory of Ship Vibration", David Taylor Model Basin Report 1451, pp. 2-6 – 2-9, December 1960;

[3.10] Petralia S., *Compendio di esplosivistica*, MARIPERMAN, La Spezia, 2000;

[3.11] Reid W. D., *The Response of Surface Ships to Underwater Explosions*, Australian Department of Defence, 1996;

[3.12] Scavuzzo R.J., Pusey H.C., *Naval Shock Analysis and Design*, The Shock and Vibration Analysis Center, HI-TEST Laboratories, Inc., Second Printing 2002;

[3.13] Shaw, J.S., "Brief Resume of Recent British Shock Trials", Ships, Shock and Vibration Bulletin No. 9., NRL S-3290, 1948;

[3.14] SMM/CN 300 DVD, *Criteri e metodi per il proporzionamento e la qualificazione antiurto dei componenti destinati alle Unità navali*, Stato Maggiore Marina, Istituto Poligrafico dello Stato, 1978;

[3.15] Szturomski B., "The effect of an underwater explosion on a ship", scientific Journal of Polish Naval Academy, 2015;

[3.16] Taylor G.I., "The pressure and Impulse of Submarine Explosion Waves on Plates", Ministry of Home Security Report, FC 235, 1941;

[3.17] Zhang A.M., Yao X.L., Li J., "The interaction of an underwater explosion bubble and an elastic–plastic structure", Applied Ocean Research 30, 159-171, 2008.

4 Mechanical shock and design methods

4.1 Mechanical shock and its general characteristics

The hull structures are an effective way of transmitting noise, vibrations, and shock waves. Their motion of response to these dynamic loads depends on their elasticity and inertia properties. The term "mechanical shock" or “impact” refers to the motion of the equipment-foundation interface, defined in a precise way: it is "described" when the kinematic behaviour of each point of the machinery-foundation interface is known.

According to SMM CN 300 DVD [4.33], if the motion of a unique system, consisting of both structures and equipment, is considered, it is important to underly that machinery and foundation "interact dynamically". This means that the structure transmits the impact stresses to the equipment, and in the same way, its motion is influenced by the inertial and elastic characteristics of the machinery itself. It can be said that the equipment exerts “dynamic feedback” on the foundation motion. An important role in the global dynamic analysis is played by the type of connection between structure and equipment. In particular, if the connection is very flexible, the equipment tends to maintain its spatial position unchanged being influenced by the motion of its foundation in a small part. If instead, the link is rigid, the machinery moves supportive with the foundation, behaving like a simple mass. In intermediate cases, the machinery is deformable, which is why each equipment-foundation system is considered as a subsystem of a more complex structure. Therefore, the motion of the hull area hit by the shock wave is influenced by the motion of all the naval structures and the machineries connected to them.

4.2 Distinctive features of the shock motion in the different parts of the naval vessel

Looking at the data, such as velocity and acceleration time histories, obtained from a UNDEX test performed on a naval ship, it is possible to note an extreme variability of results, which can be different even with small shifts in the position of the measurement sensor. This uncertainty occurs considering that the structure is continuous, and its deformation is the result of the superposition of a large number of natural modes. However, the examination of the results of many experimental tests was important to identify some characteristics, common to the motion of groups of structures, that allow the description of the phenomenon in a summary manner.

When equipment is mounted on the hull plating, it is subjected to the maximum accelerations among those affecting the vessel. As seen in the previous chapters, the shock wave is characterized by a high-pressure peak. Due to the magnitude of the pressure, the elastic reactions are negligible on a plating

panel. For this reason, the panel is accelerated to a high velocity in a very short time, with accelerations of the order of thousands of times that of gravity. A typical acceleration-time diagram measured on equipment rigid mounted on the plating panel of the hull is represented in **Figure 4.1**. The maximum acceleration occurs at the beginning of the motion, considering that the pressure wave similarly has an initial maximum. The phase of positive acceleration, which is very short, is followed by a phase of slower deceleration, during which the panel, under the action of the elastic forces, slows down, stops, and reverses its motion until the equilibrium position. As a result of the water dissipation, in the absence of pressure pulses after the first, the panel generally stops at the equilibrium without any oscillation.

Equipment inside the hull, rigidly mounted to the structures in the area affected by the shock wave, performs a quite different motion from that previously examined (See **Figure 4.2**). This difference is caused by the stiffness of intermediate structures between the equipment and the plating and by the elasticity of the hull structure in general. Due to these attenuation phenomena, the acceleration of the equipment is no longer characterized by an initial maximum, but it starts from zero and reaches the maximum value in a non-zero time, which can be shorter or longer, depending on the structural stiffness. The peak value of the acceleration is also significantly lower than the previous case, while the oscillation period increases. The acceleration phase is followed by a phase of rapid deceleration, after which the equipment slows down, stops, and reverses its motion. Once the equilibrium position is reached, it generally performs a few strongly dampened oscillations caused by the friction of seawater.

Finally, there is the case of stiff equipment rigidly mounted on a deck. The performed motion is shown in **Figure 4.3,** as a result of the impulse transmitted through the connecting structures, is oscillatory and much less dampened than that of machinery positioned on the hull. When considering superstructures, the peak acceleration values become significantly lower than the case of the hull-mounted equipment, while the damping decreases. The shock pulse provides a poorly damped motion if the structures considered are far from the hull plating. This phenomenon is of vital importance for the shock scantling of equipment mounted on the decks, to avoid unwanted resonances.

The described cases are very general, considering that the same rigid equipment, when mounted on a deck area, far enough from the pillars, behaves following a poorly damped motion. If, on the other hand, it is located close to a pillar, its acceleration and damping increase. The shock motion is different if the equipment is mounted at the centre of a bulkhead or at the edges. In the latter case, its behaviour is very similar to that of hull-mounted equipment. In addition, it must be considered that the motion of each machinery is also influenced by the response of near equipment.

Despite the presence of a large number of local situations, it is conventionally possible to define a limited number of zones of "equal impact". This definition refers to conditions of equal severity of the explosion. The number and description of possible zones is different from ship to ship. A possible subdivision, reported in [4.33], valid for a naval vessel is as follows:

- Zone I: external plating below the waterline
- Zone II: underwater hull until one meter from the waterline, including decks and bulkheads connected to it
- Zone III: decks and bulkheads under the main deck, up to one meter from the waterline
- Zone IV: main deck and superstructures.

The trend of acceleration is very different according to the considered zone, especially for zone I (of the external plating of the hull), which is subject to the highest acceleration, as can be noted from **Figure 4.4**.

It has been said that the definition of "equal impact" is valid for equipment rigidly fixed to the structure. The only variable that is possible to change is the mass of the machinery, so it is necessary to evaluate the influence on the shock motion of this parameter. As the equipment weight increases, the maximum acceleration decreases, while its oscillatory motion tends to slow down. Therefore, the equipment dissipates, through its inertia, the foundation motion. In **Figure 4.5**, it is shown the law of motion for two types of machinery of different weights mounted on the hull structure. It can be noted that the mass increase generates both the reduction of maximum accelerations and the slowdown of the foundation motion.

The previous examples of ideal motion of the different structures of a ship are made assuming that all the points of the equipment-foundation interface are characterized by the same shock. In reality, especially in the case of large machinery, the interface points closest to the explosion can be characterized by very different motions from those farther away. In addition, the direction of motion is not necessarily vertical, but it depends on the position of the structure with respect to the explosion geometry.

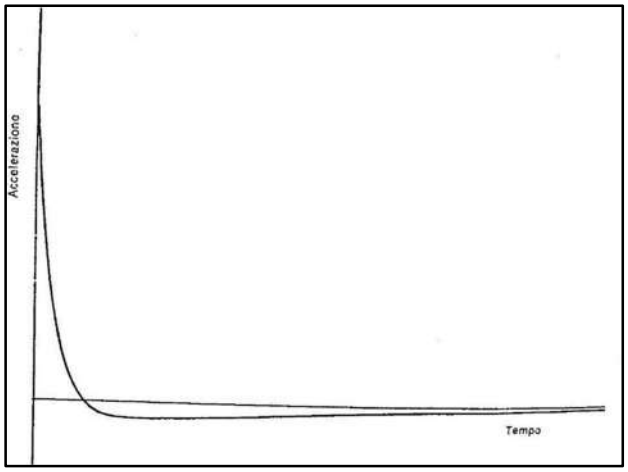

Figure 4.1 Example of acceleration-time graph of an equipment rigid-mounted on a plating panel (SMM [4.33])

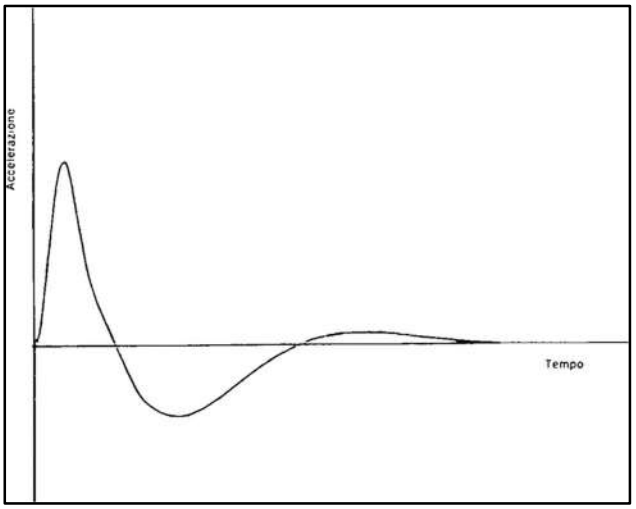

Figure 4.2 Example of acceleration-time graph of an equipment rigid-mounted on a structure connected to the hull (SMM [4.33])

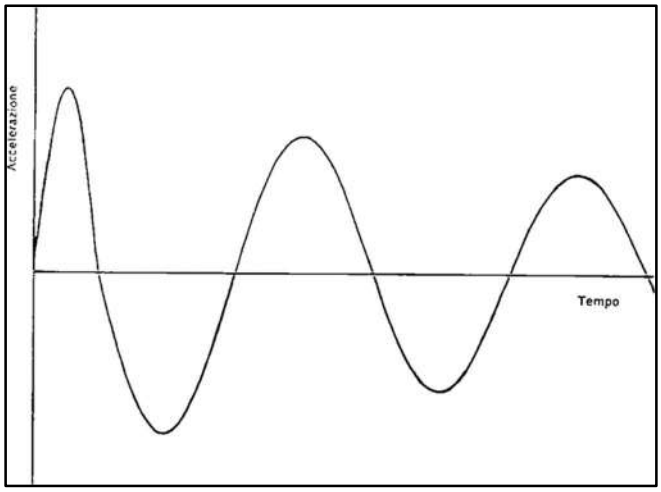

Figure 4.3 Example of acceleration-time graph of an equipment rigid-mounted on a deck (SMM [4.33])

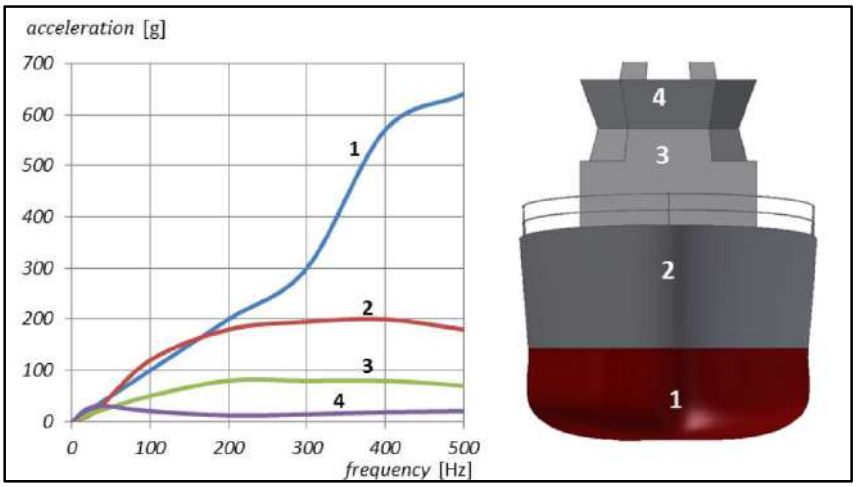

Figure 4.4 Zones of equal impact severity (Szturomsky [4.37])

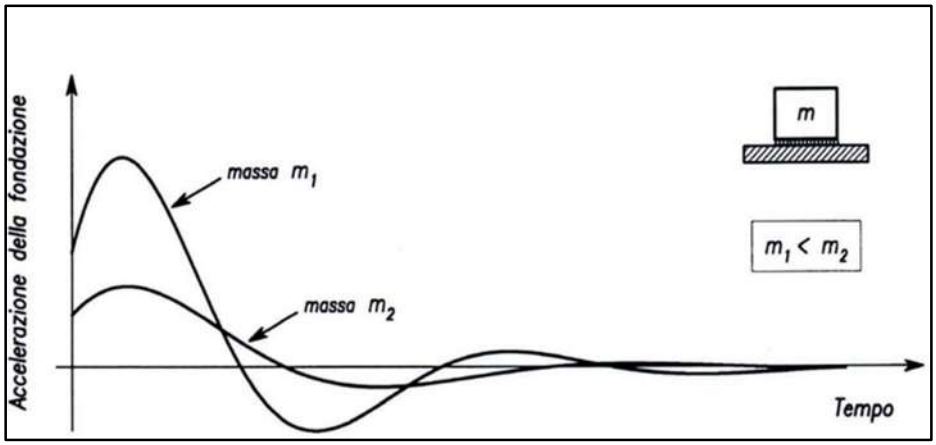

Figure 4.5 Effect of the mass of a rigid equipment on the acceleration of foundation (Marinò [4.20])

4.3 Analysis of the phenomenon in the frequency domain: Shock Response Spectrum

The shock test data are collected by measurement sensors, which are able to achieve displacements, velocities, accelerations and strains in the time domain. Sometimes, however, it is more convenient to express the same data in the frequency domain. Among the advantages of this description approach, there is the possibility of obtaining a synthesis of experimental data, since a large amount of information of the shock is generally ignored, while it is easier to obtain e.g. an average in the frequency domain. In addition, appreciably different functions in time domain can have similar frequency responses, represented by a unique graph in frequency domain. The frequency response diagrams are called Shock Response Spectrum (SRS), which can be produced using simple algorithms, as reported by De Silva in [4.8]. These methods allow the transformation into frequency domain of amplitude data which were a function of time. In practice, the signal is broken down into a series of signals at different frequencies and for each of them the maximum value is considered: in this way it is possible to represent on a graph the trend of the peaks of amplitude as a function of the frequency values. The methodology used for the calculation of the SRS is to consider the system in study as it was made by a large number of subsystems. Each of them is constituted by a single degree-of-freedom linear oscillator, type spring-mass, characterized by its natural frequency of vibration. These linear oscillators are mounted on a single base, loaded by the shock wave. Each component will oscillate according to its own vibration mode, so that it is possible to measure the oscillations peaks, registering on a diagram in frequency domain, as shown in **Figure 4.6**. One of the parameters that is necessary to define, when an SRS is built, is the damping. In **Figure 4.7**, an example of SRS, calculated at different critical damping value, is shown. Looking at the graph, it is possible to note the critical frequencies to which the maximum accelerations of the system correspond.

If damping is neglected, it is possible to refer to a triaxial SRS, in which displacement, velocity and acceleration are represented as a function of frequency. However, this is an acceptable approximation, as real systems still have a damping ratio, but small and often negligible. These graphs are called "pseudo-velocity" diagrams. In **Figure 4.8** an example of triaxial SRS, obtained by a shock measurement, is shown, in which acceleration, velocity and displacement are reported in a single curve. The pseudo-velocity is usually represented on the ordinate axis, the displacement is represented on the 45 degrees positively inclined axis, and the acceleration on the 45 degrees negatively inclined axis. It is possible to distinguish several regions in this type of triaxial SRS. In the zone of the lowest frequencies (A zone), the shock produces a rapid change in velocity. In particular, the spectrum tends asymptotically to the maximum value of displacement. At some intermediate frequencies (B zone), some response peaks are shown, as in the case of resonance. When the frequencies of the SRS increase, as in the C zone, the single degree of freedom system becomes stiffer. At high frequencies,

the value of the acceleration in the SRS tends asymptotically to the maximum. This would be true if the system, made by different single degree-of-freedom linear oscillators, had negligible masses and perfectly rigid springs.

It is possible to derive a conventional SRS, obtained as an envelope of several spectra, as reported by SMM CN/300 DVD [4.33]. It consists of a broken polygon, in which the two sides inclined by 45 degrees represent constant displacement s_0 (at low frequencies) and constant acceleration $a_0 = \omega^2 s_0$ (at high frequencies). Between these two sides a horizontal line at constant velocity ($v_0 = \omega s_0 = \frac{a}{\omega}$) is interposed, which extends between two frequencies called lower limit frequency (f_i) and upper limit frequency (f_s). These latter values are easily predictable, once known a_0, v_0 and s_0, using the following formulas:

$$f_i = \frac{v_0}{2\pi s_0} \tag{4.1}$$

$$f_s = \frac{a_0}{2\pi v_0} \tag{4.2}$$

STANAG 4142 [4.34] and STANAG 4549 [4.36] rules define NATO Standard shock levels corresponding to conventional shock spectra, univocally defined by the three parameters a_0 , v_0 and s_0. In this way, NATO requirements are commonly defined in order to obtain the shock verification of structures, equipment, and foundations.

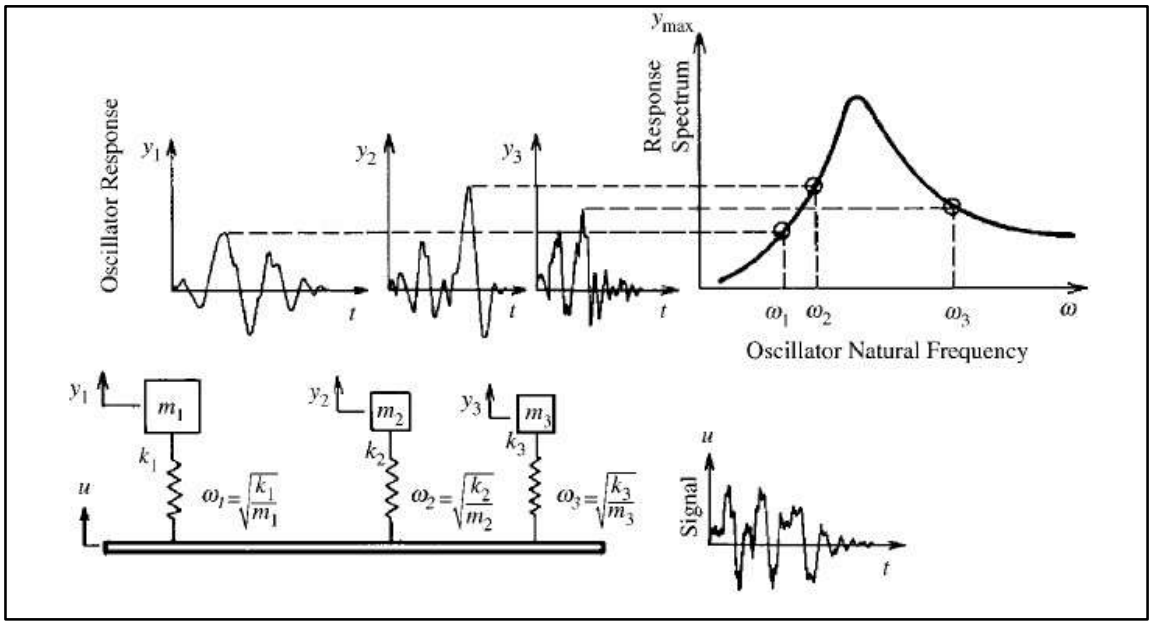

Figure 4.6 Construction methodology of Shock Response Spectrum (De Silva [4.8])

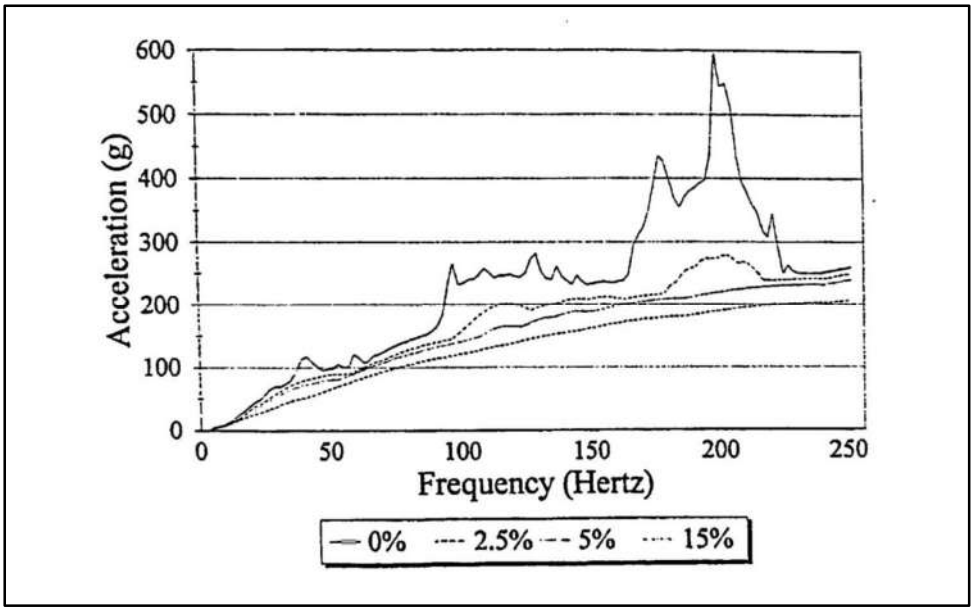

Figure 4.7 SRS defined at different damping ratios (Reid [4.28])

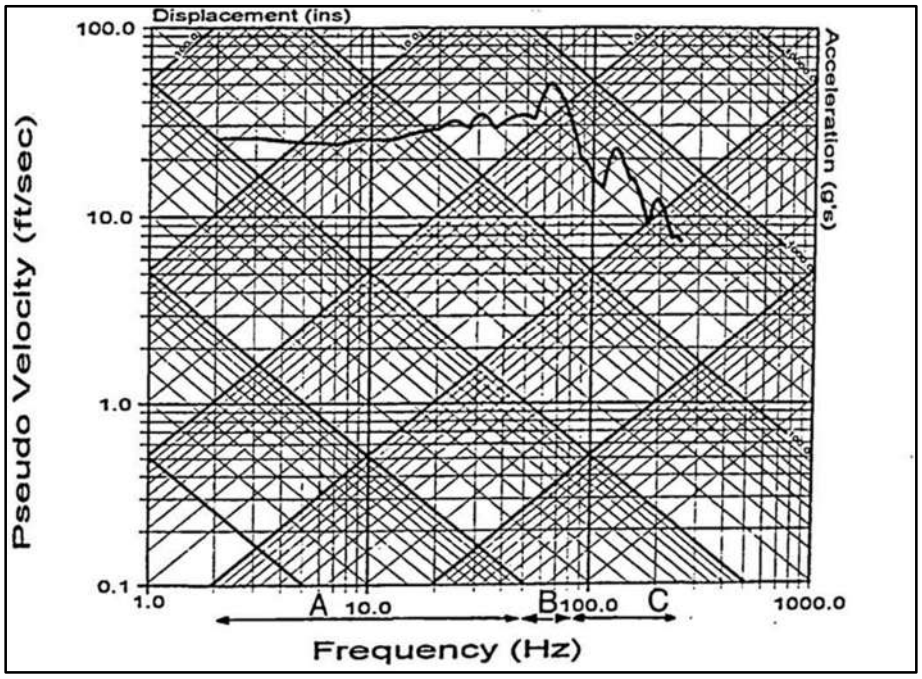

Figure 4.8 Example of a triaxial SRS of an undamped pulse measured using a shock machine. Sections A, B and C refer to those regions of the spectrum that may be related to different types of motions of the on-board equipment (Reid [4.28])

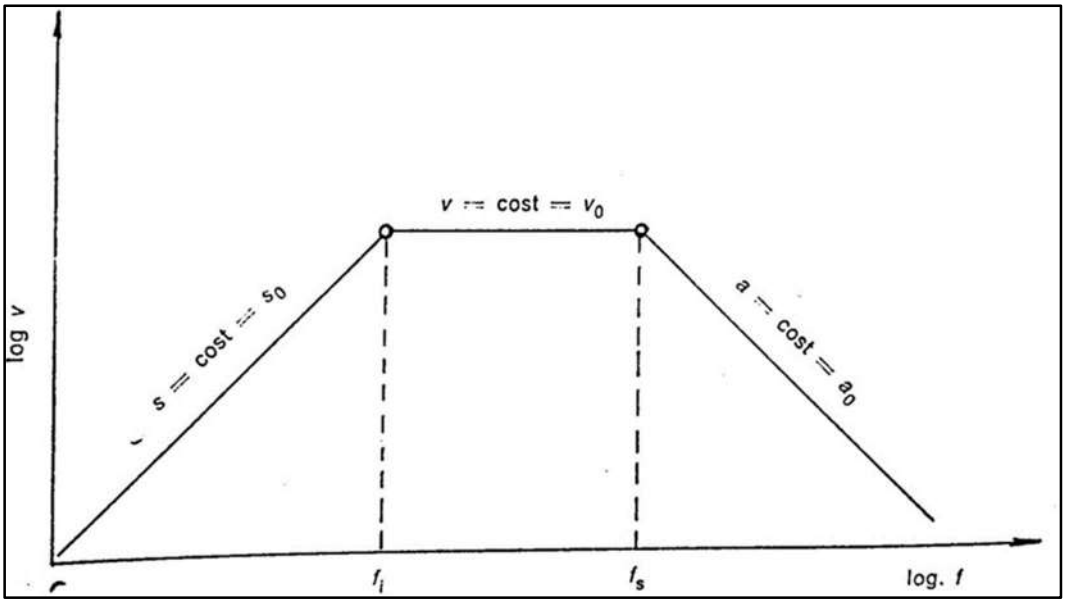

Figure 4.9 Conventional SRS (SMM [4.33])

4.4 Shock protection and assessment criteria

War experience and UNDEX tests have shown that even explosions of a modest nature can cause serious damage to the naval ship equipment, compromising the vessel's survivability.

For this reason, one of the requirements for the machinery, systems and onboard equipment of a military ship, is the feature of resistance to UNDEX impact. Therefore, machinery must be properly designed to withstand a shock of maximum severity successfully. However, shock resistance can be of two types: structural and functional strength. In the case of structural strength, the equipment must keep its integrity after the impact, while referring to functional resistance the machinery may be deformed, but it must be able to perform its function. In general, it is not possible to state that equipment that maintains its structural strength can still perform its mission: for example, a shock pulse can trigger a switch or close a valve, damaging vital functions. Similarly, equipment that maintains its functions, but not its integrity, could cause damage to the crew or other systems, compromising other vital machinery.

Italian Navy identifies the classes of resistance to UNDEX shocks according to NAV 30 A001 [4.25]. This rule, in order to determine the type of qualification suitable for the equipment analyzed, groups into three classes the machinery and the systems on board concerning the importance they have regarding the survivability of the vessel. They are:

- Class A for vital equipment which must be verified to withstand a severe grade A shock impact, without being limited in their functional performance and structural integrity.
- Class B for machinery whose failure of functionality does not affect the safety and operational efficiency of the naval vessel

- Class C for equipment which is not essential for the survivability of the ship.

In general, for grade A, it is referring to a shock of maximum severity, while for grade B it is considered an impact of lower intensity (generally B = 1/3 A), which must be identified from time to time according to the specifications dictated by the rule.
An overview of some of the common international standards related to shock qualifications and rules is reported by Ang and Han in [4.1].
In general, in the "shock policy" document, for each naval vessel, the qualifications required for each type of equipment and the related foundation structure, are reported, specifying the classes of functional importance previously defined. To perform a correct shock scantling, according to this document, it is possible to realize:

- UNDEX tests against ships on full scale
- Tests on shock machines
- Structural design by calculation.

4.5 UNDEX tests against ships on full scale

The most convincing verification of the shock resistance of structures and equipment is undoubtedly that carried out by the explosion of an underwater charge against a ship on a full scale. This type of test has also the advantage of affecting entire systems, providing immediate indications regarding their ability to maintain their functionality during and after the explosion. However, they are not easily feasible, considering that:

- They cannot be conducted against operating naval vessels except if made with reduced severity compared to those normally assumed at the time of design. The shock resistance prescribed for military ships is based on severe scenarios, able to produce significant damage to the hull structure.
- A single explosion is often insufficient considering that only the hull area close to the point of explosion is significantly affected by the pressure wave. Therefore, it may be necessary to explode several charges, on one side and the other of the hull, along the entire length of the ship.
- The high cost of testing.

In addition, they cannot be performed in an early phase of design, when a preliminary assessment of shock scantling is required.

4.6 Tests on shock machines

The term shock machine refers generically to any device on which it is possible to install equipment including its foundation, to subject it to shocks of adjustable severity defined until certain limits.
The shock machines used by the Navy, according to NAV 30 A001 [4.25] and MIL S 901 S [4.23], and currently located at the Naval Support and Experimentation Center in La Spezia (CSSN), are classified into three types:

- Light Weight Shock Machines (LWSM) for testing specimens of weight which does not exceed 115 kg
- Medium Weight Shock Machines (MWSM) for testing specimens of weight between 115 kg and 3000 kg;
- High Weight Shock Machines (HWSM), also called "barges", for tests on specimens of weight between 3000 and 30000 kg.

Recently, US Navy MIL DTL 901 E [4.22] rule introduced the Medium Weight Deck Simulating Shock Machine (DSSM), in order to shock verify the machinery of medium weight mounted on the superstructures, where the ship deck frequency at installation location is less than or equal to 37 Hz.
Generally, the structure under test, inclusive of machinery and mountings, is considered shock verified after the impact if it results essentially intact or it does not suffer any limitation on its performance without constituting a possible threat to people or things. In special cases, the Navy defines the minimum final performance desired to consider the shock tests satisfactory. More details about the shock machines' methodology of tests are reported by NAV 30 A 001 [4.25].

4.7 State of the art of design methods by calculation

4.7.1 Preliminary remarks

Nowadays, rules allow using calculations to assess the shock effects on machinery and ship structures if experimental tests are not available. However, this is often the case in an early phase of design, where there is not enough time to perform tests and calculations become crucial to obtain a reliable shock scantling.
In most cases, it is not necessary to model the whole UNDEX phenomenon, including fluid, structures and their interaction, but the analysis can be performed considering only the mechanical shock properties, namely only in terms of displacements, velocities and accelerations of structures. This happens, for example, for the shock scantling of machinery and the relevant foundations. As previously reported, the design strategies that can be adopted are reported in the "shock policy"

document, where the shock requirements, including the severity of loads, for each type of equipment are shown. Separated analyses are performed in case it is necessary to assess the structural response of the hull girder caused by the bubble pulse or the local effect of the shock wave on panels or valves of the hull. In these cases, the Fluid-Structure Interaction numerical approach may be applied to obtain the shock verification. Alternatively, the shock pressure can be applied directly to the hull, but it must ensure that the simulated phenomenon is conservative to avoid an undersized scantling.

4.7.2 Mechanical shock analysis of machinery and foundations: calculation methods

The analysis of the shock motion of machinery and related foundations is carried out according to three main methodologies:

- Quasi-static approach
- Statistic method in frequency domain (Shock Response Spectrum method)
- Dynamic analysis in the time domain.

In the case of vital A class and B class, the shock method proposed must reach the following targets:

- Verify that the maximum stresses in combination with those present under normal operating conditions are lower than the allowable ones;
- Check the corresponding displacements in order to avoid impacts between nearby equipment, causing the loosing of functionality of the system.

The calculations can be performed using traditional lumped models or, alternatively, modern finite element software.

4.7.2.1 Quasi-static approach

The quasi-static approach is based on the idea of performing a calculation in which a fictitious static load is applied on the structure in analysis. The hypothesis made is that the applied quasi-static load generates on the structure the same stresses and strains as those obtained by applying the actual dynamic loads. Therefore, they are usually referred to as “equivalent static loads”. They are considered as mass forces, equally distributed on the assembly equipment-foundation, in the direction of the shock. If P is the weight of equipment and a is a coefficient of proportionality, called "dynamic load coefficient" or "load factor", the fictitious static force can be written as: $dF = adP$.

The shock verification is made by performing separate calculations for explosions which happen in the vertical, transversal and horizontal direction.

This is the approach, historically used, and described in SMM/CN 300 DVD [4.33], in which it is referred as Simplified Dynamic Analysis (SDA). According to this method, it is necessary to determine the load factors a, which are provided in literature by graphs based on experimental data

collected during explosion tests on ships in full scale, valid for a certain location on board, impact direction, type of naval vessel and class of protection (A, B and C). The load factor a is a function of the natural frequency f and the real weight P or alternatively the apparent weight P_a, as shown in **Figure 4.10**. To consider the effects of interaction between foundation and equipment, the concept of apparent weight P_a is introduced. The quantitative determination of the apparent weight P_a is carried out by the simple formula $P_a = \alpha P$, where P is the real weight of the system, while α is a numerical coefficient conventionally called "dynamic feedback factor". These factors can be achieved by experimental graphs as that reported in **Figure 4.11**. On the x-axis there are the apparent weights, on the y axis the natural frequencies, and the curves correspond to a different "dynamic feedback factor". It is a recursive process: it is necessary to enter the graph imposing $P_a = P$, obtaining the related α value at the known natural frequency. Then, it is possible to recalculate P_a proceeding until convergence.

Nowadays, instead of those graphs provided by SMM [4.33], the quasi-static calculations are often realized using SRS, as those described by STANAG 4370 [4.35], and shown in **Figure 4.12**. Three different graphs are presented referring to the three directions of explosions. It is possible to enter the graph imposing the natural frequency of the system f, in which foundation, equipment and mountings are considered, achieving the maximum value of velocity v_0. Then, the related maximum value of acceleration a_0, which must be applied at the basis of the structure, can be obtained considering that for triaxial SRS it is valid the relationship: $a_0 = 2\pi f v_0$.

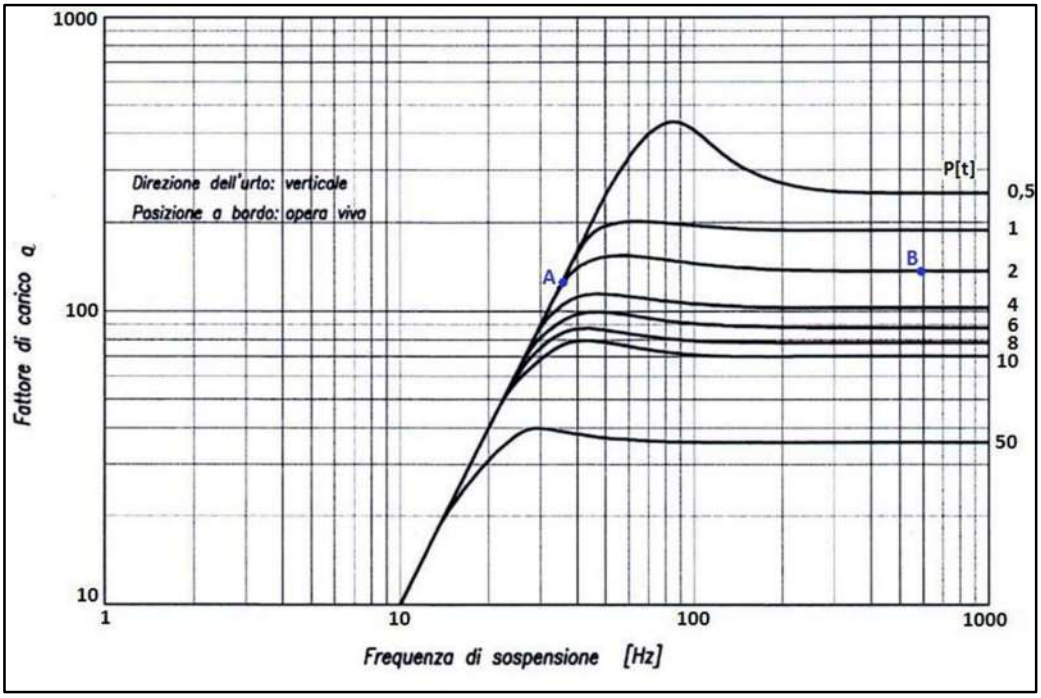

Figure 4.10 Load factors as a function of the real weight P of the equipment (SMM [4.33])

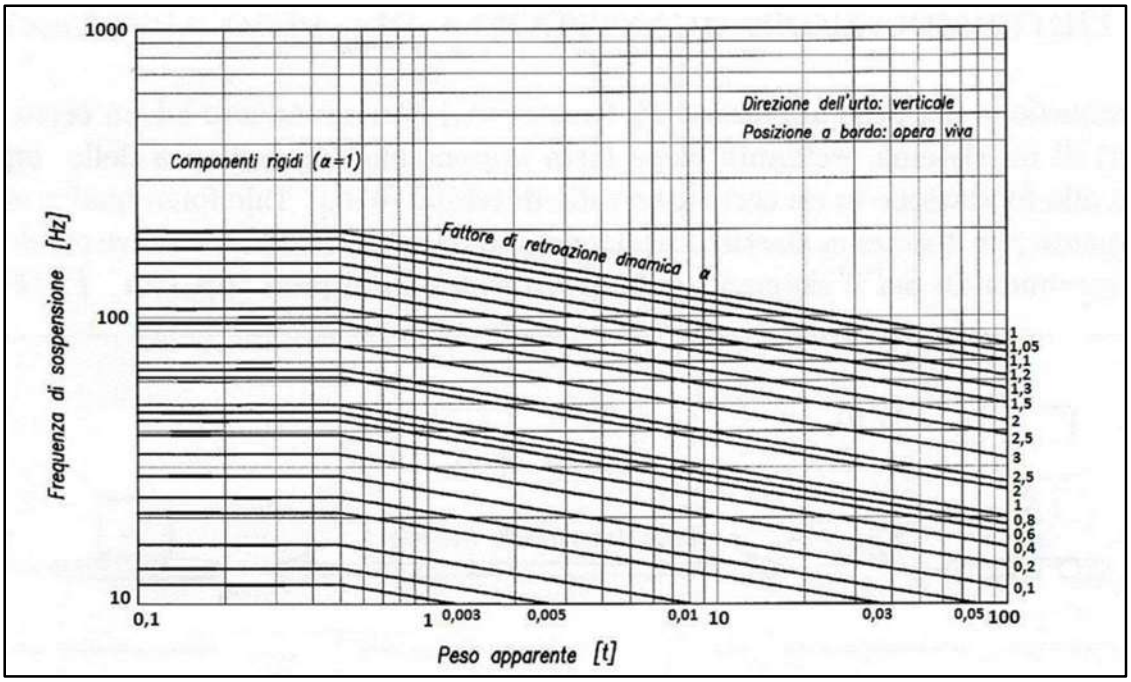

Figure 4.11 Dynamic feedback factors for the determination of apparent weight (SMM [4.33])

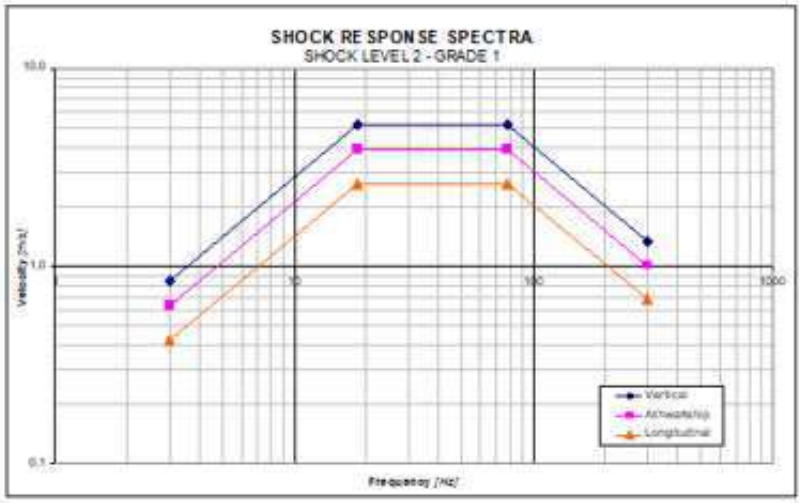

Figure 4.12 SRS for shock verification (Fincantieri [4.11])

4.7.2.2 Shock Response Spectrum method

4.7.2.2.1 Generalities

The SRS method, traditionally used in civil engineering for earthquake protection, consists in a statistical method, in which an SRS, as the one in **Figure 4.12,** is used as input for the shock analysis. The structure, in function of the modal masses associated with the natural frequencies, is subjected to a shock response, determined statistically according to the SRS of input.

For each structure, natural frequencies of vibration must be calculated. The equation of motion expressed in matrix form is:

$$[M]\{\ddot{x}\} + [K]\{x\} = 0 \tag{4.3}$$

where [M] and [K] are the matrix of mass and stiffness respectively.

Substituting within the equation a solution of the type $x = \bar{x}sen(\omega t)$ and grouping the terms provides the following expression:

$$([K] - \omega^2[M])\{\bar{x}\} = 0 \tag{4.4}$$

Eq. 4.4. is an eigenvalue problem. By placing the determinant of the above equation equal to zero, it is possible to derive the pairs of eigenvalues ω^2 and eigenvectors $\{\bar{x}\}$ classically reported as ϕ. Each eigenvalue ω^2 corresponds to a natural frequency of the system and each eigenvector ϕ to the relative shape. Eigenvectors ϕ are normalized so that the following relations are obtained:

$$\phi^T[M]\phi = I \tag{4.5}$$

$$\phi^T[K]\phi = \Omega^2 \tag{4.6}$$

where I is the identity matrix and Ω^2 is a diagonal matrix, whose terms on the diagonal are the eigenvalues ω^2. In this way the eigenvectors are orthogonal to each other and independent, which means that it is possible to excite one frequency and the related shape without stimulating the others. Once the natural frequencies and related eigenvectors have been evaluated, it is necessary to derive the modal mass of each vibration mode. It can be considered as the part of the total mass excited by the shock motion in each way considered. The sum of the effective modal masses is equal to the total mass of the system.

It is possible to construct a rigid body vector obtained as a linear combination of the elastic modes of vibration multiplied by scale factors ε, selected to obtain a unitary displacement in each node of the model. This normalized vector D_r is defined as:

$$D_r = \sum \phi\varepsilon \tag{4.7}$$

These scale factors, known as participation factors P, are derived for each vibration mode (marked by the subscript "a") using the following expression:

$$P_a = \frac{\phi_a^T[M]\{D_r\}}{\phi_a^T[M]\phi_a} \tag{4.8}$$

Considering, for the properties shown above, $\phi^T[M]\phi = I$ and D_r as the vector of unit displacements, the relation can be expressed as the following summation:

$$P_a = \sum_{i=1}^{N} \phi_{ia} M_i \tag{4.9}$$

where N represents the number of degrees of freedom of the system, M_i is the mass of the i-th degrees of freedom, and ϕ_{ia} is the component of the eigenvector related to the i-th degree of freedom

corresponding to the a-th mode of vibration. The effective modal mass is nothing more than the square of this participation factor and it is calculated as:

$$M_{effa} = \sum_{i=1}^{N} (\phi_{ia} M_i)^2 \tag{4.10}$$

The vibration modes, which are relevant in the determination of the shock response, are those whose sum of the total effective masses reaches at least 80% of the total mass.

The characteristics of the response of the system in analysis can now be calculated. The peak acceleration of response a_{ia} for each modal mass at each frequency ω is determined by the corresponding value of the input spectrum A_0 at that frequency and by the participation factor P_a related to the mode considered. Therefore, it turns out:

$$a_{ia} = P_a \phi_{ia} A_0 \tag{4.11}$$

The velocities v_{ia} and displacements u_{ia} are calculated as follows:

$$v_{ia} = \frac{P_a \phi_{ia} A_0}{\omega} \tag{4.12}$$

$$u_{ia} = \frac{P_a \phi_{ia} A_0}{\omega^2} \tag{4.13}$$

All other responses of the system such as stresses, strains and forces can be calculated, when the displacements for each frequency are known. For example, it is possible to assess the elastic force of a spring n for a mode a in the following formula in which i and j are the nodes that the spring connects:

$$F_{na} = K_n (u_{ia} - u_{ja}) \tag{4.14}$$

Finally, to achieve the structural response of the system, it is necessary to proceed by making a statistical sum of the responses of the various vibration modes. A common approach is to consider the mean quadratic value of all the responses for which it results:

$$\Gamma_{peak} = \sqrt{\sum (\Gamma_i)^2} \tag{4.15}$$

in which Γ_i represents any response (acceleration, stress, etc...) corresponding to the i-th mode.

Another method developed at the Naval Research Lab and reported by O'Hara and Belsheim in [4.27], for calculating these response values, is called NRL sum, which takes into account the effect of the major modal response Γ_{max}. It turns out in this case

$$\Gamma_{NRL} = |\Gamma_{max}| + \sqrt{\sum (\Gamma_i)^2 - (\Gamma_{max})^2} \tag{4.16}$$

This Shock Response Spectrum method is applicable if the system behaves in a linear manner and if the points of the boundary connecting with the structure move in the same direction. It is also less

accurate if a part of the structure in analysis move according to an axis orthogonal to the direction of the shock pulse. Another disadvantage of the method is that it does not take into account the time in which each mode reaches the maximum response: this is the reason for which it is necessary to statistically combine the structural responses. Other details about the method are reported by de Silva in [4.8].

4.7.2.2.2 Dynamic Design Analysis Method (DDAM)

The Dynamic Design Analysis Method (DDAM) is a method for the design and anti-shock qualification of equipment and structures approved and proposed by NAVSEA in document 0908-LP-00-3010 [4.26]. It is based on the SRS method with some significant differences. In particular, the DDAM takes into account the different features of stiffness and mass of structures and foundations compared to those of machinery. This feature becomes particularly important when considering systems that weigh thousands of tons on flexible foundations or flexible decks' structures. A review of the methodology is made by Remmers et al. in [4.29].

Analytically DDAM proceeds as the SRS method. Natural frequencies, modes of vibration, participation factors and modal masses are calculated. While the SRS approach leads to the determination of the responses of the equipment by considering for each frequency the input values obtained from a single SRS graph, the DDAM, on the other hand, calculates the shock level for each frequency starting from a family of SRS, properly calibrated on the dynamic characteristics of the structure under study.

DDAM uses the following two equations, reported in [4.9], to calculate the shock input velocities V_0 and accelerations A_0, from which the system's response is then derived:

$$V_0 = VF_i \frac{VA(VB + W)}{(VC + W)} \tag{4.16}$$

$$A_0 = AF_i \frac{AA(AB + W)}{(AC + W)} \tag{4.17}$$

The velocity value V_0 is first converted to acceleration, multiplying it by the frequency value in rad/s and dividing it by the acceleration of gravity g, and then compared with A_0: the smallest of the two values represents the shock input acceleration A_{equiv}.

The coefficients' values of the above equations are reported by O'Hara and Belsheim in [4.27]. In particular, their value takes into account the position on board the component and the type of mounting (hull, deck and plate), as shown in **Figure 4.13**.

In addition, the coefficients VF_i and AF_i represent the different severity of the impact in the three directions of motion, while W is the effective modal weight expressed in kips (1000 lbs). It is derived from the effective modal mass with the following formula:

$$W = \frac{M_{eff}g}{1000}\ [kips] \tag{4.18}$$

where g is the acceleration of gravity.

The effective modal weight W in the equations reduces the response of the structure at some frequencies: this represents the effect of a very large weight on a flexible foundation. It can be noted that, for example in **Figure 4.14**, at the frequency of 50 Hz the input acceleration obtained is less than that considered without taking into account the effect of the weight of the component. The two straight lines represent the results of the two equations A_0 and V_0 considering the modal weight W equal to zero, while the final acceleration of input, calculated including the modal weight W, is represented in blue.

The previously described effect is called "spectrum dip" and it is explained by Scavuzzo et al. in [4.30]. There is a noticeable reduction in the SRS amplitude for very heavy equipment at the natural frequencies of the foundation, for which there is a reduction in the spectrum curve, as shown in **Figure 4.15**.

Once the input value A_{equiv} has been determined, it is possible to assess the structural response of the system proceeding as in the case of spectral analysis, obtaining the value of the response of each mode and then adding statistically by using the NRL sum shown by Eq. 4.16.

DDAM is a good method in terms of calculation and results achieved, and it represents an alternative to calculations in the time domain. However, the coefficients used must always be updated to adapt them to new naval ships. As previously reported, the approach is also linear and does not consider the superpositions of motion in different directions.

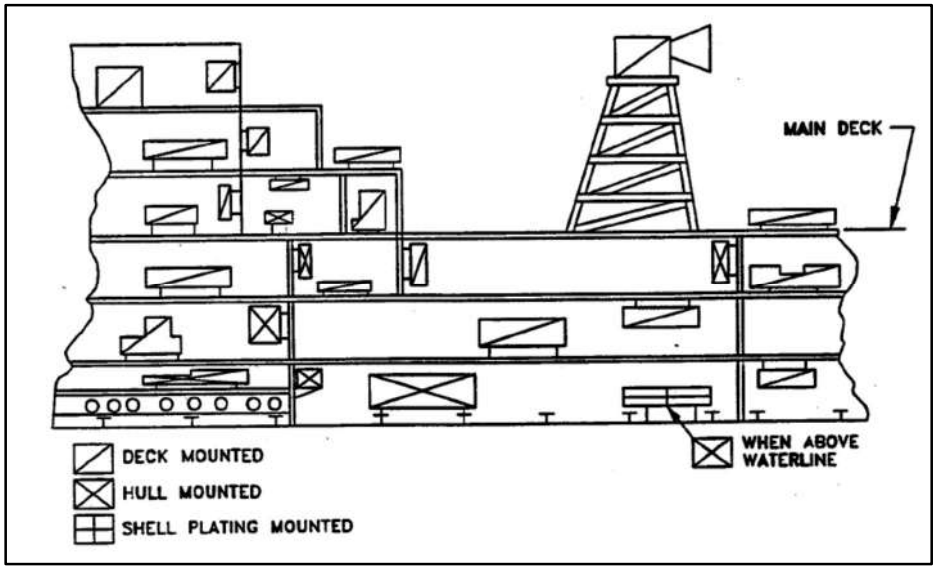

Figure 4.13 Classification of equipment and type of foundation (NAVSEA [4.26])

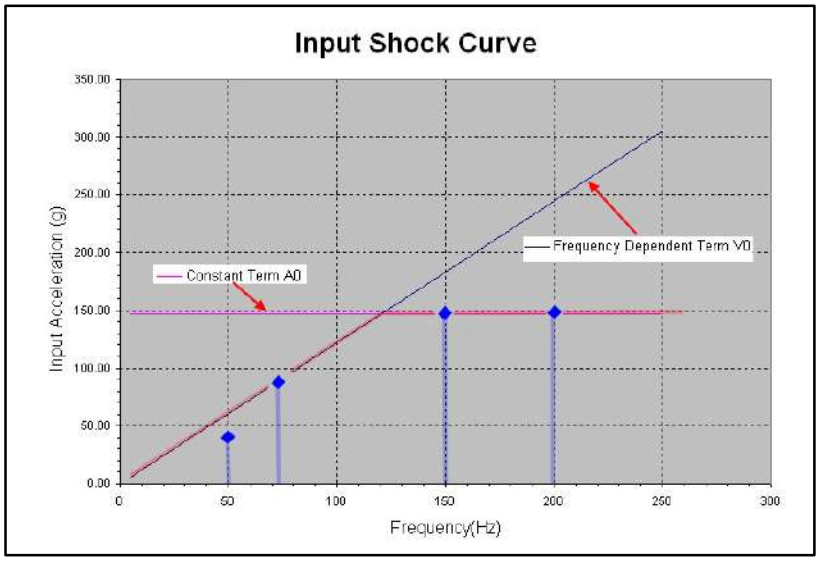

Figure 4.14 Hypothetical shock curve derived from DDAM equations (DDAM [4.9])

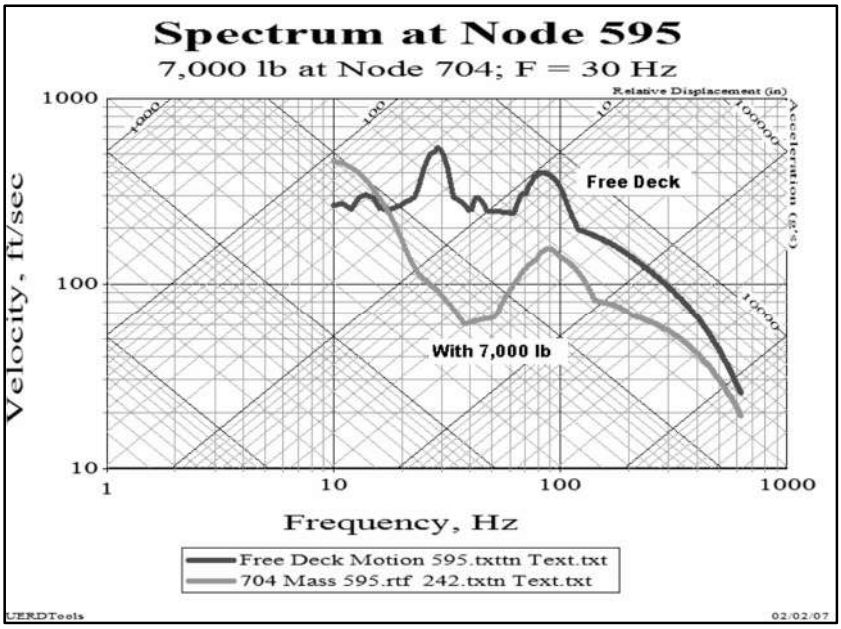

Figure 4.15 Depression in the shock spectrum at 30 Hz due to a weight of 7000 lb (Scavuzzo et al. [4.30])

4.7.2.3 Dynamic analysis in time domain

The dynamic analysis in time domain, also called in SMM/CN 300 DVD [4.33] Complete Dynamic Analysis (CDA), consists in applying at the basis of the structure in study a displacement or velocity or acceleration time history in order to simulate the complete dynamics of the phenomenon.

An example of shock input in terms of velocity time history is shown in **Figure 4.16**. These time history loads can be achieved by the SRS graphs used for shock verification, and available in the shock policy document, using the following relations reported in STANAG [4.35]:

$$T_1 = \frac{v}{a} \tag{4.19}$$

$$T_2 = \frac{2d}{v} \tag{4.20}$$

$$a = 0.549\, a_0 \tag{4.21}$$

$$v = 0.952\, v_0 \tag{4.22}$$

$$d = 1.136\, d_0 \tag{4.23}$$

where a_0, v_0 and d_0 are respectively the maximum acceleration, velocity and displacement of standard triaxial SRS (**Figure 4.9**), while a, v, and d are the respective values in the time domain.

Therefore, it is necessary to solve for each time step the differential equation of the dynamics, which can be written in general form, reported e,g. by Clough and Penzien [4.6], as:

$$[M]\{\ddot{x}\} + [C]\{\dot{x}\} + [K]\{x\} = \{f(t)\} \tag{4.24}$$

where $[M]$, $[C]$ and $[K]$ are the matrix of mass, damping and stiffness, $\{x\}$ is the solution of displacements, and $\{f(t)\}$ is the shock time history applied on the structure.

Different numerical methodologies exist for solving this problem. In particular, explicit and implicit approaches are often used. Their theoretical explanation is reported by de Silva in [4.8]. In general, implicit integration methods are unconditionally stable, but they require more effort in terms of computational time than explicit approaches. The latter, instead, are subjected to the Courant–Friedrichs–Lewy condition for convergence (Bathe [4.3]). For small structures, in which refined mesh are used, the necessity of verification of this condition leads to use a very short time step, increasing computational effort. Therefore, in these cases, implicit methodologies should be used. In any case, no guidelines are available in the literature on how to perform this calculation, obtaining numerical results which are in agreement with experimental data. The proposed and validated design strategy developed within this PhD project is shown in Chapter 6.

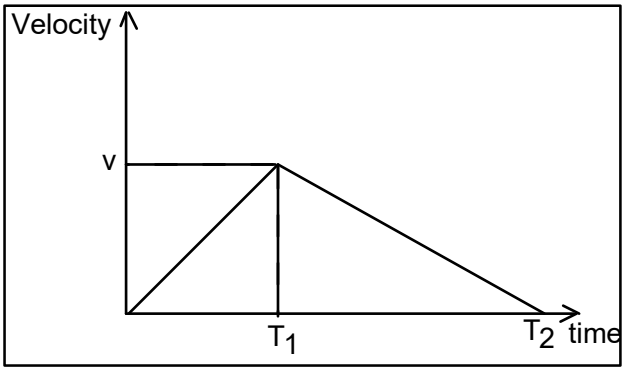

Figure 4.16 Shock input in terms of velocity time history (STANAG [4.35])

4.7.3 FSI modelling

In certain cases, the modelling of structures only is not enough to obtain the verification of the shock requirement. In the case of hull structures, for example, or when the whipping phenomenon is analysed, the entire phenomenon, including fluid, structure and their interactions, should be considered.

Nowadays several numerical methods are available, that can be used to model the UNDEX phenomenon, FSI is simulated in an attempt to predict the structural response. A good summary of the available approaches is reported in [4.38], where fluid descriptions, constitutive materials for naval panels, and different solving methods such as FEM (Finite Element Method), FVM (Finite Volume Method), BEM (Boundary Element Method), and SPH (Smooth Particle Hydrodynamics)

are described. A benchmark of computation methods organized by different numerical codes is reported by Mair in [4.19].

This numerical modelling is extremely challenging for naval architects, considering that the first shock pulse occurs in a very short time (order of a few milliseconds), while bubble pulse effects affect the ship late in time (order of seconds), as explained in the previous chapters, and reported by Keil [4.17]. In addition, phenomena such as reflection, cavitation, and diffraction are not well understood, and not easily modelled in a numerical representation. The effort necessary to simulate the entire phenomenon can result too heavy also for modern computational devices. Therefore, some assumptions must be made. Traditionally, the study of whipping is usually carried out separately from the determination of the effects of the shock pulse. The latter is, in fact, dominated by high frequencies, it loads the ship structures locally, acting mainly on the bottom panels and internal machinery, while the pulsation of the gas bubble influences the low frequencies, causing the global response of structures. This allows separate modelling.

4.7.3.1 Analytical and numerical approaches for whipping assessment

When the global effects of whipping are considered, only the bubble pulse phenomenon is used as load input. Brainard in [4.5] modified Hicks' [4.16] model to calculate the equations of pressure pulses caused by the gas bubble, verifying its effects on a destroyer modelled at first as a 2-D beam. This approach is currently used in an early design phase. Hicks' [4.16] model, corrected by Vernon [4.40], is adopted by the CETENA research center as reported by Dambra in [4.7] to verify the whipping response of naval ships. The pressure time histories in function of the bubble radius, as those reported in **Figure 4.17**, are used as input for the calculation. The ship in finite element representation is modelled like a beam and discretized by using elements and related nodes in a number between 20 and 30, a quantity that in the literature has given good results for low-frequency calculations (see **Figure 4.18)**.

The masses are concentrated in the nodes and the stiffnesses are distributed between the various elements. The equation of motion of the system results:

$$([M_s] + [M_a])\ddot{u}(t) + ([C_s])\dot{u}(t) + ([K_s] + [K_a])u(t) = ([M_a] + [M_b])\dot{v}(t) \qquad (4.25)$$

in which u is the generalized displacement, v is the velocity of the previous obtained by Hicks model and $[M_s]$, $[C_s]$ and $[K_s]$ are the matrix of the mass, damping and stiffness of the ship, $[M_b]$ is the matrix of the buoyancy mass, $[M_a]$ are is the matrix of added mass and $[K_a]$ is the hydrostatic stiffness. If the added masses are known, an eigenvalue analysis can be employed to obtain the first three or four vibration modes of the vessel. Then, the transient response of the hull is obtained by a dynamic analysis using the finite element method.

Recently, different approaches have been used to simulate the whipping phenomenon, as for example coupled FEM and Boundary Element Methods (BEM), as shown by Zhang et al. [4.41].

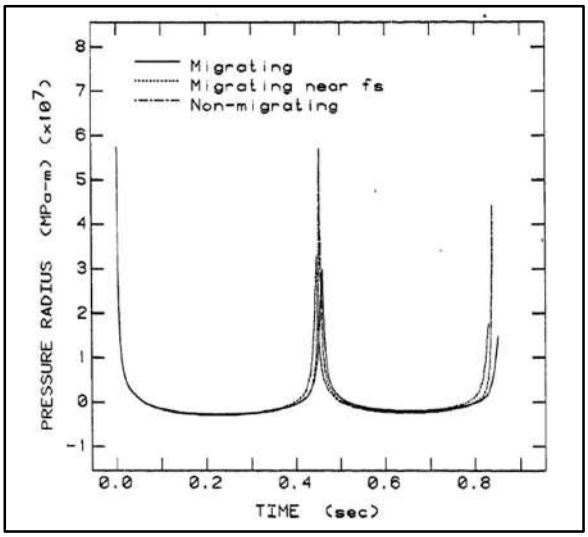

Figure 4.17 Pressure per radius of the bubble pulses considering migration and free surface effects (Vernon [4.40])

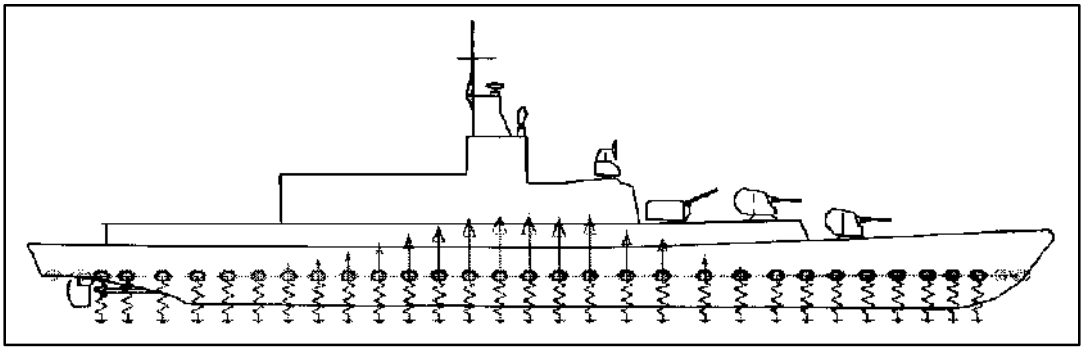

Figure 4.18 Modeling of the hull girder for whipping assessment (Dambra [4.7])

4.7.3.2 Comprehensive simulation of the structural response in the time domain

The numerical modelling of effects caused by the first shock wave can be particularly challenging considering that not only FSI must be modelled, but also a cavitation algorithm should be included in the simulation. Different approaches are used to study this phenomenon.

4.7.3.2.1 Doubly Asymptotic Approximation (DAA)

An approximate technique, commonly used to predict the UNDEX response, as reported by Scavuzzo and Pusey in [4.31], is the Doubly Asymptotic Approximation (DAA). The principles of this special Boundary Element Method (BEM) are shown by Geers in [4.13] [4.14]. A FSI equation is applied at the hull-water interface, in which the dynamic load of the shock wave and the effects of the variation

of this load due to the motion of the hull are included. Using this BEM method, it is not necessary to model the fluid around the ship, but only the water interface elements. This interaction equation considers both the high-frequency response to the shock wave and the low-frequency effects associated with the vibration modes of the ship in the water. The definition of "Doubly Asymptotic" depends on the fact that it provides good results at both low and high frequencies. Initially, it did not take into account the phenomena of local cavitation, but it was then modified to better simulate these negative effects on the hull.

The doubly asymptotic approximation equation of the first order DAA_1 can be written as:

$$[M_f]\{\dot{p}_s\} + \rho c[A_f]\{p_s\} = \rho c[M_f]\{\dot{u}_s\} \tag{4.26}$$

where:

- $[M_f]$ is the matrix of the added masses of the wet surface of the structure
- $\{u_s\}$ is the vector of the velocities of the particles of the reflected wave
- $[A_f]$ is the matrix area of the wet surface
- $\{p_s\}$ is the vector of the pressure of the reflected wave
- ρ is the density of the fluid
- c is the speed of sound.

The velocity of the structure $\{\dot{x}\}$ is related to the velocity of the particles of the incident wave and reflected by the following relationship:

$$[G]^T\{\dot{x}\} = \{u_i\} + \{u_s\} \tag{4.27}$$

where:

- $[G]$ is the correlation matrix between the displacements of the structure and the wet surface
- $\{x\}$ is the vector of the structural displacements of the finite element model
- $\{u_i\}$ is the vector of the velocities of the particles of the incident wave
- $\{u_s\}$ is the vector of the velocities of the particles of the reflected wave.

Deriving $\{u_s\}$ from this last relation, and inserting it into the first expression, the first order DAA equation of the fluid surface becomes:

$$[M_f]\{\dot{p}_s\} + \rho c[A_f]\{p_s\} = \rho c[M_f]([G]^T\{\ddot{x}\} - \{\dot{u}_i\}) \tag{4.28}$$

The hull response equation, considering the structural matrices of mass, damping and stiffness, which are respectively $[M_s]$, $[C_s]$ $[K_s]$, results:

$$[M_s]\{\ddot{x}\} + [C_s]\{\dot{x}\} + [K_s]\{x\} = \{f\} \tag{4.29}$$

where $\{f\}$, the load vector of a structure submerged by an acoustic wave, can be written as:

$$\{f\} = -[G][A_f](\{p_i\} + \{p_s\}) \quad (4.30)$$

in which $\{p_i\}$ and $\{p_s\}$ represent respectively the vector of the incident and reflected nodal pressure. The simultaneous resolution of the two equations of the fluid-structure interaction leads as a result to the dynamic response of the structure.

A more accurate solution can be obtained by using the doubly asymptotic approximation of the second order, called DAA_2, explained by Scavuzzo [4.31]. An example of application of this method to predict the shock response of a battleship is reported by Liang and Tai [4.18].

Felippa and DeRuntz [4.10] modified the method to include cavitation effects. To consider these effects, a mesh of acoustic fluid must be added around the ship in the calculation. A bilinear constitutive behaviour is simulated in cavitating fluid, for which, when cavitation occurs, the fluid volume is truncated at the boundaries with the structures. Therefore, in this condition, zero pressure is created at the boundaries. Underwater Shock Analysis (USA) code for fluid combined with LS-Dyna explicit finite element software is used for these types of calculation as shown by Shin [4.32] in **Figure 4.19**.

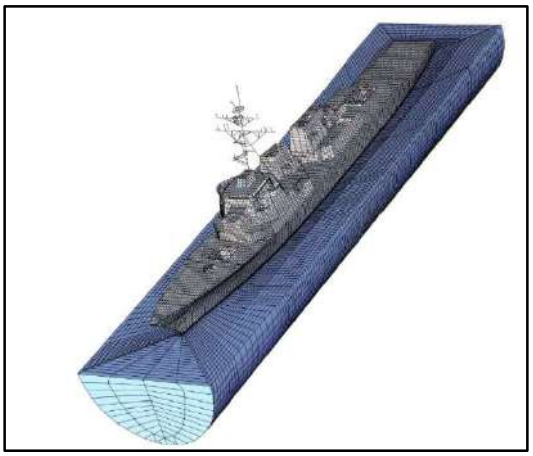

Figure 4.19 FSI modelling using the DAA approach (Shin [4.32])

4.7.3.2.2 Fully coupled FSI approaches

These methods consist of modelling, with the help of different numerical methods, both the structure of the ship and the fluid that surrounds it. Therefore, the propagation of the wave inside the fluid is simulated until its impact on the structure of the vessel. In this way, both the modelling of the shock wave and the interface between fluid and structure depends on the type of method used. This approach can provide problems of a computational nature related to the computation cost of the mathematical model; therefore, some simplification must be made.

As suggested by Tran et al. [4.38], these approaches can be divided as:

- Acoustic-Lagrangian (A-L)

- Eulerian-Lagrangian (E-L)
- Coupled BEM-FEM
- Coupled SPH-FEM

The A-L approach consists in simulating the fluid using the acoustic approximation and the structures referring to the classical FE lagrangian environment. As an example, Zong et al. [4.42] used the commercial finite element code ABAQUS-explicit to simulate the effects of a stiffened plate and compared results with experimental data, then applying the same numerical set-up to a whole ship. Using this approximation, the cavitation phenomenon is neglected. In addition, the fluid elements are always connected to the structural ones, which can cause a bias in case of large deformations. However, this method can result in a short effort of calculation.

The E-L method allows the building of fluid mesh using the Eulerian approach, and that of the structure applying the Lagrangian approach. The fluid interpolation of coordinates is often solved considering the Arbitrary Lagrangian-Eulerian (ALE) approach, which better allows the representation of large deformations of solid and fluid mesh. Using this method, it is possible to solve the equations of the state of fluids, including any algorithms for cavitation. For example, Avachat and Zhou in [4.1] used a fully coupled E-L method in order to investigate the failure mode of a glass-fiber/epoxy composite laminate. Gannon in [4.12] modelled the close-in explosion in the proximity of a submerged cylinder using an E-L explicit method, available in LS-DYNA, including explosion gases in the simulation and comparing results with experimental data. In some cases, the fluid is simulated using a Finite Volume discretization, typical of CFD methods. More details about these design methodologies are reported in Chapter 8. However, these types of approaches can be very expensive in terms of computational time, considering the necessity of suitable mesh refinement in the fluid to obtain realistic results. In addition, problems of numerical instability caused by the large deformations of mesh often occur.

The coupled BEM-FEM methods have been explained in the previous paragraph: in most of them, the DAA approximation is used to consider FSI.

In the end, the coupled Smoothed Particle Hydrodynamics (SPH)-FEM refers to a meshless model, which, as reported by Tran [4.38], is able to assess for large deformations, but it is affected in the late response by the effects of gravity and buoyancy. Ming in [4.24] made this type of calculation considering a close-in explosion on a naval ship, obtaining preliminary good results. However, more experimental data are necessary to verify the effectiveness of this method.

Generally, using these approaches the field of study is restricted to the analysis of the effects of the first shock wave. Bradbeer in [4.4] used a fully coupled FSI approach in which a plane wave approximation is used to consider the FSI interaction in order to predict the effects of the primary

shock wave on a frigate, neglecting the bubble pulse phenomenon. Mathew in [4.21] simulated the effects of far-field explosions using a simplified FSI model, referring to the first shock peak of pressure.

As a summary, the FSI methods described are the Acoustic-Lagrangian (A-L), the coupled BEM-FEM, the Eulerian-Lagrangian (E-L), and the coupled SPH-FEM. The A-L approaches use the acoustic approximation for fluid, resulting in fast calculations, but often neglecting cavitation. The coupled BEM-FEM, in which also DAA is included, are very efficient, considering that they do not require fluid modelling. Some corrections for cavitation simulation are available. The E-L methods allow in principle the FSI simulation of the complete phenomenon in case of large deformations, but they require high cost in terms of computational effort and a previous theoretical and experimental comparison. The SPH-FEM are attractive for their meshless nature. However, they are computationally expensive and even now a matter of research.

In Chapter 8, the effectiveness of some of these numerical methods is analysed, validating the design model strategies provided according to theory and experimental results.

4.8 Bibliography

[4.1] Ang B. H., Han M. J., "Managing shock requirements of shipboard equipment", DSTA Horizons, 2014;

[4.2] Avachat S., Zhou M., "Novel experimental and 3D Multiphysics computational framework for analyzing deformation and failure of composite laminates subjected to water blasts", International Journal of Impact Engineering 106, 223-237, 2017;

[4.3] Bathe K. J., Finite element procedures, Bathe K.J., Watertown, 2014;

[4.4] Bradbeer N. I. C., "Implications for Underwater Shock Response of Adopting Simplified Structural Styles in Warships", Doctor of Philosophy thesis, Department of Mechanical Engineering, UCL, 2013;

[4.5] Brainard B. C., "An Underwater Explosion-Induced Ship Whipping Analysis Method for use in Early-Stage Ship Design", Master of Science thesis, Faculty of Virginia Polytechnic Institute and State University, Blacksburg, 2018;

[4.6] Clough R.W., Penzien J., Dynamics of structures, Computer & Structures Inc., 377-381, Berkeley, 1995;

[4.7] Dambra R., Rossi V., Codice WHILE2000 (rev.1.0): Manuale utente, CETENA Report n.7654 - May (in Italian), 2001;

[4.8] De Silva C. W., *Vibration and Shock Handbook*, Taylor & Francis Group, LCC, 2015;

[4.9] *Dynamic Design Analysis Method (DDAM) Handbook*, NEi Software, Westminster, 2009;

[4.10] Felippa, C.A., DeRuntz, J.A., 1991. Acoustic fluid volume modeling by the displacement potential formulation, with emphasis on the wedge element. Computers & Structures 41 (4), 669-686.

[4.11] Fincantieri, "L'esplosione subacquea non a contatto: requisiti e metodi di progettazione delle navi militari", PPT presentation, 2020;

[4.12] Gannon L., "Simulation of underwater explosions in close-proximity to a submerged cylinder and a free-surface or rigid boundary", Journal of Fluids and Structures 87, 189–205, 2019;

[4.13] Geers, T. L., 1978. Doubly asymptotic approximation for transient motions of submerged structures. J. Acoust. Soc. Am. 64 (5), 1500–8.

[4.14] Geers, T. L., 1971. Residual potential and approximate method for three-dimensional fluid structure interaction problems. J. Acoust. Soc. Am. 49 (5, Part 2), 1505–10.

[4.15] Geers, T. L., Hunter, K. S., 2002. An integrated wave-effects model for an underwater explosion bubble. Acoustical Society of America.

[4.16] Hicks, A.N., "The Theory of Explosion-Induced Ship Whipping Motions", Naval Construction Research Establishment, NCRE Report R579, 1972;

[4.17] Keil A.H., "The Response of Ships to Underwater Explosions", Society of Naval Architects and Marine Engineers, New York, 16-17 Novembre 1961;

[4.18] Liang C., Tai Y., "Shock responses of a surface ship subjected to noncontact underwater explosions", Ocean Engineering, 2005;

[4.19] Mair, H. U., "Benchmarks for submerged structure response to underwater explosions", Shock and Vibration 6, 169–181, 1999

[4.20] Marinò A., Appunti di *"*Corso di Navi Militari e Sommergibili*"*, Università di Trieste, 2012;

[4.21] Mathew A. K., “Modeling Underwater Explosion (UNDEX) Shock Effects for Vulnerability Assessment in Early Stage Ship Design”, Master of Science thesis, Faculty of Virginia Polytechnic Institute and State University, Blacksburg, 2018;

[4.22] MIL-DTL-901-E, *Shock tests, h.i. (high-impact) shipboard machinery, equipment, and systems, requirements*, United States Department of Defense, 2017;

[4.23] MIL-S-901-D, *Shock tests, h.i. (high-impact) shipboard machinery, equipment, and systems, requirements*, United States Department of Defense, 1989;

[4.24] Ming F. R., Zhang A.M., Xue Y.Z., Wang S.P., “Damage characteristics of ship structures subjected to shockwaves of underwater contact explosions”, Ocean Engineering 117, 359–382, 2016;

[4.25] NAV-30-A001, *Norme per l’esecuzione delle prove d’urto su macchinari ed apparecchiature di bordo, Ministero della Difesa*, Istituto Poligrafico dello Stato, 1986;

[4.26] NAVSEA 0908-LP-0003010 Rev. 1, *Shock design criteria for surface ships*, Direction of Commander, Naval Sea Systems Command, Settembre 1995;

[4.27] O’Hara G.J, Belsheim R.O., *Interim design values for shock design of shipboard equipment*, U.S. Naval Research Laboratory, Washington D.C., Febbraio 1963;

[4.28] Reid W. D., *The Response of Surface Ships to Underwater Explosions*, Australian Department of Defence, 1996;

[4.29] Remmers G.M., O’Hara G.J., Cuniff P.F., “Review Dynamic Design Analysis Method DDAM”, Shock and Vibration, Vol 3, pp. 461-176, John Wiley & Sons, Inc, 1996;

[4.30] Scavuzzo R.J., Hill G.D., Saxe P.W., “The spectrum dip of deck mounted systems”, Shock and Vibration, 2010;

[4.31] Scavuzzo R.J., Pusey H.C., *Naval Shock Analysis and Design*, The Shock and Vibration Analysis Center, HI-TEST Laboratories, Inc., Second Printing 2002;

[4.32] Shin Y. S., “Ship shock modeling and simulation for far-field underwater explosion”, Computers and Structures 82, 2211–2219, 2004;

[4.33] SMM/CN 300 DVD, *Criteri e metodi per il proporzionamento e la qualificazione antiurto dei componenti destinati alle Unità navali*, Stato Maggiore Marina, Istituto Poligrafico dello Stato, 1978;

[4.34] STANAG 4142, *Shock resistance analysis of equipment for surface ships*, NATO Standardization Agreement, Maggio 2001;

[4.35] STANAG 4370, *Environmental Testing - AECTP-100 – 600*, NATO Standardization Agreement, 2016.

[4.36] STANAG 4549, *Testing of surface ship equipment on shock testing machines*, NATO Standardization Agreement, Maggio 1995*;*

[4.37] Szturomski B., "The effect of an underwater explosion on a ship", scientific Journal of Polish Naval Academy, 2015;

[4.38] Tran P., Wua C., Saleh M., Neto L.B., Nguyen-Xuan. H., Ferreira A.J.M., "Composite structures subjected to underwater explosive loadings: a comprehensive review", Composite Structures 263 113684, 2021;

[4.39] Vannucchi de Camargo F., "Survey on Experimental and Numerical Approaches to Model Underwater Explosions", Journal of Marine Science and Engineering, 2019.

[4.40] Vernon T.A., "Whipping Response of Ship Hulls from Underwater Explosion Bubble Loading", Technical Memorandum 86/225, Defence Research Establishment Atlantic, 1986;

[4.41] Zhang A.M., Yao X.L., Li J., "The interaction of an underwater explosion bubble and an elastic-plastic structure", Applied Ocean Research 30,159-171, 2008;

[4.42] Zong Z., Zhao Y., Li H., "A numerical study of whole ship structural damage resulting from close-in underwater explosion shock", Marine Structures 31, 24-43, 2013.

5 The underwater shock effects on naval composite structures: state of the art

5.1 Generalities

Composite materials have been used in marine industry for decades for their good mechanical properties compared to their light weight and for their good characteristics of resistance to corrosion. Nowadays, the research in the sector is growing constantly, increasing their knowledge, qualities, and performance. In naval applications they combine the low magnetic properties with the good qualities as energy absorbers in case of shock loads. These performances become crucial in the vulnerability design of minesweepers.

Composites structures differ from the common steal or aluminum ones because they must be properly designed to optimize their mechanical features for a specific application. In a certain sense, composites can be defined as “smart materials”. This happens because they are made by a mix of two or more materials, whose mechanical properties must be combined to obtain the desired result. Laminates of Fiber Reinforced Plastic (FRP) are the most common used in shipbuilding. A single laminate is realized by the sum of different plies (laminas), each one made by the combination of the reinforcing fibers and the matrix of polymeric resin (see **Figure 5.1**). Basically, the fiber reinforcements support primary loads, while the matrix transfer loads between plies, in particular shear stresses. The mechanical properties of a FRP laminate strongly depend by the type and the weave of the fibers, the matrix materials and the orientation and combination of the plies in the laminate’s stacking sequence. More details are reported by Green [5.16].

In maritime applications, they can be used in the form of single skin, considering a single laminate with different layers, or of sandwich, where a core material, such as PVC or balsa, can be interposed between skins made by FRP plies. In naval shipbuilding E-glass fibers, which are common, cheaper, and also have good mechanical properties, are often combined with polyester or epoxy resins. In this case, we refer to GFRP (Glass Fiber Reinforced Plastic).

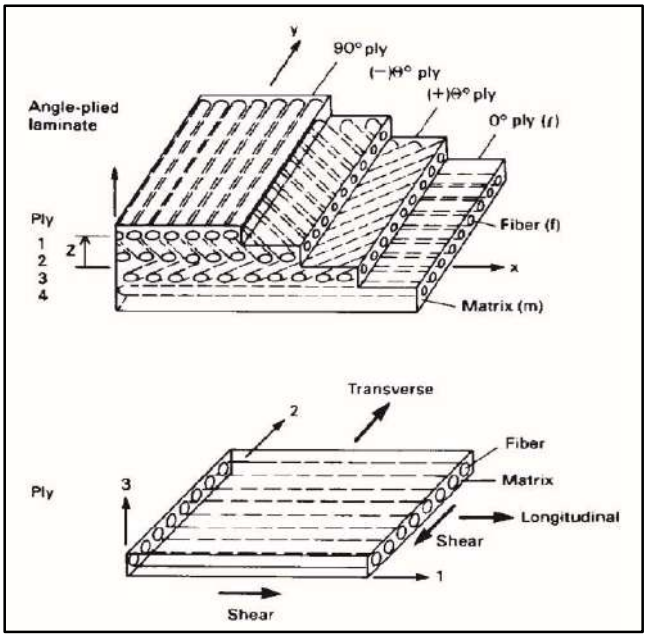

Figure 5.1 Composite laminate scheme (Green [5.16])

5.2 Hints about micromechanical and macromechanical properties

In any case, the mechanical response of the composites is different from that of the other isotropic materials (steel or aluminum), whose elastic properties does not depend by the viewing direction. In fact, they show an anisotropic behaviour such that the mechanical response depends by the direction of load application. In practical applications, the laminates can be defined as orthotropic materials considering that three axes of symmetry can be defined. These means that no. 9 elastic constants are sufficient to fully characterized these materials. Referring to principal axes X, Y, Z, these constants are the Young moduli (E_x, E_y, E_z), the Poisson moduli ($\nu_{xy}, \nu_{yz}, \nu_{xz}$) and the Shear moduli ($G_{xy}, G_{yz}, G_{xz}$). A representation of the resulting stresses in this reference system is shown in **Figure 5.2**.

For the single ply, the mechanical features can be obtained using the classical rule of mixtures, in which standard properties of fibers and matrix are combined to obtain the behaviour of the lamina, standard formulations, as the Halpin and Tsai one [5.17] to assess unknown transversal properties, and, eventually, experimental tests. However, it must be taken into account that these characteristics can be strongly influenced, more than the case of isotropic materials, by the manufacturing method and the production process which can cause the presence of unwanted voids or defects. More details are reported by Green in [5.16]. Therefore, tests obtained according to ASTM standards are commonly used in maritime shipbuilding to obtain a reliable characterization of composites.

The structural response of the laminate, instead, depends by the sum of the contributions of each lamina. Therefore, macromechanic properties must be evaluated. The commonly adopted strategy is to refer to the classical laminate theory, well-explained by Daniel in [5.10]. Starting from the lamina properties, it is possible to achieve the characterization of the laminate, using a linear and additive formulation. However, some assumptions must be made. The composite plate is considered relatively thin and subjected to a plane state of stress, a condition that can be consider true when forces and moments acts in the plane only. This means that the stress components in the thickness direction ($\sigma_z, \tau_{xz}, \tau_{yz}$) are neglected. Basically, from the mechanical properties and the orientation of the single laminas a stiffness matrix is built in order to derive from the loads the strain and the curvature of the laminate. Then, considering a linear distribution of strains along the thickness, deformations and related stresses, using constitutive equations, are obtained for each ply. Also stress distribution is linear, but it can be discontinuous between plies in case of differences in the elastic properties of each layer (see **Figure 5.3**).

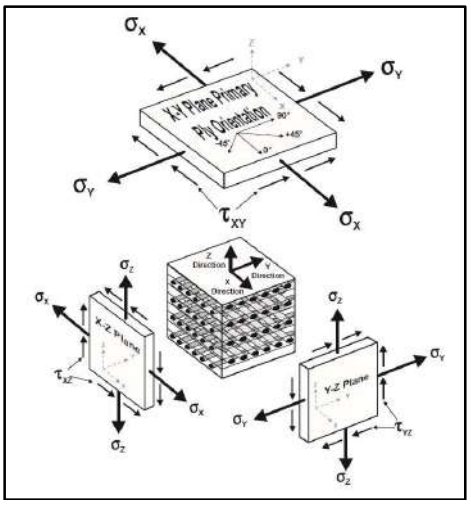

Figure 5.2 Representation of the stresses in the principal reference system (Green [5.16])

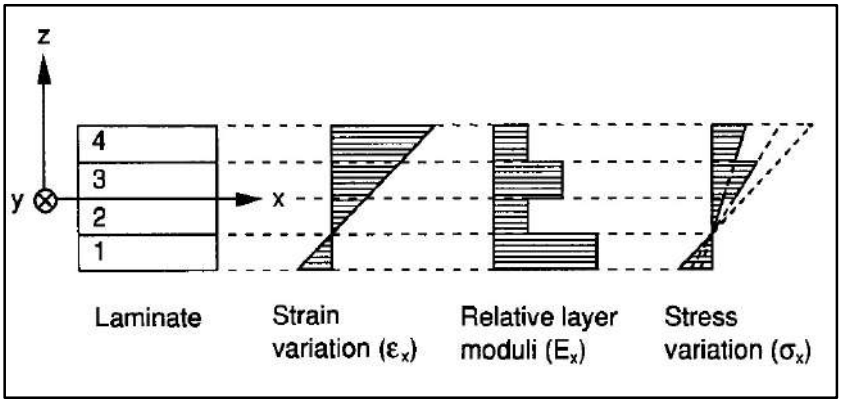

Figure 5.3 Strain and stress distribution along the thickness of a laminate (Daniel [5.10])

5.3 Limit states and failure modes

In the design process it is necessary to evaluate which limit state is important to consider in order to verify the correct scantling of the structures. Some considerations must be made in case of composites, analyzing the differences that occur referring to isotropic materials, such as steel.

In the case of steel, the material behaviour is elasto-plastic. Therefore, limit states of yielding and plastic collapse must be determined. They depend by the material properties in a particular stress condition. In case of impacts or shock loads, these mechanical features are connected to the duration of the load condition, and therefore by the strain rate. Dedicated and often expensive tests, as described by Sreenivasan and Ray [5.31], are necessary to obtain their law of dynamic characterization.

In naval shipbuilding, yielding is the most governed limit states. Well-known Von Mises criterion is commonly used to determine this limit in case of multi-axial stress conditions. However, in particular cases, plastic deformations residuals can be accepted. This can be the case of shock scantling, assuming that the severe shock load considered is rare in the life of the ship. The plastic deformation can be accepted if it does not affect the functionality of the machinery as reported in SMM rule [3.14]. Other limit states, which depend by both stress state and geometry, must considered, such as buckling, in case of thin and slender structures, fatigue for cicle loads, brittle fracture, etc…

Composites, instead, show a virtually elastic behaviour up to a brittle fracture. A comparison of the stress-strain curves obtained by the tension test for common steel and a composite ply (rovimat) is shown in **Figure 5.4**. It can be noted that the maximum deformation in the elastic regime is very higher than the one of steel: this feature provide a good quality of shock energy absorption, as well as ensuring the almost linear mechanical behaviour of the material. As it happens for steel, their structural response can change in case of impacts or shock loads. More details are reported in the following paragraphs.

More than for steel, the limit states of composites are closely linked to failure modes, which are often difficult to define uniquely. Failure in the laminates can be caused by the breaking of a single ply or a group of plies (intralaminar failure) or the detachment between layers (interlaminar failure). As limit states, referring to intralaminar failure, we can define the First Ply Failure (FPF) or the Ultimate Laminate Failure (ULF). FPF consider the failure of the first single ply as a limit to not overcome in the composite scantling. Classical laminate theory can be applied, as it considers a plane state of stress in which intralaminar stresses ($\sigma_x, \sigma_y, \tau_{xy}$) are included. Therefore, under the considered load conditions, the state of stress on each layer is calculated, and the ply strength is determined in the comparison with a limit state criterion. The most used are the maximum stress and the maximum

strain criteria, which compare respectively, one by one, the maximum components of the stress or the strain tensor with the allowable stresses or strains, and the Tsai Hill or the Tsai Wu criteria, in which a unique criterion is used to consider all the components of the stress tensor. More details, including other criteria, are available in literature as reported by Daniel in [5.10]. An example of comparison of the different criteria is shown in **Figure 5.5**, where, considering a unidirectional composite subjected to a particular biaxial stress state ($\sigma_x, \sigma_y = 0.2\sigma_x$), for each angle of incidence of the tension stress σ_x with reference to the principal direction of the fibers, the allowable stresses are reported. The red curves represent the maximum stress criterion, the blue ones the maximum strain, the dashed red curve the shear limits that are common to both these criteria, and the black and the green ones which refer to Tsai-Hill and Tsai-Wu limit states. Stress values under these curves are considered admissible, according to the reference criterion. It can be noted that the Tsai-Hill one is the more conservative respect to the others.

In some cases, the failure of the first ply limit states can be too much conservative. In this case, the ultimate capacity of the composite must be considered, referring to ULF limit state. Generally, a progressive damage scheme is followed in which the distribution of the stresses on the laminate is estimated, excluding one by one the contribute of each damaged ply. It could happen that, in case of severe loads, extreme layers can reach failure before the others, therefore the load must be supported by the inner plies.

When the type of failure is interlaminar, instead, different limit states should be considered. Fatigue, elastic buckling, or brittle cracking must be evaluated, taking into account that they depend by both material properties and structural geometry. In this case, the state of stress, which is responsible of the damage, is not bi-dimensional anymore, but it results to be three-dimensional. This means that the stress components in the thickness direction ($\sigma_z, \tau_{xz}, \tau_{yz}$) cannot be neglected. Therefore, the classical laminate theory is not valid, as it refers to a plane state of stress. Delamination can occur at the free edges of a panel also when a pure tensile loading is applied. In fact, the plane state of stress assumption is not valid in presence of geometric discontinuities where out-of-plane stress components arise. In **Figure 5.6** the interlaminar stresses occurrence at the free edges (y=0) is shown. The interlaminar strength of the laminate is not easy to assess, as it is a matrix-dominated property, depending by the chemical and interfacial properties of the matrix. Dedicated tests are always necessary, while numerical methods should be properly calibrated according to experimental results. The delamination can occur under three different modes: the opening mode (I), the sliding shear mode (II) and the tearing mode (III), as shown in **Figure 5.7**. The delamination law depends by the opening mode considered, as it can be associated to a different cohesive law defined at the interface of plies. In **Figure 5.8** an example of definition of cohesive law is presented, in which the displacement Δ

between two layers is expressed in function of the interlaminar stress τ. The parameters governing this function are the steepness of the linear part K, the maximum stress τ_{max}, and the fracture toughness, namely the energy release rate (G_{IC}), which is the energy necessary to separate laminas, corresponding to the area under the triangle shown in **Figure 5.8**. These parameters should be set in the framework of a numerical method according to experimental tests results, as reported by Maggiani in [5.23].

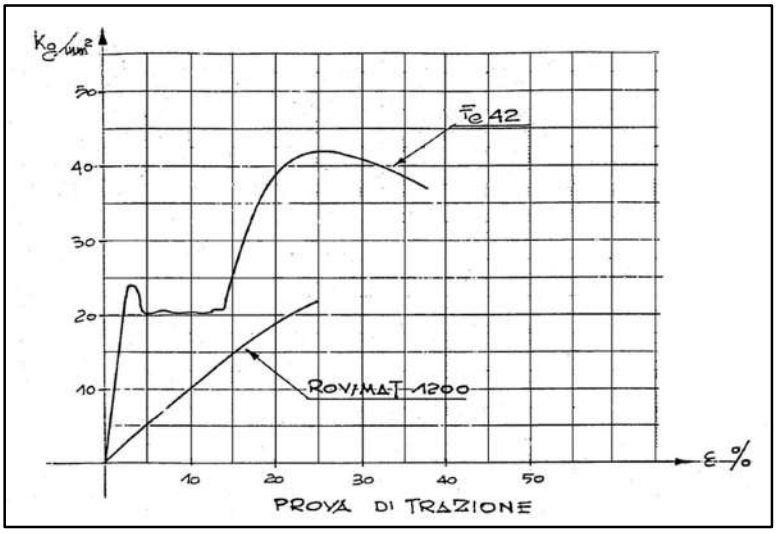

Figure 5.4 Example of stress-strain curves obtained by a tension test for steel and composite materials (MARISTAT [5.32])

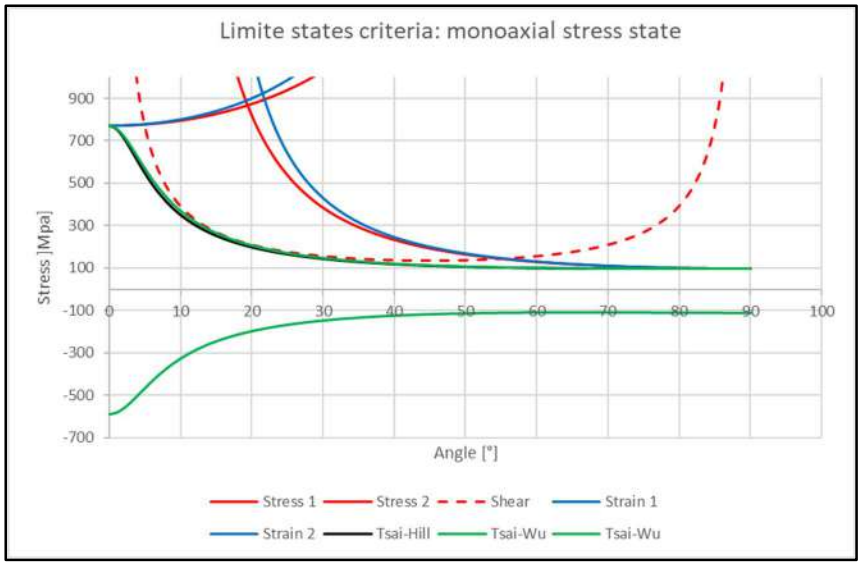

Figure 5.5 Comparison of different limit states criteria for a unidirectional composite subject to a monoaxial stress state

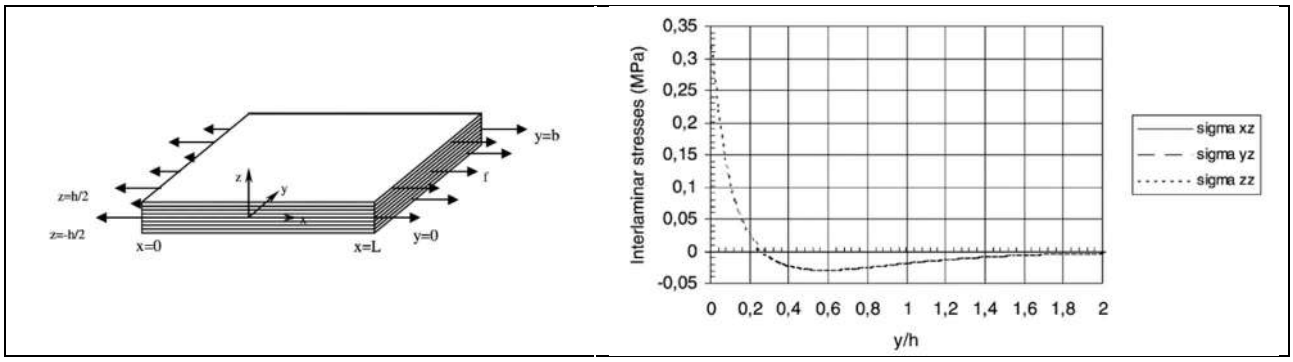

Figure 5.6 Interlaminar stresses at the free edges in a panel with a tension load (Lorriot et al. [5.22])

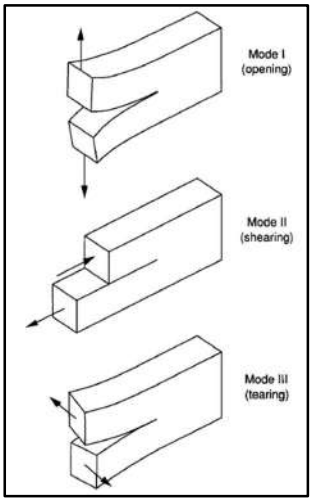

Figure 5.7 Opening modes of delamination (Daniel [5.10])

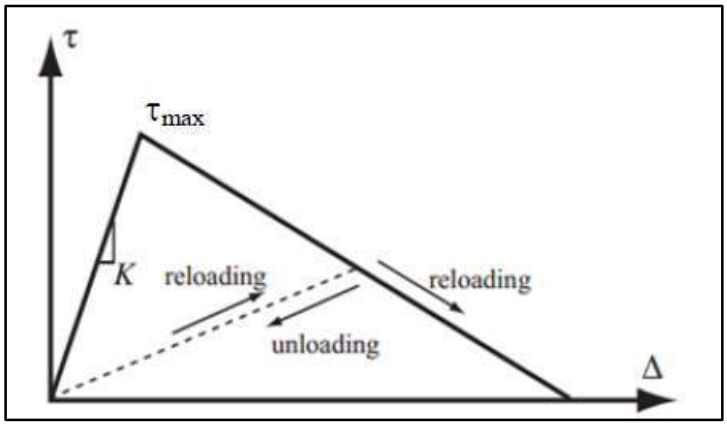

Figure 5.8 Cohesive law for delamination (Maggiani et al. [5.23])

5.4 Effects of impacts caused by UNDEX on composite materials

5.4.1 Failure modes and numerical assessment

The damage caused by the impact of the shock wave of the UNDEX phenomenon can be particularly severe on composite material.

In literature, especially in aeronautic field, effects of impacts on composites are classified according to the velocity and the duration of the impacts. Generally, according to [5.14], they are divided into low-velocity impacts, where peak velocity is less or equal than 10 m/s, high-velocity impacts, in which velocity values are between 10 and 100 m/s and ballistic impacts for higher velocities. Therefore, to properly design composites, it is important to understand the mechanical of the failure modes associated with these impulsive loads, which are different according to the velocity of impact. Interlaminar and intralaminar failure can provide different effects in the laminate. A review of the types of cracking connected to different failure modes is shown in **Figure 5.9**. The intralaminar failure modes can occur in the form of matrix cracking, fiber breakage and fiber/matrix debonding, while the interlaminar ones can be opening dominated cracks, often caused by buckling phenomena, and shear dominated cracks.

For high-velocity or ballistic impacts, as reported by [5.14], the damage is localized in the zone of the impact, which can be a cause of material penetration in severe cases, while for the low-velocity ones the energy is distributed in a wider area. As reported by Xu & Rosakis in [5.36], interlaminar cracks caused by out-of-plane share (τ_{xz}, τ_{yz}) are the dominant failure modes in case of low-velocity impacts on layered materials and sandwich structures. Also, intra-laminar matrix cracking is shown, but after the beginning of delamination. Therefore, a 3-D state of stress must be taken into account in each numerical method which has the aim of assessing failure caused by impact. Feng and Aymerich in [5.12] underlined the importance of consider constitutive models for interlaminar and intralaminar failure modes in numerical approaches. In open literature, cohesive elements have been used to simulate delamination caused by low-velocity impact, as reported by Aymerich et al. in [5.6]. However, their properties must be set according to a cohesive law, such as that shown in **Figure 5.8**, which should be calibrated according to experimental data. In **Figure 5.10**, a representation of these elements in ADINA^{TM} finite element software is shown: 3-D cohesive elements are set between 3-D solid elements used to model the three-dimensional mechanical properties of composite layers. Nowadays, even if cohesive models can be useful to simulate interlaminar delamination, they are still not able to predict matrix cracking phenomena, which occur in the out-of-plane direction. As reported by [5.27], matrix cracking can appear as shear cracking, with an inclination of 45° in the out-of-plane direction, and bending cracking, extended vertically in the through-thickness direction. Richardson

& Wisheart in [5.26] underlined that in case of low-velocity impacts, the grow of matrix cracking can lead to delamination in a phenomenon that is called "critical matrix crack". Coexistence of matrix cracking and delamination in case of impacts is shown in **Figure 5.11**. Therefore, in these cases, the using of cohesive models should be combined to failure criteria which consider matrix cracking, such as example, the Hashin's model [5.18].

Another important phenomenon, which is not easy to consider in numerical method, but which influence the impact response of composites, is the so called "fibre bridging". Delamination cracks can interact with misaligned or inclined fibres as reported by Spearing & Evans in [5.30]. They made different experiments showing as the resistance to brittle fracture increases in case this phenomenon occurs, resulting in higher values of energy release rate (G_{IC}) necessary for delamination. Examples of delamination occurrence with or without "fibre bridging" is shown in **Figure 5.12**. A review of the studies available in literature is made by Khan [5.19]. Zhang et al. [5.37] studied the effects of interfacial debonding and sliding on fracture characterisation of unidirectional fibre-reinforced composites, highlighting that they are two important mechanisms in increasing composite toughness. This phenomenon depends by the interface between the matrix and fibres, being influenced by different features, such as matrix properties, coatings and manufacturing methods. Cavano &Winters in [5.9] studied the effects of different coatings in composite toughness, affirming that generally a weak matrix-fibre interface leads to an increasing in impact resistance, resulting in fibre bridging and fibre pull-out, but to a decreasing in resistance to quasi-static load. Gaiotti et al. in [5.13] showed that two laminates, characterized by the same stacking sequence, but made by using different techniques (prepreg and infusion method), when subjected to a compressive load, result in a case in a brittle fracture, showing interlaminar debonding, and in the other case in a though fracture. In this last kind of damage, the fibre-matrix interface is interested, resulting in fibre bridging phenomenon. Numerical methods can be used to simulate this phenomenon, but they must be properly set according to experimental data. As an example, in ADINA^{TM} manual [5.1], special "rebar" elements are presented, which can be used to simulate the behaviour of fibres in a volumetric matrix, as shown in **Figure 5.13**. In these elements, constraints equations are built to connect volumetric nodes with the truss ones. In any cases, these equations must be set by the users according to tests, considering that fibre bridging depends by several variables (matrix properties, coatings and manufacturing methods), which influence is not even clarified yet.

In literature not many tests are available in which effects of underwater explosions on composite materials are reported. In addition, a limit of these tests is that the impact region is relatively small compared to the entire specimen, resulting in localized failure modes, which can be different compared to global response obtained in naval structures. Mouritz et al. in [5.25] made UNDEX tests

on GFRP laminates used for the construction of Bay class minehunters of the Australian Navy. The specimens were made of E-Glass vinyl ester resin, in which layers of biaxial woven roving were alternated to plies of chopped strand mat, as it was the configuration of the skins of the foam core sandwiches in the hull laminate. As shown in **Figure 5.14**, two test configurations, referring to air-backed and water-backed conditions, were realized. As expected, failure modes occur only in the air-backed condition, because in the water-backed the plate behave as it was transparent to the shock wave. In particular, matrix cracking caused by the bending moment occurs, as it shown in picture a) of **Figure 5.15**. These cracks propagate vertically, being stopped by fibers in case they are normal respect to the crack direction of propagation, or crossing around reinforcements in the other cases (see pictures b) and c) of **Figure 5.15**). Extensive delamination is shown in case of severe impacts, as a result of post-mortem analysis in picture d) of **Figure 5.15**. Mouritz et al. [5.25] suggest using toughened polymer matrices, in which small rubber bubble are blended, to stop the propagation of matrix cracking along thickness.

LeBlanc & Shukla in [5.21] show that the primary damage caused by underwater explosion in E-Glass vinyl ester resin biaxial laminates is delamination, where also minimal matrix cracking and fiber breakage was observed. Latourte et al. in [5.20] made further UNDEX tests, obtaining as a result that, when the impulse increase, matrix microcracking and ultimately fiber fracture always occur as well as delamination failures. The experiments were about quasi-isotropic E-Glass vinyl ester resin plates and sandwich panels with PVC foam core. GFRP plates show microcracking and delamination particularly extended close to the edges of the panel where bending modes effects are important and interlaminar shear provide interlaminar fracture as shown in picture a) of **Figure 5.16**. In the centre of the panel matrix, where biaxial stretching is maximum, matrix cracking is extended in the thickness direction, producing as a result fibre failure (see picture b) in **Figure 5.16**). In case of sandwiches the failure modes are affected by the interaction between core and skins, resulting in delamination and skin debonding.

The reference to these experimental tests allows us to underline the importance of considering in the application of numerical methods a three-dimensional stress state, in order to predict intralaminar and interlaminar damage. Wei et al. in [5.34] considered as failure criteria the Hashin's model [5.18] to predict intralaminar failure, while they use cohesive elements to assess delamination, referring to the case of study of Latourte et al. [5.20], an example of which is shown in **Figure 5.16**. A comprehensive criterion in which failure modes (in-plane and delamination) of E-Glass epoxy resin laminates have been predicted successfully has been used in the work of Le Blank & Shukla in [5.21].

However, the application of methods, in which 3-D and cohesive elements are used to model delamination, on a full-scale ship UNDEX case is hardly feasible, considering the computational

effort necessary to simulate fluid-structure interactions and multilayer solid/shell and cohesive elements used to model composites. In addition, matrix cracking and fibre bridging phenomenon are not easy to be simulated, if properly tests are not performed to calibrate numerical models. Matrix-fibre interface properties, which affects the dynamic response of composites, depend by different variables, such the type of matrix, the manufacturing method, the coatings, etc… In any case, this phenomenon is still a matter of research, considering that the analysis of experimental tests available in literature has led to divergent conclusions about the effects of fiber-matrix interaction on the dynamic behaviour of composites. It seems that further tests are necessary to understand the micromechanics of the phenomenon. Therefore, nowadays, shock characterization must be made case by case, for the single composite laminate. The dynamic characterization of the shock transient response of new mine countermeasures vessels' fiberglass is described in Chapter 7.

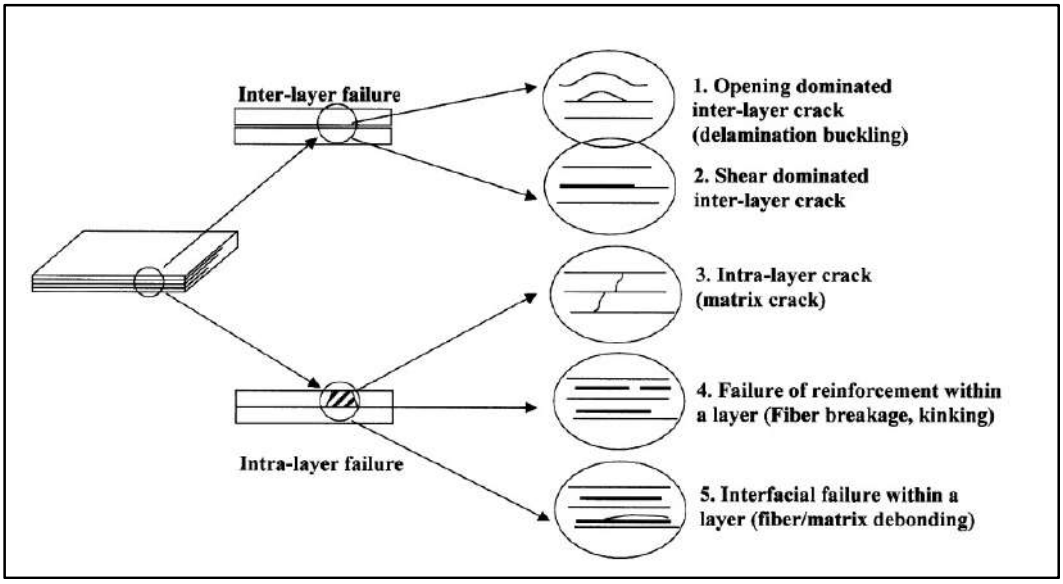

Figure 5.9 Failure modes and cracking of composite materials (Xu & Rosakis [5.36])

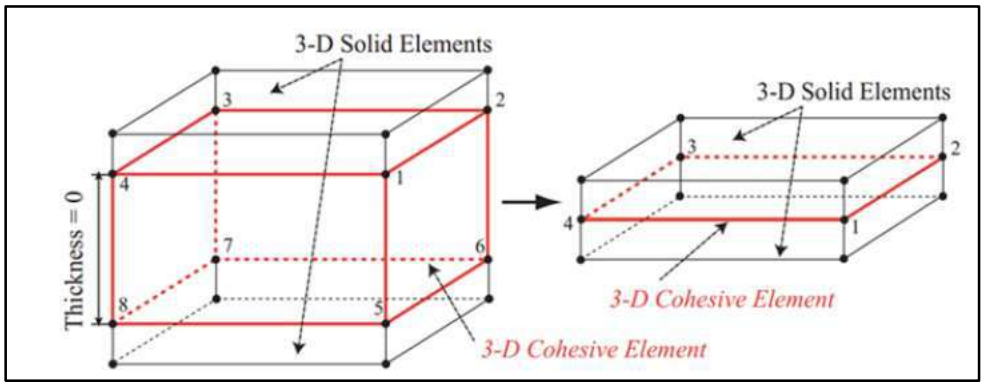

Figure 5.10 Representation of 3-D cohesive elements in ADINA™ software (Maggiani [5.23])

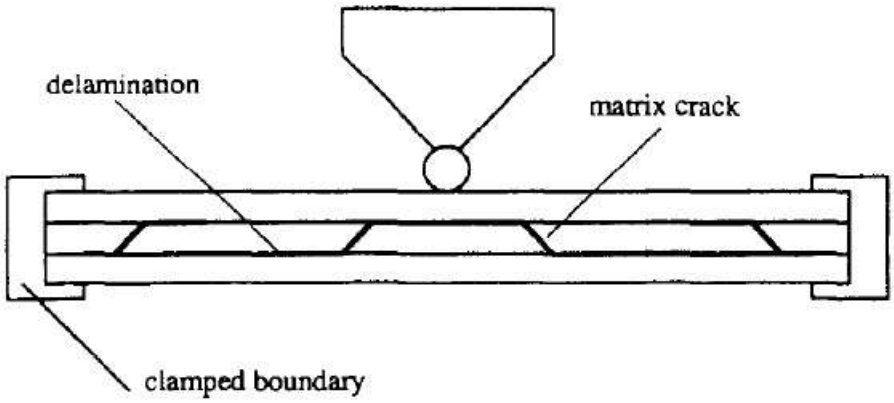

Figure 5.11 Matrix cracking and delamination in case of low-velocity impacts (Richardson [5.26])

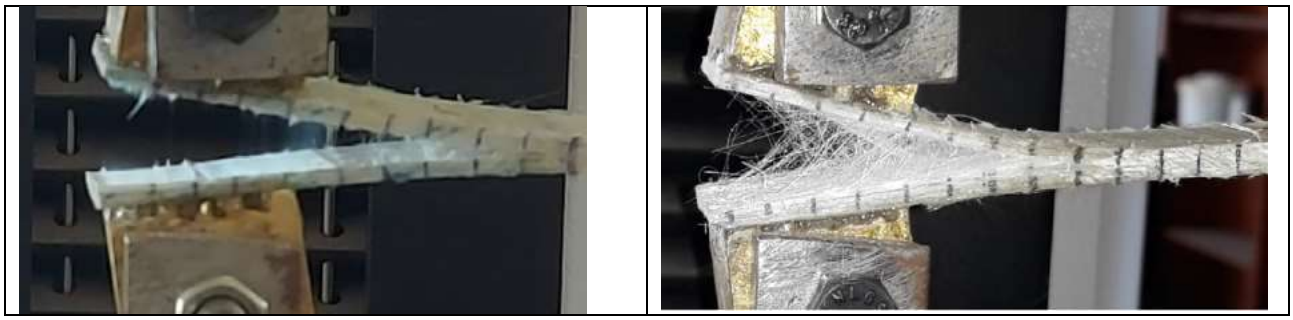

Figure 5.12 Delamination without fibre bridging (on the left) and with fibre bridging (on the right) (Elhadary et al. [5.11])

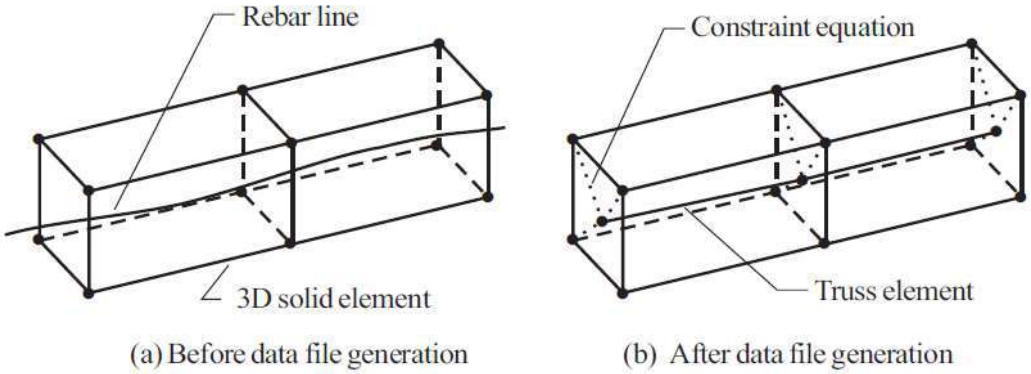

Figure 5.13 "Rebar" elements in ADINA^{TM} software [5.1] for fibre bridging modelling

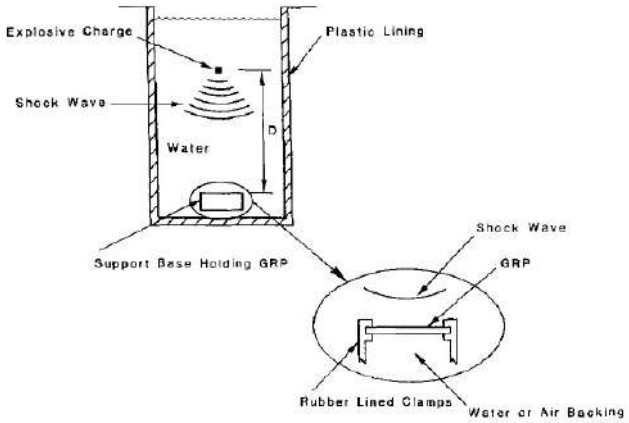

Figure 5.14 Underwater explosion tests on GFRP made by Mouritz et al. [5.25]

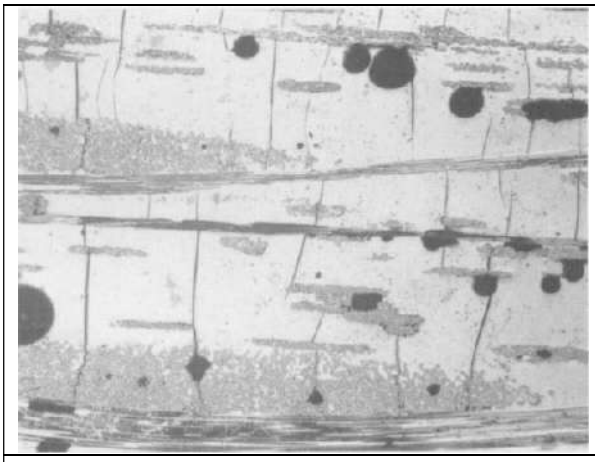

a) Cracks in the resin shown by optical micrograph

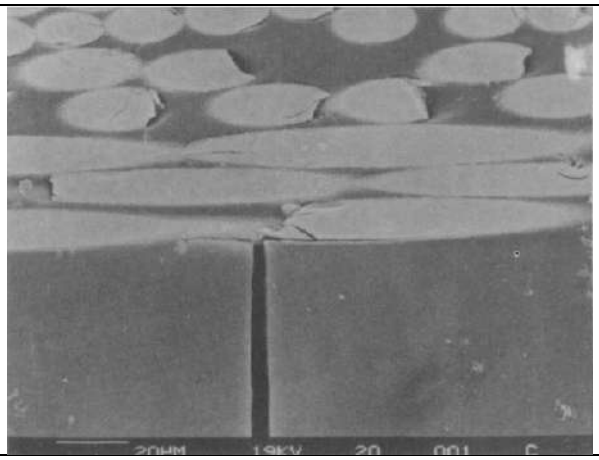

b) A crack stopped by a fiber shown by scanning electron micrograph

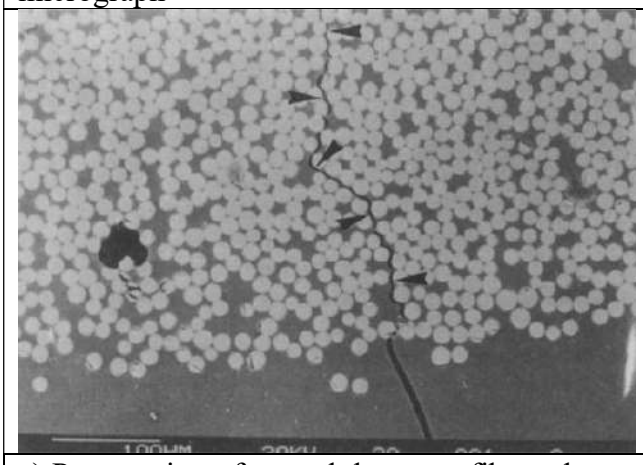

c) Propagating of a crack between fibers shown by scanning electron micrograph

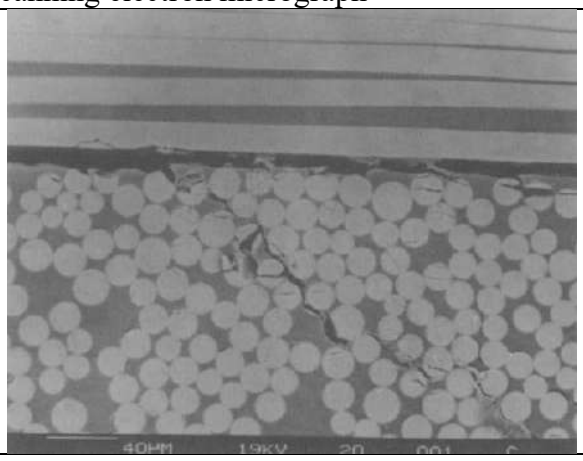

d) Delamination between layers shown by scanning electron micrograph

Figure 5.15 Failure modes of GFRP caused by UNDEX according to Mouritz et al. tests [5.25]

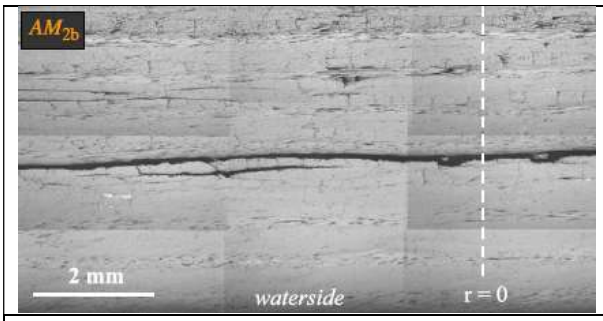

a) Microcracking and delamination shown by optical micrograph	b) Extensive delamination and fiber fracture at the center of the panel

Figure 5.16 Failure modes of GFRP caused by UNDEX according to Latourte et al. tests [5.20]

5.4.2 Dynamic behaviour

As reported by Barrè et al. [5.7] and by Welsh and Harding [5.35], the mechanical behaviour of composites depends by the strain rate, namely it is governed by the impact velocity. An example of stress-strain curves obtained in dynamic tests by using a Hopkison Bar for a woven-reinforced E-Glass GFRP is reported in **Figure 5.17**. It can be noted that a small increment in the steepness of the curves is obtained for intermediate strain rate (22/s), while a larger one is measured for the highest strain rate (1260/s). In addition, ultimate strength is increasing with the impact velocity, depending also by the changing in the failure modes. Barrè et al. [5.7] and Welsh and Harding [5.35] both agree that composite stress-strain curves are strongly influenced by the matrix properties and the matrix-fibers interaction. Therefore, the elastic Young modulus seems to depend mostly by the matrix modulus and strength. However, not many data are available in literature, and often results are obtained with different experimental methods, with reference to composites of different weaving, stacking sequence, matrix composition, etc... An example of this dependence for different E-glass poly ester and epoxy resin laminates is shown in **Figure 5.18**.

Historically, when effects of UNDEX on composite materials are predicted, this dynamic behaviour is often neglected. However, some attempts in including in numerical models have been made in the last decades. LeBlanc and Shukla [5.21][5.21] studied experimentally and numerically the effects of UNDEX to some E-glass composites, assuming that the material inputs are determined from quasi-static tests data. Batra and Hassan [5.8] calculated fiber-reinforced composite response to shock, including strain rate effects in shear modulus and transversal elastic modulus, though no validation by experimental comparison was reported. Wei et al. [5.34] validated a numerical method to study the UNDEX structural response for unidirectional E-glass laminates and sandwiches, considering the delamination phenomenon as depending by a strain rate sensitive law and starting from the failure mechanisms shown by Latourte et al. [5.20]. Arora et al. [5.2] highlighted the importance of boundary

conditions on the structural response caused by the underwater blast to glass fiber-reinforced plastics and sandwiches. A complete review of experimental and numerical methods used to assess the UNDEX response of composites is reported in the work of Tran et al. [5.33]. Despite efforts of researchers outlined in open literature, the dynamic transient response to UNDEX of fiberglass laminates seems not clearly defined yet. An experimental and numerical method, with the aim of obtaining the dynamic characterization of E-Glass polyester biaxial laminates, is described in Chapter 7.

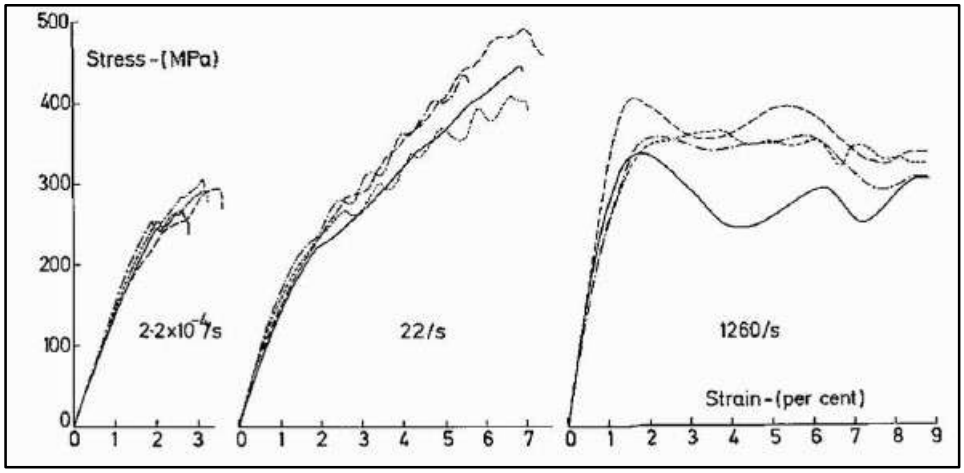

Figure 5.17 GFRP stress-strain curve dependence by strain rate (Welsh and Hardening [5.35])

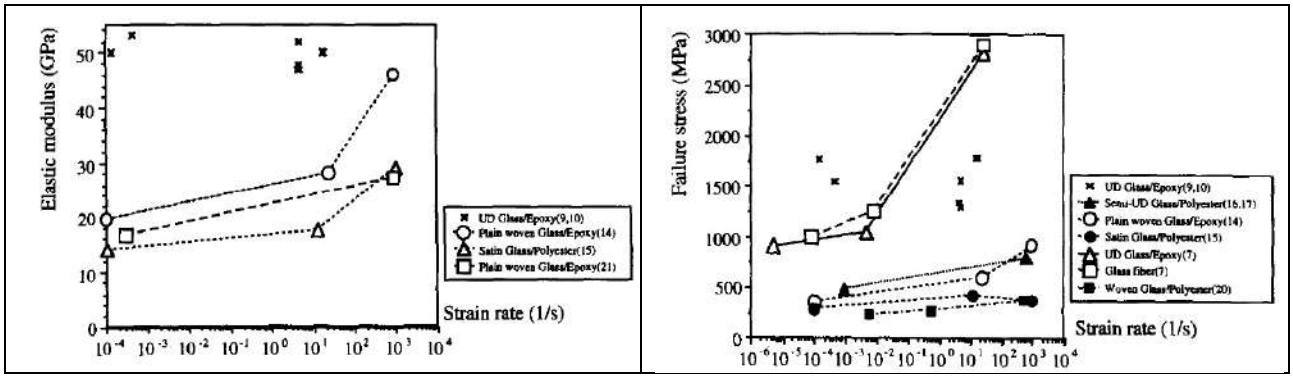

Figure 5.18 Effects of strain rate on Elastic modulus and failure strength for different waving and matrix-fibre combinations of E-Glass laminates (Barrè et al. [5.7])

5.5 Bibliography

[5.1] ADINA, *Theory and Modeling Guide* Volume I-III, ADINA R & D Inc., Watertown, 2015;

[5.2] Arora H., Hooper P., Dear J., "The effects of air and underwater blast on composite sandwich panels and tubular laminate structures", Exp. Mech. 52 (1), 59–81, 2012;

[5.3] Avachat S., Zhou M., “High-speed digital imaging and computational modeling of dynamic failure in composite structures subjected to underwater impulsive loads”, International Journal of Impact Engineering 77, 2015;

[5.4] Avachat S., Zhou M., “Compressive response of sandwich plates to water-based impulsive loading”, International Journal of Impact Engineering 93, 2016;

[5.5] Avachat S., Zhou M., “Novel experimental and 3D Multiphysics computational framework for analyzing deformation and failure of composite laminates subjected to water blasts”, International Journal of Impact Engineering 106, 223-237, 2017;

[5.6] Aymerich F., Dore F., Priolo P., “Simulation of multiple delaminations in impacted cross-ply laminates using a finite element model based on cohesive interface elements”, Composites Science and Technology 69, 1699–1709, 2009;

[5.7] Barrè S., Chotard T., Benzeggagh M.L., “Comparative study of strain rate effects on mechanical properties of glass fibre reinforced thermoset matrix composites”, Composites Part A 27A, 1169-1181, 1996;

[5.8] Batra R.C., Hassan N.M., “Response of fiber reinforced composites to underwater explosive loads”, Composites Part B 38, 448–468, 2007;

[5.9] Cavano P. J., Winters W. E., *Composite impact strength improvement through a fiber/matrix interface*, National Technical Information Service, Springfield, 1975;

[5.10] Daniel I. M., Ishai O., *Engineering Mechanics of Composite Materials*, Second Edition, Oxford University Press, New York, 2006;

[5.11] Elhadary M., Hamdy A., Shaker W., “Effect of fiber bridging in composites healing”, Alexandria Engineering Journal 61, 2769–2774, 2022;

[5.12] Feng D., Aymerich F., “Finite element modelling of damage induced by low-velocity impact on composite laminates”, Composite Structures 108, 161–171, 2014;

[5.13] Gaiotti M., Rizzo C. M., Branner K., Berring P., “An high order Mixed Interpolation Tensorial Components (MITC) shell element approach for modeling the buckling behavior of delaminated composites”, Compos. Struct. 108, 657-666, 2014;

[5.14] Gholizadeh S., “A review of impact behaviour in composite materials”, International Journal of Mechanical and Production Engineering, Volume- 7, Issue-3, pp 2320-2092, 2019;

[5.15] Ghoshal R., Mitra N., “On core compressibility of sandwich composite panels subjected to intense underwater shock loads”, Journal of Applied Physics 115 024905, 2014;

[5.16] Green Associates E., *Marine Composites*, Eric Greene Associates, 1999;

[5.17] Halpin J. C., Nicolais L., Materiali compositi: relazioni tra proprietà e struttura, Ingegnere Chimico Italiano 7:173, 1971;

[5.18] Hashin, Z., Failure criteria for unidirectional fiber composites. J. Appl. Mech. 32947, 329, 1980;

[5.19] Khan R., “Fiber bridging in composite laminates: A literature review”, Composite Structures 229 111418, 2019;

[5.20] Latourte F., Gregoire D., Zenkert D., Wei X., Espinosa H.D., “Failure mechanisms in composite panels subjected to under water impulsive loads”, J. Mech. Phys. Solids, 2011;

[5.21] LeBlanc J., Shukla A., “Dynamic response and damage evolution in composite material subjected to underwater loading: experimental and computational comparisons”, Compos. Struct. 92, 2421-2430, 2010;

[5.22] Lorriot Th., Marion G., Harry R., Wargnier H., “Onset of free-edge delamination in composite laminates under tensile loading”, Composites Part B: Engineering, Volume 34, Issue 5, Pages 459-471, ISSN 1359-8368, 2003;

[5.23] Maggiani G., Boote D., Gaggero T., Gaiotti M., Rizzo C. M., “Calibration of the Cohesive Parameters of Fiberglass Reinforced Plastic Plates with an Embedded Delamination by Experiments”, Proceedings of the Twenty-seventh (2017) International Ocean and Polar Engineering Conference, San Francisco, CA, USA, 25-30 June, 2017;

[5.24] Mori L. F., Queheillalt D. T., Wadley H. N. G., Espinosa H. D., “Deformation and Failure Modes of I-Core Sandwich Structures Subjected to Underwater Impulsive Loads”, Experimental Mechanics 49, 257–275, 2009;

[5.25] Mouritz A.P., Saunders D.S., Buckley S., “The damage and failure of GRP laminates by underwater explosion shock loading”, Composites, Volume 25, Number 6, 1994;

[5.26] Richardson M. O. W., Wisheart M. J., *Review of low-velocity impact properties of composite materials*, Composites Part A 27, 1123-1131, 1996;

[5.27] Safri S., Sultan M.T.H., Jawaid M., *Damage analysis of glass fiber reinforced composites*, Durability and Life Prediction in Biocomposites, Fibre-Reinforced Composites and Hybrid Composites, 133-135, 2019;

[5.28] Smith C. S., *Design of Marine Structures in Composite Materials***,** Elsevier, Applied Science, 1990;

[5.29] SMM/CN 300 DVD, *Criteri e metodi per il proporzionamento e la qualificazione antiurto dei componenti destinati alle Unità navali*, Stato Maggiore Marina, Istituto Poligrafico dello Stato, 1978;

[5.30] Spearing S. M., Evans A. G., "The role of fiber bridging in the delamination resistance of fiber-reinforced composites", Acta metal. mater. Vol. 40, No. 9, pp. 2191-2199, 1992;

[5.31] Sreenivasan P. R., Ray S. K., *Mechanical Testing at High Strain Rates*, Encyclopedia of Materials: Science and Technology, Elsevier, pp. 5269-5271, 2001;

[5.32] Stato Maggiore della Marina, *Guida al progetto delle navi militari*;

[5.33] Tran P., Wua C., Saleh M., Neto L.B., Nguyen-Xuan. H., Ferreira A.J.M., "Composite structures subjected to underwater explosive loadings: a comprehensive review", Composite Structures 263 113684, 2021;

[5.34] Wei X., Tran P., De Vaucorbeil A., Ramaswamy R.B., Latourte F., Espinosa H.D., "Three-dimensional numerical modeling of composite panels subjected to underwater blast", Journal of the Mechanics and Physics of Solids 61, 1319-1336, 2013;

[5.35] Welsh L., Harding J., "Effect of strain rate on the tensile failure of woven reinforced polyester resin composites", Journal de Physique Colloques 46 (C5), 405-414, 1985;

[5.36] Xu L. Roy & Rosakis Ares. J., "Impact failure characteristics in sandwich structures. Part I: Basic failure mode selection", International Journal of Solids and Structures 39, 4215-4235, 2002;

[5.37] Zhang X., Liu H.Y., Mai Y.W., "Effects of fibre debonding and sliding on the fracture behaviour of fibre-reinforced composites", Composites: Part A 35, 1313–1323, 2004.

6 Definition of some guidelines for the shock design using the finite element method

6.1 Introduction and motivation of the work

Nowadays, the use of finite element methods for shock assessment is a common practice in shock design, especially in the early phases. However, the choice of the modelling strategy and the fundamental inputs often depends by the designer's experience, even if the simulation involves only structures in a simplification of the full UNDEX phenomenon.

As reported in Chapter 4, rules allow the shock verification by means of calculation if tests are not available. In some cases, simplified approaches, such as quasi-static methods, which are more conservative, and statistical SRS approaches, such as DDAM methods, which do not consider non linearities, does not satisfy the shock requirements. In these cases, a dynamic transient method should be used, which is more complex but more generally applicable, starting from a displacement, velocity or acceleration time history. This last choice, in particular, can cope with non-linear problems, unlike the statistical SRS approaches (being an analysis in frequency domain implicitly linear). It is particularly useful to analyse the shock response of equipment mounted on its foundations by means of non-linear mountings in order to obtain directly the simulated behaviour of the structure.

In any case, no detailed modelling strategies, procedures, and inputs have been provided in literature on how to perform this type of analysis, hence the need of research. Therefore, the aim of this Chapter is to provide some reliable guidelines useful in the design phase to perform a dynamic calculation: the validation of the model is checked comparing the numerical results with data achieved from tests, properly designed for the purpose, carried out according to the MIL S 901 D medium weight shock standard.

As a case of study, the shock behaviour of a typical foundation structure is analysed, considering that in the military common practice, the machinery is shock tested, according to MIL S 901 D [6.12] standards, while the relevant foundations are normally verified by calculation. In early design phases, in fact, it is in general not possible to test the equipment including the relevant structural foundations, then a verification criterion must be assessed. In this Chapter, dedicated shock tests are carried out onto a typical foundation structure and measurements are compared with Finite Element (FE) results obtained by non-linear dynamic implicit calculation with the purpose of validating the FE proposed procedure.

At first, experimental and numerical modal analysis are performed in parallel to estimate natural frequencies and to define an adequate time step for further dynamic calculations. Then, implicit dynamic calculations, according to Bathe Method, explained in [6.1] and [6.2], are run, imposing as

dynamic load input the displacement time histories experimentally measured by means of accelerometers at the base of the structure, and considering only gravity as static load input. Calculations and experimental shock tests are carried out considering both rigid connections and elastic mountings, modelled with connector elements simulating their stiffness and damping. In the FE simulation three different models of mounting are proposed to evaluate their accuracy with reference to the experimental results. The validation of the calculation method is checked comparing its results with test data achieved using the high-impact shock machine for medium weight. The results of the comparison are presented for both the rigid and the elastic case. They have been published in [6.9] and [6.10].

6.2 Experimental analysis

6.2.1 Test set-up

The experimental analysis consists in testing a foundation structure made by two 275 JR steel parallel UPN 100 beams, 1.2 m long. A 250 kg mass is used to simulate the weight of the machinery. In the first series of tests the mass is directly bolted to the foundation beams; in the second, instead, it is connected to these beams by mountings, type POWERFLEX PWHS0953008 [6.15].

Experimental modal analysis (EMA), as described by Ewins [6.7], was carried out suspending the structure on four rubber bands, see **Figure 6.1**. The hammer-roving method is used, which consists in hammering three times (in order to get a mean value of Frequency Response Function – FRF) in the three directions X, Y and Z (longitudinal, transversal and vertical) with an instrumented hammer in a single reference point (no. 45 in **Figure 6.2**) and in moving a triaxial accelerometer for each test in 44 different points (see Figure 6.3). The sampling frequency is 1000 Hz which is more than adequate for this work interest band of analysis that is from 0 to 450 Hz.

The nine FRFs functions measured in each point are analyzed using the Me Scope Ves [6.11] commercial software to obtain natural frequencies, damping and modal participation factors. The number of peaks for each function is counted using the Multi-Reference CMIFs (Complex Mode Indicator Functions) algorithm in the Me Scope Ves environment. The curve fitting function for the determination of the natural frequencies and related Eigenvalues is carried out using the Multi-Reference Quick Fit method. **Figure 6.4** and **Figure 6.5** show examples of FRFs: the black curve is the signal measured, the red curve, instead, is that reconstructed by the software through curve fitting algorithm. **Figure 6.6** shows natural frequencies, damping (in percentage and half power band as well) and modal participation factors in the three directions, X, Y and Z.

The modal analysis was deemed necessary both to validate the analysis model and to define an adequate shock test set-up.

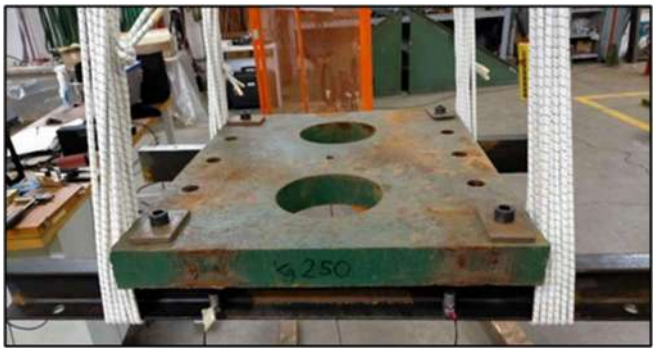

Figure 6.1 Experimental modal analysis structure

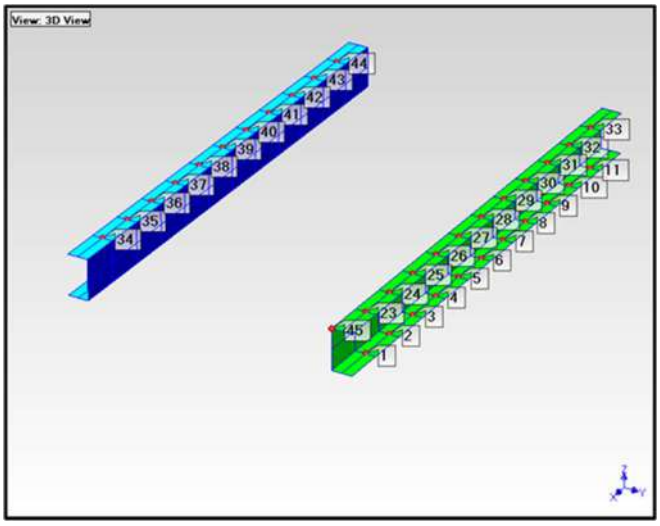

Figure 6.2 Experimental modal analysis: measurement point scheme

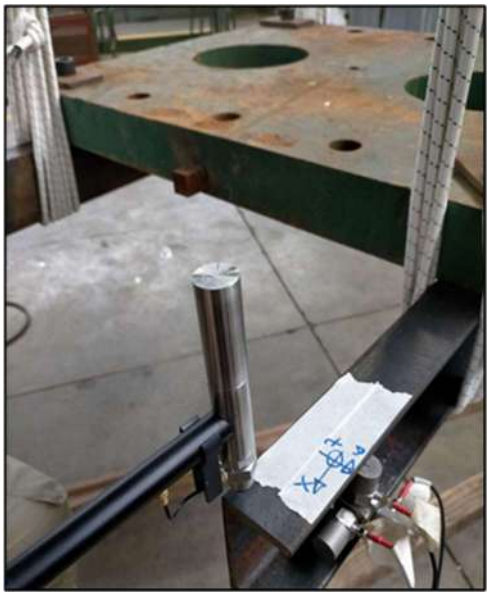

Figure 6.3 Experimental modal analysis: vertical hammer and accelerometers in point no. 1

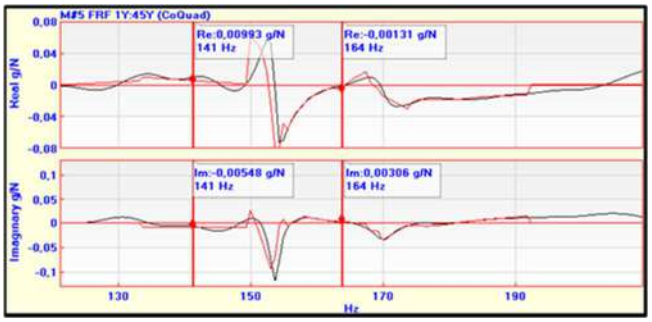

Figure 6.4 Example of measured (black) and curve fitted (red) FRF close to 152 Hz

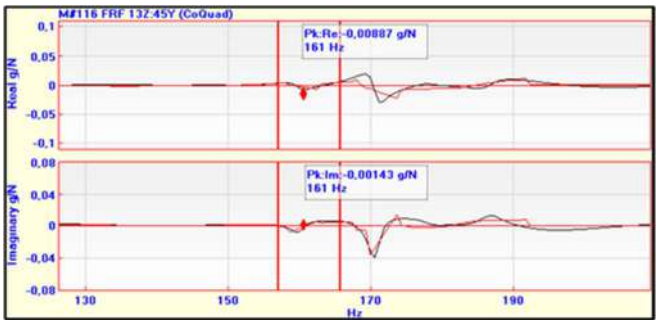

Figure 6.5 Example of measured (black) and curve fitted (red) FRF close to 161 Hz

Select Mode	Frequency Hz	Participation	Damping (%)	Damping Hz
1	152	(0,16,0,98,-0,03)	0,893	1,36
2	161	(-0,09,0,12,-0,98)	0,814	1,31
3	174	(0,97,0,00,-0,22)	0,608	1,06
4	283	(0,96,-0,09,0,00)	0,387	1,09
5	314	(0,03,-0,91,-0,13)	0,369	1,16
6	366	(-0,97,0,02,0,13)	0,464	1,7

Figure 6.6 Experimental natural frequencies, damping and modal participation factor in the three directions (X, Y and Z)

6.2.2 Rigid shock test setting and testing

For the shock tests a MIL S 901 D [6.12] medium weight shock machine (MWSM), described in its theoretical behaviour by Clements [6.3], is used, connecting the structure under test to the machine anvil table by means of standard mounting platforms. Accelerometers are set on the supporting channels to obtain the displacement time history at the foundation basis. The weight reference (350 kg) is chosen according to the MIL S 901 D [6.12] rule criteria. In this value, it is considered the sum of the 250 kg of mass, the foundation beams and the standard mounting fixture weight. Shock loadings are produced in the vertical direction, varying the anvil table travel and the height of hammer drop. The structural response is measured by means of six strain gauges (no. 1-2-6 uniaxial and no. 3-4-5 triaxial rosette), that are bonded onto the foundation beams, close to the rigid connection of the mass. The sampling frequency of all measurements is 50 kHz. See **Figure 6.7** and **Figure 6.9**.

Figure 6.7 Rigid shock test: accelerometers setting. Accelerometers on supporting channels are circled

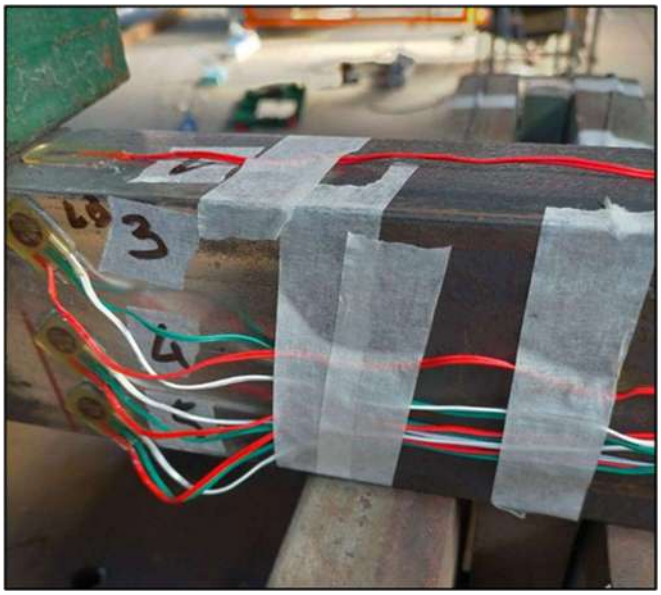

Figure 6.8 Rigid shock test: strain gauges no. 1 (on top faceplate), 3, 4 and 5 (on web) set up

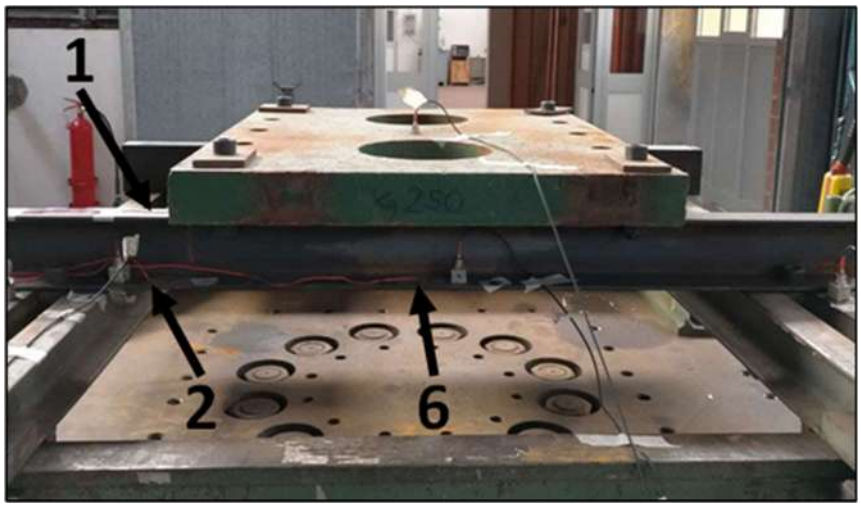

Figure 6.9 Rigid shock test: strain gauges no. 1 (on top faceplate), 2 and 6 (on bottom faceplate) set up

Eight vertical shock tests were carried out, increasing gradually the height of the drop hammer and varying the anvil table travel, as shown in **Table 6.1** and **Figure 6.10** and **Figure 6.11**.
The signals measured on the top faceplate (strain gauges no. 1) and on the top web (strain gauges no. 3) show the increase up to yielding from test no. 5 and onwards when the hammer height increases up to 600 mm (see **Figure 6.12** and **Figure 6.13**).
The Fast Fourier Transform (FFT) diagrams made by strain gauges measurements confirm the EMA results showing the natural frequency in the vertical direction at 169 Hz, even if this has less energy during a shock impact and it tends to lose in the background noise (**Figure 6.14**). Moreover, this frequency analysis shows that during the shock test other operational frequencies are observed at 59 Hz and 127 Hz, which exist only in connection with the shock condition, but are not identified by EMA. These natural frequencies are caused by the frequency of installation support. In particular, 59 Hz is the natural frequency of the medium weight shock machine, as it is reported in the work of Clements [6.3].

Table 6.1 Rigid shock test schedule for medium weight shock machine

Test	Hammer height	Anvil table travel
#	m	m
1	0.300	0.076
2	0.300	0.076
3	0.300	0.076
4	0.300	0.076
5	0.600	0.076
6	0.600	0.038
7	0.600	0.076
8	0.600	0.038

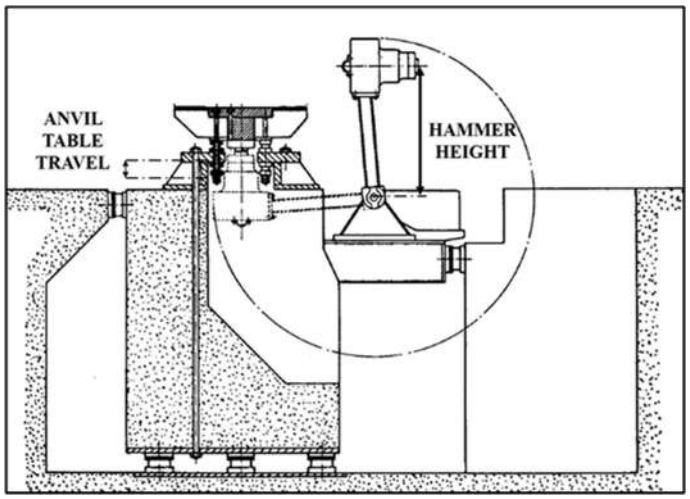

Figure 6.10 MIL S 901 D medium weight shock machine scheme

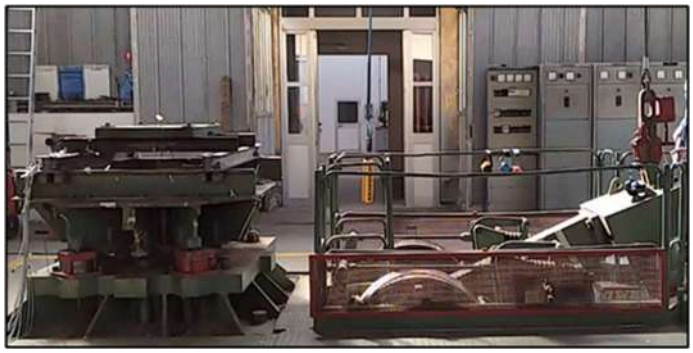

Figure 6.11 Rigid shock test drop positioning

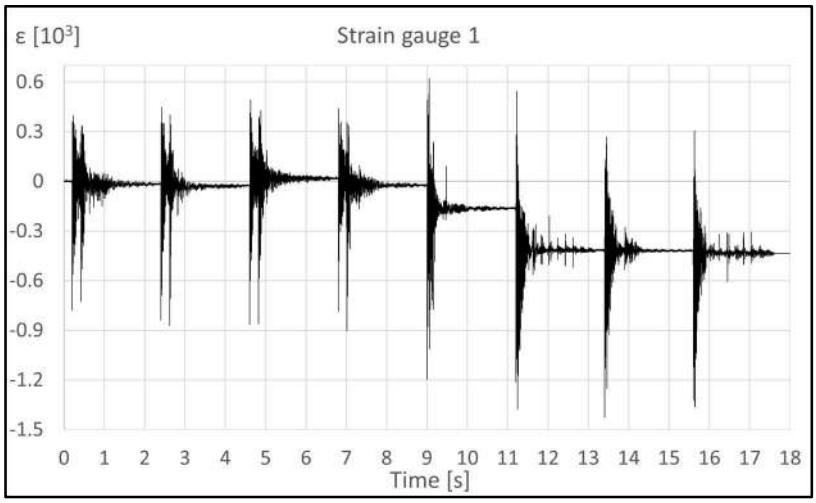

Figure 6.12 Strain gauges no. 1 (top faceplate): longitudinal strain measurement sequence

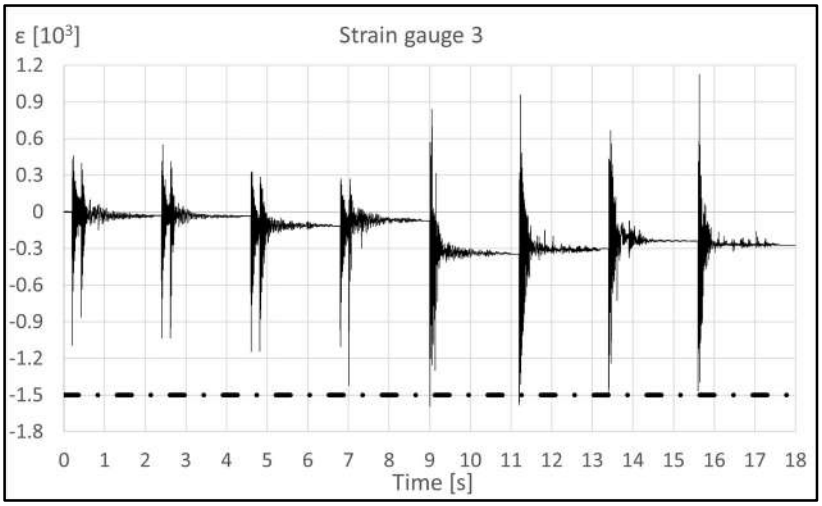

Figure 6.13 Strain gauges no. 3 (top web): longitudinal strain measurement sequence. The dashed line represents the static yield threshold

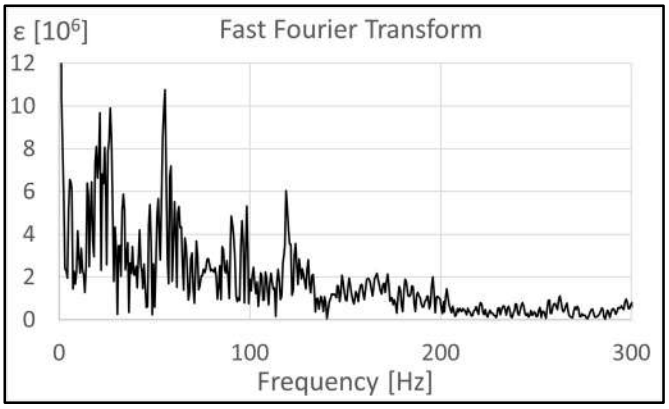

Figure 6.14 Example of FFT diagram made by Strain gauge no. 3 measurements in Test no. 4

6.2.3 Elastic shock test setting and testing

The shock test set-up is the same of the previous series of tests, but in this case the structure has been mounted on shock machine complete with elastic mountings (n° 4 antishock and antivibration stainless steel cable dampers of company Powerflex model number "PWHS0953008") (see **Figure 6.15** and **Figure 6.16**). In addition, a triaxial rosette strain gauge (no. 7) on web top is added to study the response close to the elastic connection (see **Figure 6.17**). The foundation beams that were yielded in the rigid shock test are of course replaced. No. 3 vertical shock tests are carried out, increasing gradually the height of the drop hammer, **Table 6.2**. In this case signals do not show plastic strain residual after the series of tests (see **Figure 6.18** and **Figure 6.19**).

Figure 6.15 Shock test with mountings set up

Figure 6.16 Shock test with mountings: effects immediately after the drop hammer (image taken from recorded video)

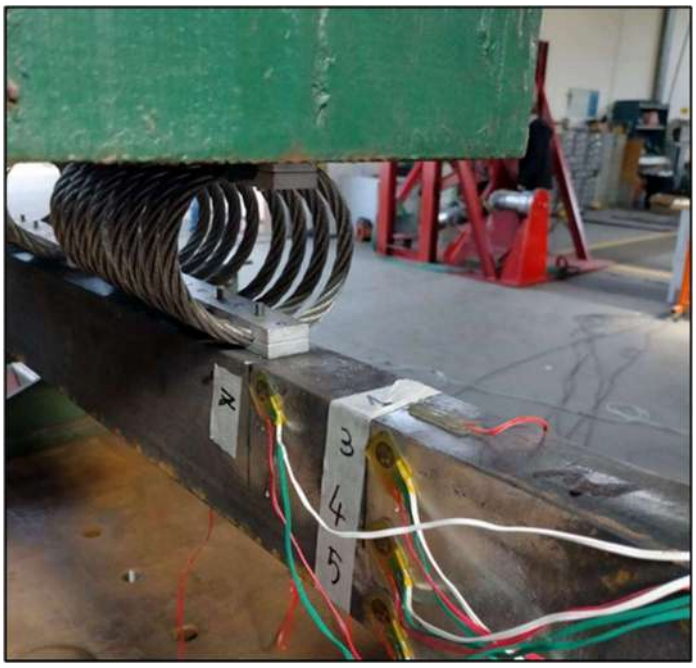

Figure 6.17 Shock test with mountings: strain gauges no. 1 (top faceplate), 3, 4, 5 and 7 (web) set up

Table 6.2 Shock test with mountings schedule for medium weight shock machine

Test	Hammer height	Anvil table travel
#	m	m
1	0.200	0.076
2	0.300	0.076
3	0.600	0.076

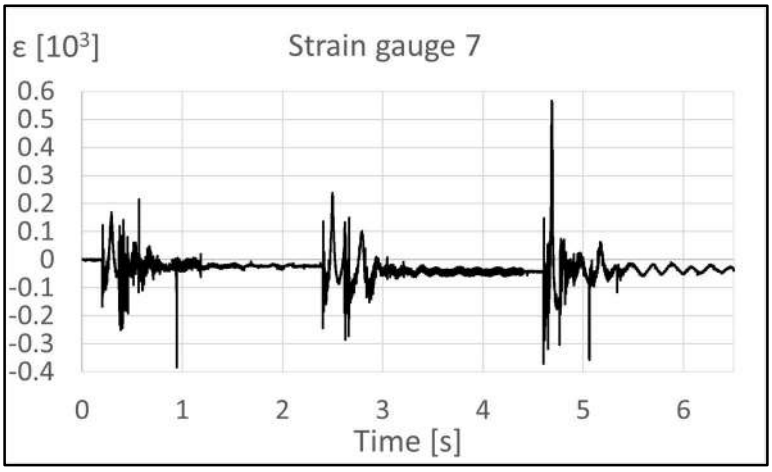

Figure 6.18 Strain gauges no. 7 (top web): longitudinal strain measurement sequence

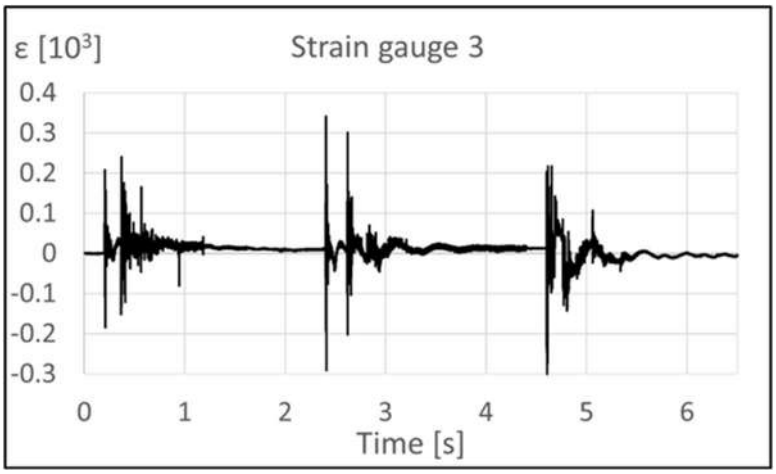

Figure 6.19 Strain gauges no. 3 (top web): longitudinal strain measurement sequence

6.3 Numerical simulation

6.3.1 Finite element method model

The numerical analysis was performed using ADINA™ [6.1] software. Two different models were built, the former considering a rigid connection, while the latter includes to modelling of an elastic support. In the FE environment the foundation is discretize into 4-nodes shell elements, while the mass is modeled using a 27-nodes volumetric element, with proper density properties (see **Figure 6.20**). The mass is supposed to be more rigid than the foundation beams, so the elastic modulus of the relevant volumetric element is imposed suitably higher ($2.0^7 \cdot 10^{12}$ N/m^2) than the one of steel beams ($2.0^7 \cdot 10^{11}$ N/m^2).

The dynamic behaviour of the foundations material (steel 275 JR) is characterized extrapolating from the HIPEBA [6.8] report the proper stress-strain curves that depend on their strain rate function (see **Figure 6.21**). The foundation is linked to the mass by means of rigid links (Coats et al. [6.5]) in the

bolted case and connector elements with proper stiffness and damping in the elastic condition. Numerical drilling stiffness problems in the 6 DOF connection nodes of rigid links and connectors to neighbouring shell nodes are solved, using soft beam elements. This kind of constraint is linked to a single node, so that the stress concentration is relevant. To get around this issue, a 0.5 mm square area of elastic shell elements is modelled around the rigid links connection nodes.

A sensitivity analysis on mesh refinement has been carried out. Results in good agreement with experimental data are obtained selecting for the FEM model a very fine mesh patterns as that suggested by classification societies' rules for the two-dimensional elements FEM models (i.e. shell elements). Therefore, the shell elements mesh is chosen considering a relatively small length (2.5 mm) for the rectangular zone (80 mm longitudinally long) of the top faceplate and of the web close to the rigid or elastic connections (**Figure 6.22**). The remaining part of the foundation is modelled by a coarser mesh (10 mm element size).

Mountings are modelled using connectors with stiffness properties defined by the non-linear symmetric curves load-displacement for compression/tension, shear and roll degrees of freedom **(Figure 6.23**) and concentrated dampers with constant damping value (10%). The curves load-displacement and the damping value have been provided by mountings suppliers. Three different mounting models are proposed: the first consists of a single connector foundation-mass, the second of eight connectors set along a row and the third of 24 connectors distributed in a matrix (**Figure 6.24**). In these two last models, the stiffness properties of each connector of a single mounting are evaluated considering that they are distributed in parallel. Moreover, the connectors are linked to the equipment using rigid links.

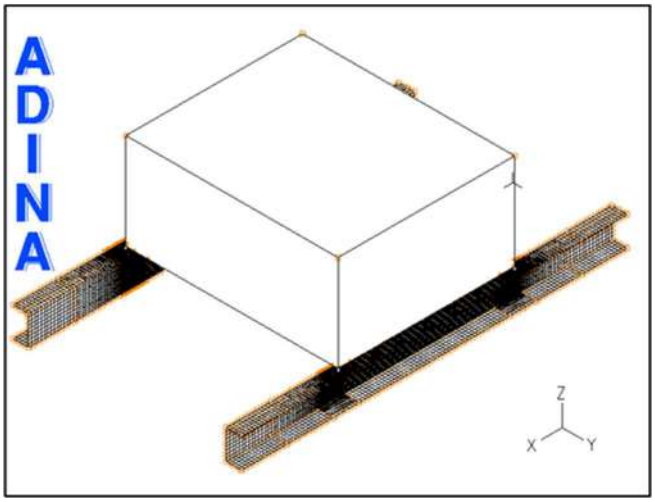

Figure 6.20 Finite element model: rigid connection case

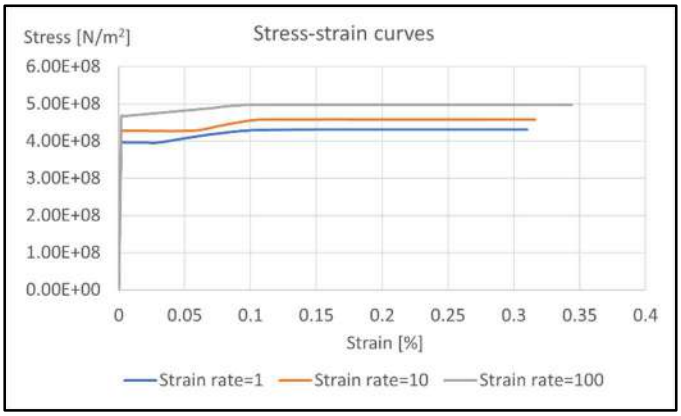

Figure 6.21 Stress-strain curves (engineering stress) depending by strain rate (see HIPEBA (2015) [6.8])

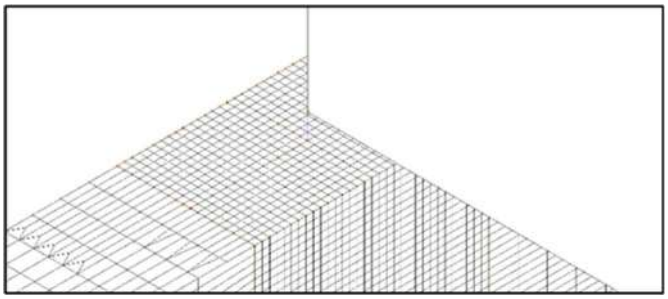

Figure 6.22 Finite element method mesh close to the rigid connection

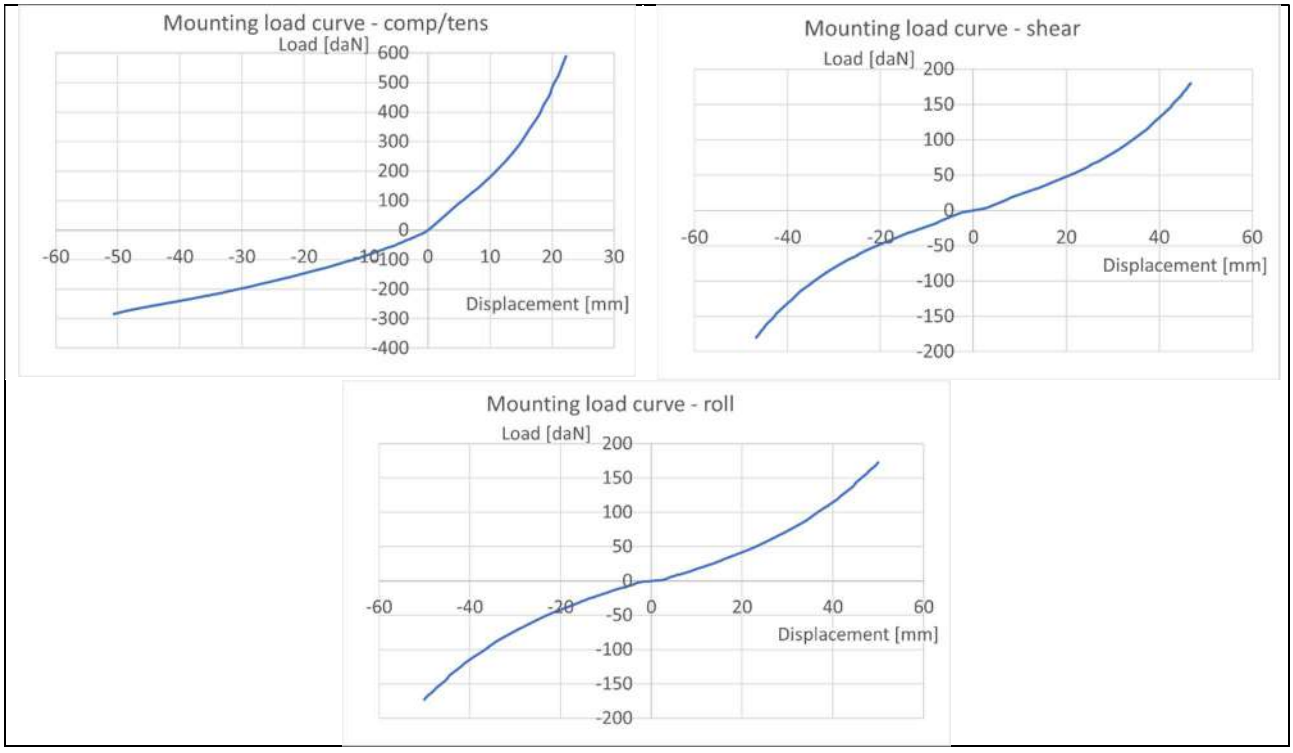

Figure 6.23 Mounting loads curves provided by mounting suppliers – Compression/tension, shear and roll

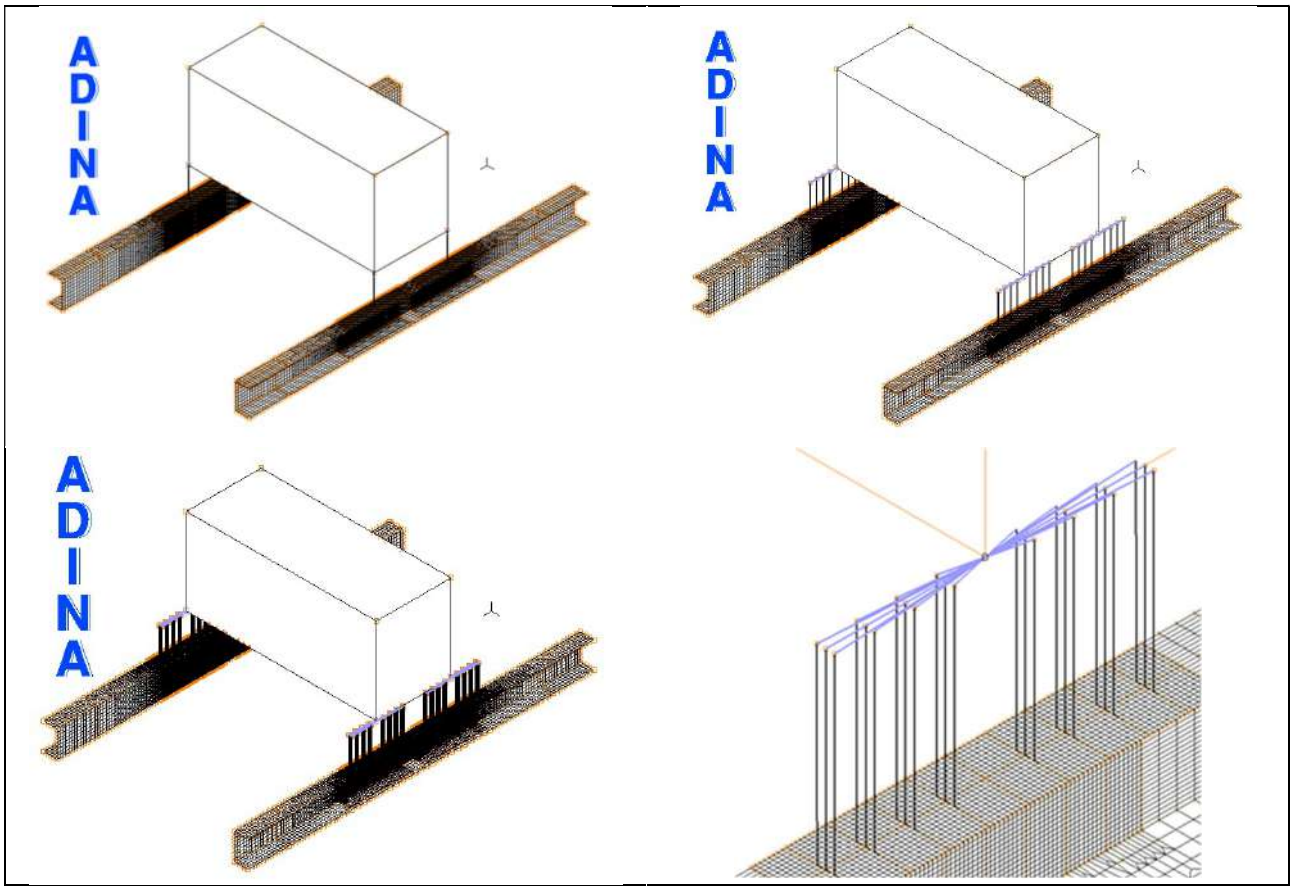

Figure 6.24 FEM mounting models with 1, 8 and 24 connectors (a particular of 24 connectors model is shown)

6.3.2 Modal analysis

A modal analysis using Enriched Subspace Iteration Method [6.1] [6.2] is performed, starting from the solution of the static problem, where only gravity as mass proportional load is applied on the model. Simple supports are used as boundary condition to simulate the structure suspended on four rubber bands (**Figure 6.25**). Natural frequencies and percentage masses are reported in Table 6.3. More of the 80%, according to NAVSEA [6.14], of the percentage masses is in the range from 0 to 450 Hz (92% only in the vertical direction Z): this confirms the validity of the choice to carry out the Experimental Modal Analysis in this band.

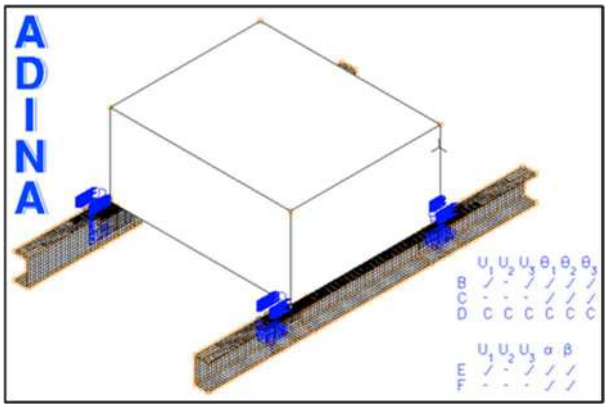

Figure 6.25 FEM modal analysis: boundary conditions

Table 6.3 FEM modal analysis: natural frequencies and percent masses

Mode No.	Frequency Hz	Percent Mass (X) %	Percent Mass (Y) %	Percent Mass (Z) %
1	132.5	0.00	66.40	0.00
2	168.3	0.00	0.00	92.16
3	168.4	68.11	0.00	0.00
4	342.8	23.47	0.00	0.00
5	411.2	0.00	0.00	0.00
6	445.2	0.00	23.84	0.00
7	474.7	0.00	0.00	0.83
8	474.8	0.00	0.43	0.00
9	477.9	0.53	0.00	0.00
10	481.1	0.00	0.00	0.00
11	565.3	0.00	0.00	0.40
12	565.5	0.00	2.25	0.00
13	568.6	0.00	0.00	0.00
14	568.8	0.13	0.00	0.00
15	602.4	0.00	0.00	0.92

6.3.3 Dynamic analysis model

A non-linear dynamic analysis is performed using implicit Bathe Method calculation [6.1] [6.2] starting from the static response, in which a zero-displacement function is imposed as boundary condition in the ideal points where the foundation is bolted to the shock machine.

The time step choice depends on the experimental and numerical modal analysis results, considering that, in the rigid connection case, the first natural frequencies are in the range of 150-175 Hz. To obtain a certain accuracy in the time step (Δt) selection, it has been chosen $\Delta t=10^{-4}$, a value that corresponds to about 1/100 of natural period. In the elastic case (presence of mountings), knowing from load displacement curve (**Figure 6.23**) the mean stiffness, it is possible to derive the natural frequency of mountings (5 Hz). The time step is selected with the same criterion of the previous case,

so $\Delta t=10^{-3}$ is chosen to achieve more accuracy. The static zero-displacement function is replaced by a displacement time history in the vertical direction (**Figure 6.26**), which values for each test are obtained integrating twice the measured acceleration time history (**Figure 6.27**). These measured values are considered valid until the end of the anvil table travel; then, a constant displacement is imposed to study the free response of the system. The experimental asymmetries are not corrected in reported data. Therefore, the same displacement time history measured by one accelerometer at one single structure corner is set as symmetric load input in the four model load application points. In addition, the displacement time history value can be biased due to the double integration operation.

These experimental time histories are used as load input considering their soundness to the standard time history curves conventionally used in the engineering practice. In fact, the energy input distribution is similar, as we can see in the comparison of the experimental and standard shock response spectrum (SRS): in **Figure 6.28**, as example, the experimental SRS of test no. 5, achieved from the non-filtered signal, is compared with the theoretical one. Theoretical standard SRS are assessed from the time history curves using the formulas reported in STANAG 4370 [6.18], currently employed in design practice. As a reference, SRS parameters d_0, v_0 and a_0, obtained by the maximum displacement d, velocity v and acceleration a achieved from the experimental time histories are reported in **Table 6.4**. In **Figure 6.29**, the related comparison of displacement time histories is reported, showing their soundness.

In a couple of cases, calculations in the dynamic analysis are run applying velocity and acceleration time histories instead of displacement ones to verify their impact on the results, without any change in the Finite Element environment.

The last time step is chosen considering 300 ms in the rigid case and 600 ms instead in the mounting condition to allow more than two free oscillations periods.

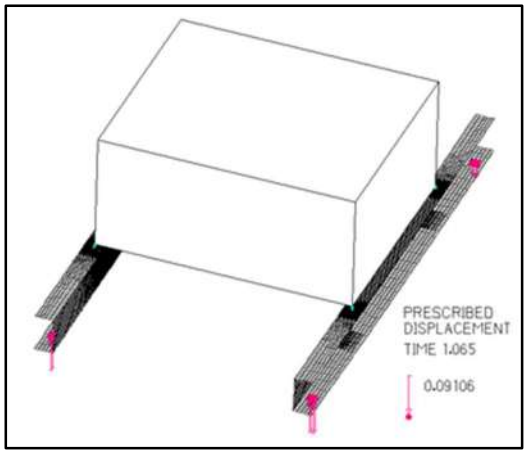

Figure 6.26 Prescribed displacement vertical time history application

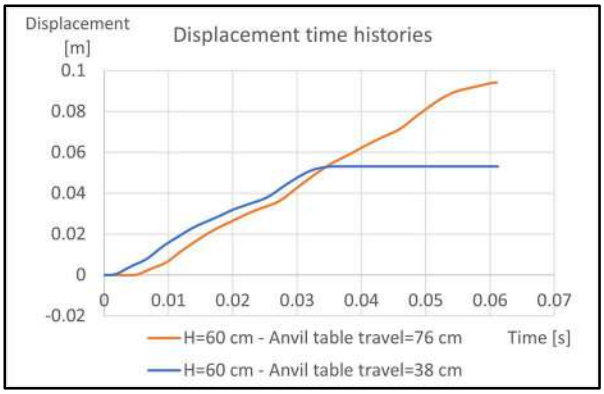

Figure 6.27 Examples of displacement time histories obtained by accelerometers measurements for the rigid condition

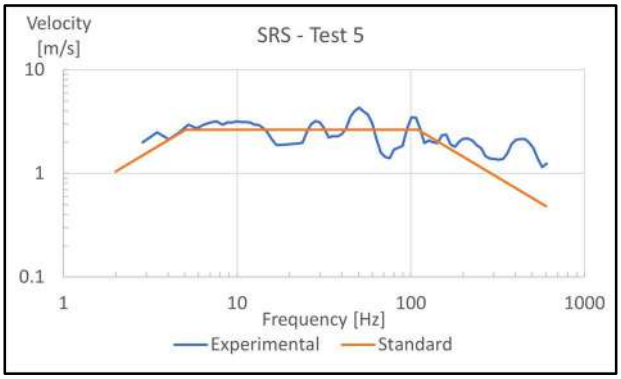

Figure 6.28 Test 5 – Experimental and Standard Shock Response Spectrum comparison

Table 6.4 Test 5 – Shock Response Spectrum parameters

d_0 [m]	v_0 [m/s]	a_0 [m/s^2]
0.083	2.63	1820

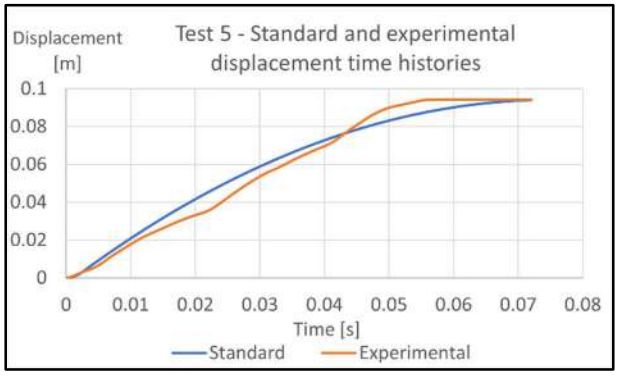

Figure 6.29 Test 5 - Standard and experimental displacement time histories comparison

6.3.4 Dynamic analysis results

From dynamic analysis results it can be seen that, when the foundation is rigidly linked by bolting, the resulting strain values are high. When the hammer height is 300 mm, plastic strain is localized close to the rigid connection (**Figure 6.30**), instead, when the hammer height increases to 600 mm, the yielding zone is extended in the neighbouring shell elements (**Figure 6.31** and **Figure 6.32**).

In the elastic connection case (with mountings), instead, the strain is relatively small, and no plastic strain is shown when the hammer height is 600 mm (**Figure 6.33**) independently from the mounting simulation strategies (1, 8 and 24 connectors).

The stress concentration in the connection nodes is large as expected, due to the model approximation, so plastic strain in these elements must be neglected.

From the comparison of the numerical strains obtained applying displacement, velocity and acceleration time histories, it has been checked that a negligible impact on the results is induced by applying velocity or acceleration time histories instead of displacement ones. Therefore, results are reported for the displacement case input, without any significant change in the numerical results.

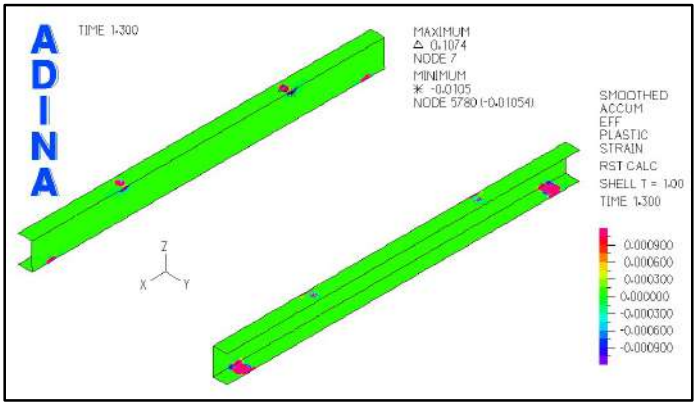

Figure 6.30 Rigid connection (hammer height=300 mm, anvil table travel=76 mm): accumulated plastic strain

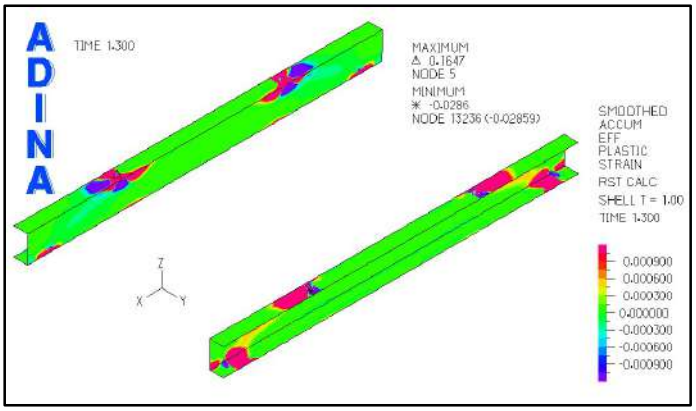

Figure 6.31 Rigid connection (hammer height=600 mm, anvil table travel=76 mm): accumulated plastic strain

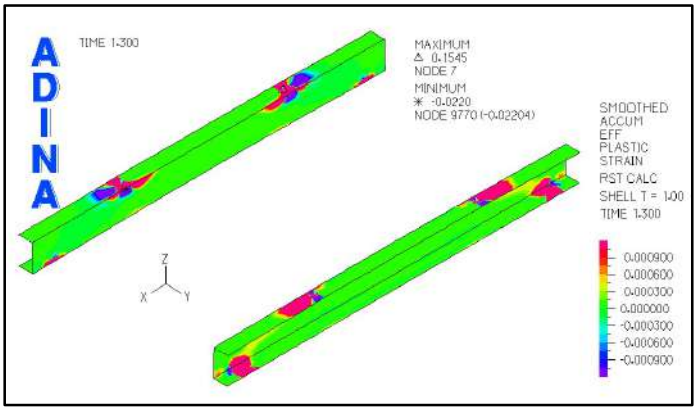

Figure 6.32 Rigid connection (hammer height=600 mm, anvil table travel=38 mm): accumulated plastic strain

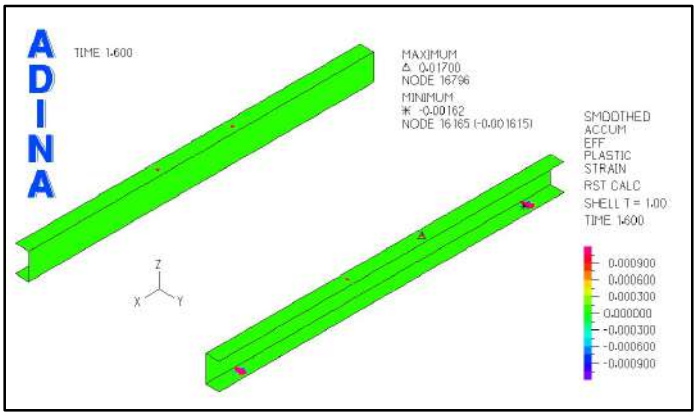

Figure 6.33 Mountings connection (hammer height=600 mm, anvil table travel=76 mm): accumulated plastic strain

6.3.5 Experimental and numerical comparison: modal analysis

Experimental and numerical modal analysis results are compared in **Table 6.5** showing satisfactory results. Frequency results, especially in vertical direction, are similar (4% error). This value of

frequency is used to determine the time step in the dynamic implicit calculation. In fact, implicit method is unconditionally stable, but to obtain a certain accuracy the time step is determined according to the first natural frequencies of the studied structure, selecting a value of about 1/100 of natural period. This choice allows to include also high order frequencies response, considering that Bathe [6.2] recommends using a value equal or less than 1/10 of the smallest natural period. Lower time step sizes are not necessary, due to the limits of the finite element methods that are not able to predict the highest frequencies response with a good accuracy, as reported by Bathe in [6.2].

Table 6.5 Modal analysis: numerical and experimental comparison results

Experimental frequency	Numerical frequency	Modal participation factor direction
Hz	Hz	Hz
152	132.5	Y-transversal
161	168.3	Z-vertical
174	168.4	X-longitudinal

6.3.6 Experimental and numerical comparison: dynamic analysis

In dynamic analysis the FEM results are in agreement with experimental data. In the rigid case, experimentally, the shock pulse induced by the 300 mm hammer height does not produce accumulated plastic strain in the strain gauges measurements and similar results are achieved by FEM (**Figure 6.34**). When the hammer height increases to 600 mm, strain gauges no. 1 and no. 3 shows up axial plastic strain. Similar strain levels are obtained with FEM calculation (**Figure 6.35**). An example of comparison of strain measurements and numerical results is shown, considering strain gauges no 1 and 3 (most stressed ones) in the severe condition of test no. 5 in the most stressed instant of time (from **Figure 6.36** to **Figure 6.38**, **Table 6.6**). The shear component considered is the engineering shear strain defined as $\gamma_{xy} = 2\ \varepsilon_{xy}$. This γ_{xy} is the angular deformation defined as the ratio between shear stress τ_{xy} and shear modulus G. In the mountings case, no yielding is found by both, measurements and calculation.

Strain numerical time histories follow the same trend of the experimental ones. Some examples are reported in **Figure 6.39** and **Figure 6.40** related to the rigid and the mountings connection. All the analyses provided the same trends and therefore the comparisons are limited to maximum values for the sake of shortness.

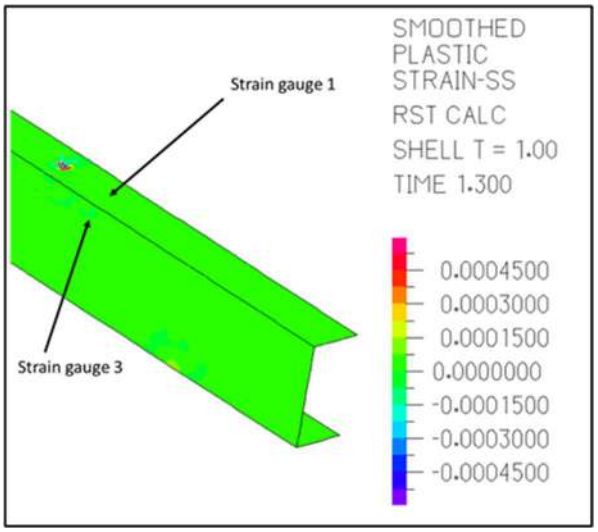

Figure 6.34 Rigid connection (hammer height=300 mm, anvil table travel=76 mm): comparison accumulated axial plastic strain

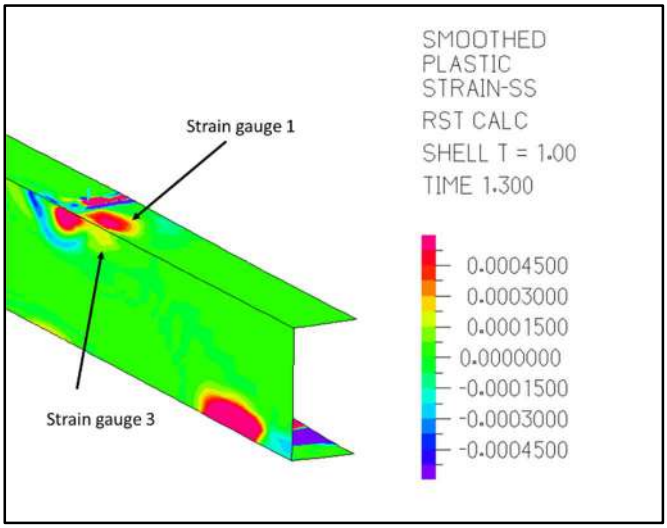

Figure 6.35 Rigid connection (hammer height=600 mm, anvil table travel=76 mm): comparison accumulated axial plastic strain

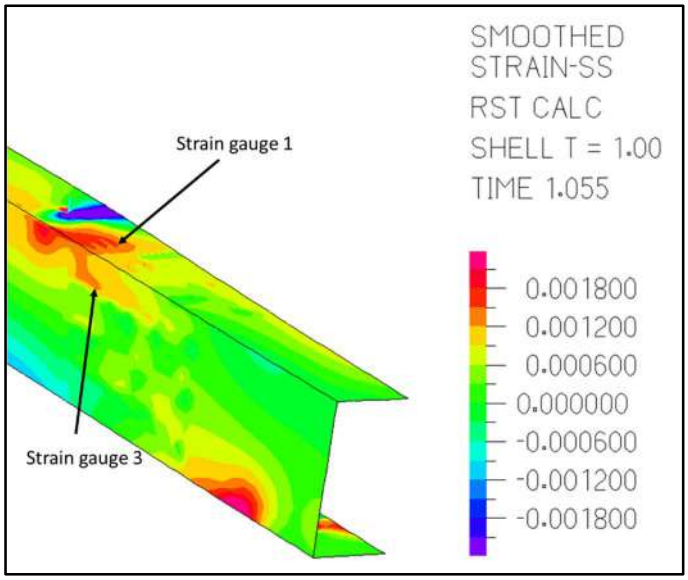

Figure 6.36 Rigid connection (hammer height=600 mm, anvil table travel=76 mm): comparison axial strain

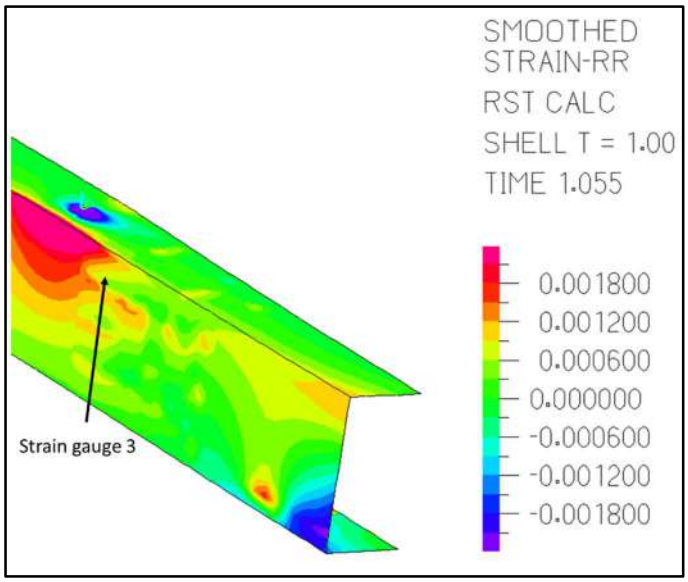

Figure 6.37 Rigid connection (hammer height=600 mm, anvil table travel=76 mm): comparison transversal strain

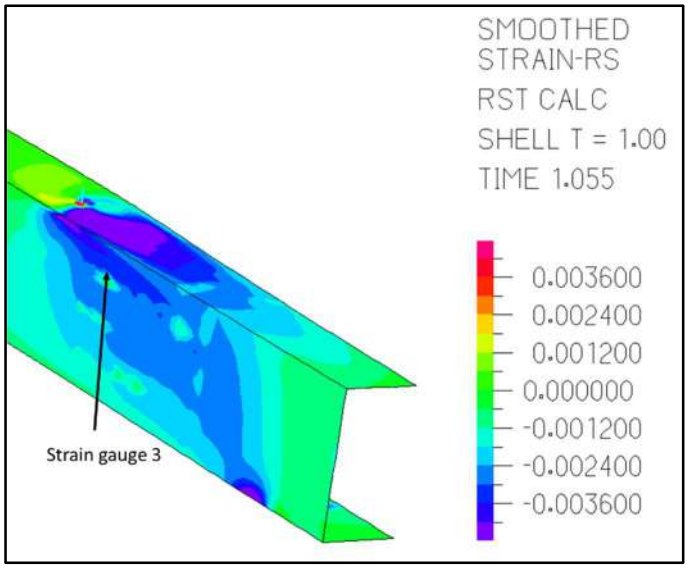

Figure 6.38 Rigid connection (hammer height=600 mm, anvil table travel=76 mm): comparison shear strain

Table 6.6 Test 5 (hammer height =600 mm): comparison numerical and experimental strain results

Strain gauge	Axial strain	FEM axial strain	Trasv. Strain	FEM transv. strain	Shear strain	FEM shear strain
	[10^{-3}]	[10^{-3}]	[10^{-3}]	[10^{-3}]	[10^{-3}]	[10^{-3}]
1	1.2	1.5	//	//	//	//
3	0.9	1.3	0.5	0.8	2.2	2.5

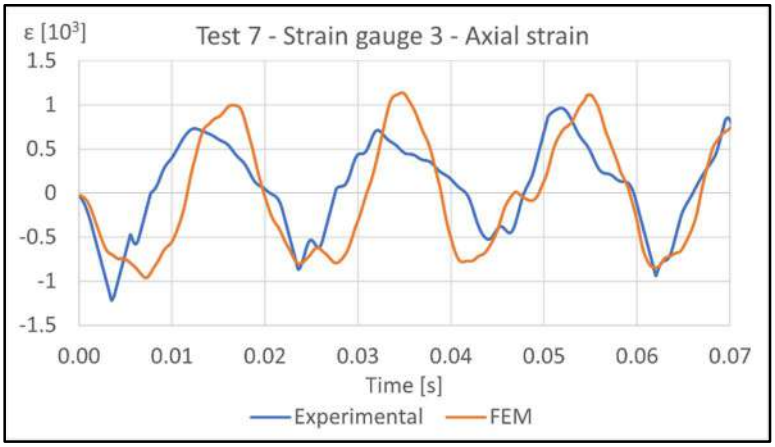

Figure 6.39 Rigid connection (Test 7) - Strain gauge 3 - Axial Strain time histories comparison

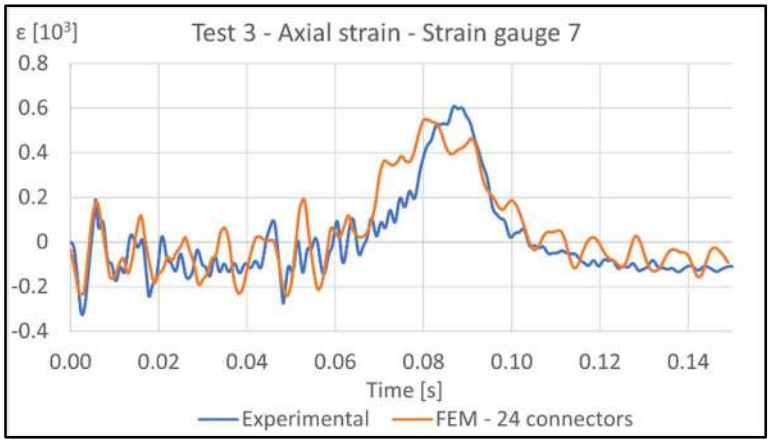

Figure 6.40 Mountings connection (Test 3) - Strain gauge 7 - Axial Strain time histories comparison (24 connectors FEM model)

6.3.6.1 Rigid connection case: comparison chart diagrams and errors table

The numerical and experimental comparison is performed considering the absolute maximum value for each strain component in the different directions (axial, transversal and shear). In the following charts (from **Figure 6.41** to **Figure 6.44**), for each strain gauge, the strains maximum values measured and the calculated ones are reported for each test. In the first diagram strains values of monoaxial strain gauges are compared with axial numerical values. Then, the strain values of rosette gages are reported in comparison with axial, transversal and shear numerical components. In tests no. 1-2-3 no input accelerometers time histories are available due to prob debonding, so only experimental strain results are shown. The average percentage error considering all tests data with respect to the FEM results for each strain component is shown in **Table 6.7**.

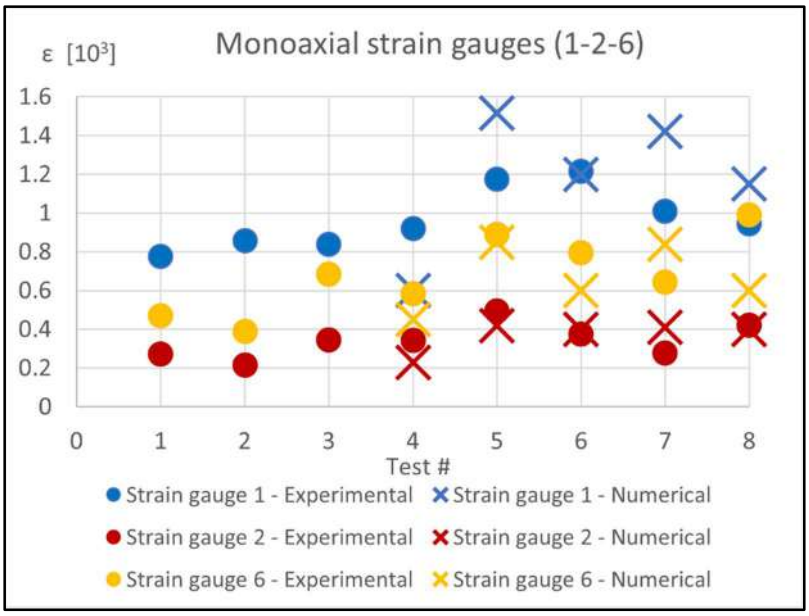

Figure 6.41 Strain gauge no. 1-2-6: axial strain comparison

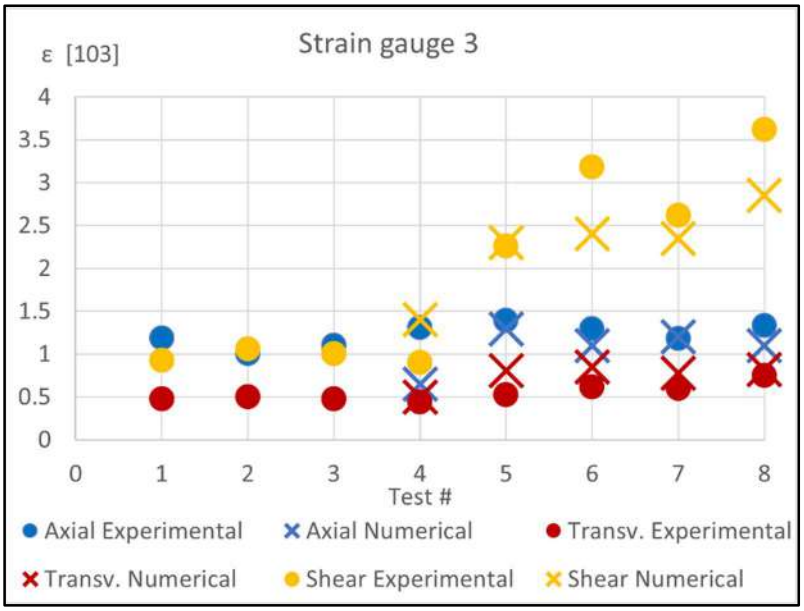

Figure 6.42 Strain gauge no. 3: strain comparison

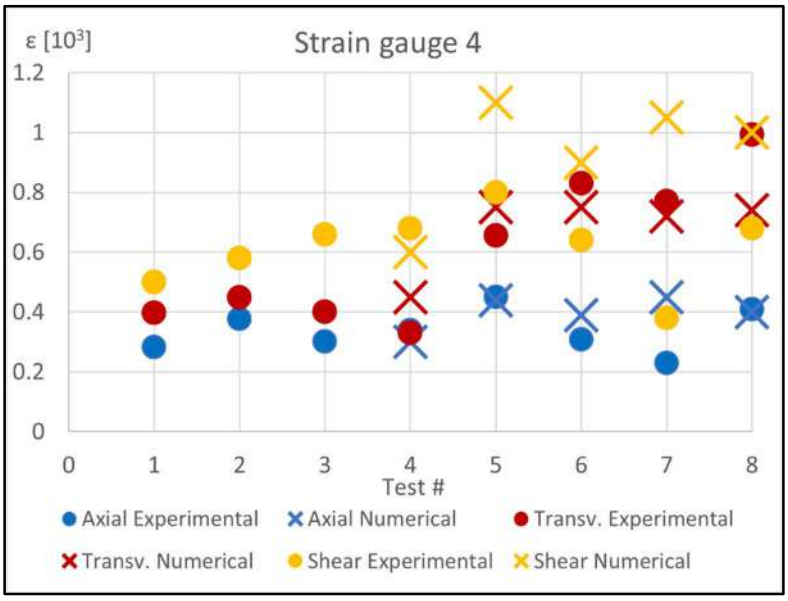

Figure 6.43 Strain gauge no. 4: strain comparison

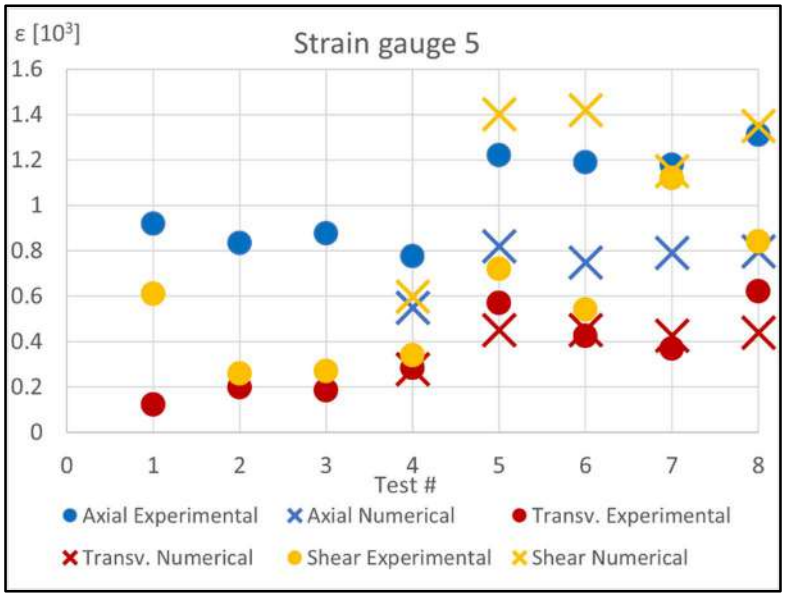

Figure 6.44 Strain gauge no. 5: strain comparison

Table 6.7 Rigid connection case: percentage errors for strain component of the numerical method

Axial	Transversal	Shear
%	%	%
-5.2	8.2	45.9

While axial and transversal strain components are satisfactorily simulated and show good agreement with test results, the shear is rather biased. This can be due to the model approximation in the simulation of the load inputs. In fact, the more relevant error occurs in the low part of the beams (strain gauge 4 and 5), close to the load application elements. The displacement time histories are set in the ideal points where the foundation is bolted to the shock machine, but the contact non-linearities are neglected. It is also worth noting that measurements were taken in one position only and mirrored on the others three supports, assuming double symmetry of the problem. Therefore, asymmetrical effect likely occurring during tests could not be accounted for.

6.3.6.2 Mountings connection case: comparison chart diagrams and errors table

The comparison is shown using chart diagrams (from **Figure 6.45** to **Figure 6.49**) as in the previous section. However, three different mounting modeling strategies have been proposed. Results are presented considering all of them, i.e. using 1, 8 and 24 link connectors to better account for longitudinal and transversal dynamic effects and interactions. The shear strain values of strain gauges nr. 5 are missing because these data are corrupted. The average percentage errors are also provided with reference to the different mounting (see **Table 6.8**).

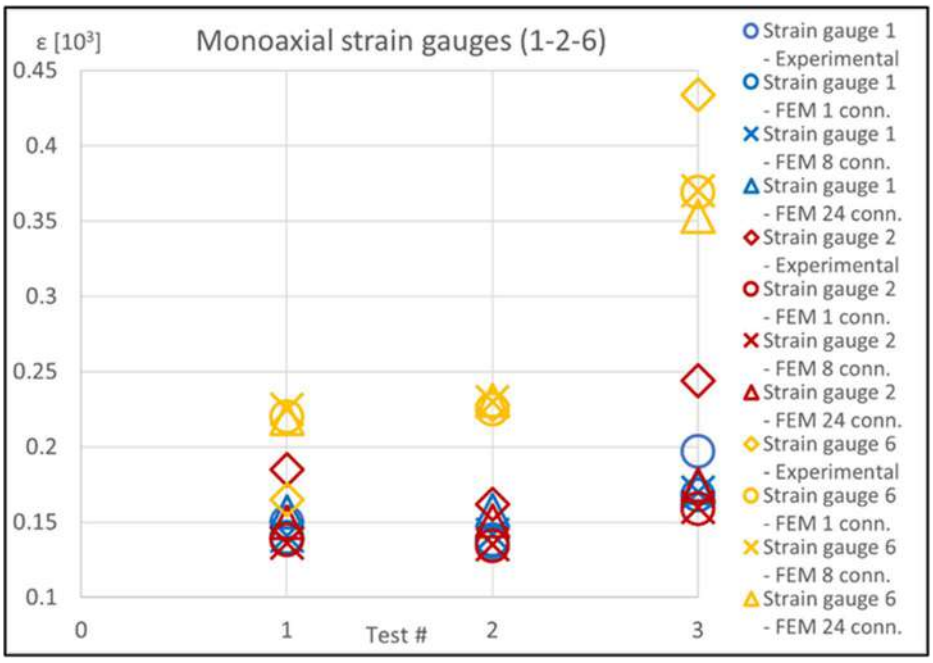

Figure 6.45 Strain gauge no. 1-2-6: axial strain comparison

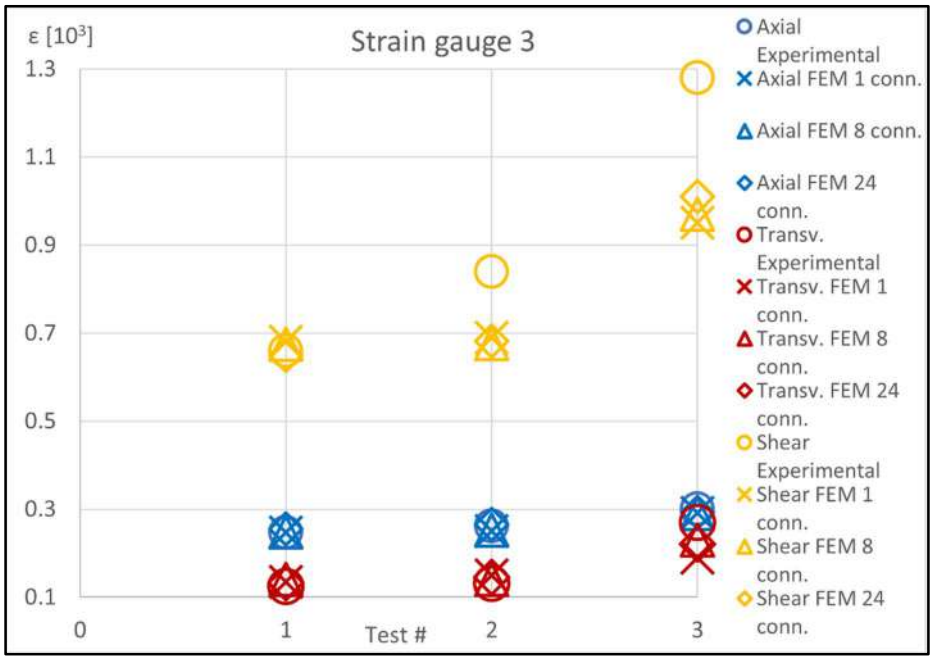

Figure 6.46 Strain gauge no. 3: strain comparison

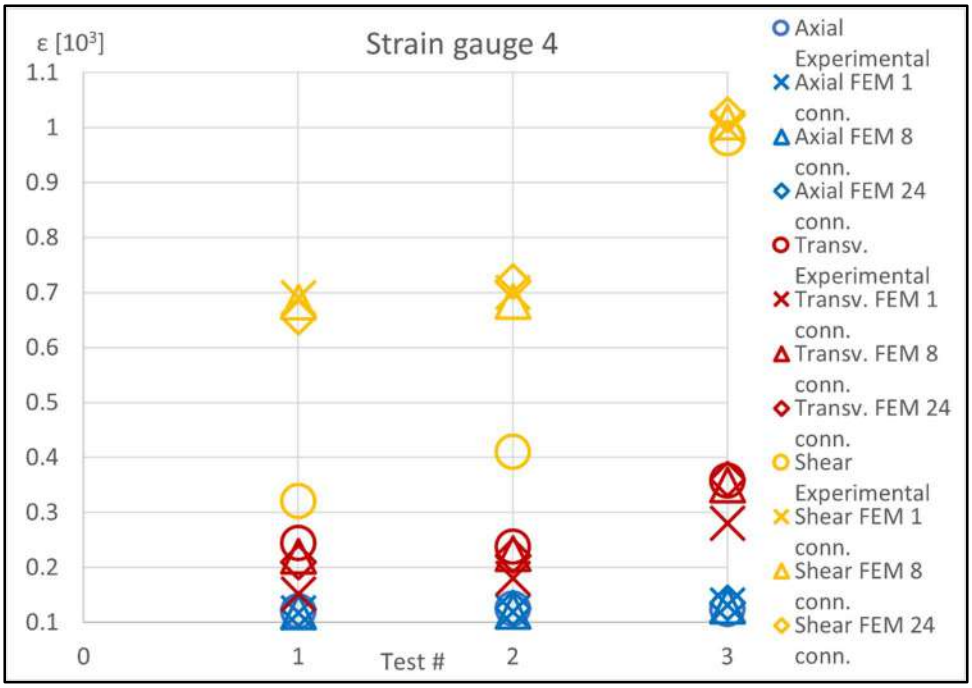

Figure 6.47 Strain gauge no. 4: strain comparison

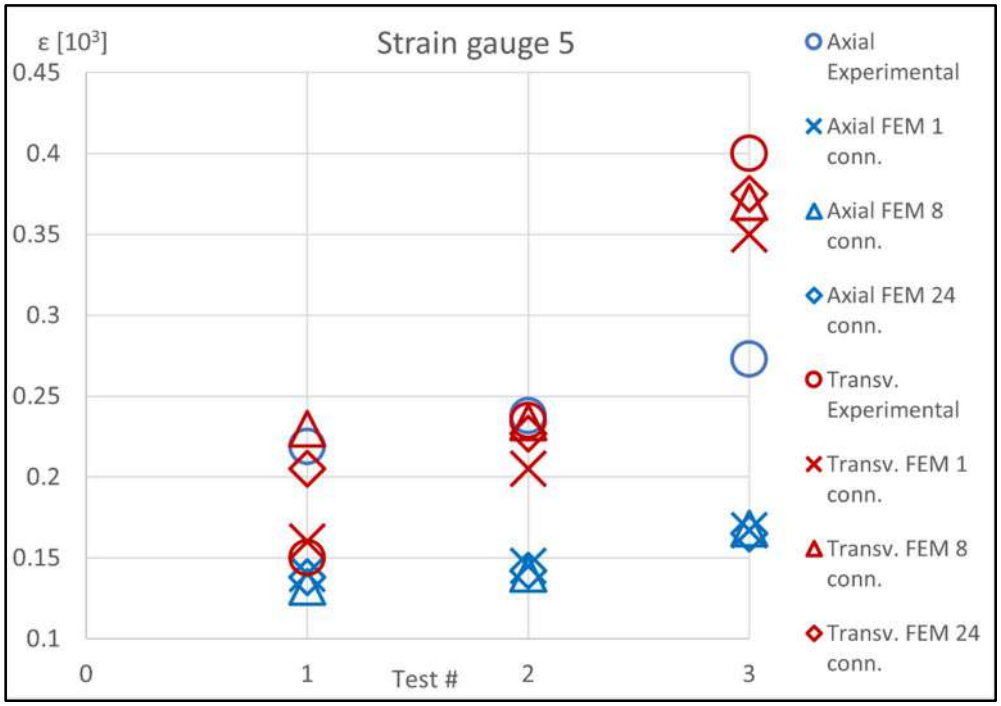

Figure 6.48 Strain gauge no. 5: strain comparison

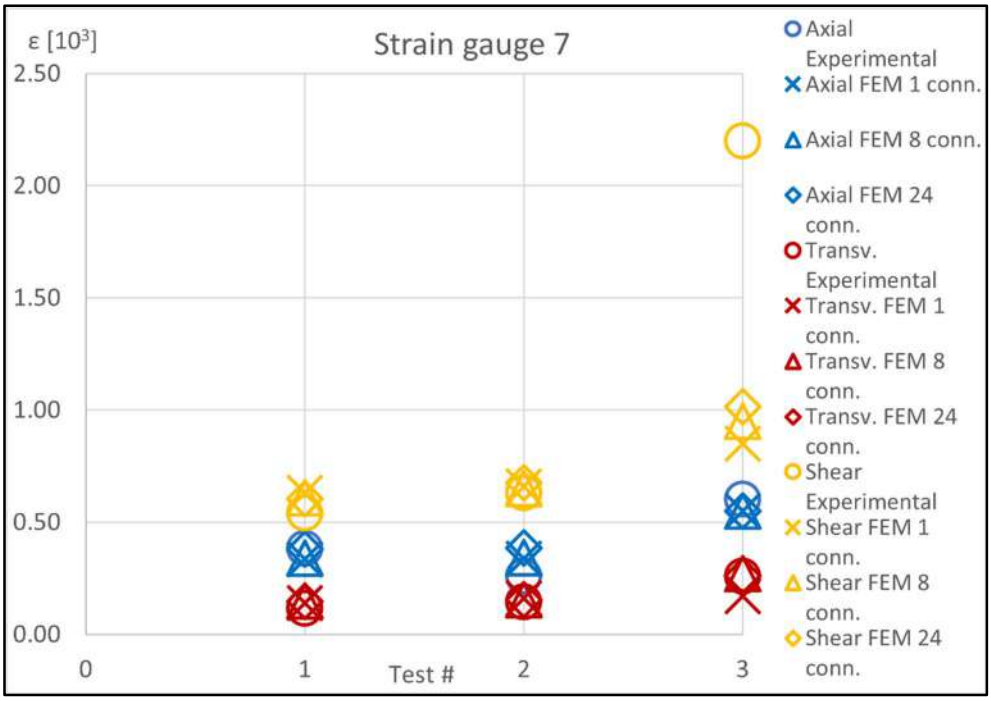

Figure 6.49 Strain gauge no. 7: strain comparison

Table 6.8 Mountings connection case: percentage errors for strain component of different numerical mountings models

Axial 1 connector	Axial 8 connectors	Axial 24 connectors	Transv. 1 connector	Transv. 8 connectors	Transv. 24 connectors	Shear 1 connector	Shear 8 connectors	Shear 24 connectors
%	%	%	%	%	%	%	%	%
-9.9	-9.5	-5.1	-9.5	6.0	3.3	16.3	16.0	17.2

The experimental vs. numerical comparison is again rather satisfactory and the enhanced simulation model contribute to reduce the bias up to very good agreement. Shear strain component is still deviating but less than the rigid connection case. It appears that mounting modeling strategy has no influence on the shear behavior.

6.4 Discussion

The comparison between non-linear dynamic implicit calculations and test results obtained according to MIL S 901 standard resulted rather satisfactory. Some reliable guidelines of shock foundation design in dynamic calculation have been provided. A very fine mesh patterns as suggested by classification societies' rules is used providing results in good agreement with experimental data, while time step should be determined according to the natural frequencies of the studied structure. No significative differences in the results are shown, applying displacement, velocity or acceleration

time histories as load input. The choice to propose different mounting models in the FE method has led to a better accuracy when the mounting simulation is more realistic (8 or 24 connectors), especially in the axial and the transversal strain component comparison (see Table 8). However, it is believed that dynamical characterization of materials is crucial and, before starting time-consuming calculations, it is worth obtaining a comprehensive dataset to feed the finite element models as such input data largely affect the numerical results.

Stress concentration effect is intrinsic in the numerical structural model at sharp notches. According to well-known theory of continuum mechanics, stresses at sharp notch tip tends toward infinite. Of course, in reality plasticization of material occurs and a micro-supporting effect in way of notch tip is postulated after Neuber. Such effect can only be avoided using conventional geometries (i.e. fictitious notch rounding) or conventional stress extrapolations, as reported by Radaj and Vormwald in [6.16]. Therefore, in the engineering practice these numerical values, shown in the FE results in the connection nodes, must be neglected.

While the work presented in this Chapter is referring to a specific and simplified foundation structure of onboard machinery items, the implemented FEM procedure could be applied to similar geometries and lay-out configurations of hull structures provided that an appropriate displacement time history at selected points is available as a loading condition. The input loads used in the present analysis and derived by rule requirements proved to be sound and effective. Even if calculations are run applying experimental time histories as load input, the implemented FEM procedure can also be considered valid using standard displacement time history loads conventionally used in the engineering practice as it demonstrated their soundness.

The most relevant differences between calculation and experiments occur for the shear strain component and require further investigation about their origin. A hypothesis could be related to the non-linearities that it wasn't possible to account for in this work (contact phenomenon, asymmetries, etc…), but that could be analyzed in future investigation, using enhanced strain measurements techniques.

Further tests are necessary to improve numerical model settings to include the structural response of marine composites. In the following Chapter, such aspects are analyzed in detail.

6.5 Bibliography

[6.1] ADINA, *Theory and Modeling Guide* Volumes I-III, ADINA R & D Inc., Watertown, 2015;

[6.2] Bathe K.J., *Finite element procedures*, Bathe K.J., Watertown, 2014;

[6.3] Clements E.W., *Shipboard Shock and Navy Devices for its Simulation,* Naval Research Laboratory, Washington D.C., 1972;

[6.4] Clough R.W., Penzien J., *Dynamics of structures*, Computer & Structures Inc., 377-381, Berkeley, 1995;

[6.5] Coats T. et al., "Component representation for shock qualified foundation structure", Shock and Vibration 10: 71-80, IOS Press, 2003;

[6.6] Dvorkin E., Bathe K.J., "A Continuum Mechanics Based Four-Node Shell Element for General Nonlinear Analysis", Engineering Computations, Vol. 1, pp. 77-88, 1984;

[6.7] Ewins, D.J., *Modal Testing: Theory, Practice and Application*, Research Studies Press LTD, Hertfordshire, 2000;

[6.8] HIPEBA, "Criteria for selection of high performance steel properties and processes definition", Complementary report deliverable d.2.1 and deliverable 2.2, 2015;

[6.9] Mannacio F., Barbato A., Gaiotti M., Rizzo C.M., Venturini M., "Analysis of the underwater explosion shock effects on a typical naval ship foundation structure: experimental and numerical investigation", MARSTRUCT 2021 Congress, Trondheim, 7-9 June 2021;

[6.10] Mannacio F., Barbato A., Di Marzo F., Gaiotti M., Rizzo C.M., Venturini M., "Shock effects of underwater explosion on naval ship foundations: Validation of numerical models by dedicated tests", Ocean Engineering 253 111290, 2022;

[6.11] ME'scope VES, *Tutorial Manual* Volume IA, Vibrant Technology Inc, Scotts Valley, 2014;

[6.12] MIL-S-901-D, *Shock tests, h.i. (high-impact) shipboard machinery, equipment, and systems, requirements*, United States Department of Defense, 1989;

[6.13] NAV-30-A001, *Norme per l'esecuzione delle prove d'urto su macchinari ed apparecchiature di bordo, Ministero della Difesa*, Istituto Poligrafico dello Stato, 1986;

[6.14] NAVSEA 0908-LP-0003010 Rev. 1, *Shock design criteria for surface ships*, Direction of Commander, Naval Sea Systems Command, Settembre 1995;

[6.15] Powerflex, "PWHS series helical standard Technical data & performance characteristics", Powerflex Srl, Limatola, https://docplayer.net/43762263-Powerflex-pwhs-series-powerflex-

pwhs-series-stainless-steel-cable-dampers-are-designed-to-preform-efficiently-without-material-or-performance-degrad.html, 2010;

[6.16] Radaj D., Vormwald M., *Advanced Methods of Fatigue Assessment*, Springer, 2013;

[6.17] SMM/CN 300 DVD, *Criteri e metodi per il proporzionamento e la qualificazione antiurto dei componenti destinati alle Unità navali*, Stato Maggiore Marina, Istituto Poligrafico dello Stato, 1978;

[6.18] STANAG 4370, *Environmental Testing - AECTP-100 – 600*, NATO Standardization Agreement, 2016.

7 Shock characterization of composite materials

7.1 Introduction and motivation of the work

Despite efforts of researchers outlined in open literature, the dynamic transient response to UNDEX of fiberglass laminates seems not clearly defined yet. However, this is an important input to use in shock calculation in order to achieve reliable results. Hence, the necessity of obtaining a dynamic characterization of the composite materials under study.

In this Chapter, the MIL S 901 D Medium Weight Shock Machine (MWSM) is used to verify the shock response of E-Glass polyester resin laminates, currently adopted as naval ship construction materials. The machine behaviour is easily reproducible using a simple mathematical mass-spring-mass model as reported by Clements [7.7]. In Clements work scientific explanations of the equivalence criteria that allows us to reproduce the effects on naval structures of UNDEX using MSWM are reported. This two-degree-of-freedom model has been updated to include damping as proposed by Alexander [7.2]. A dedicated structure, specially designed for these tests to induce large deflections, is used to support the fiberglass specimens. Before verifying shock response, the mechanical properties of the materials are characterized using Experimental Modal Analysis (EMA) by following the guidelines reported in [7.10]. These preliminary tests represent the starting point of the research allowing us to obtain an initial setting of the numerical method. Modal analyses and shock tests are performed for specimens of different materials, thicknesses and weights.

A finite element model is eventually built up applying the same strategies used in the previous Chapter, and it is fed by the composite material characterization achieved by EMA results to simulate the MWSM tests as defined by Clements [7.7]. To reduce the influence of errors in the peak load velocities, as reported in [7.7], shock inputs of numerical models are set according to experimental data. In the end, the numerical and experimental comparison is aimed at validating the modelling strategies. As a result, the whole procedure, including preliminary EMA and shock analysis, in which experimental, numerical and theoretical efforts are combined together, enable us to characterize the shock transient response of naval E-glass biaxial laminates and to provide time- and cost-effective design assessments. The methodology and the results obtained have been published in [7.14] [7.15].

7.2 Modal analysis

7.2.1 Experimental Modal Analysis

The fiberglass laminate specimens object of this study are square cross section beams with nominal length and breadth 2500x250 mm, different thicknesses (20, 40 mm), weights per unit area (shown in the text as G1 and G2 g/m^2 for reasons of industrial secrecy) and produced by four different companies (identified as A, B, C and D). For a given laminate thickness, specimens of G1 and G2 areal weights differ in their stacking sequence by the number of layers. Namely, for a given thickness, a beam of G1 areal weight is made by more layers than that of G2 areal weight. There are no differences in the stacking sequences of the different beams of the four manufacturers, but a quality control, resulting in a repeatability study, is necessary to characterize these materials.

The EMA is used to analyse the free vibration of these fiberglass laminate beams, which are simply supported almost at their ends; a free span between supports is set to a value of 2250 mm as shown in **Figure 7.1**. The hammer-roving method is used, considering 13 measurements points along the beam axis and achieving the corresponding Frequency Response Functions (FRFs). The driving points used as reference for the FRFs measurements are points no. 6 and 7 (see **Figure 7.1** and **Table 7.1**). The goal of these tests is to estimate the modal parameters (natural frequencies and damping) and corresponding modal shapes of the given specimens. Me Scope Ves commercial software [7.16] is used for the determination of the natural frequencies and related Eigenvalues from FRFs measurements, performing the quick curve fitting function available in the software environment. In **Figure 7.2** an example of FRF is shown: the measured signal is reported using the black curve, while the numerical function is represented by the red one. This curve fitted FRF is reconstructed by the software through quick curve-fitting algorithm, available in Me Scope Ves environment [7.16]. To obtain accurate results, the range in which curve fitting algorithm is performed is limited to the frequencies of interest for this study as usually done in this kind of analyses. As it will be better explained in the following paragraphs, only flexural modes are considered, therefore the calculation is stopped at a certain frequency as highlighted by the drop in magnitude of the red curve in **Figure 7.2**.

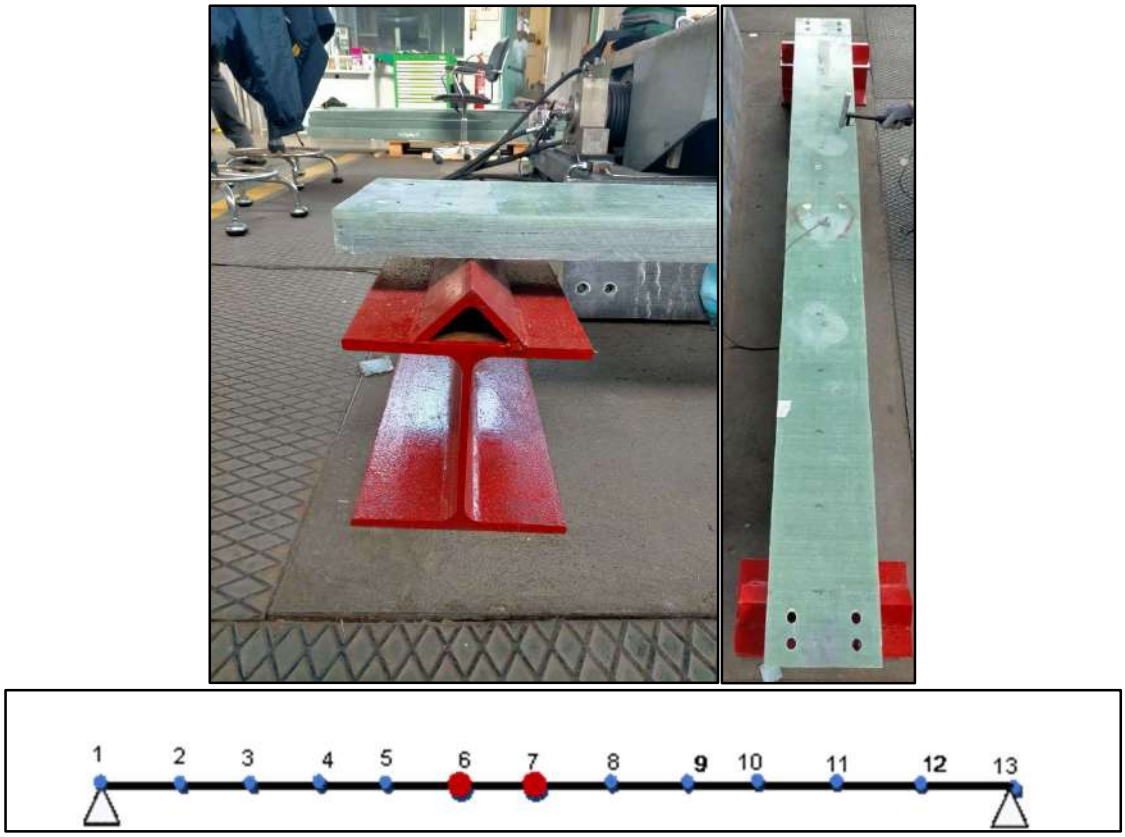

Figure 7.1 Experimental Modal Analysis set-up and measurement points

Table 7.1 Summary of Experimental Modal Analysis test specifications

Method and set up	Sensor(s)	Acquisition	Post processing
Hammer roving (13 measurement points) on a simply supported beam (2250 mm free span)	Accelerometer: MEGGITT 7251 A (Sensitivity 490 mV/g) Instrumented hammer: Bruel&Kjær type 8202	Spectrum Analyzer Ono-Sokki CF 3650; Sample Frequency 1000 Hz; Averaging: 5 measurements	Me'Scope Ves Software

Figure 7.2 Example of measured (black) and curve fitted (red) FRF - Manufacturer "B" specimen, G2 g/m^2, 40 mm thickness

7.2.2 Analytical formulation and numerical method

Natural frequencies obtained by experimental modal analyses are used to determine the axial Young Modulus of fiberglass laminates, according to ASTM Standard [7.5]. The beam theory for simply supported beams [7.8], allows calculating the longitudinal Young Modulus for each flexural mode E_n as:

$$E_n = \frac{4\pi^2}{A_n{}^2}\frac{f_n \rho S l^4}{J} \tag{7.1}$$

where ρ is the material density, J is the inertia modulus of the beam, S its cross-section area and l its free span. A_n values are different for each vibration mode and are available in literature [7.8].
A mean value of longitudinal Young modulus E_L is assessed for each specimen, simply dividing the sum of the axial Young modulus for each mode E_n by the number of modes n.

$$E_L = \frac{\sum_n E_n}{n} \tag{7.2}$$

Then, using this averaged Young modulus, it is possible to recalculate the natural frequencies f_n for each mode and comparing results with experimental data. In the numerical FE model, the material is characterized considering its orthotropic behaviour: the same E_L value previously assessed is also used for the transversal Young modulus E_T, to reproduce the biaxial properties and accounting for the stacking sequence of the specimen laminates. Shear modulus G_{LT} and Poisson ratio ν_{LT} are obtained by quasi-static tests performed using torsion and tension machines according to ASTM standards [7.3] [7.4]. The beam is discretized using 4-nodes multi-layered shell elements having 5 x 5 mm size and Mixed Interpolated Tensorial Components (MITC) formulation, used to model the composite behaviour in the works [7.11] [7.12], and described in [7.9]. Supports are placed at 125 mm from beam ends. In ADINA™ environment their position is represented using letters “B” and “C”. In the description of these fixities, it can be noted that translations (U) are fixed, while rotations (θ, α, β) are free (see **Figure 7.3**). The FE modal analysis is run using the Enriched Subspace Iteration Method, available in ADINA™ software, to estimate natural frequencies and modal shapes [7.1] [7.6]. From the results of this analysis, it is also possible to achieve the modal participation factors for each mode. A weighted and averaged Young modulus can also be estimated from these values, including the energetic contribute of each mode. The formula becomes:

$$E_L = \frac{\sum_n a_n E_n}{n} \tag{7.3}$$

in which coefficients a_n indicate in percentage the energetic contribute of each mode. They are determined according to modal participation factors assessed by numerical modal analysis. The a_n values, estimated considering the first four modes, are reported in **Table 7.2**.

The Young modulus, determined by the weighted formulation, does not differ substantially from that calculated by arithmetic average: this difference is on average of -3%. In the following, calculation results are reported considering the case of the arithmetic averaged Young Modulus.

In **Table 7.3** mechanical properties of the materials, including Young modulus obtained by EMA, are shown. To assess the missing transversal properties, the well-established Halpin-Tsai equations are used [7.13]. The stacking sequences for each laminate are not reported for confidentiality reasons, but natural frequencies results are shown (from **Figure 7.4** to **Figure 7.6**).

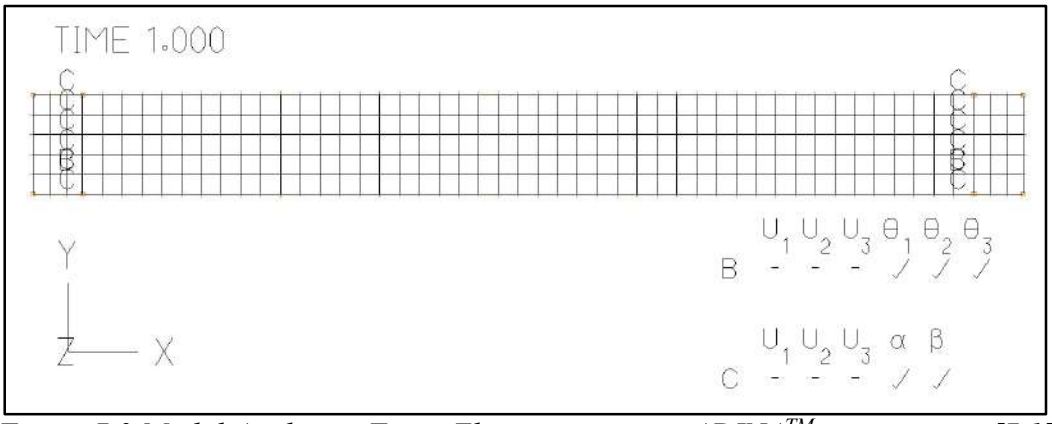

Figure 7.3 Modal Analysis - Finite Element setting in ADINA^{TM} environment [7.1]

Table 7.2 Coefficients used to estimate the weighted averaged Young modulus in Eq. 7.3

a_1 [%]	a_2 [%]	a_3 [%]	a_4 [%]
90.5	1.2	7.1	1.2

Table 7.3 Mechanical properties of the materials

Manufacturer /Weight	Thickness [mm]	E_L [GPa]	E_T [GPa]	E_N [GPa]	G_{LT} [GPa]	G_{LN} [GPa]	G_{TN} [GPa]	ν_{LT} [-]	ν_{LN} [-]	ν_{TN} [-]	Volume fraction [range]
A G1	20	15.9	15.9	10.2	4.5	3.7	3.7	0.20	0.39	0.39	
B G1	20	14.2	14.2	10.5	4.5	3.8	3.8	0.20	0.40	0.40	
C G1	20	17.2	17.2	10.5	4.5	3.8	3.8	0.19	0.40	0.40	
D G1	20	16.0	16.0	10.5	4.5	3.8	3.8	0.21	0.40	0.40	
A G2	20	18.9	18.9	10.9	4.5	3.9	3.9	0.20	0.41	0.41	
B G2	20	17.1	17.1	10.4	4.5	3.7	3.7	0.20	0.39	0.39	0.34 - 0.46
C G2	20	17.1	17.1	10.6	4.5	3.8	3.8	0.19	0.40	0.40	
D G2	20	18.2	18.2	10.7	4.5	3.8	3.8	0.20	0.40	0.40	
A G2	40	18.1	18.1	10.9	4.5	3.9	3.9	0.19	0.41	0.41	
B G2	40	17.0	17.0	10.4	4.5	3.7	3.7	0.21	0.39	0.39	
C G2	40	16.9	16.9	10.6	4.5	3.8	3.8	0.20	0.40	0.40	
D G2	40	18.2	18.2	10.7	4.5	3.8	3.8	0.20	0.40	0.40	

7.2.3 Numerical, analytical and experimental comparison

In the plots, shown from **Figure 7.4** to **Figure 7.6**, the flexural natural frequencies up to the 4th modal shape, measured by EMA and calculated both analytically and numerically, are reported for each specimen of different manufacturers ("A", "B", "C", "D"). In **Table 7.4**, the convincing comparison between numerical and experimental flexural shapes is shown. The experimental ones are extracted by Me Scope Ves commercial software [7.16].

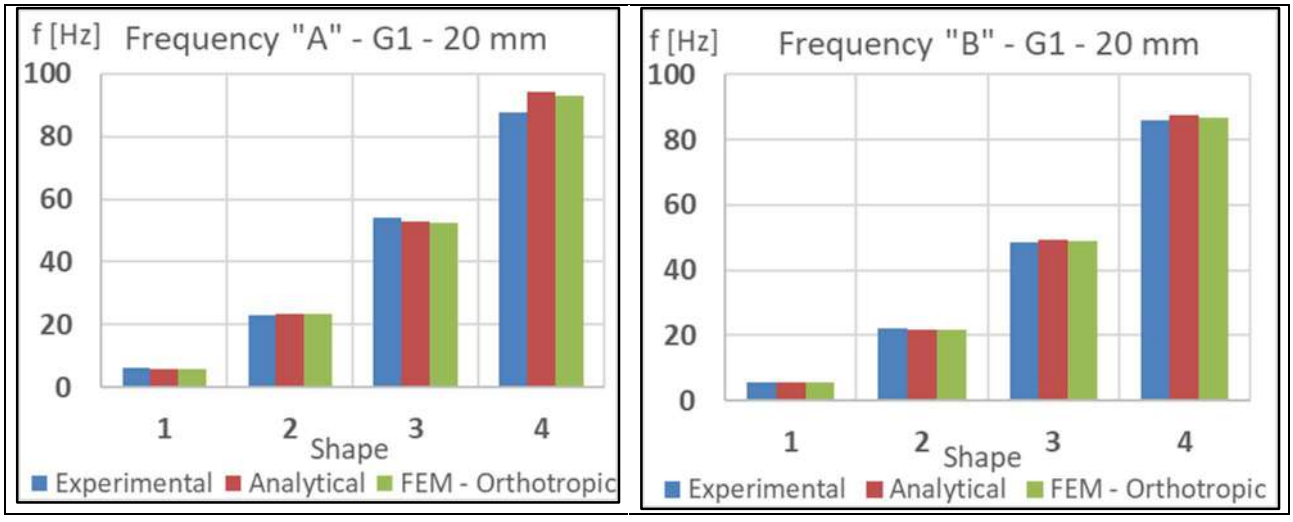

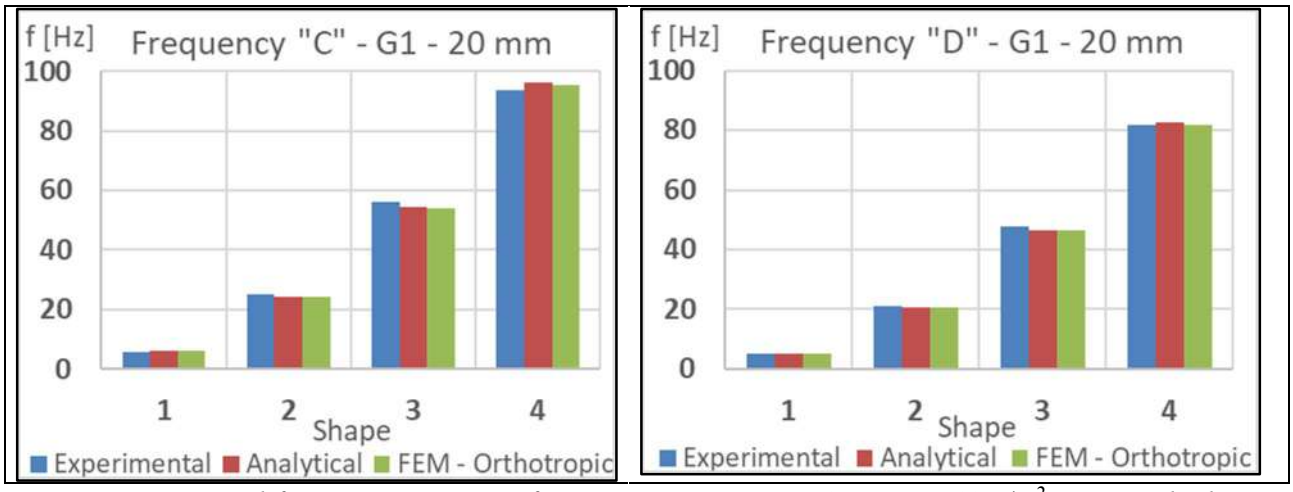

Figure 7.4 Natural frequencies – Manufacturers "A", "B", "C", "D", G1 g/m^2, 20 mm thickness

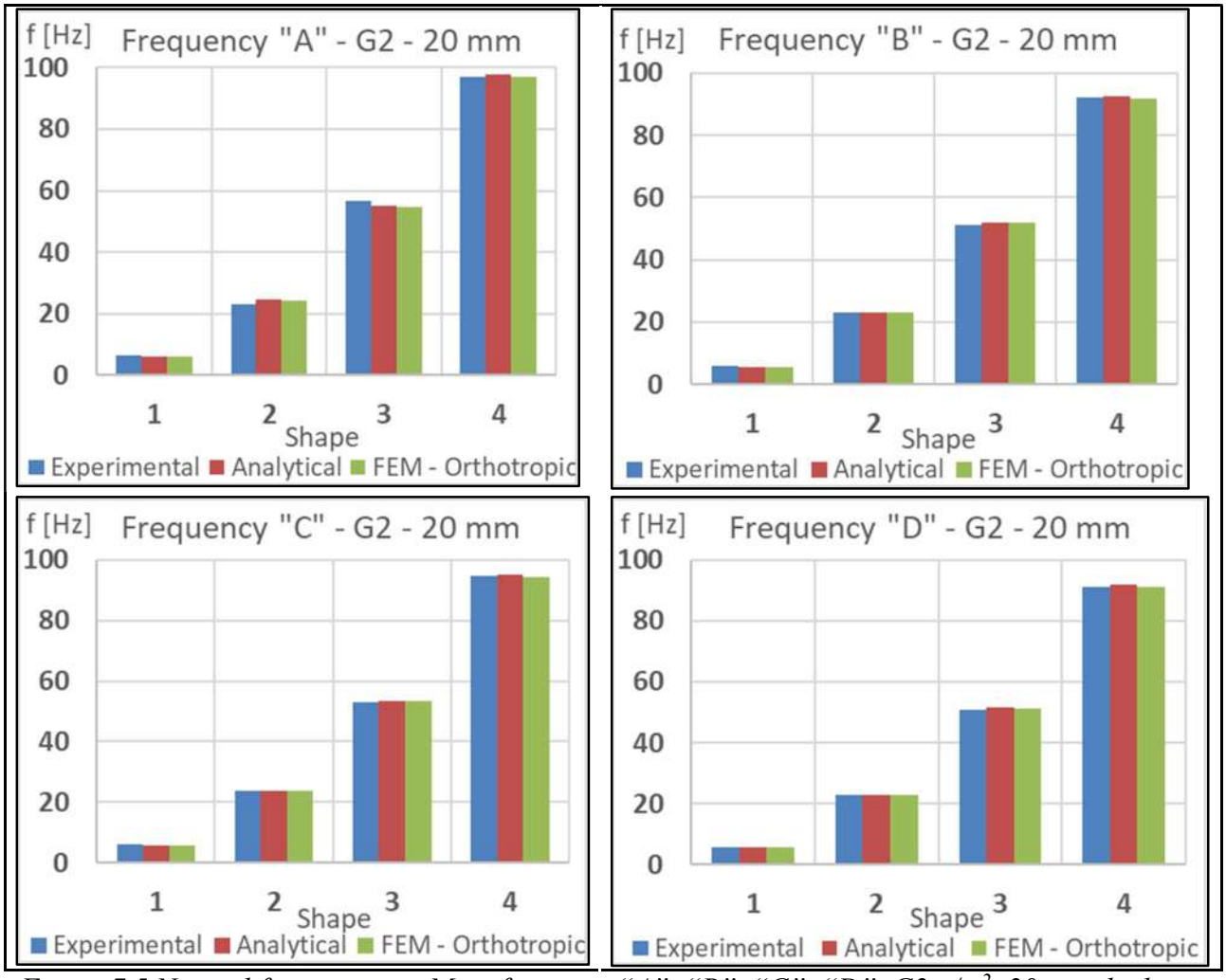

Figure 7.5 Natural frequencies – Manufacturers "A", "B", "C", "D", G2 g/m^2, 20 mm thickness

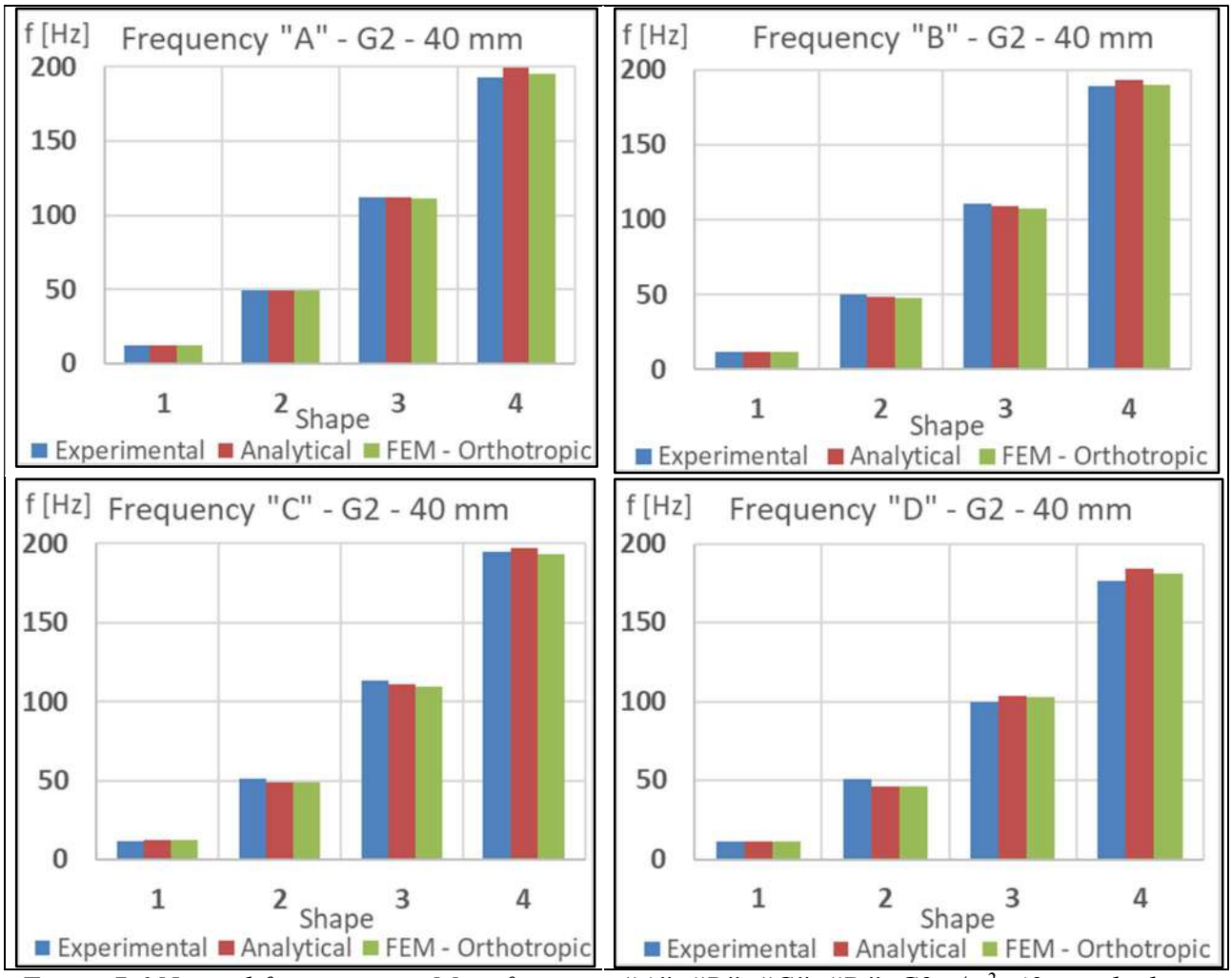

Figure 7.6 Natural frequencies – Manufacturers "A", "B", "C", "D", G2 g/m^2, 40 mm thickness

Table 7.4 First modal flexional shapes: numerical and experimental comparison

Numerical (FEM)	Experimental (EMA)
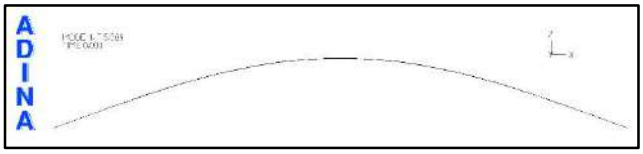	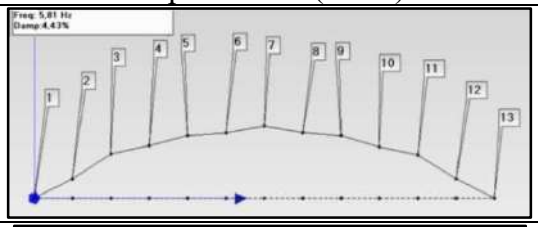
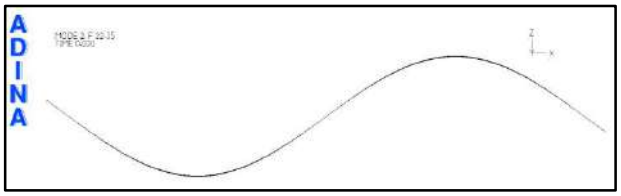	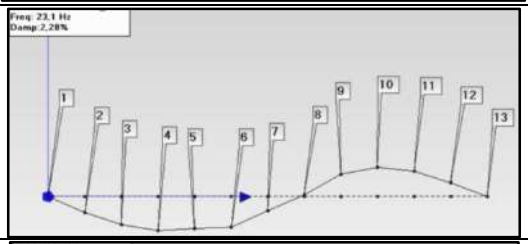
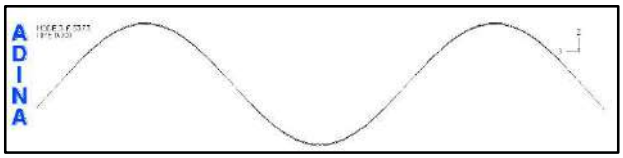	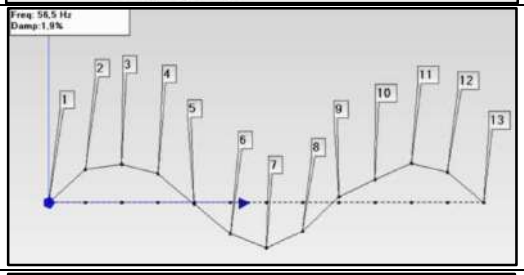
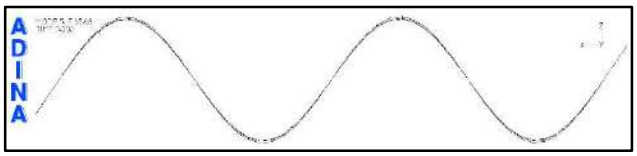	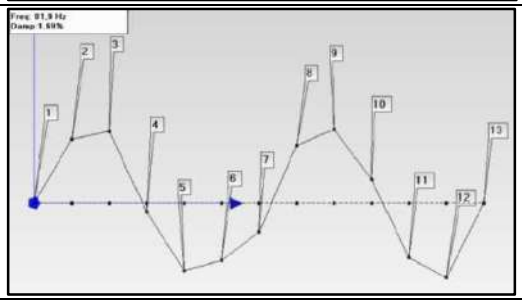

7.2.4 Discussion

A good agreement is obtained in the numerical and experimental comparison, resulting in a small average percentage error of natural frequencies for each flexural mode as shown in **Table 7.5**. From the analysis of the plots in which natural frequencies are compared (from **Figure 7.4** to **Figure 7.6**), it can be noted that differences in the numerical, theoretical, and experimental results become more evident for the fourth mode, but in some cases, also the second and the third experimental modes can show frequencies that are slightly higher or lower than the calculated ones. This special behaviour is attributed to the imperfections of the composite materials, depending on their manufacturing method. This confirms the importance of performing a preliminary EMA to obtain a reliable initial setting of the applied numerical methods. It is also shown that natural frequencies values increase when specimens of lower thickness (20 mm) are compared with the ones of higher thickness (40 mm). This

mechanical property will be significant in the analysis of shock tests results. Numerical and experimental shapes follow the very same trend (see **Table 7.4**). However, the 4th experimental mode is suffering the geometric aliasing, due to the relatively low number of measurement points chosen for these tests. After this mode, the aliasing phenomenon becomes relevant. For this reason, it is not possible to distinguish a flexural shape from a torsional one, therefore the analysis is stopped. In addition, as a result of the finite element calculation, over 76% of the percentage masses in the vertical direction is given by the contribution of the first four flexural modes: this confirms the validity of the choice to carry out the EMA in this frequency range. The first modal frequency is also important to properly set the time step (to about 1/100 of the first natural period to obtain a certain accuracy) for subsequent dynamic calculations.

Table 7.5 Average percentage error of natural frequencies in the numerical analysis for each flexural mode

1st mode [%]	2nd mode [%]	3rd mode [%]	4th mode [%]
0.3	-1.5	-1.0	1.6

7.3 Shock analysis

7.3.1 Shock tests setting and measurements

As mentioned, the shock tests are carried out using the MIL S 901 D medium weight shock machine. The specimens are connected to the testing device by means of a dedicated structure, specially designed for these tests to induce large deflections. According to the cited rule, standard mounting fixtures are used to link the structure under test and the anvil table. The boundary conditions are conceived to avoid unwanted stress concentrations at beam ends. The fiberglass beams are constrained so as they are free to rotate and translate at ends, where they are bolted to purposely designed rollers. A 60 kg calibrated mass, free to translate in the vertical direction, is rigidly connected to the centre of the specimen span by means of two metal plates bolted together in a sandwich configuration. See **Figure 7.7**.

To measure the structural response, six linear strain gauges are set in the longitudinal direction along the beam axis. They are divided symmetrically: three on the top face and three on the bottom face of the specimen. On the top face, strain gauge no. 1 is set on the left side (400 mm apart from midspan), no. 2 at midspan and no. 3 on the right side (400 mm apart from midspan). On the bottom face, the same configuration is applied for strain gauges no. 4-5-6. To evaluate the input velocity, useful for

subsequent dynamic calculation, four accelerometers are installed: no. 1 on the mass, no. 2-3 on the rollers and no. 4 on the anvil table. See **Figure 7.8** and **Table 7.6**.

Additionally, a high-speed camera, type GoPro Hero 4, characterized by 240 frames per second acquisition speed and shutter speed in auto mode, is suitably placed to record the tests and to measure the maximum deflection of the beam: to achieve this result a graduated scale is drawn on the centre column of the supporting structure.

For each specimen, six shock tests were carried out, increasing gradually the hammer height from 600 mm to 1700 mm. The shock tests are numbered in increasing order from test number 1, corresponding to 600 mm hammer height to shock test number 6 that refers to 1700 mm hammer height (**Table 7**). Anvil table travel is set constant to 76 mm.

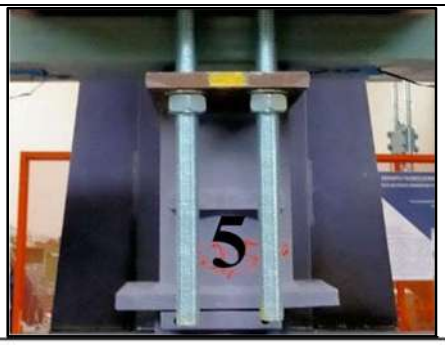

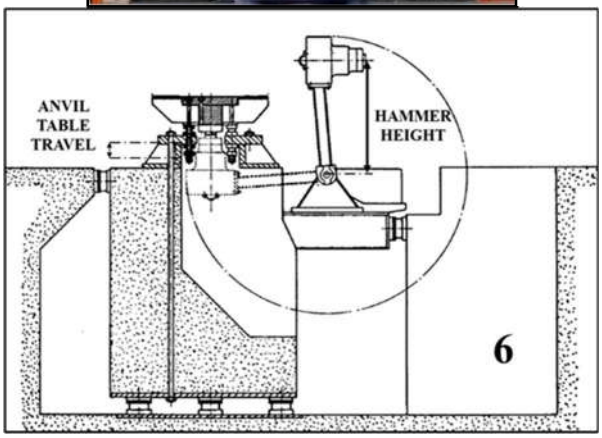

1. MIL S 901 D medium weight shock machine anvil table
2. Standard mounting fixtures
3. Dedicated support structure specially designed for the tests
4. Rollers
5. Calibrated mass (60 kg) connected to the composite beam
6. MIL S 901 D medium weight shock machine scheme

Figure 7.7 MIL S 91 D Shock test set-up and particular of the calibrated mass

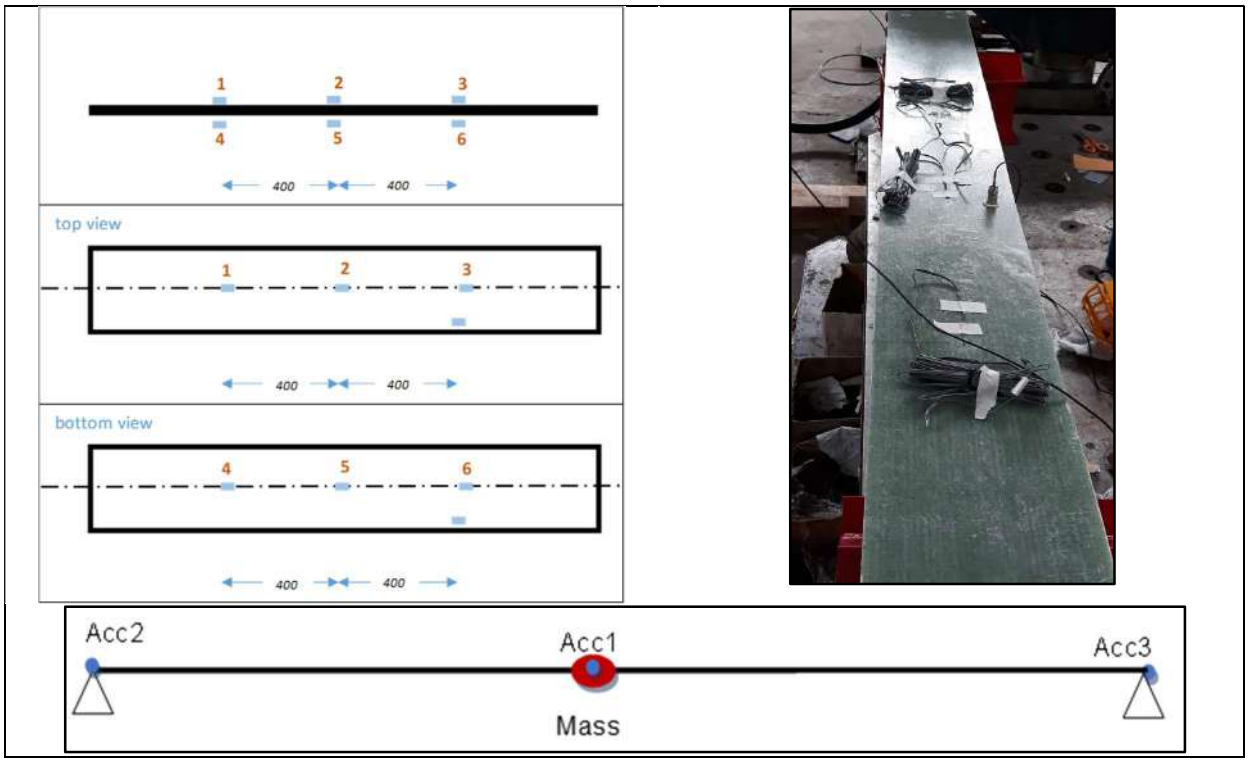

Figure 7.8 Strain gauges (top figure) and accelerometers (bottom figure) positions on the specimen

Table 7.6 Summary of Medium Weight Shock Machine test specifications

Sensor(s)	Acquisition	Post processing
Nr. 4 Accelerometer: MEGGITT 7251 A	Dewetron DEWE 3020, Sample frequency 50 kHz	Dewetron DEWE 3020
Nr. 6 monoaxial strain gauges: BFLAB-5-5-10 LJCT-F	IMC-Cronos CS-5008-FD, Sample frequency 50 kHz	IMC FAMOUS 7.0

Table 7.7 Shock tests schedule for each specimen

Specimen #	No. Impacts	Hammer height [mm]	Manufacturer	Weight [g/m^2]	Thickness [mm]
1	6	600, 800, 1000, 1200, 1400, 1700	A	G1	20
2	6	600, 800, 1000, 1200, 1400, 1700	B	G1	20
3	6	600, 800, 1000, 1200, 1400, 1700	C	G1	20
4	6	600, 800, 1000, 1200, 1400, 1700	D	G1	20
5	6	600, 800, 1000, 1200, 1400, 1700	A	G2	20
6	6	600, 800, 1000, 1200, 1400, 1700	B	G2	20
7	6	600, 800, 1000, 1200, 1400, 1700	C	G2	20
8	6	600, 800, 1000, 1200, 1400, 1700	D	G2	20
9	6	600, 800, 1000, 1200, 1400, 1700	A	G2	40
10	6	600, 800, 1000, 1200, 1400, 1700	B	G2	40
11	6	600, 800, 1000, 1200, 1400, 1700	C	G2	40
12	6	600, 800, 1000, 1200, 1400, 1700	D	G2	40

7.3.2 Mathematical model and finite element method

The numerical analysis is performed using the ADINA™ finite element software [7.1]. The behaviour of the MSWM, loaded with a dead-weight, is simulated applying the mathematical model proposed by Clements [7.7]. According to this theoretical approach, the whole MSWM configuration can be outlined as a simple system type mass-spring-mass. The anvil is replaced by a mass $\mathbf{M_a}$ (2030 kg); its behaviour during shock tests is reproduced considering that it moves in the vertical direction with an initial velocity $\mathbf{V_a}$, when hit by the hammer. The support structure is represented by another mass $\mathbf{M_s}$ (1900 kg) connected to the anvil table by a spring, simulating the supporting channel stiffness **K**. In the $\mathbf{M_s}$ value, the standard mounting mass is included. The **K** value is chosen, considering that the average MSWM natural frequency is 65.2 Hz [7.7]. In this model, also damping and displacement limits of the anvil table travel (76 mm) are included. The damping value is set to 4% of the critical one, considering the amplitudes of motion maxima caused by the impact. In addition, the fiberglass specimen is connected to the support structure by means of rollers, characterized with their mass $\mathbf{M_r}$

(50 kg), free to rotate and to translate in the longitudinal (X) direction, see **Figure 7.9**. The composite beam is rigidly connected to a mass **M** (set to 96 kg to consider the weight of the calibrated mass, the steel plates and the connection bolts), free to move in the vertical direction (Z) with its velocity $\mathbf{V_m}$, after the anvil table impact. See again **Figure 7.9.**

In the software environment, as mentioned, 5 x 5 mm MITC 4-nodes multilayer shell elements are used for the fiberglass specimen, characterized by mechanical features achieved by EMA and actual density properties measured experimentally. The masses are represented by concentrated masses in some points. The mass of the structure $\mathbf{M_s}$ is connected to the anvil mass $\mathbf{M_a}$, using a linear spring, characterized with its values of stiffness **K** and damping **C**. In particular, to obtain the desired value of damping ratio $\boldsymbol{\xi}$ (4%), it is necessary to define the related damping coefficient **C** in the linear spring setting of the numerical model. This coefficient is estimated from the classical formula of structural dynamic [7.8] shown in Eq. 7.4.

$$c = 2\xi\sqrt{km} \tag{7.4}$$

3-D contact algorithms [7.1] are used to simulate the contact between the hitting mass and the composite beam specimen and to reproduce the anvil table travel limits. The mass in the centre, ideally hit by the anvil, is connected by rigid links to four rigid surfaces, two on the top and two on the bottom of the beam, representing the two plates bolted together in a sandwich configuration. These surfaces are in contact with the composite elements using the default 3-D Contact Algorithms (Compliance Factor $1e^{-10}$, Coulomb Friction 0.1), in which they are regarded as targets and the specimen surface as contactor. In this case, a 3-D Contact Algorithm is set, considering the self-contact of the fiberglass specimen. A similar configuration is simulated for the rollers, connected by rigid links to two rigid surfaces, set one on the top and the other on the bottom of the fiberglass beam ends. These rigid surfaces are in contact with the composite elements, using a 3-D Contact Algorithm, type Constraint Function (Compliance Factor $1e^{-10}$, Coulomb Friction 0.1), characterized by a Normal Contact w-friction parameter relatively large ($1e^{-8}$) to avoid the sliding between surfaces and composite elements and the consequent losing contact. The rollers (point concentrated masses) are connected to the mass structure $\mathbf{M_s}$ by constraint equations, type all-translation, in which only vertical translation is transferred from the rollers master nodes to the mass structure slave node. A direct matrix input is used to assign zero stiffness to rollers in longitudinal X direction and transversal Y rotation. To consider the effective position of their centre of mass, each roller is connected by a rigid link to a concentrated mass of the measured weight $\mathbf{M_r}$**.** The anvil is connected by means of rigid links to two rigid surfaces free to move in the vertical direction Z for a distance equal to the anvil table travel. To reproduce this end stop, two rigid surfaces are set to limit the anvil table travel: some

3-D Contact Algorithms, type Constraint Function (Compliance Factor $1e^{-10}$, Coulomb Friction 0.1), are used, imposing the two anvil surfaces as contactors and the two limit surfaces are targets. A 3-D Contact Algorithm more is set, considering the self-contact of the limit surfaces, to avoid losing contact problems. These surfaces are fixed in the space. To obtain this result, they are connected by rigid links to a point mass with all degrees of freedom constrained. For each mass rigidly connected to a rigid surface a soft spring element is set to avoid problems of losing the sixth degree of freedom. See **Figure 7.10**.

The applied loading conditions are the initial velocities of the anvil table ($\mathbf{V_a}$) and of the mass ($\mathbf{V_m}$), i.e. the maximum initial velocities after the impacts, obtained integrating the accelerometers measurements during the MSWM shock tests. Gravity as mass proportional load is applied on the whole model.

A non-linear dynamic analysis is performed applying the implicit Bathe Method time-integration [7.1] [7.6], in which the time step selection depends on the results of the EMA. In fact, the first natural frequencies are in the range of 5-6 Hz. Therefore, to obtain a certain accuracy in the results, time step (Δt) selection has been chosen as low as $\Delta t=10^{-3}$, a value that corresponds to about 1/100 of the structure natural period. As far as boundary conditions is concerned, the anvil mass and the mass connected to the specimen are constrained in longitudinal X direction and in transversal Y rotation, so they can move only in vertical Z direction.

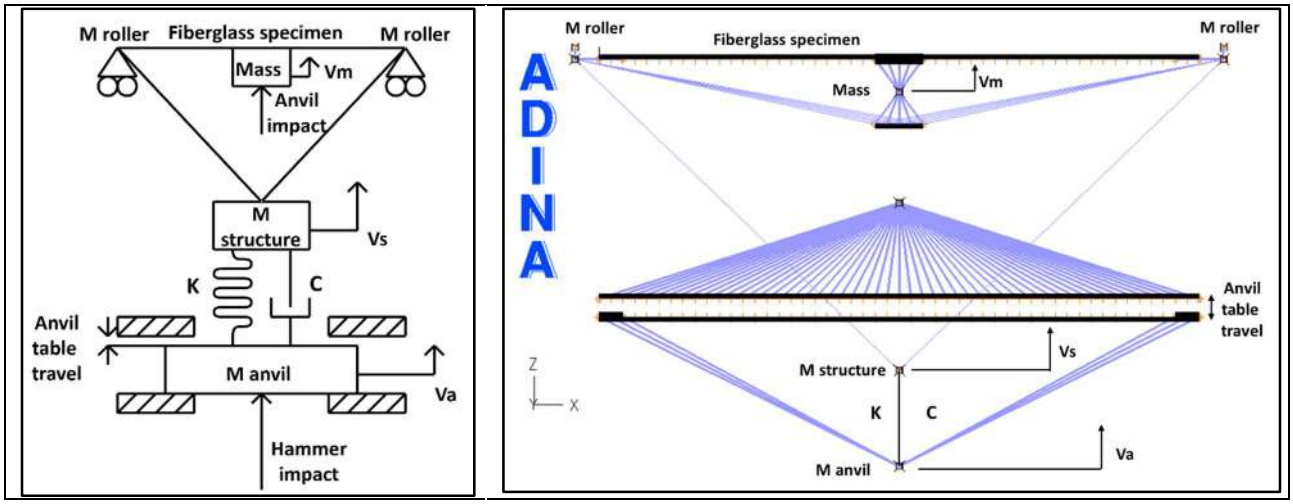

Figure 7.9 Shock test model and depiction in FE environment (XZ plane)

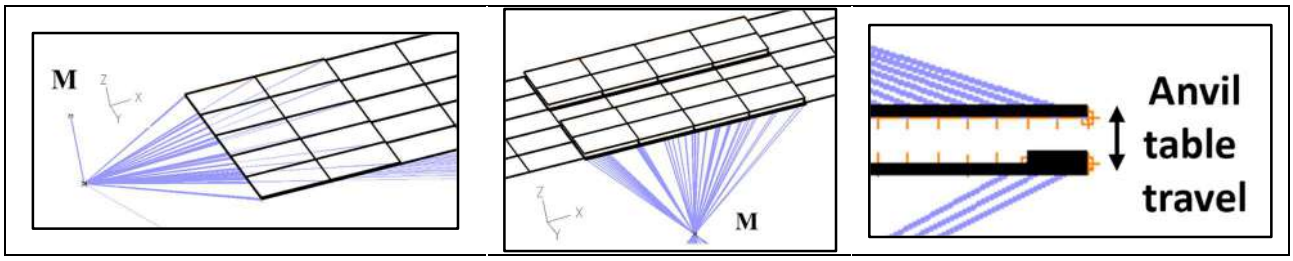

Figure 7.10 Particulars of the FE roller characterized by its mass M (left picture), the central calibrated mass (M) joined to the specimen in a sandwich configuration (picture in the middle) and the limits of the anvil table travel (right picture)

7.3.3 Results and comparison

From accelerometer measurements, maximum impact velocities are obtained, integrating the measured acceleration time histories. To obtain a better accuracy and avoid peak load velocities errors, as reported in [7.7], the peak anvil velocity numerical input $\mathbf{V_a}$ was set to achieve the maximum velocity value of the structure $\mathbf{V_s}$ equal to the average of the peak velocity values obtained integrating the time histories of accelerometers no. 2-3 on the rollers (**Figure 7.8**). Peak anvil and peak mass velocities are used as input velocity conditions for dynamic calculations: these values, along with the mean values of all peak velocities measured, are shown for each impact from no. 1 (600 mm hammer height) to impact no. 6 (1700 mm hammer height) as shown in **Figure 7.11**.

The maximum deflection of the fiberglass specimens is acquired by the images taken from the recorded videos, using the graduated scale located in the centre of the support structure. The measurement is realized, considering that the runners are free to move in the vertical direction only. Therefore, a straight line is drawn on digital images, connecting the beam ends, in order to define the reference point of the deflection: the measurement is taken from the reference line to the first metal plate connecting the beam and the mass. Some examples are reported in graphs from **Figure 7.12** to **Figure 7.14** where the maximum deflection δ of the most stressed impact is shown (no. 6). The comparison between results assessed from numerical calculation and measurements taken by the recorded videos is reported in plots of **Figure 7.15**.

Some examples of the axial maximum strain values calculated by the ADINA^{TM} software for some of the most stressed impacts (no. 6) are shown in **Figure 7.16, Figure 7.17** and **Figure 7.18**. The complete comparison for each series of tests is shown in plots, in which the hammer height and the measured and calculated axial strain for each strain gauge position is reported. See from **Figure 7.19** to **Figure 7.21**.

The numerical model is perfectly symmetric. Thus, only a strain value is reported for symmetric strain gauge positions (1 and 3 for tension, 4 and 6 for compression). Asymmetries of the experimental data are also shown.

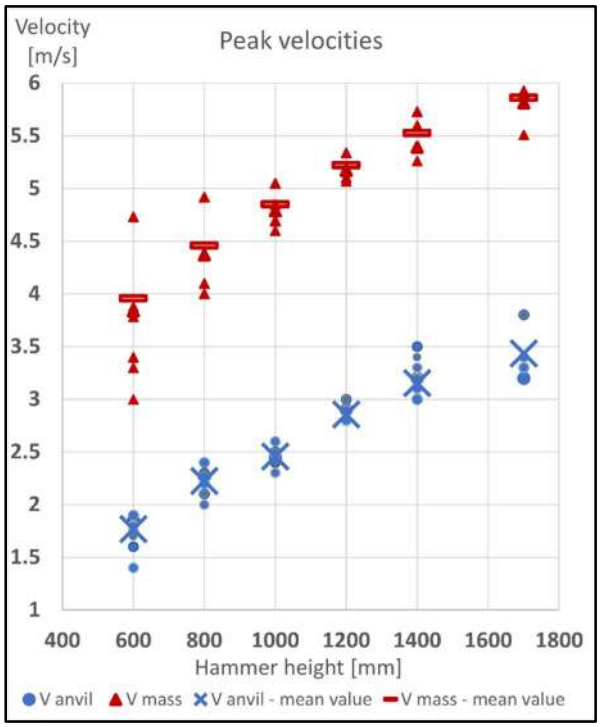

Figure 7.11 Anvil table and mass peak velocities (V_a and V_m) for each impact produced by different hammer heights

Figure 7.12 Impact no. 6 - Maximum deflection (380 mm) for G2 g/m^2, 20 mm, manufacturer "D" specimen (image taken from a recorded video

Figure 7.13 Impact no. 6 - Maximum deflection (420 mm) for G1 g/m^2, 20 mm, manufacturer "D" specimen (image taken from a recorded video)

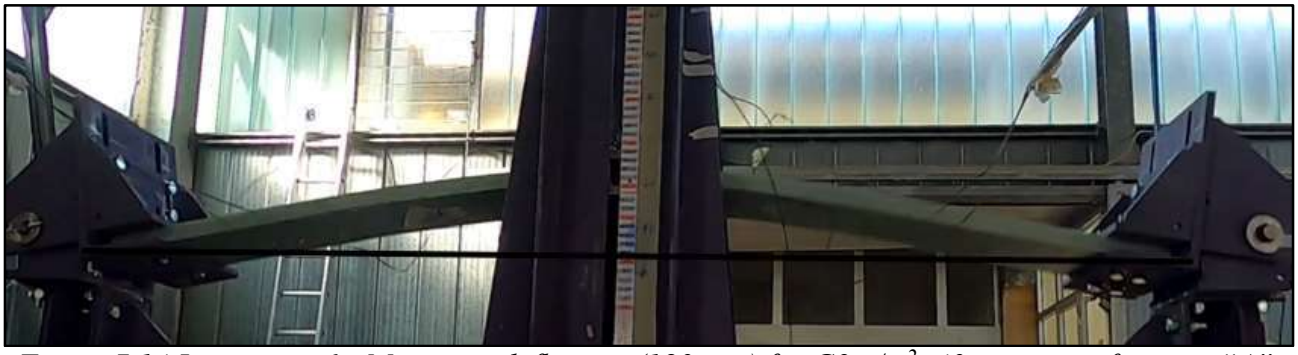

Figure 7.14 Impact no. 6 - Maximum deflection (180 mm) for G2 g/m^2, 40 mm, manufacturer "A" specimen (image taken from a recorded video)

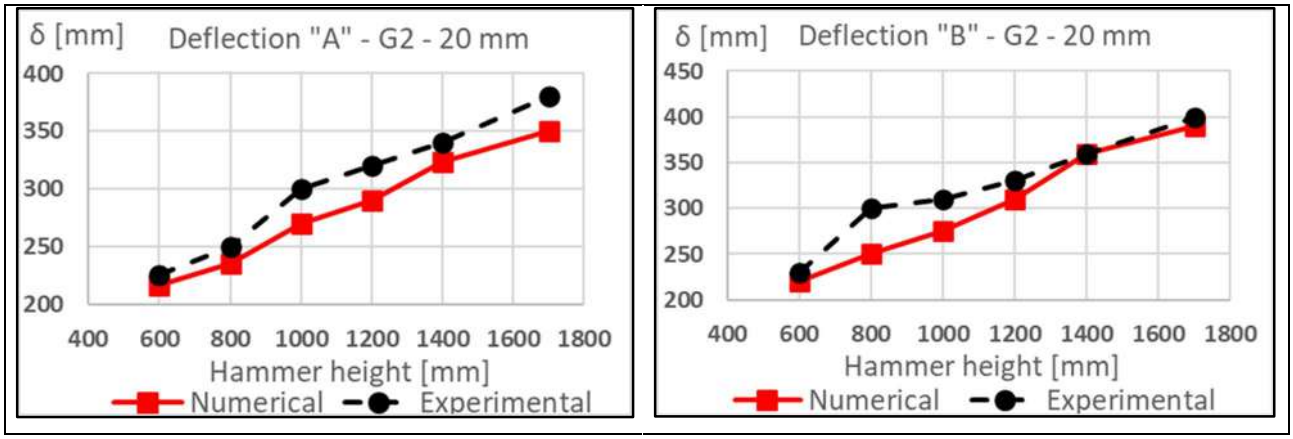

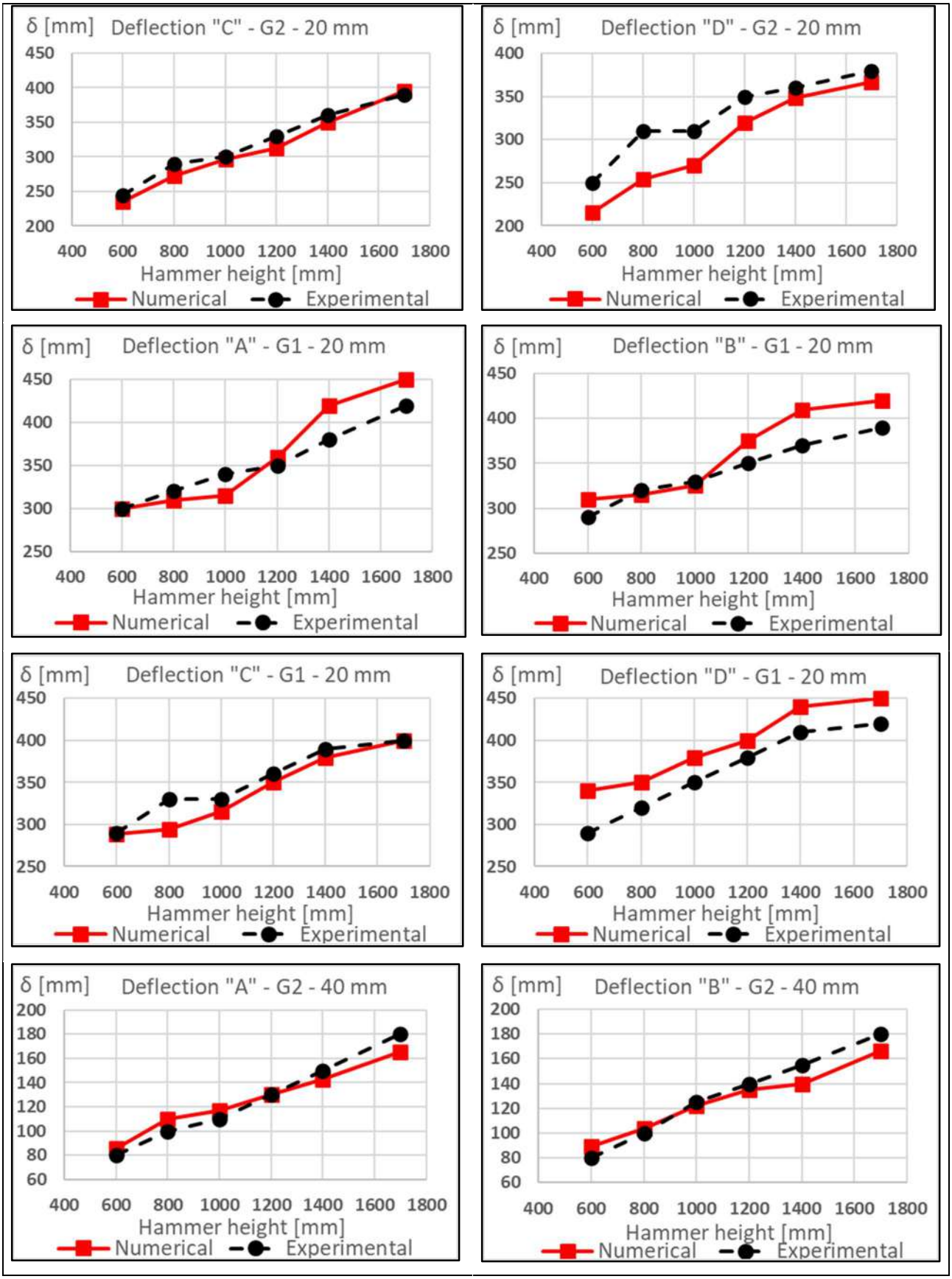
δ [mm] Deflection "C" - G2 - 20 mm
450
400
350
300
250
200
400 600 800 1000 1200 1400 1600 1800
Hammer height [mm]
Numerical
Experimental
δ [mm] Deflection "D" - G2 - 20 mm
400
350
300
250
200
400 600 800 1000 1200 1400 1600 1800
Hammer height [mm]
Numerical
Experimental
δ [mm] Deflection "A" - G1 - 20 mm
450
400
350
300
250
400 600 800 1000 1200 1400 1600 1800
Hammer height [mm]
Numerical
Experimental
δ [mm] Deflection "B" - G1 - 20 mm
450
400
350
300
250
400 600 800 1000 1200 1400 1600 1800
Hammer height [mm]
Numerical
Experimental
δ [mm] Deflection "C" - G1 - 20 mm
450
400
350
300
250
400 600 800 1000 1200 1400 1600 1800
Hammer height [mm]
Numerical
Experimental
δ [mm] Deflection "D" - G1 - 20 mm
450
400
350
300
250
400 600 800 1000 1200 1400 1600 1800
Hammer height [mm]
Numerical
Experimental
δ [mm] Deflection "A" - G2 - 40 mm
200
180
160
140
120
100
80
60
400 600 800 1000 1200 1400 1600 1800
Hammer height [mm]
Numerical
Experimental
δ [mm] Deflection "B" - G2 - 40 mm
200
180
160
140
120
100
80
60
400 600 800 1000 1200 1400 1600 1800
Hammer height [mm]
Numerical
Experimental

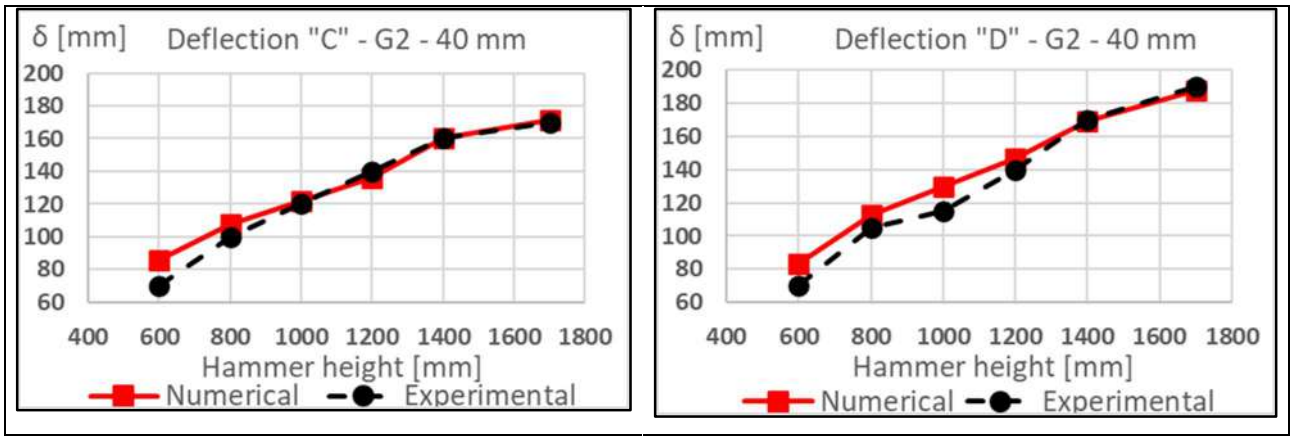

Figure 7.15 Maximum deflection – Experimental vs. numerical comparison

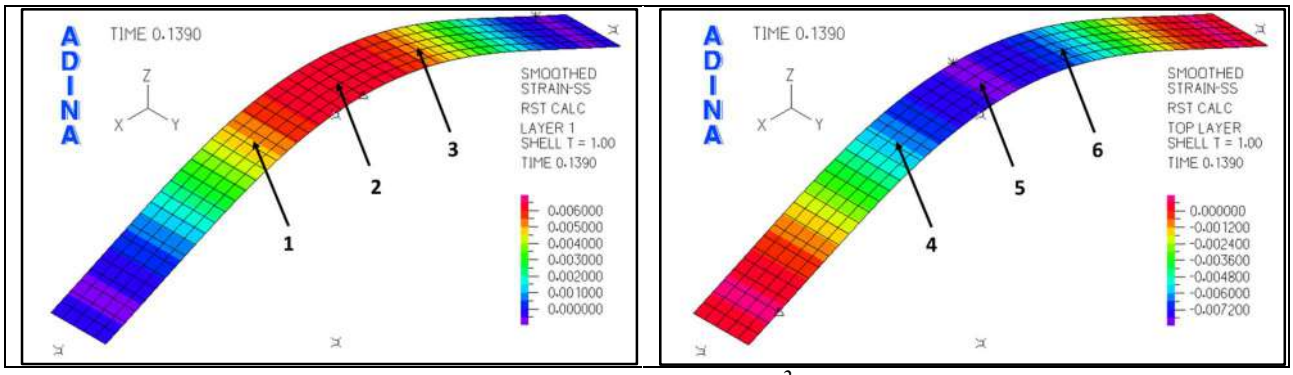

Figure 7.16 Numerical axial strain – Impact no. 6 – G2 g/m^2 – 20 mm – Manufacturer "C" – Time step 0.139 s – Tension (left) and Compression (right)

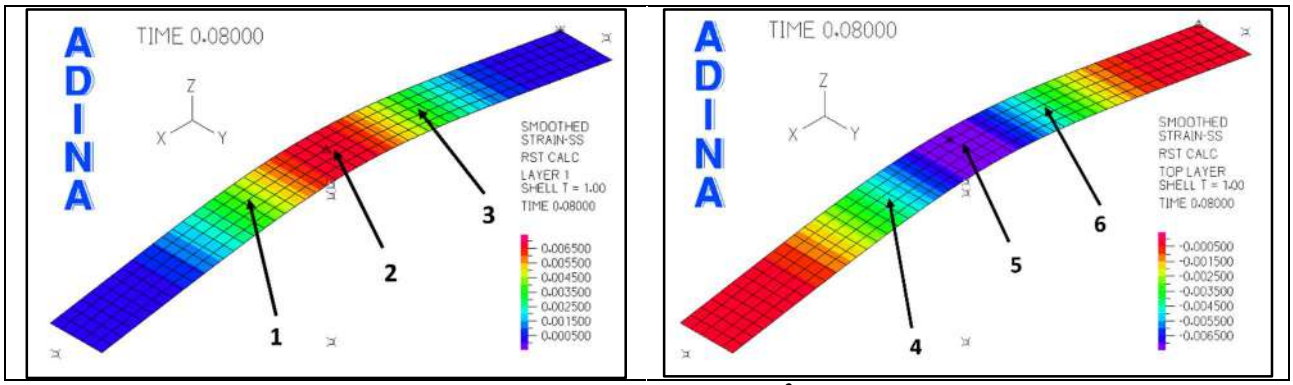

Figure 7.17 Numerical axial strain – Impact no. 6 – G2 g/m^2 – 40 mm – Manufacturer "A" – Time step 0.080 s – Tension (left) and Compression (right)

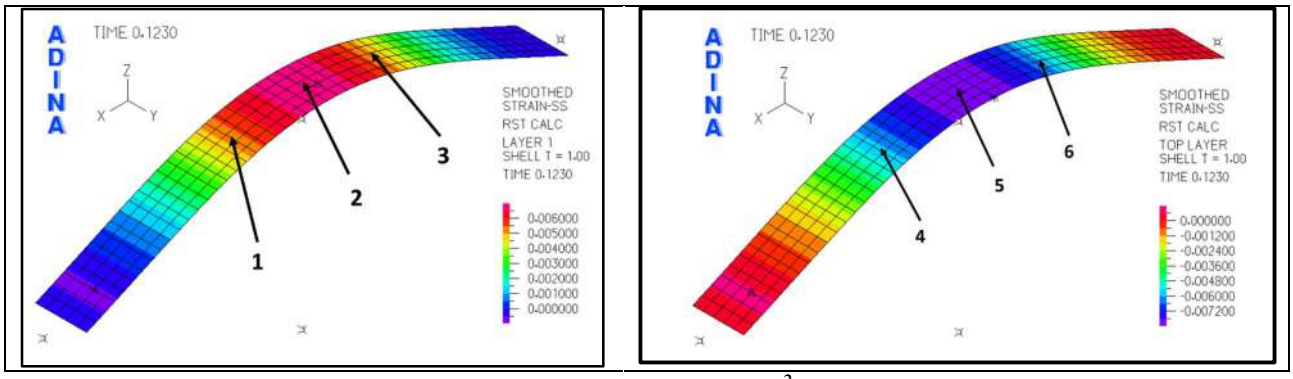

Figure 7.18 Numerical axial strain – Impact no. 6 – G1 g/m^2 – 20 mm – Manufacturer "C" – Time step 0.123 s – Tension (left) and Compression (right)

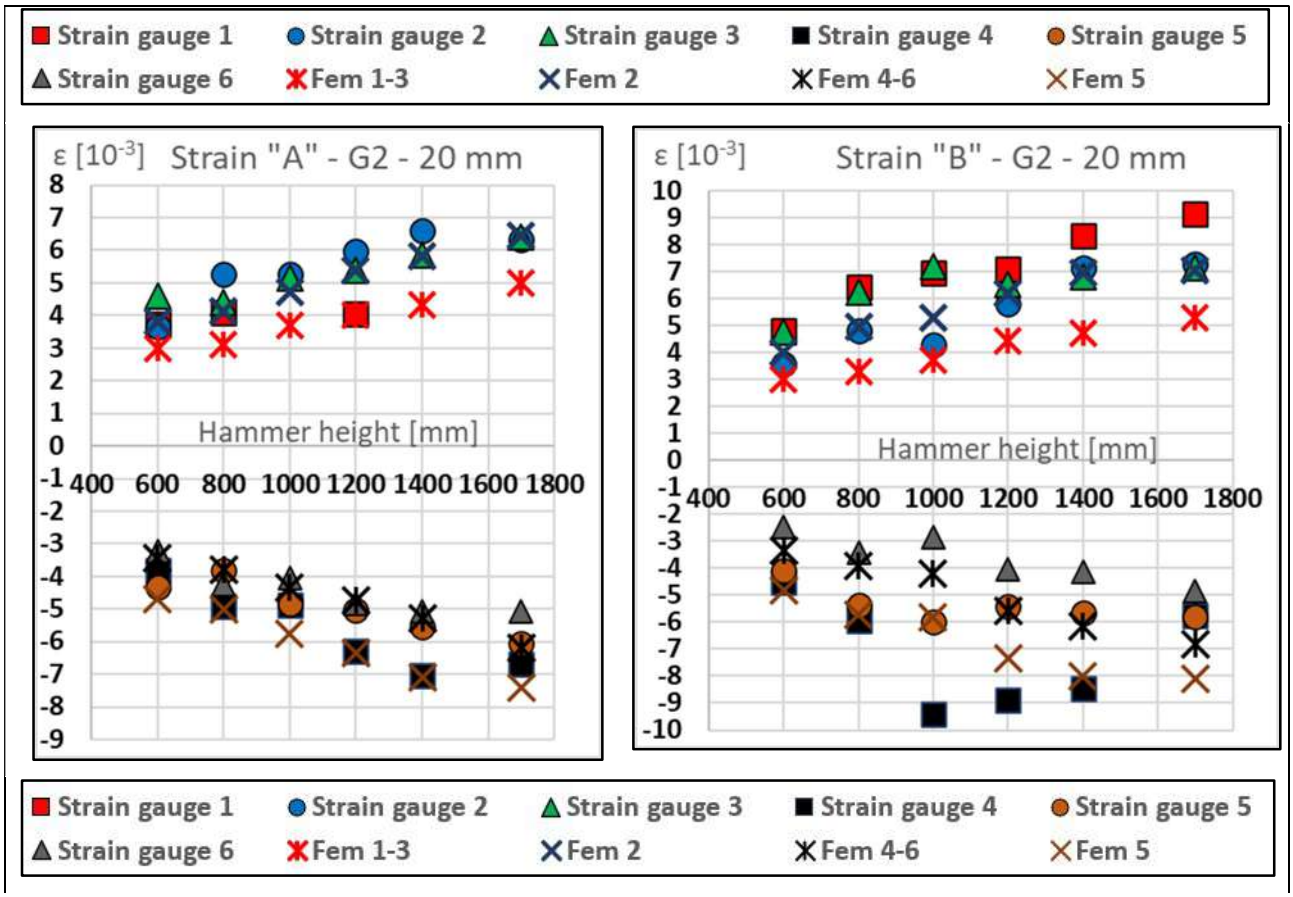

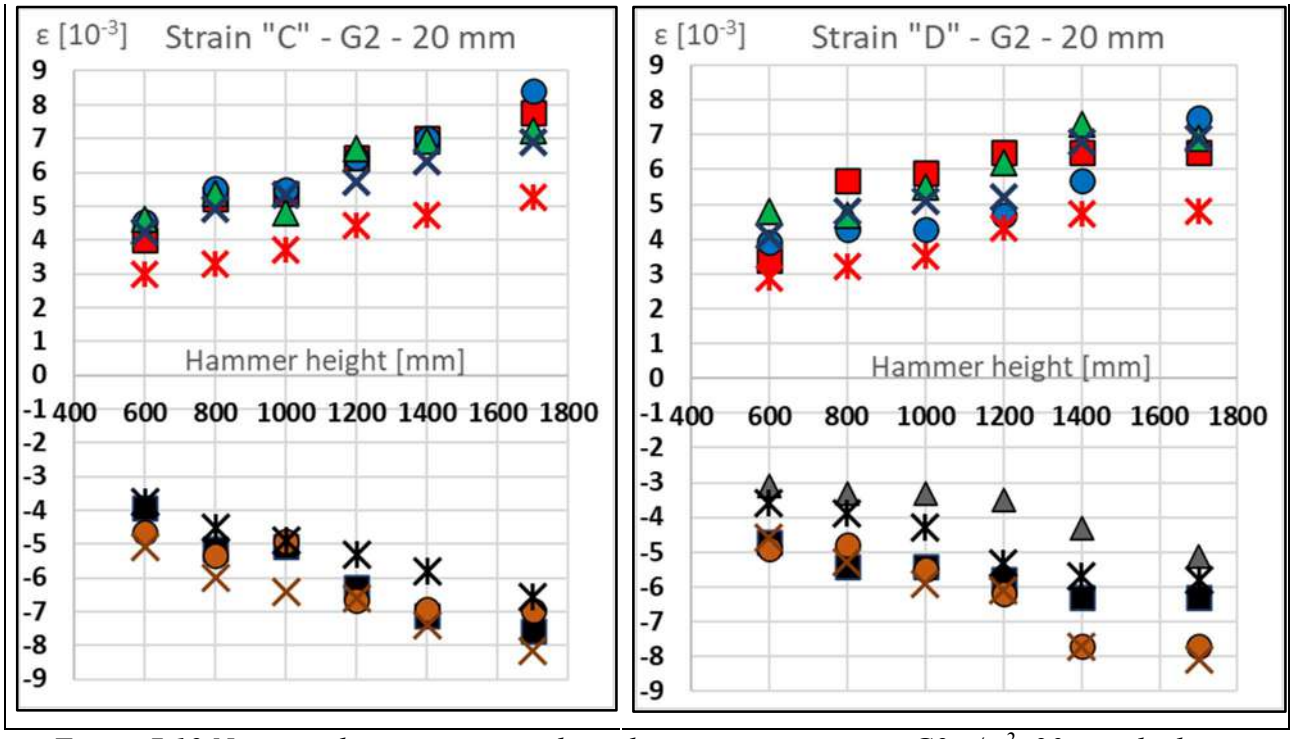

Figure 7.19 Numerical vs. experimental axial strain comparison – G2 g/m^2, 20 mm thickness specimens

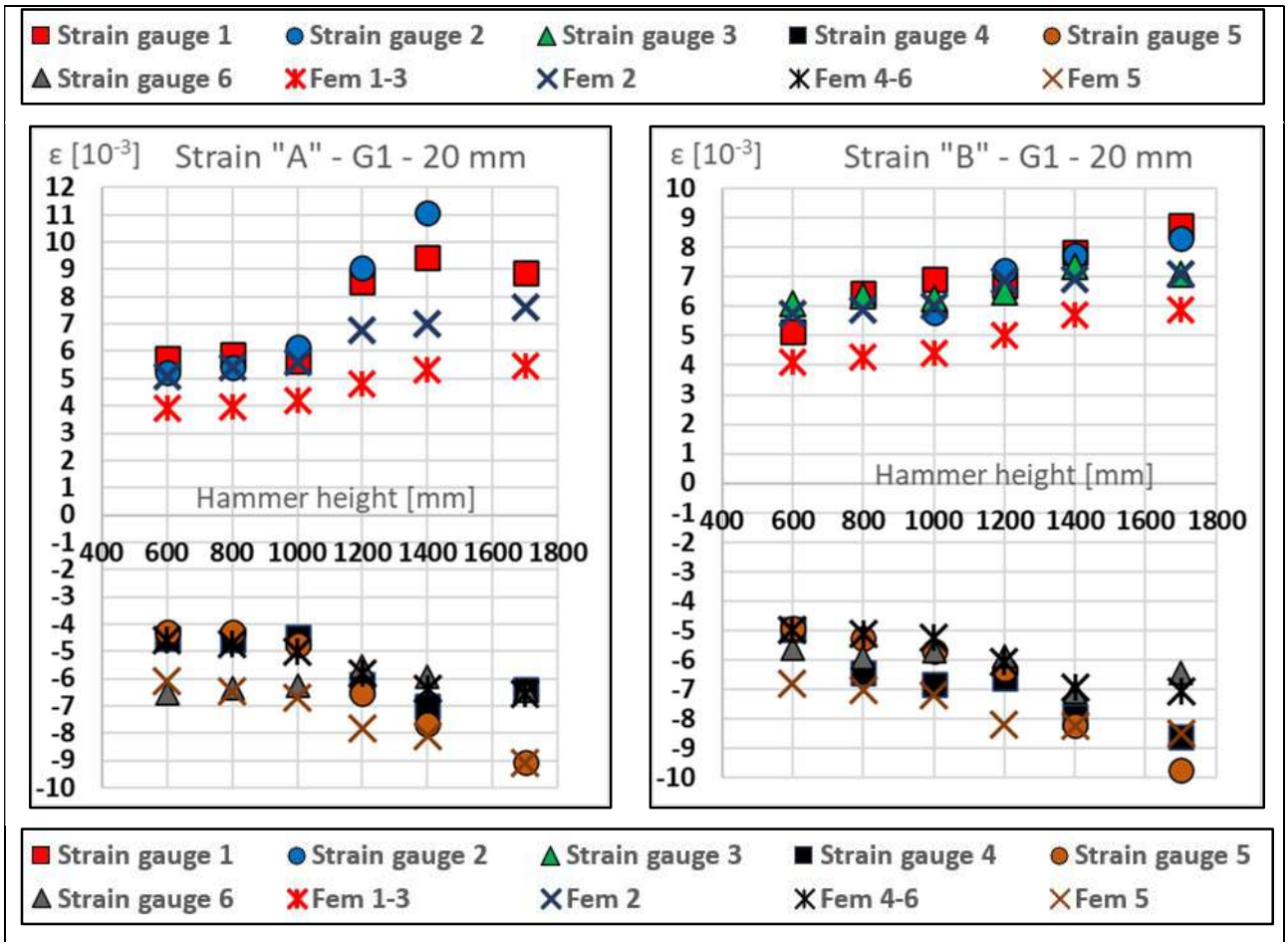

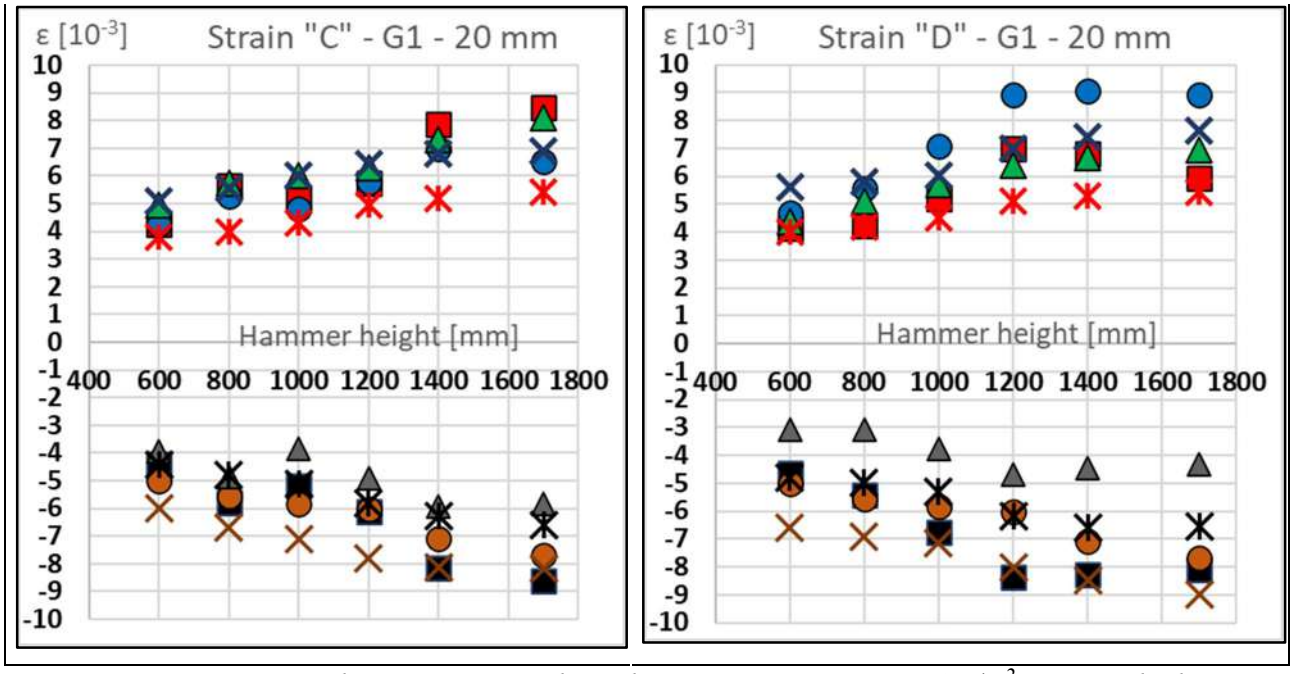

Figure 7.20 Numerical vs. experimental axial strain comparison – G1 g/m^2, 20 mm thickness specimens

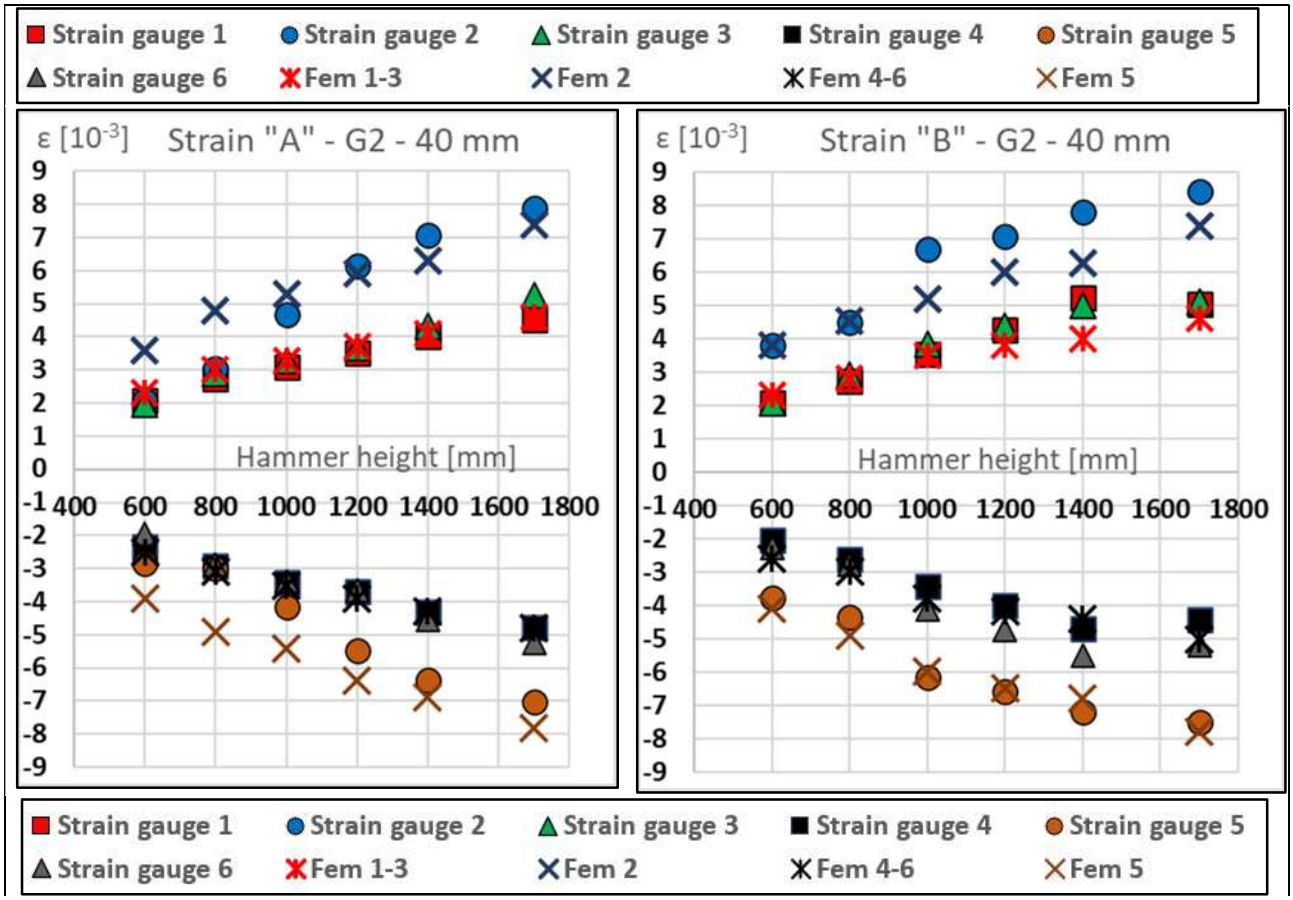

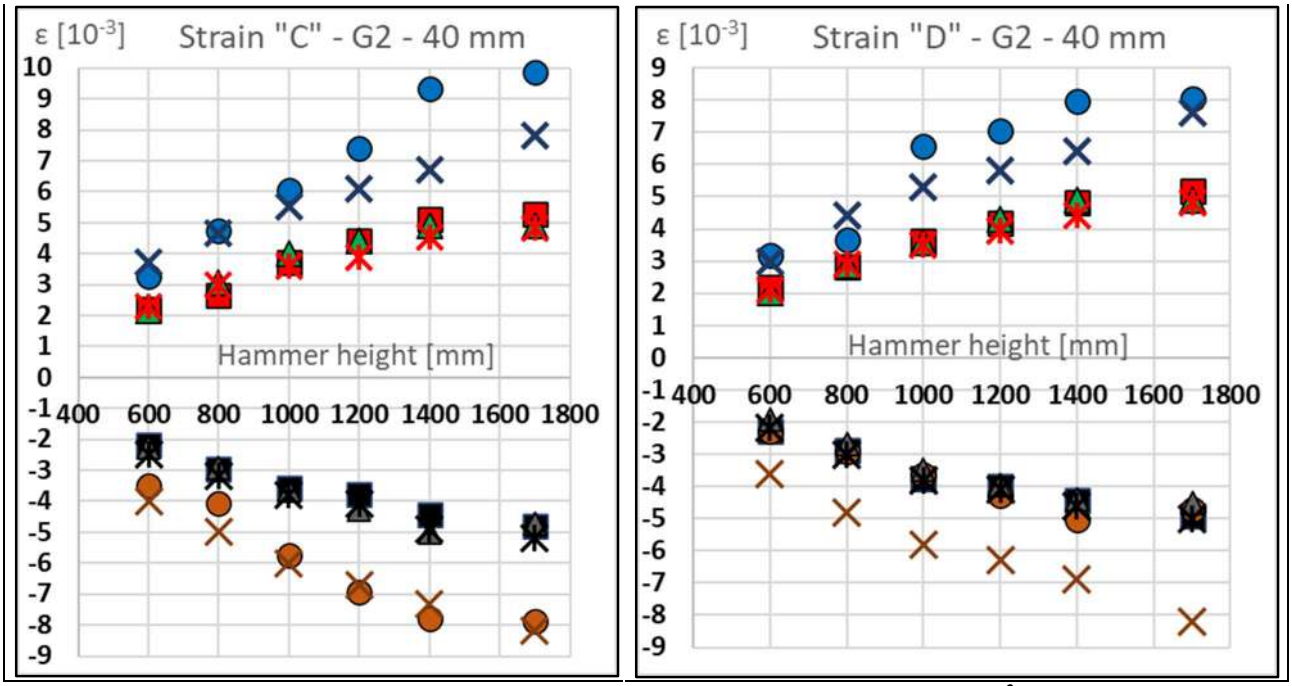

Figure 7.21 Numerical vs. experimental axial strain comparison – G2 g/m^2, 40 mm thickness specimens

7.3.4 Discussion

The shock phenomenon has been simulated by applying the measured peak velocities for each impact of the calibrated mass and the anvil table as input loads on the finite element model. This turns out as a reasonable strategy considering the favourable comparison between experimental and numerical Shock Response Spectrum (SRS) of maxima absolute accelerations, where 5% damping ratio ξ has been imposed according to [7.20].

The SRS calculations refer to the acceleration measured by the accelerometer no. 1, located on the calibrated mass, and the acceleration calculated by the FE software at midspan of the composite beam. In ADINA^{TM} environment a post processing of the results is realized, performing a floor response spectrum analysis from time history data in which 5% damping ratio ξ has been set. In **Figure 7.22**, exemplarily, the comparison is reported for the most stressed test, no. 6, showing that the energy distribution is similar, especially in the low frequencies range (10-300 Hz), where the structural response is more consistent.

This is confirmed by the Fast Fourier Transform (FFT) of strains, where quasi-static response is very large and first natural frequencies are in the range. The FFT operation is performed considering the signal in the time window of interest (from the hammer impact to the mass fall on the anvil), allowing a significant comparison with numerical estimates. The computation time step is however set in this case to $2 \cdot 10^{-5}$ in order to obtain the same signal length and FFT resolution.

In **Figure 7.23** an example of FFT comparison is shown, highlighting a similar trend in the results and a low difference of the first numerically estimated frequency compared to the experimental one (48 Hz vs 39 Hz). This can be due to the approximation of the numerical model, in which the mass is connected to the composite beam by means of perfectly rigid surfaces, without considering the actual stiffness of steel sandwich plates used in the tests. Therefore, the numerical frequency response appears slightly more rigid in the experimental comparison. However, this has no significant influence in the numerical results, as shown in the deflection and strain comparison.

The numerical maximum deflections are in fact in good agreement with experimental data, resulting in an average percentage error lower than 0.6%. However, we must consider that the video-camera is characterized by 240 frames per second acquisition speed (a frame every 0.004 s). Referring to finite element results, the maximum deflection rate is on average ranging approximately from 20 mm in 0.004 s for the fastest impacts to 6 mm in 0.004 s for the slowest impacts. A percentage error from 1% to 5% should therefore be added.

In addition, perspective view in images analysis can lead to an extra error of $\pm$20 mm. Considering the worst cases, the maximum percentage error in the deflection comparison is about 5%, that is rather a satisfactory result considering the complexity of the experimentation.

Strain numerical time histories follow the same trend of the experimental ones. Some examples are reported in **Figure 7.24**. All the analyses provided the same trends and therefore the comparisons have been limited to maximum values for the sake of shortness (from **Figure 7.19** to **Figure 7.21**). Numerical average errors in maximum axial strain calculation for tension (strain gauges no. 1-3) and compression (strain gauges no. 4-6) are reported in **Table 7.8**. It can be noted that, especially experimental tension values, are slightly higher than numerical results. This deviation can be due to the asymmetries of the problem, which are neglected in the numerical analysis. In this respect, it can be noted that experimental data of the 40 mm thickness specimen are more symmetric, and this difference is reduced (See **Figure 7.21** and **Table 7.9**). In fact, from the analysis of the 20 mm thickness specimen (**Figure 7.19** - **Figure 7.20**) it is evident that strain gauges in symmetric positions measure strain values that can be different from each other up to $4 \cdot 10^{-3}$ ε, especially in compression. In addition, the strain gauges set in the midspan doesn't report values higher than those measured by the symmetric ones, as it happens instead in the numerical method. On the other way, analyzing the 40 mm thickness specimen (**Figure 7.21**), it can be noted that symmetric strain gauges measure almost coincident values, while midspan strain gauges report a higher value than the others. This behaviour is in agreement with the symmetric numerical results obtained by the finite element calculation.

In same samples related to cases of specimens of different thicknesses, weights and companies, numerical strains and deflections have been calculated, using as input the mechanic characterization of the materials obtained by weighted average (Eq. 7.3). No significative differences in the results (strains gap is less than 1%) are obtained comparing this calculation with that realized characterizing material by arithmetic average formula for the determination of longitudinal Young modulus (Eq. 7.2). Therefore, they are not reported in the text for a matter of shortness. In addition, the same conclusion is reached, when calculations are performed in same cases imposing a different damping ratio value (5%) in the linear spring setting as that used by Alexander in [7.2]: negligible differences in the results have been found.

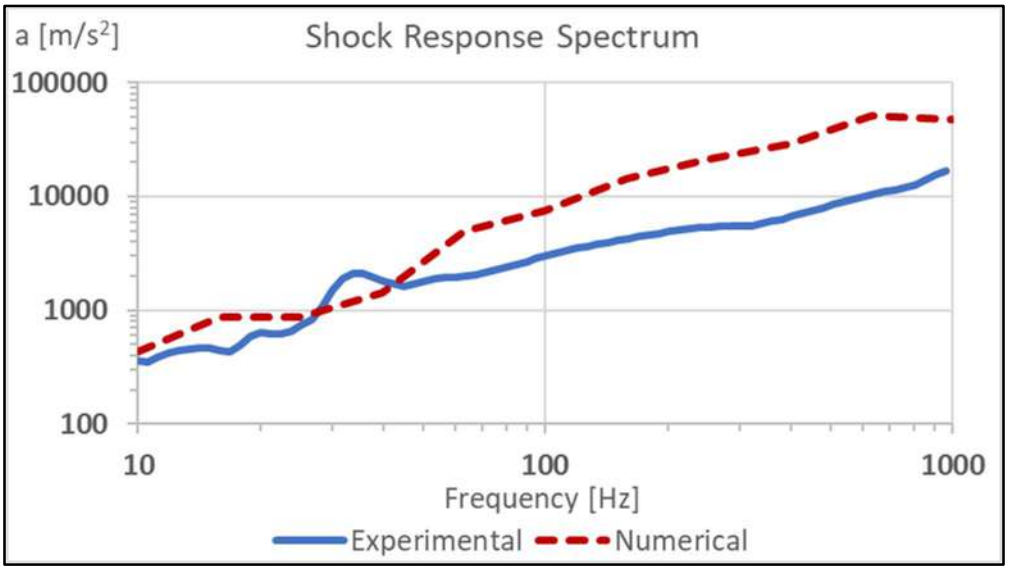

Figure 7.22 Experimental and numerical Shock Response Spectrum comparison – Test 6, manufacturer "A", G2 g/m², 40 mm thickness specimen

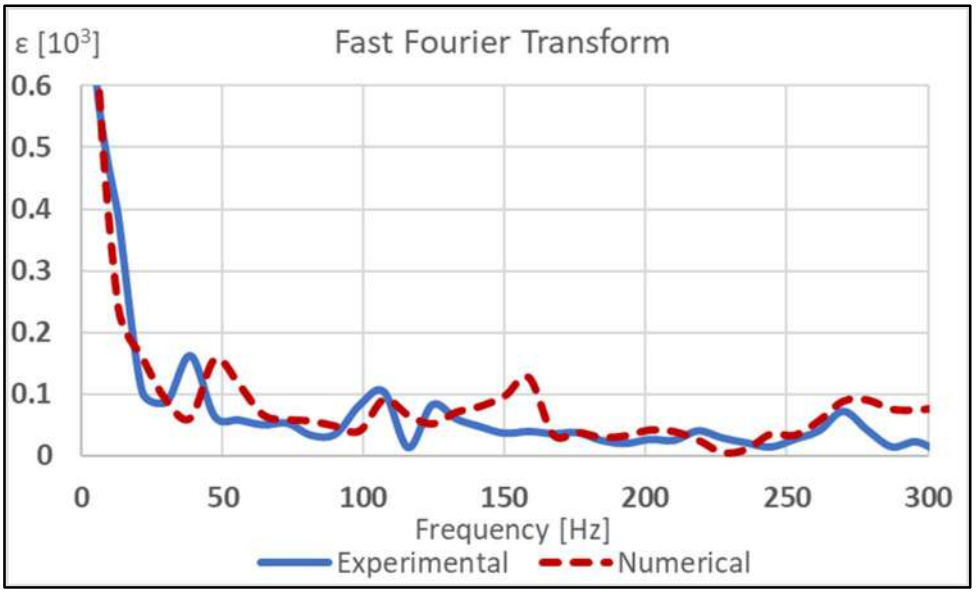

Figure 7.23 Experimental and numerical Fast Fourier Transform comparison – Test 6, manufacturer "A", G2 g/m², 40 mm thickness specimen, strain position no. 1

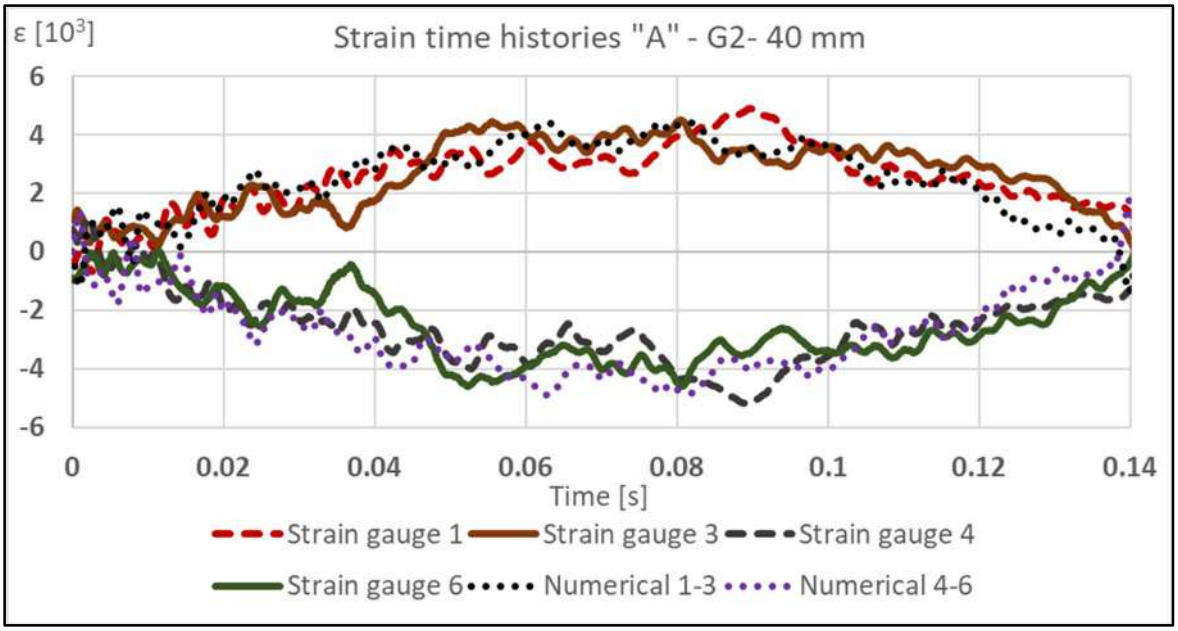

Figure 7.24 Experimental and numerical strain time histories comparison – Test 6, manufacturer "A", G2 g/m², 40 mm thickness specimen, strain gauges no. 1-3-4-6

Table 7.8 Average percentage errors for maximum axial strain in tension and compression of the numerical method

Tension [%]	Compression [%]
-12.4	7.6

Table 7.9 Average percentage errors for maximum axial strain in tension and compression of the numerical method for G2 g/m^2, 40 mm thickness specimens

Tension [%]	Compression [%]
-2.5	6.9

7.4 Considerations

A numerical method, developed on theoretical basis and validated by experimental data, has been built to characterize dynamic properties of naval E-glass biaxial fiberglass laminates, predicting their transient response to an underwater shock explosion scenario. As a summary, Experimental Modal Analysis has been carried out to obtain a first characterization of materials by determination of natural frequencies and to define the time step for the dynamic calculation. After this, a shock test has been performed using MIL S 901 D Medium Weight Shock Machine to verify the shock response of naval ship construction fiberglass laminates, while a Finite Element model is built to reproduce this Shock Machine behaviour. In the end, the comparison of experimental and numerical results was realized to validate the model and characterize the mechanical properties of composites.

The comparison between experimental data and numerical calculations can be considered very satisfactory, despite significant nonlinearities of the studied system. The small bias in tension strain values can be due to the asymmetries of the problem not modelled in the numerical method. However, when the thickness increases and maximum deflection decreases as a consequence, the test results become more symmetric and this deviation less important.

The idea to compare deflections by videos and strain deformations by strain gauges was useful to have a better understanding of the phenomenon, resulting in a good setting of the numerical modelling strategy. In particular, composites can be represented using MITC 4-nodes multilayer shell elements, in which mechanical properties, including dynamic Young modulus, must be properly set. A dynamic implicit calculation, in which the time step is selected according to the results of modal analysis, can be carried out, imposing as initial conditions the calibrated mass and anvil table peak impact velocities requested (**Figure 7.11**). A simple model mass-spring-mass can be updated to include the impact mechanism of the calibrated mass that causes the fiberglass deflection, properly defining a 3-D contact algorithm, as previously reported. The fiberglass boundary conditions (rollers) should be properly set to show the vertical velocity of the support structure and to be free to rotate and translate in the axial direction. Contact algorithms can be also used to connect rollers to composite elements and to simulate the limits of the anvil table travel (see **Figure 7.9** and **Figure 7.10**).

The choice to use mechanical properties of the materials achieved by EMA analysis to characterize composites in the dynamic numerical method has proved to be acceptable also to predict the shock transient response of the structures as shown in the numerical vs experimental comparison. In this work only longitudinal Young modulus is determined dynamically by the selection of flexural modes in EMA analysis, while other parameters are achieved by quasi-static tests. This kind of characterization has turn out to be valid considering that also the shock response seems to be mainly a flexural phenomenon. This opens for a relatively straightforward material characterization, limiting the need of complex experimental shock trials to few selected laminates. In fact, it can be used not only to verify the shock response of plane laminates, but also to design more complex naval structures in order to select of the proper stacking sequences.

The post processing of experimental and numerical signals (FFT, SRS and time histories comparison) shows their similarities, despite the approximations introduced in the numerical model. Therefore, this relatively easy-to-implement theoretical model, appropriately corrected according to experimental data and implemented through finite element models, can be considered effective to characterize the dynamic transient response of composite material structures.

Further tests are necessary and are indeed already planned to study the composite damage mechanisms and its predictability using numerical methods. However, collected data are sufficient for the scope of the present analysis.

7.5 Bibliography

[7.1] ADINA, *Theory and Modeling Guide* Volumes I-III, ADINA R & D Inc., Watertown, 2015;

[7.2] Alexander J.E., "Damped 2DOF Model of MIL-S-901D Medium-Weight Shock Machine Test", Sound & Vibration, www.SandV.com, 2016;

[7.3] ASTM Standard E 132 – 17, *Standard Test Method for Poisson's Ratio at Room Temperature*;

[7.4] ASTM Standard E 143 – 20, *Standard Test Method for Shear Modulus at Room Temperature*;

[7.5] ASTM Standard E 1876 – 07, *Standard Test Method for Dynamic Young's Modulus, Shear Modulus, and Poisson's Ratio by Impulse Excitation of Vibration*;

[7.6] Bathe K.J., *Finite element procedures*, Bathe K.J., Watertown, 2014;

[7.7] Clements E.W., *Shipboard Shock and Navy Devices for its Simulation,* Naval Research Laboratory, Washington D.C., 1972;

[7.8] Clough R.W., Penzien J., *Dynamics of structures*, Computer & Structures Inc., 377-381, Berkeley, 1995;

[7.9] Dvorkin E., Bathe K.J., "A Continuum Mechanics Based Four-Node Shell Element for General Nonlinear Analysis", Engineering Computations, Vol. 1, pp. 77-88, 1984;

[7.10] Ewins, D.J., *Modal Testing: Theory, Practice and Application*, Research Studies Press LTD, Hertfordshire, 2000;

[7.11] Gaiotti M. & Rizzo C. M., "Finite element modeling strategies for sandwich composite laminates under compressive loadings", Ocean Engineering 63, 44-51, 2013;

[7.12] Gaiotti M., Rizzo C. M., Branner K., Berring P., "An high order Mixed Interpolation Tensorial Components (MITC) shell element approach for modeling the buckling behavior of delaminated composites", Compos. Struct. 108, 657-666, 2014;

[7.13] Halpin J. C., Nicolais L., Materiali compositi: relazioni tra proprietà e struttura, Ingegnere Chimico Italiano 7:173, 1971;

[7.14] Mannacio F., Di Marzo F., Gaiotti M., Guzzo M., Rizzo C.M., Venturini M., "Characterization of underwater shock transient effects on naval E-glass biaxial fiberglass laminates: An experimental and numerical method", Appl. Ocean Res. 128 103356, 2022;

[7.15] Mannacio F., Di Marzo F., Gaiotti M., Guzzo M., Rizzo C.M., Venturini M., "Shock characterization of fiberglass composite laminates: numerical and experimental comparison", NAV 2022 Conference, Genoa, 15-17 June 2022;

[7.16] ME'scope VES, *Tutorial Manual* Volume IA, Vibrant Technology Inc, Scotts Valley, 2014;

[7.17] MIL-S-901-D, *Shock tests, h.i. (high-impact) shipboard machinery, equipment, and systems, requirements*, United States Department of Defense, 1989;

[7.18] NAV-30-A001, *Norme per l'esecuzione delle prove d'urto su macchinari ed apparecchiature di bordo, Ministero della Difesa*, Istituto Poligrafico dello Stato, 1986;

[7.19] NAVSEA 0908-LP-0003010 Rev. 1, *Shock design criteria for surface ships*, Direction of Commander, Naval Sea Systems Command, September 1995;

[7.20] STANAG 4141, *Shock testing of equipment for surface ships*, NATO Standardization Agreement, 1976.

8 Design method analyses to predict FSI effects caused by non-contact underwater explosion on minesweepers

In this Chapter, different numerical approaches are used to to predict the FSI effects caused by non-contact UNDEX on board of a typical single skin fiberglass, single hull, minesweeper. Material and structural features, openly reported by Green Associates in [8.12], are modelled in the Finite Element simulator, where the orthotropic behaviour of E-glass polyester resin laminates is considered as well. It is known that some national companies are used to predict the UNDEX effects on a ship panel, applying directly a double pressure on the structure in analysis as it is calculated from the air-backed plate theory, without including the fluid in the calculation. Calibrated dampers are set on the structure to simulate the sea water damping until pressure drop to zero. Then, a restart analysis, in which dampers are excluded, is used to consider the cavitation phenomenon in the simulation. It has been chosen to go further this approximation to include the fluid effects in the calculations.

Therefore, sea water is modelled using different approaches. Calculations are performed separately using an approximate FE approach, easy-to-apply in an early design phase, a classical fully-coupled FSI approach encompassing Computational Fluid Dynamics (CFD) and finite element method (FEM) and a Volume of Fluid (VOF) with cavitation approach. In the following, they are mentioned respectively as approximate FE, full FSI and VOF for simplicity's sake.

Within the approximate FE approach, the fluid is simulated using 3-D fluids elements, available in the finite element environment, without the need to apply any CFD software. Full FSI and VOF approaches, instead, need the combination of CFD and FE software to obtain the desired results, with the difference that in VOF approach the equations in fluid are solved using a Finite Volume method, according to theory explained by Eymard et al. [8.8], to include cavitation in simulation.

At first, as a preliminary benchmark, a simplified model, in which a parallelepiped of fluid is built, is analysed in order to calibrate the simulations. In particular, the results obtained by the VOF method, which requires more effort for the calculation setting, are shown. To verify their accuracy, they are compared with theory and tests performed on a rectangular panel by Ramajeyathilagama and Vendhan in [8.21].

In the end, the numerical results, obtained by all the approaches (approximate FE, full FSI and VOF), are compared with experimental data obtained by a full-scale test realized in past years, whose comprehensive description is reported in [8.18]. Namely, strain measurements on a hull plating are compared with numerical estimates. Eventually, it is shown that the proposed modelling strategies, validated by experimental data, can provide effective design assessments, where the accuracy in the results increases in parallel with the computational effort.

8.1 Numerical models

The FE software used for this application is ADINA^{TM} [8.1]. Different numerical models are built in which the approximate FE method, the full FSI and the VOF approaches are used separately to predict the structural response of the same explosion scenario. Differences in modelling and simulation are presented. In particular, in the approximate FE method a coupled fluid-interaction model is built in which fluid and solid elements are modelled in the FE environment only, without the necessity of solving Navier-Stokes equations as used in CFD methods. The VOF algorithm, instead, allow us to simulate cavitation pressure in the CFD environment.

As a summary, in **Table 8.1** the list of all the FSI methodologies, that are nowadays available, is synthetized, in which a check mark is placed if a specific component (structure, water, vapor, explosion gases) can be simulated by the particular model. The methodologies are ordered from left to right, order in which the computational effort increases. The approaches employed in this thesis allow to simulate water and structure, if the Approximate FE, which can be included in the FE + Acoustic Fluid methods, and the Full FSI approach (CFD+FE) are considered, and also vapor if VOF with cavitation method is applied. All the approaches request the structure modelling in the FE environment: details are reported in the following text.

Table 8.1 Summary of the FSI numerical methodologies available to predict UNDEX, including Finite Element (FE), Boundary Element Methods (BEM), Doubly Asymptotic Approximation (DAA), Computational Fluid Dynamics (CFD), Volume of Fluid (VOF) and Smooth Particle Hydrodynamics (SPH)

Simulated component	**FSI Methodology**						
	FE+ Pressure Load	FE+ Acoustic Fluid	FE+BEM (DAA)*	FE+CFD	FE+VOF	FE+CFD (explicit)*	FE+SPH*
Structure	✓	✓	✓	✓	✓	✓	✓
Water		✓	✓	✓	✓	✓	✓
Vapor					✓		
Explosion gases						✓	✓

*Corrections to consider cavitation in term of cut-off pressure are available.

8.1.1 Approximate Finite Element approach: fluid modelled in finite element environment

The approximate FE approach consists in simulating fluid, structures and their interaction in the FE environment, without the necessity of computing CFD calculations. These elements can be directly coupled to the structures, considering that the structural motions cause fluid flows normal to the structural boundary, while the fluid pressures cause additional forces to act on the structure. As reported in the ADINA^{TM} manual [8.1], some assumptions are made, when using these special elements. The medium is assumed to be inviscid, irrotational, with no heat transfer, incompressible or almost incompressible, with relatively small displacements of the fluid boundary, and maximum fluid velocity below the sound speed. Non-linear subsonic formulation for fluid velocity, well described by Sussman and Sundqvist [8.23], is used to reproduce the fluid flow. To employ this formulation, fluid pressure p is assumed to depend only by the density ρ and by no other variables, such as e.g. the temperature. The numerical relationship reported in [8.1] is the following:

$$\rho = \rho_0 \left(1 + \frac{p}{k}\right) \tag{8.1}$$

in which ρ_0 is the fluid density when $p = 0$ and k is the bulk modulus of the fluid.
As a result, in the FE calculation, an additional nodal degree of freedom is set, associated to the fluid potential ϕ. Therefore, only an additional equation per node is solved by the software, referring to a classical FE formulation, where only structural elements are imposed. Material properties of sea water are set in the 3-D fluid elements formulation, considering that only bulk modulus (2.2 GPa) and fluid density (1023 kg/m^3) are necessary.

8.1.2 Full FSI approach: fluid modelled in CFD environment

The simulation is also carried out performing calculations using the CFD routines of the ADINA environment, i.e. by applying the general Navier-Stokes equations. This full FSI approach requests the modelling of fluid in CFD environment, while structures are built in the FE software. Also, the FSI logic is different, considering that solid and fluid mesh are treated separately and then coupled by the solver, uploading step by step their coordinates.
And as before, a “slightly compressible” model of the fluid, in which density changes with pressure, is chosen, according to Eq. 8.1. However, unlike the approximate FE method, Navier Stokes equations are numerically solved for the fluid, as reported by the ADINA^{TM} manual [8.1] and

explained by Bathe [8.2]. These three equations express the conservation of masses, momentums and energy, and can be written in a fixed Cartesian coordinates frames, neglecting heat transfer contribute, as:

$$\frac{\partial \rho}{\partial t} + \nabla \cdot (\rho \mathbf{v}) = 0 \tag{8.2}$$

$$\frac{\partial \rho \mathbf{v}}{\partial t} + \nabla \cdot (\rho \mathbf{v}\mathbf{v} - \boldsymbol{\tau}) = \mathbf{f}^B \tag{8.3}$$

$$\frac{\partial \rho E}{\partial t} + \nabla \cdot (\rho \mathbf{v} E - \boldsymbol{\tau} \cdot \mathbf{v}) = \mathbf{f}^B \cdot \mathbf{v} \tag{8.4}$$

where ρ is the density of the fluid, t is the time, $\mathbf{v}$ is the velocity vector, $\boldsymbol{\tau}$ is the stress tensor, $\mathbf{f}^B$ is the body force vector of the fluid medium and E is the specific total energy.
The stress tensor and the specific total energy are expressed as follows:

$$E = \frac{1}{2}\mathbf{v} \cdot \mathbf{v} + e \tag{8.5}$$

$$\boldsymbol{\tau} = (-p + \lambda \nabla \cdot \mathbf{v})\mathbf{I} + 2\mu\mathbf{e} \tag{8.6}$$

in which e is the specific internal energy, p is the pressure, λ and μ coefficients of fluid viscosity and $\mathbf{e}$ is the velocity strain tensor, defined as:

$$\mathbf{e} = \frac{1}{2}(\nabla \mathbf{v} + \nabla \mathbf{v}^{\mathrm{T}}) \tag{8.7}$$

However, different coordinate frames of reference must be applied. An Arbitrary-Lagrangian-Eulerian (ALE) approach is used to properly account for the deformations of the interface panels in the computational domain, caused by the fluid-structure interaction. The fluid flow is described by an arbitrary coordinate system to consider the fact that fix boundaries are described in a Eulerian system, while the deformed structures are in a Lagrangian system. Therefore, the Navier-Stokes equations discussed so far need to be rewritten in the ALE system. Details are reported in the software manual [8.1]. A transient analysis is performed, in which a dynamic implicit method, Runge-Kutta second order type, reported as "ADINA composite scheme" in the software environment, is used. Detailed explanations about this integration method are given by Bathe and Zhang [8.3]. The default integration parameter $\alpha = {}^{1}/_{\sqrt{2}}$ is chosen, following the guidelines reported in [8.1], considering that this value is proven to give minimum truncation error for linear systems. This method has a second order accuracy and is unconditionally stable.

Structure and fluid model are built separately. Two fluid-structure interfaces are set respectively in the FE and the CFD environment, in which a no-slip condition of the fluid is assumed [8.1]. A two-way, fully coupled, FSI is performed, where the deformation of the solid influences the fluid flow and the fluid traction affects the structural deformations. A direct solution method, also called the simultaneous solution method, well-explained by Zhang and Bathe in [8.27], is used, where fluid equations and the solid ones are combined and treated in one matrix system, i.e. using a monolithic scheme. To solve the linearized equation of the coupled system, the Newton-Raphson method is performed as reported in [8.27]. ALE boundary conditions are set on geometry. This means that displacements of boundary nodes defined on fluid-structure interface geometry are obtained using ALE formulation, solving Laplace equation [8.1] [8.27].
In this full FSI analysis, each ADINA-F node requires four degrees of freedom, while each node in the interior of a potential-based mesh of the approximate FE method requires only one degree of freedom. Bulk modulus and fluid density are considered with the same values reported in the previous section, but the water viscosity is added with a value of $8.9 \cdot 10^{-4}$ Pa·s.

8.1.3 VOF with cavitation approach: fluid modelled in CFD environment

The VOF approach requests the modelling of fluid using the CFD simulator as the previous case, but a Finite Volume method is used to discretize fluid equations. A donor-acceptor scheme is used to evaluate the value of mass-ratio at faces of finite volumes, as reported by Hirt [8.14]. This surface-capturing method is used to perform calculations in which immiscible fluids coexist, being able to track and locate the fluid-fluid surfaces. Properties of each species of fluid are reported in the computational domain, solving an additional scalar transport equation:

$$\frac{\partial \phi_i}{\partial t} + \mathbf{v} \cdot \nabla \phi_i = 0 \qquad\qquad i = 1, \dots, n \tag{8.8}$$

where ϕ_i is the mass ratio of the single species, n is the total number of species, $\mathbf{v}$ is the velocity vector. The following constraint is valid, considering that volume of the fluids is constant:

$$\sum_{i=0}^{n} \phi_i = 1 \tag{8.9}$$

A cavitation model is associated with this VOF method, where a mixture of liquid (first species) and vapor (second species) is considered.
The mixture density ρ_m is calculated using the following equation:

$$\rho_m = f_v \rho_v + f_l \rho_l \tag{8.10}$$

where ρ_v is the vapor density, ρ_l is the liquid density (sea water) and f_v and f_l are the related volume fractions, defined as:

$$f_v = \frac{V_v}{V_v + V_l}, \qquad f_l = 1 - f_v \tag{8.11}$$

Therefore, the transport equation of the liquid volume fraction becomes:

$$\frac{\partial f_l}{\partial t} + \nabla \cdot (f_l \mathbf{v}) = -\frac{1}{\rho_l} \dot{m} \tag{8.12}$$

The mass transfer between vapor and liquid $\dot{m}$ is calculated according to the Zwart, Gerber and Belamri (ZGB) [8.29] cavitation model, as below:

$$\dot{m} = \begin{cases} C_{dest} \rho_v \dfrac{3 f_{nuc} f_l}{R} \sqrt{\dfrac{2}{3} \dfrac{p_v - p}{\rho_l}} & if\ p \le p_v \\ -C_{prod} \rho_v \dfrac{3 f_v}{R} \sqrt{\dfrac{2}{3} \dfrac{p - p_v}{\rho_l}} & if\ p > p_v \end{cases} \tag{8.13}$$

where p is the pressure in the fluid, p_v is the vapor pressure, f_{nuc} is the nuclear site volume fraction, R is the bubble radius, C_{dest} and C_{prod} are user-defined, flow condition dependent parameters. Values used for these UNDEX analyses are reported in **Table 8.2**. In the numerical set-up, as reported in the manual [8.1], the vapor is set as default material associated to the element group in the definition of the material properties.

The VOF method is implemented in the software by applying 8-nodes 3-D FCIB-C elements, which differ from FCBI elements used in the full FSI approach, considering that all degrees of freedom are applied at the center of each element, while the final solution is interpolated at the corners in the post-processing phase. The ALE approach for coordinates in the numerical domain, applied in the Full FSI approach, is also valid for this VOF method. However, considering the configuration of FCIB-C elements, the direct approach, used in the previous case, cannot be considered to couple fluid and solid equations. Therefore, an iterative method, called partitioned method and explained by Zhang and Bathe in [8.27], is applied. Fluid and solid equations are fully coupled. They are solved individually in succession, following an iterative process until convergence. Also, non-linear equations in fluid are solved in an iterative way, using the segregated method reported in the software manual [8.1]. Hence, in short, two separate models are computed and coupled here instead of the single monolithic model approach applied in the full FSI solution. To obtain physically acceptable solutions, this method must be fully convergent. However, convergence is not easily obtained by

users if numerical controls are not properly set. In **Table 8.3** the set-up of basic parameters used as input in these calculations is shown.

The transient analyses can be performed using both the two implicit time integration methods available in the software: the Euler and the Composite scheme. The "Euler α-method" is an unconditionally stable integration scheme of the first order. The default value of $\alpha = 1$ is chosen, considering that this scheme coincides with the Euler backward method, as reported by Bathe [8.2]. The "ADINA composite scheme", used also in the Full FSI approach, is slower, because it requests that each iteration is divided into two sub-steps, but it has a second order accuracy and is unconditionally stable. The default integration parameter $\alpha = {}^{1}/_{\sqrt{2}}$ is chosen also in this case.

In addition, a simple model, in which a parallelepiped of fluid is built, is used to calibrate the method, verifying its results according to theory, before the application to the ship section.

Table 8.2 Fluid and cavitation parameters in VOF simulations

Parameter	**Value**	**Unit of measurement**
Water density (ρ_l)	1023	kg/m^3
Vapor density (ρ_v)	0.023	kg/m^3
Water bulk modulus	$2.2 \cdot 10^9$	Pa
Vapor bulk modulus	$1.4 \cdot 10^5$	Pa
Water viscosity	$8.9 \cdot 10^{-4}$	Pa·s
Vapor viscosity	$1.5 \cdot 10^{-5}$	Pa·s
Vapor pressure	2339	Pa
Nuclear site volume fraction (f_{nuc})	$5 \cdot 10^{-4}$	-
Bubble radius (R)	$1 \cdot 10^{-6}$	m
C_{dest}	200	-
C_{prod}	0.01	-

Table 8.3 Numerical control parameters adopted in the numerical set-up

Control parameter	**Numerical set-up adopted**
Pressure-velocity coupling method	SIMPLE
Space discretization accuracy order	First order
Interpolation scheme for pressure	Standard
Interpolation scheme for nodal variable	Second order
Solver for moving mesh	Sparse
Background mesh used to update moving mesh	Original mesh
Equation solver	AMG type 1
Pressure-Implicit with Splitting of Operators (PISO) scheme	NO
Tolerances convergence criteria	$1 \cdot 10^{-5}$
Minimum iterations	5
Number of initial iterations	5
Primary relaxion factor of velocity for outer iterations	0.75
Primary relaxion factor of pressure for outer iterations	0.3
Primary relaxion factor of displacement for outer iterations	1
Primary relaxion factor of VOF for outer iterations	0.99
Secondary relaxion factors of all variables for outer iterations	1
Inner relaxion factor of velocity	0.01
Inner relaxion factor of pressure	0.01
Inner relaxion factor of displacement	0.1
Inner relaxion factor of VOF	0.1

8.2 Parallelepiped benchmark

The VOF with cavitation method is validated at first theoretically, verifying if the numerical pressure is in agreement with that one calculated from the air-backed plate theory, and then experimentally, referring to the data of some UNDEX tests performed on a steel panel that are available in open literature. Details are reported in the following text.

8.2.1 Theoretical validation

In this first part of the benchmark three different models, in which VOF with cavitation method is used, are built, in order to verify their theoretical accuracy in simulating the effects of the shock phenomenon caused by an underwater explosion on a shell plate in composite material. In each model a parallelepiped of fluid is built, applying at the bottom a shock wave pressure, and setting at the top a composite plate, constrained by simple supports. Three models are built in which different levels of accuracy are obtained, increasing the total length of the parallelepiped and refining mesh and time step. For the last model the results obtained by using the two different integration methods for transient analyses, Euler α-method and ADINA composite scheme, are compared.
The first is a coarse model (**Figure 8.1**) in which:

- the parallelepiped is 20 meters long
- the shell plate is a square of 1x1 meter
- the mesh size is of 170x170x**500** mm
- the time step used is of 10^{-4} seconds
- the peak pressure used as load normal traction is about $2 \cdot 10^{6}$ Pa
- Euler α-method integration scheme is applied

The second is a refined model (**Figure 8.2**), in which the mesh has been refined in the direction of the shock wave propagation and the time step has been reduced, while the parallelepiped is elongated to 50 meters to reduce the numerical instability that occurs when the model is too short, and the mesh is quite refined. The modelling features are the following:

- the parallelepiped is **50 meters long**
- the shell plate is a square of 1x1 meters
- the mesh size is of 170x170x**31** mm

- the time step used is of 10^{-6} seconds
- the peak pressure used as load normal traction is about $2 \cdot 10^{6}$ Pa
- Euler α-method integration scheme is applied

The third model is refined in the vertical direction using the same mesh size of the previous one, but it refers to a larger shell plate (3x3 meters) (**Figure 8.3**). In addition, the normal traction peak load is set to a higher value than the previous cases. Its characteristics are:

- the parallelepiped is 50 meters long
- the shell plate is a square of **3x3 meters**
- the mesh size is of 330x330x**31** mm
- the time step used is of 10^{-6} seconds
- the peak pressure used as load normal traction is about $\mathbf{5 \cdot 10^{6}}$ **Pa**
- Euler α-method integration and ADINA composite scheme are applied, comparing different results

A particular of the mesh of the refined models close to the shell plates is reported in **Figure 8.4**.
In all these methods the following initial conditions are set on the fluid volumes to ensure that the fluid material is composed by only water at the beginning of the calculation:

- nodal pressure is set to $1 \cdot 10^{5}$ Pa which correspond to the atmospheric pressure
- VOF species is equal to 1.

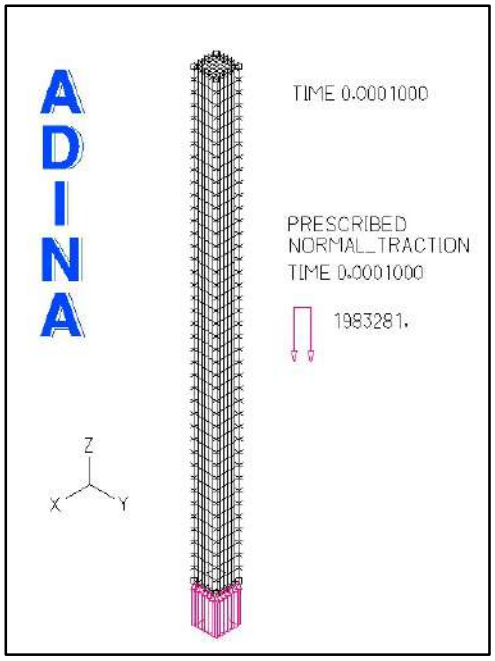

Figure 8.1 Coarse model (1x1 meter of plate size)

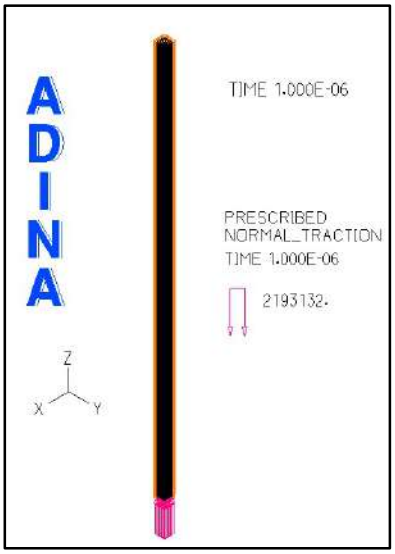

Figure 8.2 Refined model (1x1 meter of plate size)

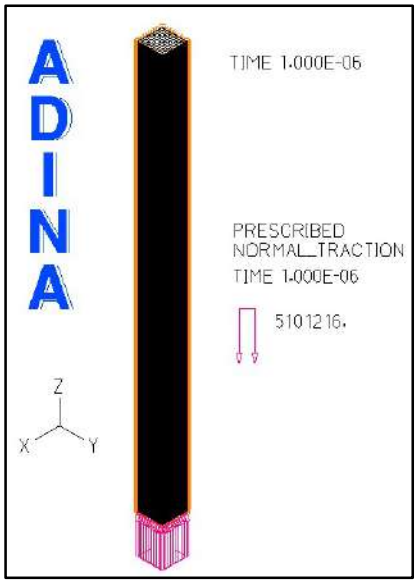

Figure 8.3 Large refined model (3x3 meter of plate size)

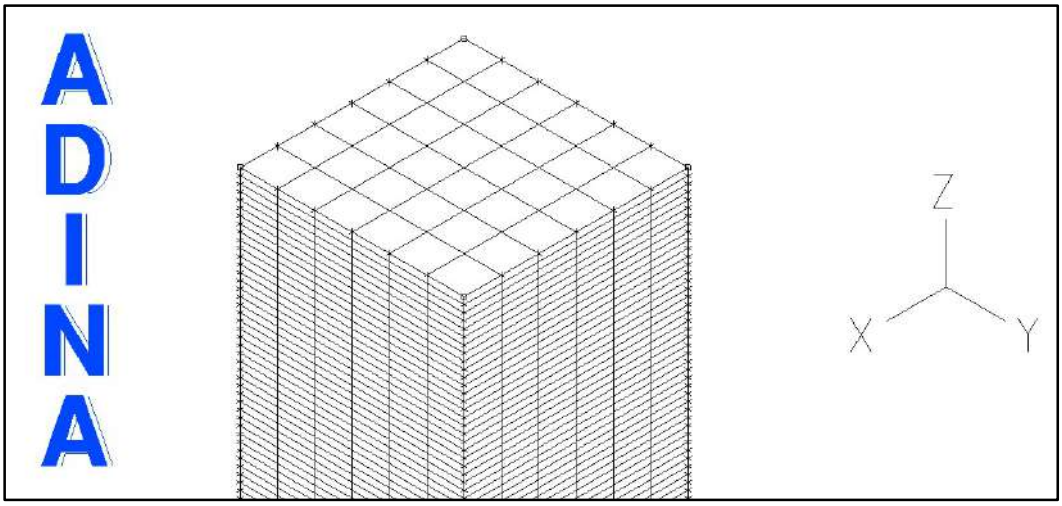

Figure 8.4 Particular of the refined models close to the shell plate

8.2.1.1 Models' analysis and results

8.2.1.1.1 Coarse model

In the coarse model the pressure is smoothed along the parallelepiped. In **Figure 8.5** this condition can be noted in the instant of the impact with the plate. The time history nodal pressure below the plate, which can be renamed as the Fluid-Structure Interaction (FSI) pressure, is reported in **Figure 8.6**. A quite smoothed peak is shown.

However, the force produced by the fluid is equal to that received by the structure, providing as a result a good FSI simulation. FSI force on the structure is extracted by the Z-Reaction calculated by the software on a node in the centre of the plate, while FSI force on the fluid is obtained by multiplying

the FSI pressure in **Figure 8.6** by the area of a single shell element (0.022 m^2). The comparison is reported in **Figure 8.7**, showing the coincidence of these forces, meaning that FSI is performed successfully.

Very slow cavitation occurs only when the nodal pressure in the whole parallelepiped drops below the vapor pressure (2330 Pa), but not immediately when this condition occurs below the shell plate. VOF species values remain close to 1.0, in which the fluid is made mainly by water (see **Figure 8.8**), therefore it can be assessed that cavitation is simulated only in terms of pressures.

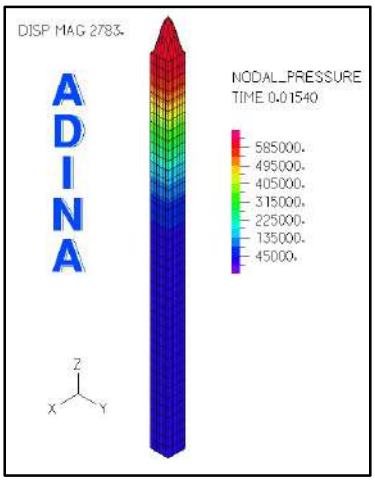

Figure 8.5 Fluid nodal pression distribution

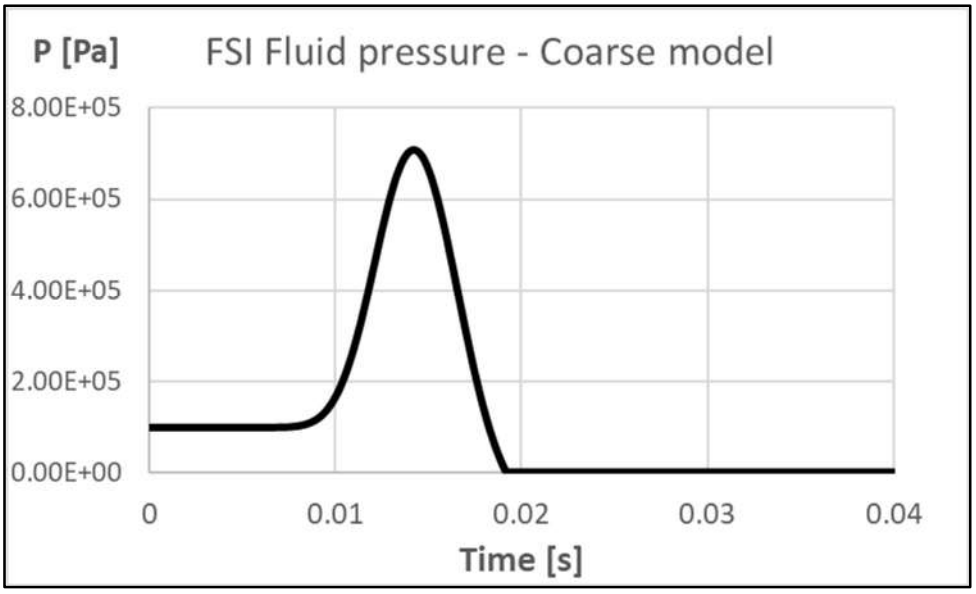

Figure 8.6 FSI nodal pressure – Coarse model

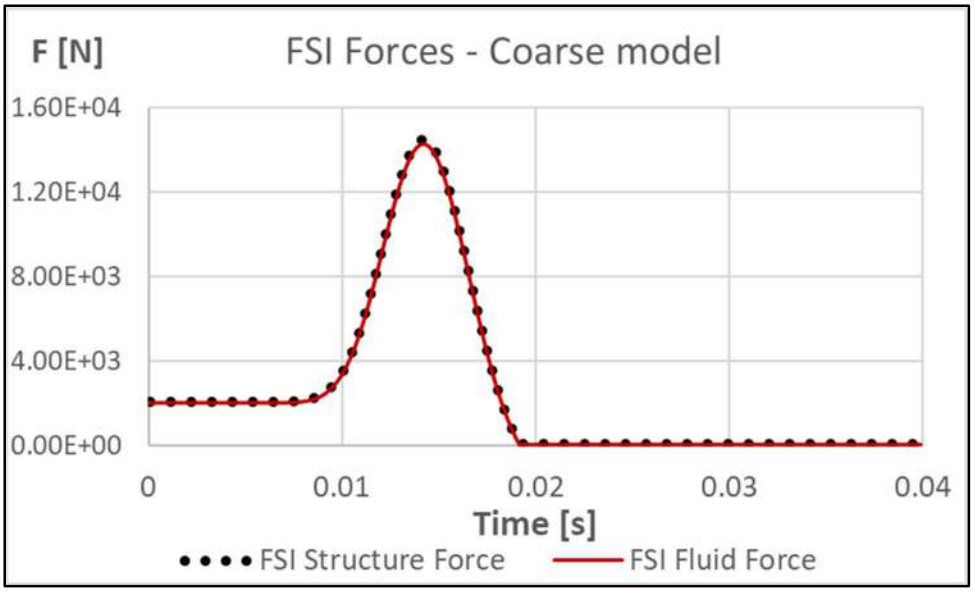

Figure 8.7 FSI Forces comparison

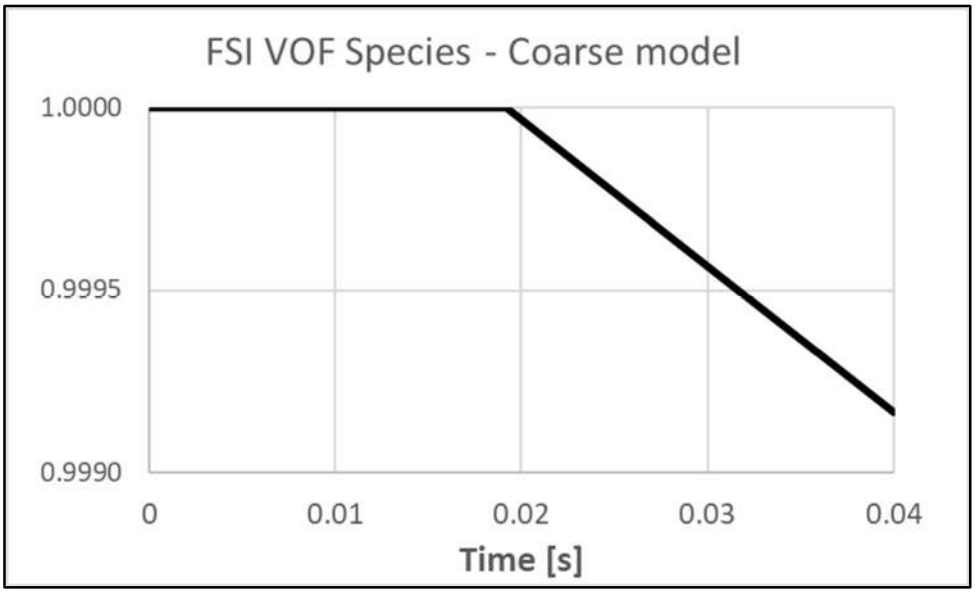

Figure 8.8 FSI VOF Species – Coarse model

8.2.1.1.2 Refined model

In the refined model the peak of pressure calculated in the fluid are less smoothed and more realistic. According to the Tailor air backed theory for an infinite plate [8.19] [8.25], the theoretical FSI pressure p_{FSI} can be calculated as follow:

$$p_{FSI} = 2p_i - \rho cv \tag{8.14}$$

where p_i is the incident pressure of the fluid, ρ is the fluid density (1023 kg/m^3), c is the shock wave celerity (1500 m/s) and v is the shell plate velocity.

In **Figure 8.9** the numerical nodal pressure time histories calculated below the panel (p_{FSI}) and at a distance of 1 meter from the panel (p_{fluid}), are reported. Their positions in the software environment are shown in **Figure 8.10**. In the numerical fluid pressure curve p_{fluid}, it can be noted that the first peak represents the incident pressure p_i, while the second is the reflected pressure p_r. The numerical FSI nodal pressure is compared with the theoretical one obtained by Eq. 8.14, in which p_i is the numerical p_{fluid}, ρc are constants and v is the numerical velocity computed at the centre of the plate. From this comparison it can be seen that the numerical p_{FSI} peak is close to the theoretical one.

In fact, when $v = 0$, in the air backed theory the peak FSI pressure is:

$$p_{FSI} = 2p_i \tag{8.15}$$

In this numerical calculation, it results that $p_{FSI} = 1.85 p_{fluid}$.

Therefore, the calculation obtained by this refined mesh gives as a result a p_{FSI} value that approaches the theoretical one ($p_{FSI} = 2p_i$).

However, in the air backed plate theory it results that the maximum velocity of the plate v_{max} occurs when $p_{FSI} = 0$. This condition is not verified, because the theory refers to an infinite plate (with negligible stiffness) while the calculation is performed considering a plate of finite dimension (1x1 meters). See **Figure 8.11** and **Figure 8.12**. To approach this condition a larger refined model must be built.

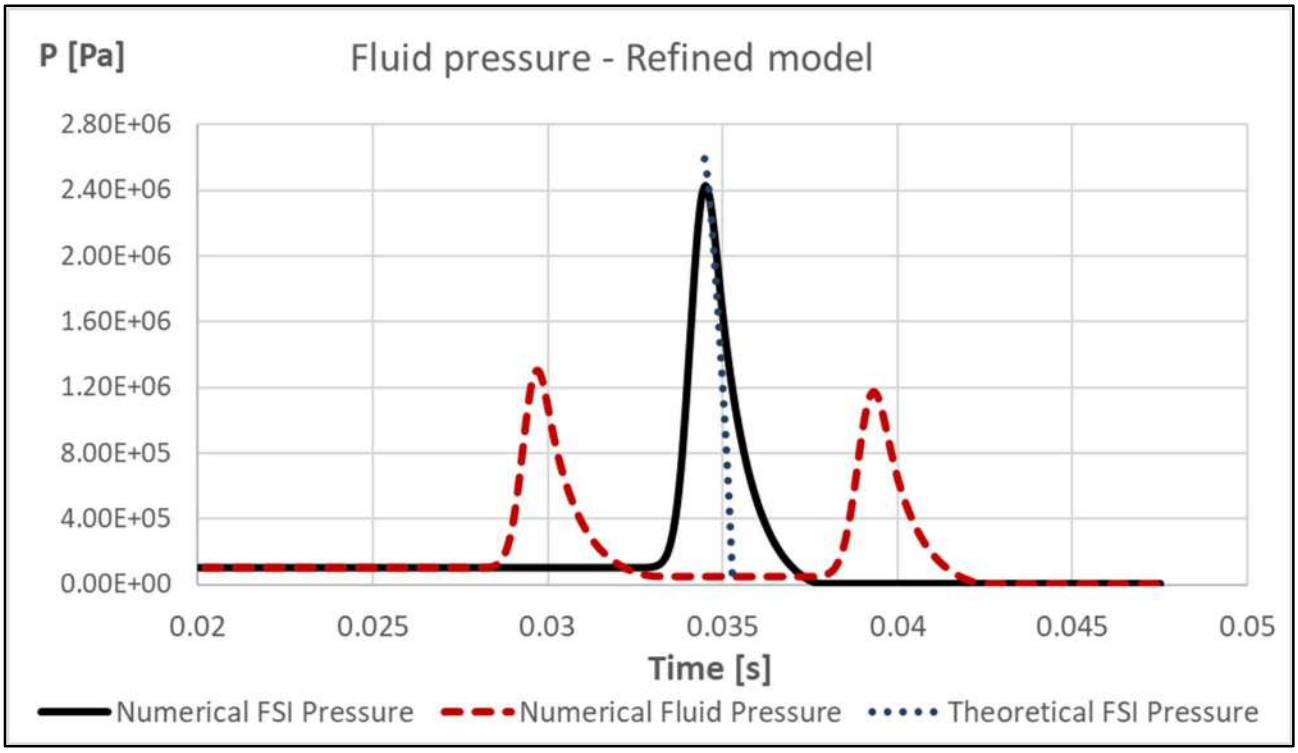

Figure 8.9 Comparison of fluid pressure time histories – Refined model

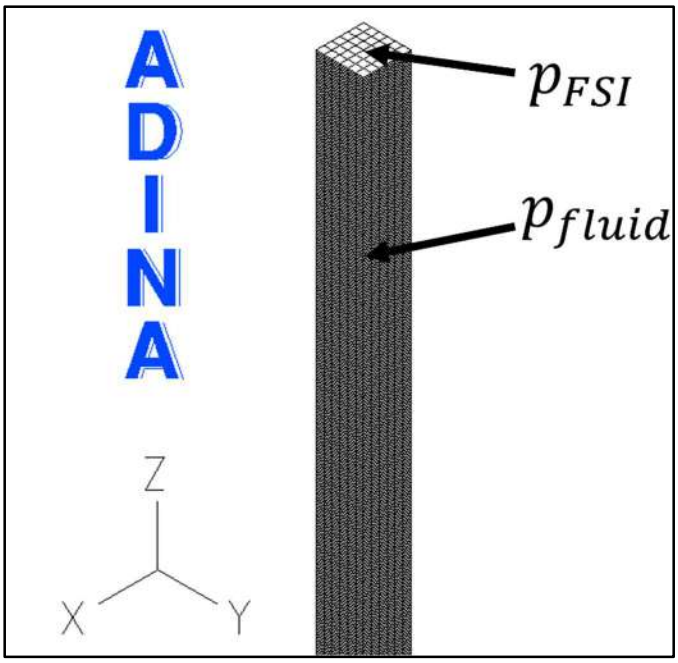

Figure 8.10 Position of numerical FSI and incident nodal pressures

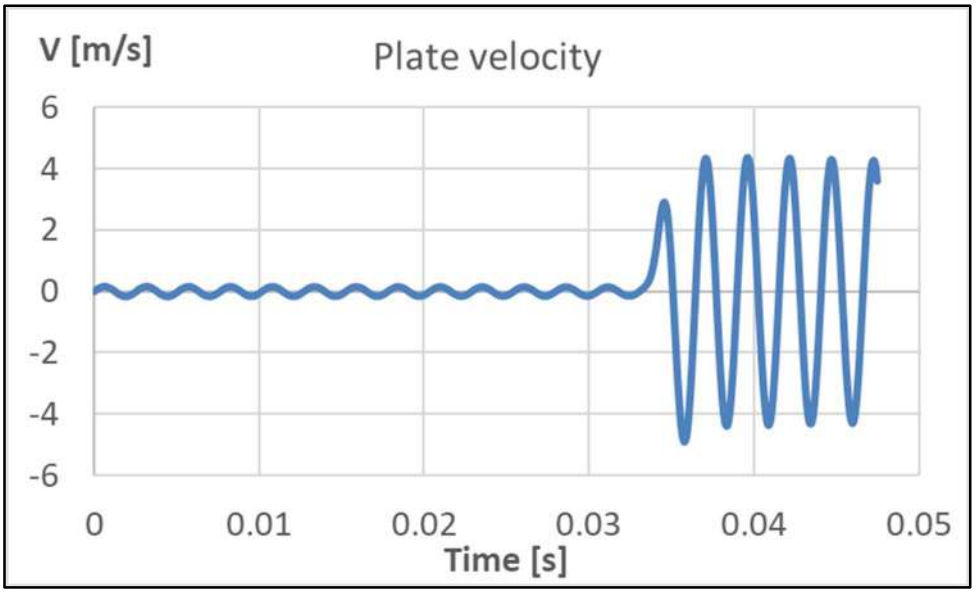

Figure 8.11 Plate Z-Velocity – Refined model

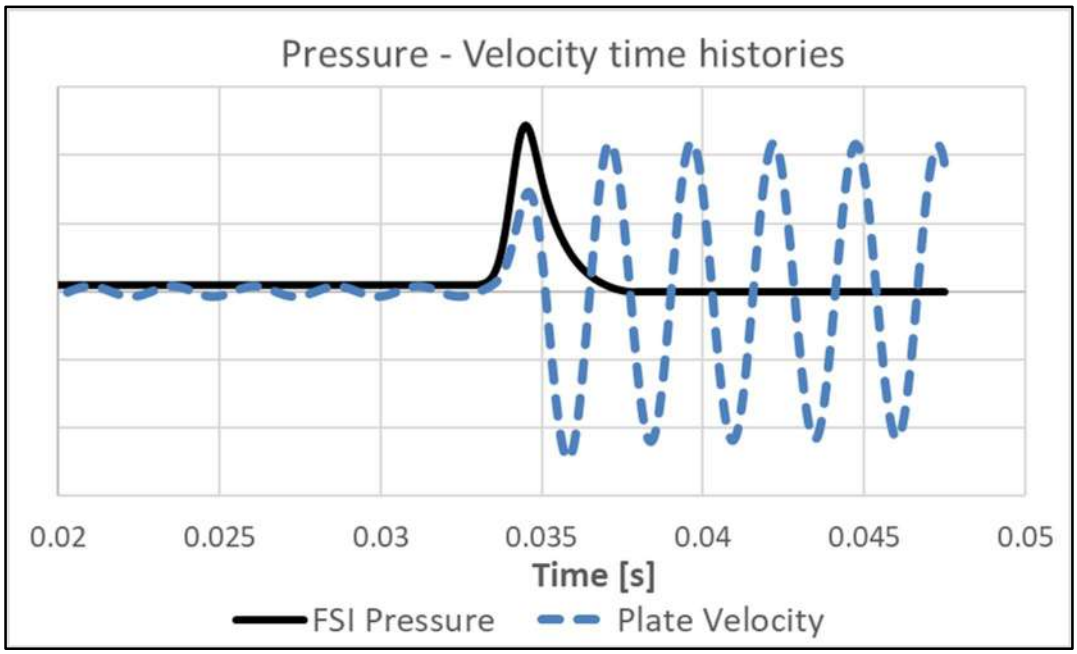

Figure 8.12 Plate Velocity and FSI pressure time histories comparison (Y axis not in scale)

8.2.1.1.3 Large and refined model

A larger model (3x3 m) is necessary to verify the theorical condition, valid for an infinite plate, according to which the maximum velocity of the plate occurs when the FSI pressure is zero. And a larger value of peak pressure has been applied to the model to increase the energy transmitted. Calculations are performed using both Euler and Composite methods and results are compared.

In this case, using the Euler method, FSI conditions are verified, as it results that $p_{FSI} = 1.85p_{fluid}$, a result that approaches the theoretical one ($p_{FSI} = 2p_i$) (see **Figure 8.13**). In addition, the maximum velocity of the plate v_{max} occurs close to the condition in which $p_{FSI} = 0$, according to the infinite plate theory, as shown in **Figure 8.14**.

After this point, when $p_{FSI} = 0$, only elastic forces act on the plate, causing the deformation.

The use of the "ADINA composite" method provide more accuracy in the determination of the peak of pressure. In **Figure 8.15** it is shown that the peak of pressure calculated using the second order composite method is sharper than that obtained using the Euler one, according to the theoretical peaks. In addition, $p_{FSI} = 1.95p_{fluid}$, which is very close to the theoretical condition ($p_{FSI} = 2p_i$). Also, maximum velocity of the plate occurs when the FSI pressure decreases to the vapor pressure, according to the infinite Taylor air-backed plate theory (see **Figure 8.16**).

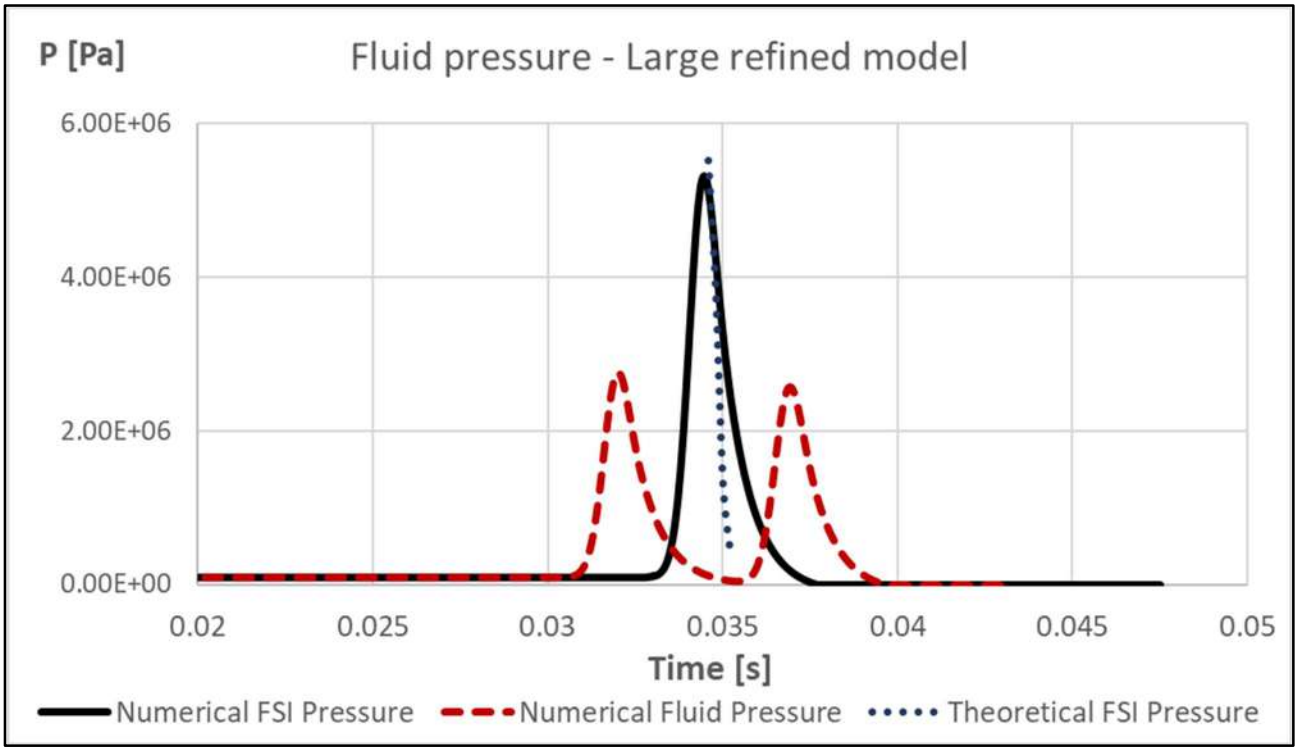

Figure 8.13 Comparison of fluid pressure time histories calculated using Euler Method – Large refined model

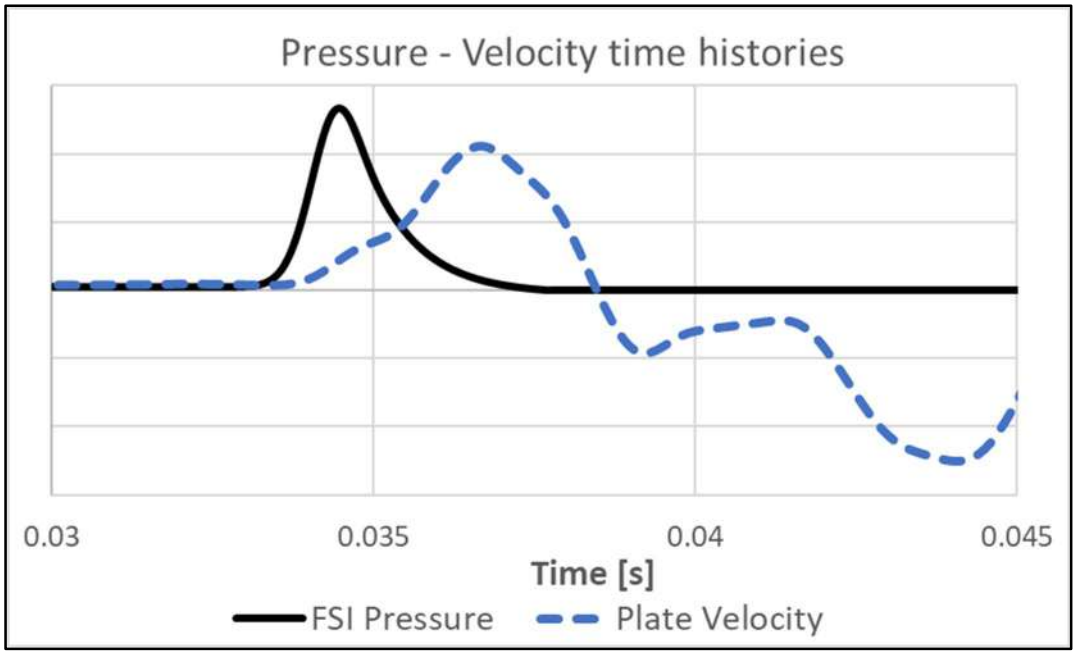

Figure 8.14 Plate Velocity and FSI pressure time histories comparison calculated using Euler method (Y axis not in scale)

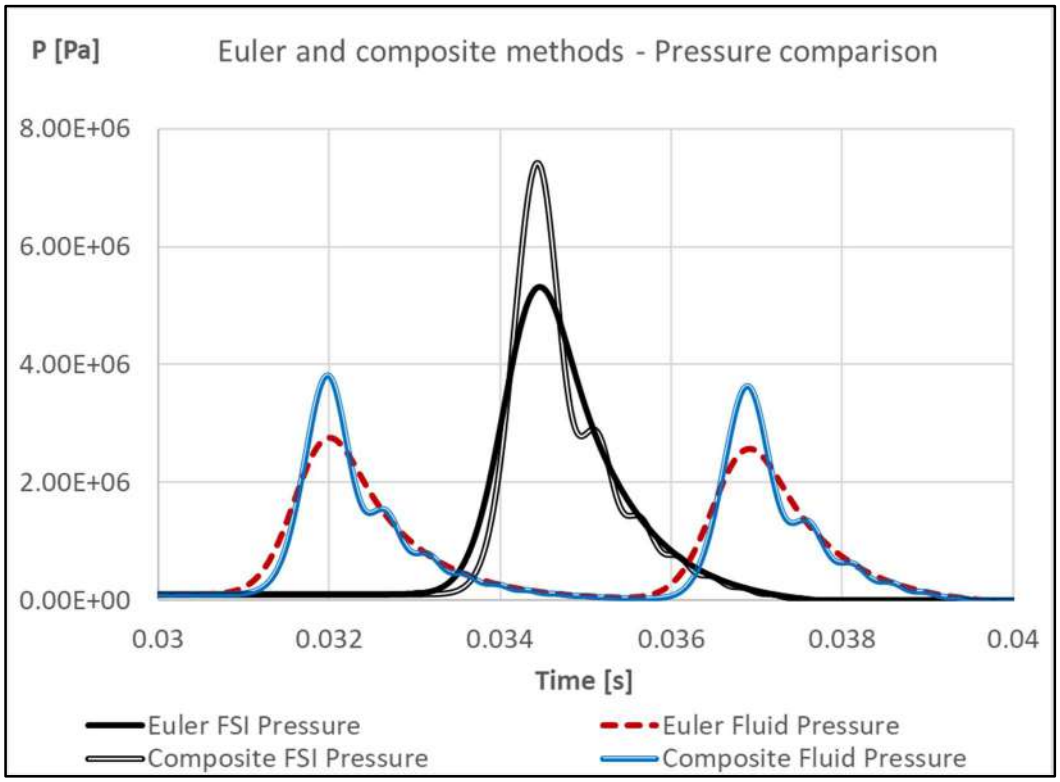

Figure 8.15 Euler and ADINA composite methods comparison of fluid and FSI pressure time histories

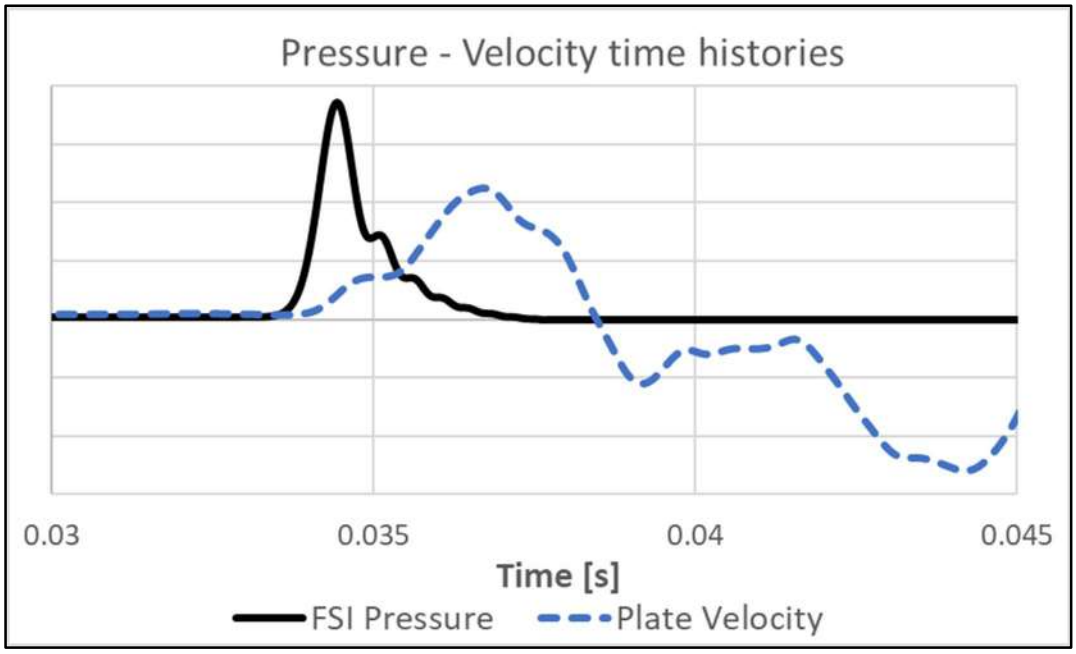

Figure 8.16 Plate Velocity and FSI pressure time histories comparison calculated using "ADINA composite" method (Y axis not in scale)

8.2.2 Experimental validation

The results obtained by using the VOF method have been compared to the experimental data shown by Ramajeyathilagama and Vendhan in [8.21]. In their tests, a mild steel rectangular panel, characterized by an exposed area of 0.30 x 0.25 m and by a thickness of 0.002 m, and set in air-backed condition, is subjected to a series of underwater explosions, increasing progressively the weight of the charges, placed at a fixed distance of 0.15 m.

Mechanical features of the plate, reported in [8.21], are included in the FE simulation. The strain rate dependence is considered applying the Johnson-Cook model for the determination of the dynamic stress-strain curve, using coefficients suggested by Vedantam et al. in [8.26].

The parallelepiped of fluid is meshed using 8-nodes volumetric elements of small size (0.007 x 0.008 x 0.006 m in the X, Y and Z direction), while the finite element model of the panel is built using no. 750 4-nodes rectangular elements. The shock pressure is applied on the bottom of the model, while the wall boundaries conditions are set on the lateral surfaces.

This is a case of near-field underwater explosion. Therefore, the bubble pulse effect should be considered as well. Therefore, the input pressure is set in which both the shock wave pressure, calculated according to the formula proposed by Cole [8.5] and used coefficients reported by Keil [8.15], and the bubble pulse pressure are included. The latter peak of pressure and the oscillation period are calculated from the formulas of Taylor [8.27] and Cole [8.5], while the impulse shape is

obtained from the graphs of Bryant and Chambers [8.4]. Details of these formulations are reported in Chapter 2.

The choice of using a particularly refined mesh allows to fully simulate the cavitation phenomenon, meaning that the water becomes vapor when FSI pressure below the panel reaches the vapor pressure. In the numerical representation, this is shown by the VOF Species number which has values less than 1. See **Figure 8.17**. In **Figure 8.18** the VOF Species time history of a node of the centre of the panel is shown in which also the cavitation closure phenomenon can be noted. In fact, the VOF Species value at first decreases and then increases to 1 in the presence of the atmospheric pressure which is set constant in the model. This phenomenon can be noted in **Figure 8.19**, where the FSI pressure below the panel is shown. The peak of pressure of the shock wave is followed by the other peaks caused by the cavitation closure.

The experimental and numerical comparison of the panel deformation for each test is shown in **Figure 8.20**. A more refined mesh for the panel (no. 15000 4-nodes rectangular elements) is adopted in the case of Test no. 8 to capture the shear failure mode, reducing numerical instability. In **Table 8.4** the numerical results in terms of permanent deformation and area of the hole are compared with the ones obtained by Zong et al. in [8.28], in which the fluid was modelled using the acoustic approximation. As reported previously, this is a case of close-in explosion, in which gases are in contact with the structure. This contribution is not modelled by the VOF method. Despite this approximation, it can be noted a very good agreement of the experimental and numerical results, especially if compared with those obtained by using the acoustic approximation where cavitation phenomenon is neglected.

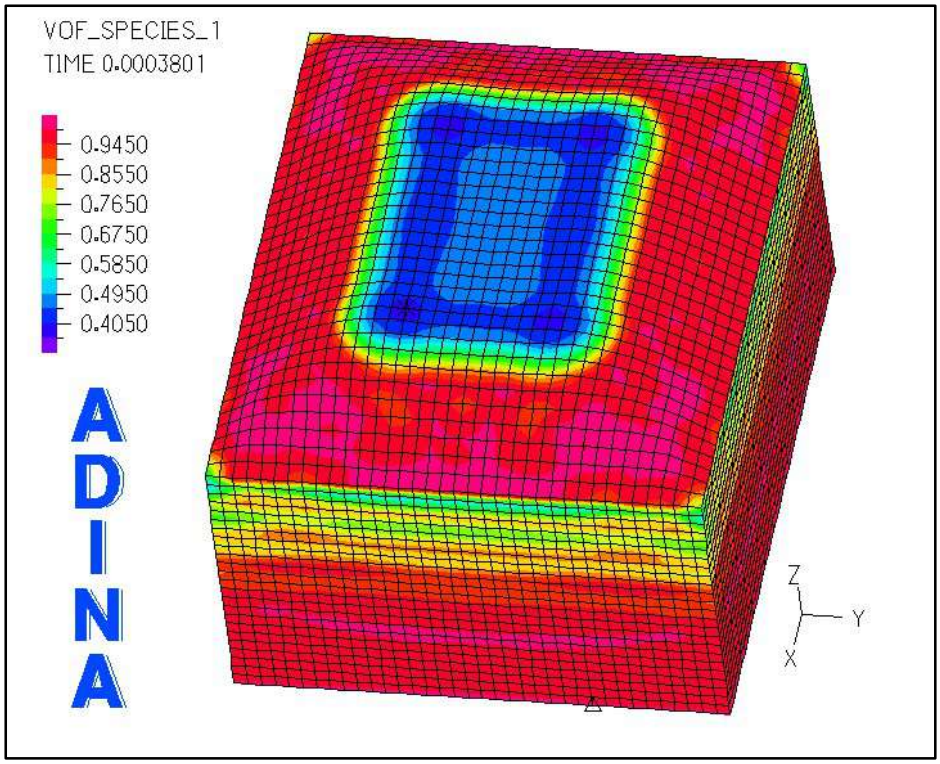

Figure 8.17 Cavitation distribution at a particular time step below the panel in the parallelepiped of fluid representation - Test no. 6 results

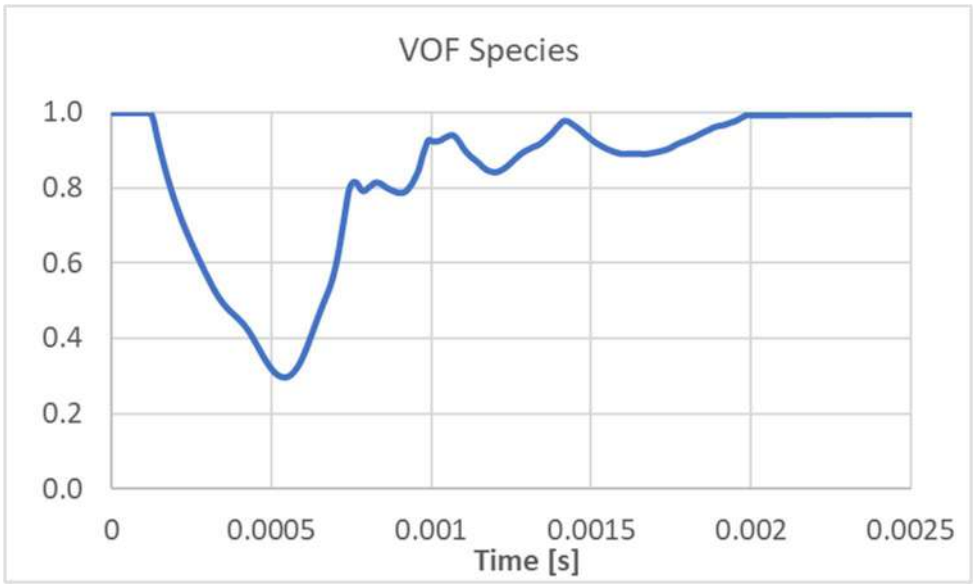

Figure 8.18 VOF Species time history of the central node of the fluid below the panel - Test no. 6 results

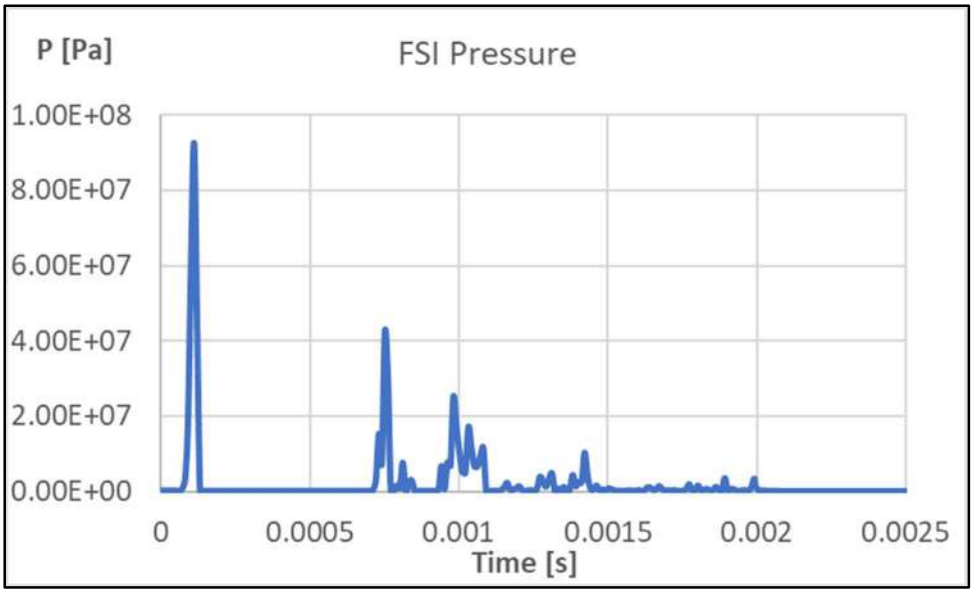

Figure 8.19 FSI pressure below of the panel - Test no. 6 results

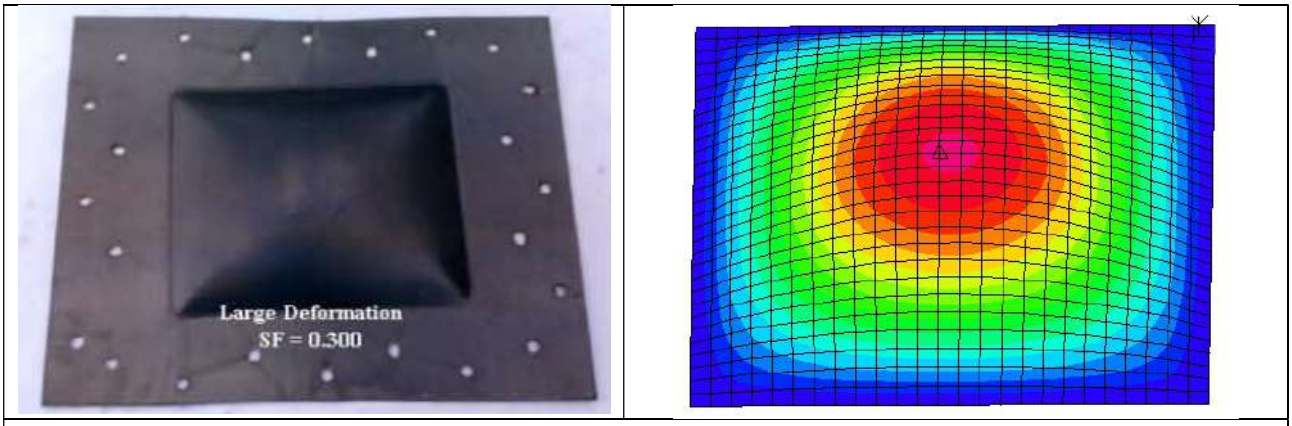

Test no. 1

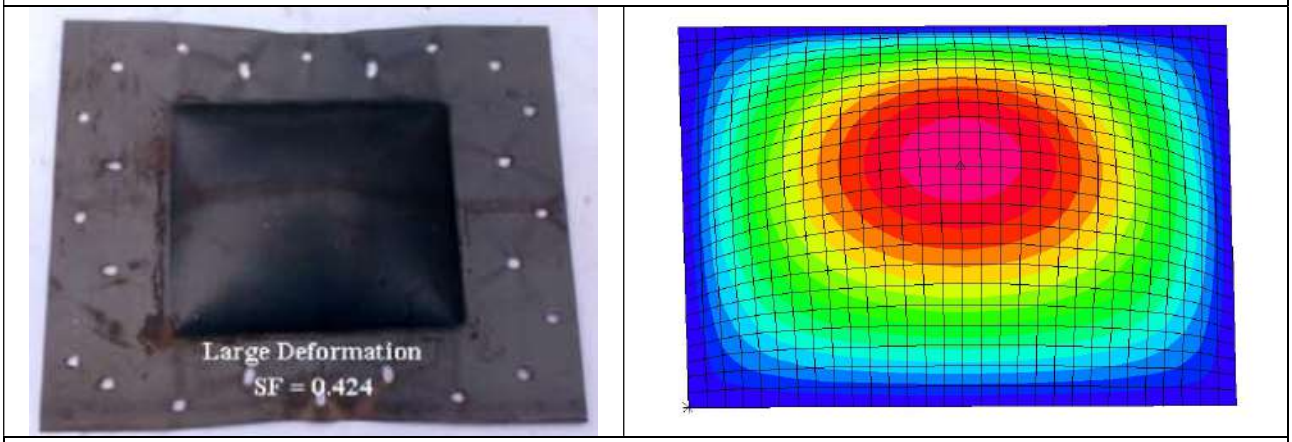

Test no. 2

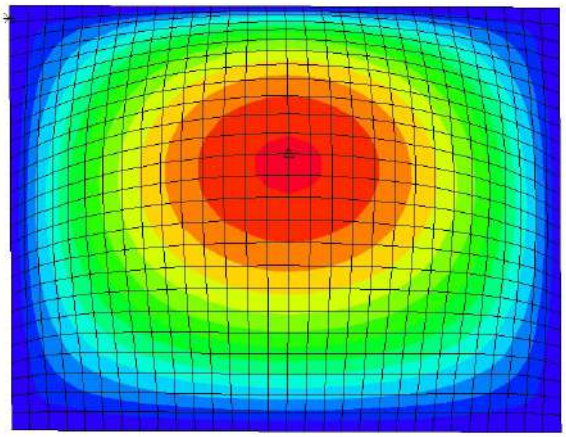

Test no. 4

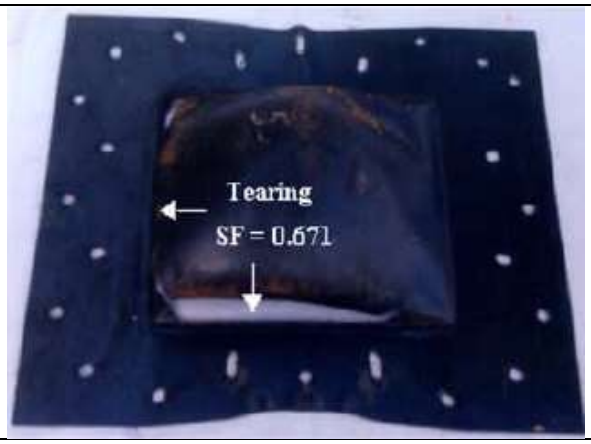

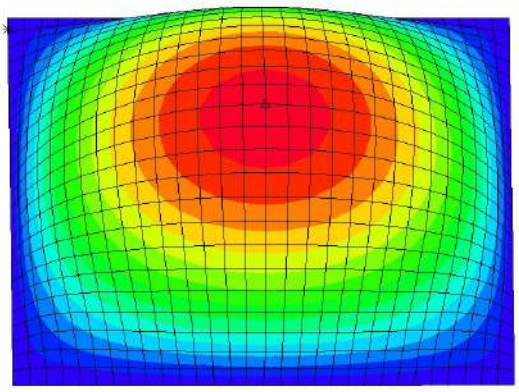

Test no. 5

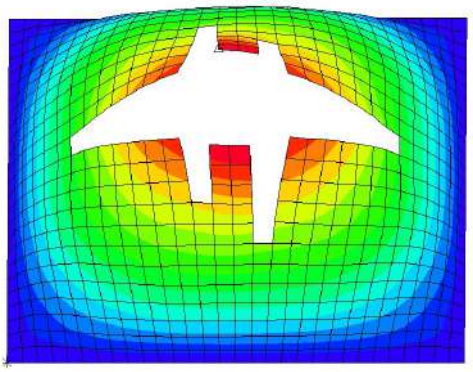

Test no. 6

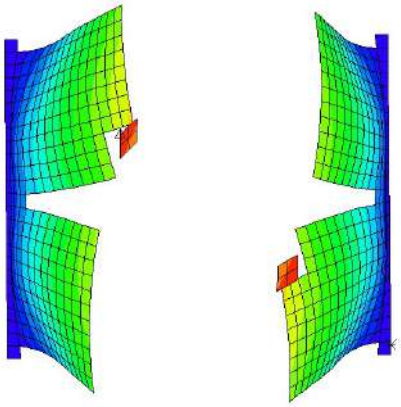

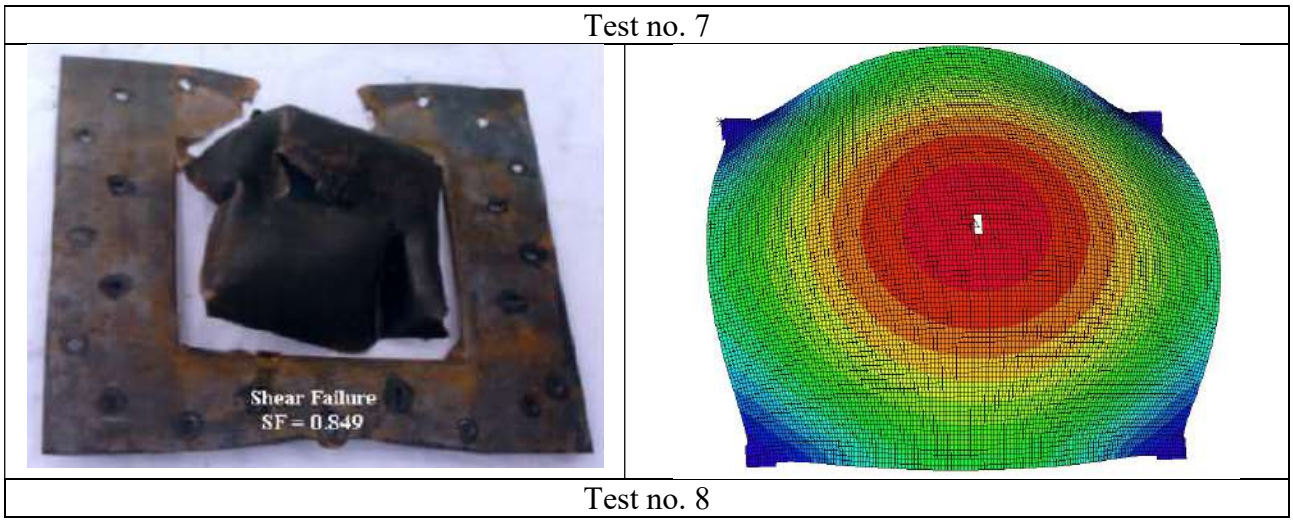

Figure 8.20 Experimental and numerical comparison of panel deformations

Table 8.4 Numerical permanent deformation (D), area of the hole (A) and relative errors obtained from the VOF method and the acoustic method used in [8.28]

Case No.	Charge weight [kg]	Experimental results D[m]/A[m^2]	Acoustic results [8.28] D[m]/A[m^2]	VOF results D[m]/A[m^2]	Acoustic errors [8.28] [%]	VOF errors [%]
1	0.01	0.0400	0.0307	0.0421	23.25	5.25
2	0.02	0.0578	0.0470	0.0581	18.69	0.52
3	0.03	0.0677	0.0602	0.0692	11.08	2.22
4	0.04	0.0864	0.0721	0.0789	16.55	8.68
5	0.05	0.1078	0.0872	0.1086	19.11	0.74
6	0.06	0.0120	0.00964	0.0114	21.11	5.00
7	0.07	0.0520	0.0478	0.0600	8.13	15.38
8	0.08	0.0750	0.0513	0.0750	31.67	0.00

8.2.3 Benchmark considerations

So far, the VOF method results in a suitable simulation of the shock phenomenon caused by underwater explosion, showing that the shock wave behaviour and the fluid structure interaction are predicted according to theoretical results. Also, forces produced by the fluid are fully transmitted to the structures, resulting in a good FSI simulation. The use of a more refined mesh or of a composite integration method, instead of the Euler one, can provide more accurate results, verifying classical air-backed plate theory. In addition, the effectiveness of this method is also verified from the comparison with the experimental results measured on the steel panel in [8.21]. The cavitation is simulated in term of cut-off pressure, meaning that after the impact FSI pressure cannot drop below the vapor pressure, if coarse meshed are used. A more refined mesh, as the one used in the

experimental comparison, allow the simulation of the vapor effects, including cavitation closure, in the numerical representation.

8.3 Full-scale test comparison

8.3.1 Test description

The full-scale shock test used as validation reference is that realized on board of a typical composite minesweeper vessel by MARIPERMAN [8.18] in late eighties. A trinitrotoluene (TNT) charge of 130 kg of weight (W) is suspended by a buoy at a depth of 29 m in a 30 m deep seabed. The shock test geometry is reported in **Figure 8.21**. The charge is set on the starboard side of the ship, perpendicular to the centre in longitudinal coordinates of the ship reference system. The distance between the charge and the keel line is R_1=103.6 m, while its distance to the closest point of the ship is R_2=100 m. The angle between the seabed and the theoretical line that connects the charge with the keel is of 15.2°. The ship draught is 2.8 m, while the beam at waterline is 9.1 m.

For this configuration, it is possible to assess the attack severity using classical indexes called Shock Factors, whose meanings are well explained by Keil [8.15].

In particular, the formula used for the Shock Factor, in which the minimum distance of the charge is considered (R_2), is:

$$SF = \frac{\sqrt{A \cdot W}}{R_2} \tag{8.16}$$

It is also useful to define a parameter that considers the distance of the charge from the keel line (R_1) and the angle of incidence of the shock wave (φ in **Figure 8.21**). In this case the formula becomes:

$$KSF = \frac{\sqrt{A \cdot W}}{R_1} \cdot \frac{1 + \cos(\varphi)}{2} \tag{8.17}$$

The A value in Eq. 8.16 and 8.17 is used to include the fact that the explosion happens in proximity of the seabed. In this case, considering that there is a sandy ground in this scenario, the A value is set to a value close to 1.5 according to experimental values found by Petralia [3.10].

As a result, the shock factor values calculated for this geometry of explosion are approximately $SF \cong 0.14$ and $KSF \cong 0.08$.

Two pressure sensors (reported as S1 and S2 in **Figure 8.21**) are set to measure the shock wave pressure close to the ship, respectively at about 15 m and 5 m of distance from the keel line. They are piezoresistive transducers type ENDEVCO 8511A, full-scale value of 35 MPa, suspended to buoys at the desired depth. Their sampling frequency is set to 40 kHz.

The signal measured by S2 sensor is reported in **Figure 8.22**, showing the comparison with the pressure calculated analytically. Classical formulas proposed by Cole [8.5], are used to determine the peak pressure P_{max} and the angle of shock pressure decay θ in time history (Eq. 8.18 – 8.19).

$$P_{max} = K\left(\frac{W^{1/3}}{R}\right)^{\alpha} \tag{8.18}$$

$$\theta = KW^{1/3}\left(\frac{W^{1/3}}{R}\right)^{\alpha} \tag{8.19}$$

In these formulas coefficients K and α are set considering those proposed by Keil [8.15] for TNT: in **Table 8.5** coefficients for each equation are shown. SI measurement system is used, therefore P_{max} is in megapascal (MPa), W in kilogram (kg), R in meter (m), and θ in millisecond (ms). The pressure in the time domain is given by the following equation provided by Cole [8.5], that is considered valid when time t is less than θ value:

$$P(t) = P_{max}e^{-\frac{t}{\theta}} \tag{8.20}$$

Monoaxial strain gauges type KYOWA KFW-5-C1-11-L100 are used to measure the structural response. In particular, three of them are set on the panel of the hull between the bottom keel and the bilge keel, in the midsection, on the right side, in correspondence of the direction of the explosion. They are applied at the centre of the midsection of the compartment, which is 6 metres long, at equal distance from the transversal bulkheads, therefore at 3 meters in longitudinal direction from both. They are oriented in the transversal direction of the hull in order to measure the local structural response of the considered panel. Gauge no. 1 is placed in way of the bottom keel, no. 2 in the centre of the panel and no. 3 close to the bilge keel (see **Figure 8.23**).

Some pictures of the TNT charge and the detonation are reported in **Figure 8.24** and **Figure 8.25**.

Table 8.5 Coefficients in peak pressure and angle decay formulas

Equation	$\boldsymbol{K}$	$\boldsymbol{\alpha}$
P_{max}	52.4	1.13
θ	92.5	-0.22

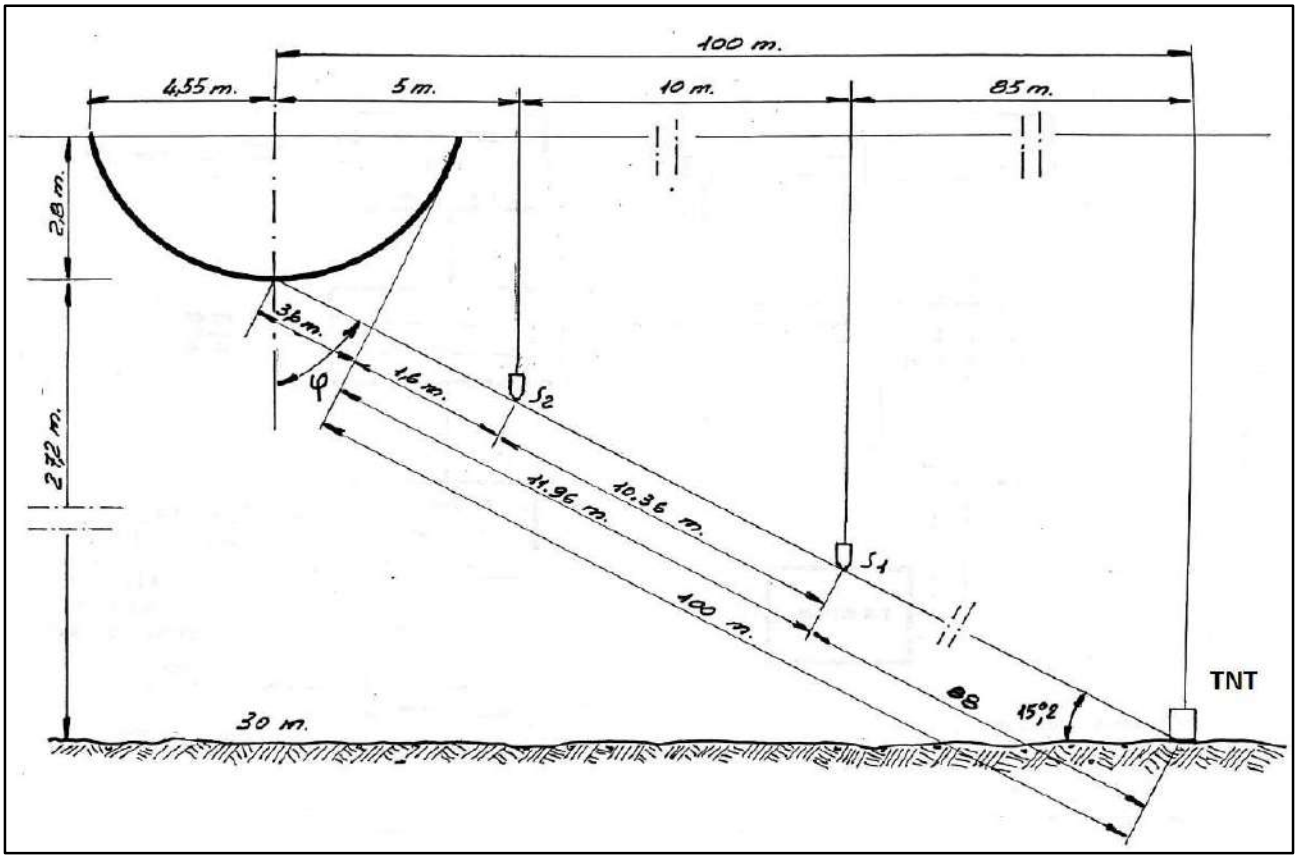

Figure 8.21 Shock test geometry

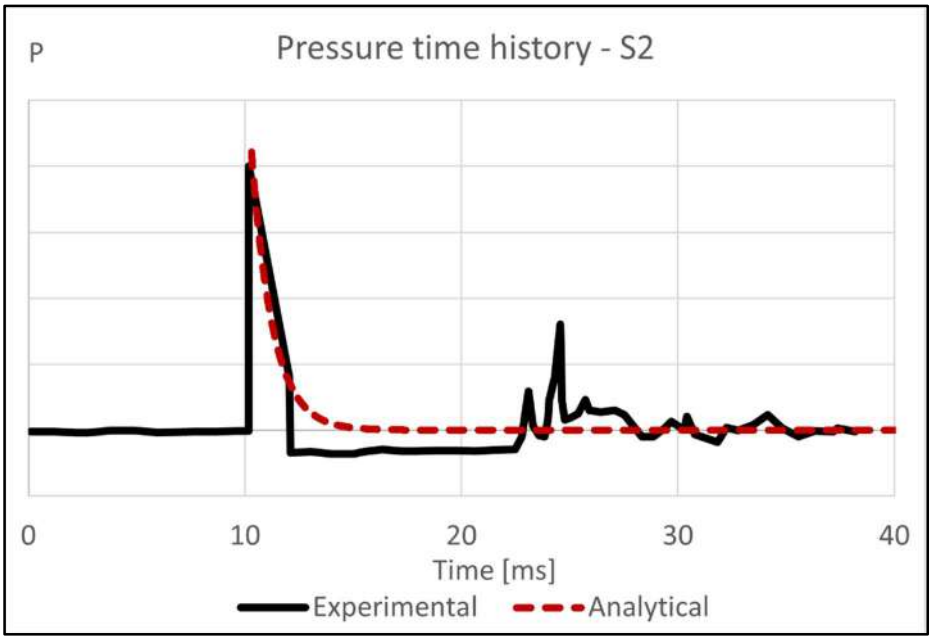

Figure 8.22 Experimental and analytical time history measured by S2 sensor

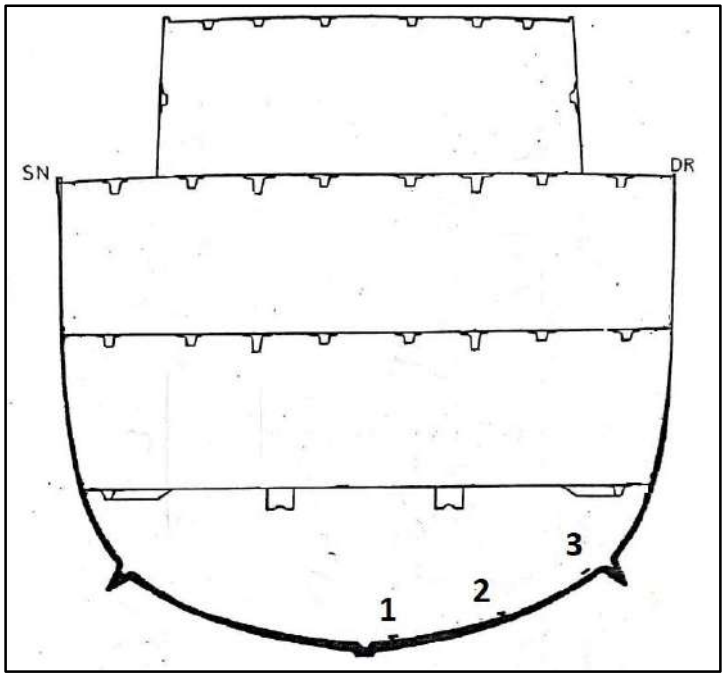

Figure 8.23 Monoaxial strain gauges setup in midship section – frontal view

Figure 8.24 130 kg TNT charge (image taken from [8.18])

Figure 8.25 Underwater shock test explosion (image taken from [8.18])

8.3.2 Structural modelling

A typical minehunter ship parallel body block is modelled in the FE environment, using two-dimensional multi-layered shell elements, having 4-nodes, 500 x 500 mm size and Mixed Interpolated Tensorial Components (MITC) formulation, already used to model composite behaviour of ship structures in [8.9] and [8.10], and further described in [8.7]. This size of mesh has been chosen according to rules for finite element analysis of ships [8.6] [8.11], in which a relatively coarse mesh can be used in a ship strength analysis when regular shapes are considered. In the numerical representation, shell plating, decks and longitudinal stiffeners are modelled duly considering their mechanical properties and shapes. In particular, Ω-shaped stiffeners are modelled using shell elements as well for webs and top-hat. About the structural properties of this minesweeper, a rather heavy single skin construction was employed, without stiffening frames on the hull shell. Therefore, no stiffeners are modelled in the software environment accordingly. Thicknesses of shell plates and stiffeners do vary from 10 to 220 mm, according to standard values for minehunter vessels, as reported in [8.12].

The considered ship block is 6 m long in longitudinal direction to represent the central compartment of the minesweeper. Simply supports are set at the free edges to approximate the transversal bulkheads constraints. In ADINA^{TM} environment their position is represented using letters “B”, “C”, “D”, “E”. In the description of these fixities, it can be noted that translations (U) are fixed, while

rotations (θ, α, β) are free (see **Figure 8.26**). In addition, calculations are performed using also full fixity at the free edges. No significant differences in the numerical results are obtained, compared to the previous case, therefore, results computed by the simply support modelling are shown in the following.

Orthotropic material properties are set in the FE calculation considering standards proposed by Smith [8.22] for naval vessels. E-glass polyester balanced woven-roving (WR) material is considered, whose properties are shown in **Table 8.6**.

Balanced biaxial properties are considered, therefore Young modulus value is set equal in longitudinal and transversal direction. To assess the missing transversal properties, the well-established Halpin-Tsai equations are used [8.13]. Therefore, orthotropic properties in longitudinal, transversal and normal direction can be assessed and set as input for the calculation. The complete material characterization is shown in **Table 8.7**. As it is reported by Greene in [8.12] "balanced" laminates should have a proportion of fibres in 0° and 90° directions. Hence, the laminate is reproduced using a stacking sequence of layers, whose orientation in 0°/90° direction can be easily set in ADINA^{TM} [8.1] using multi-layered shell elements [8.7].

Table 8.6 Composite material properties proposed by Smith [8.22]

Material	Fibre Volume Fraction V_f	Density [kg/m^3]	Young Modulus E [Gpa]	Poisson Modulus [ν]	Shear Modulus [Gpa]	Tensile Strength [MPa]	Comp. Strength [MPa]	Shear Strength [MPa]
E-glass polyester (balanced WR)	0.34	1700	15	0.2	3.5	250	210	100

Table 8.7 Orthotropic composite material properties used as input of the calculation

E_L [GPa]	E_T [GPa]	E_N [GPa]	G_{LT} [GPa]	G_{LN} [GPa]	G_{TN} [GPa]	ν_{LT} [-]	ν_{LN} [-]	ν_{TN} [-]
15	15	10	4.5	3.6	3.6	0.2	0.4	0.4

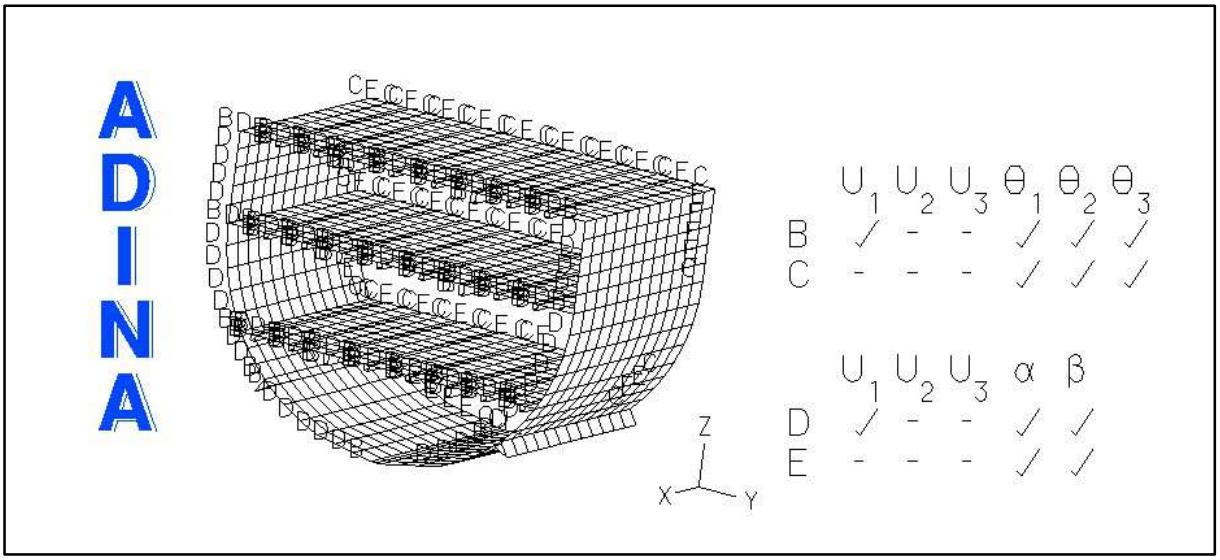

Figure 8.26 Midship section in finite element environment

8.3.3 Approximate FE and Full FSI approaches: fluid modelling

A corresponding slice of sea water, having the same longitudinal length of the minesweeper section, is modelled starting from the position of S2 pressor sensor in **Figure 8.21**. Transversally, it is extended to about 30 m on the left side of the ship, to avoid reflection of the shock wave from boundaries, when it passes over the ship (see **Figure 8.27**). The shock pressure is applied in the same position (S2) of the measurement signal on a spherical surface where the shock front is supposed to be distributed when it moves from the charge. In addition, atmospheric pressure is set on the free surfaces of the fluid, and hydrostatic pressure is placed on the outlet surface on the slice of modelled sea portion.

Using the approximate FE approach, the fluid around the ship slice is modelled using 3-D potential-based fluid elements, available in the structural part of the FE software. Eight nodes volumetric elements, characterized by a 500 x 500 x 500 mm mesh size are chosen.

Boundary conditions are simulated on the surfaces of the fluid domain using interface elements. When fluid surfaces are in contact with shell structural elements, fluid-structural interface elements are built by the software. Each node contains both, potential degree of freedom and displacement degrees of freedom. To obtain this result, fluid mesh must be compatible with the structural one. Namely, related nodes are set coincident. In the simulation environment, this happens along the minesweeper hull, in the submerged part. Mesh resulting in fluid and structure, and node positioning are shown in the YZ planar view of **Figure 8.28**.

Potential interfaces type inlet-outlet are placed on surfaces where shock and hydrostatic inputs of pressure are set respectively, assuming that the displacements of the boundary are not significant for

the calculation. In addition, a free-surface boundary condition is considered on surfaces where atmospheric pressure is applied. In this case, the free surfaces show some displacements when the shock pressure moves. Rigid-wall boundary conditions are automatically imposed by the software on the other surfaces where no other boundary conditions are placed and where no structural interface elements are set. A slip condition of the fluid is assumed, without any tangential flow constriction. No potential interface elements are set on these walls.

A non-linear dynamic analysis is performed applying the implicit Bathe method time-integration [8.1] [8.2], using a time step of 10^{-4} seconds, shown to be valid to assess the shock response of structures in [8.16] [8.17].

In the full FSI model, the geometry of the problem and the choice of the mesh remain the same of the previous approximate FE model, but the Runge-Kutta second order type, "ADINA composite scheme", is used for the transient analysis. Pressure loads are set as normal tractions in the same positions as those employed in finite element method shown in **Figure 8.27**. Also, free surfaces are set, where atmospheric pressure is imposed. Wall-boundaries are used on the other surfaces, in which a slip condition of the fluid is applied. This implies that the normal component of the velocity vector of the flow is prescribed to be zero, while the tangential components is left free.

Eight nodes 3-D ADINA-F fluid elements of 500x500x500 mm mesh size are used, defining a laminar fluid, in which sea water properties are set.

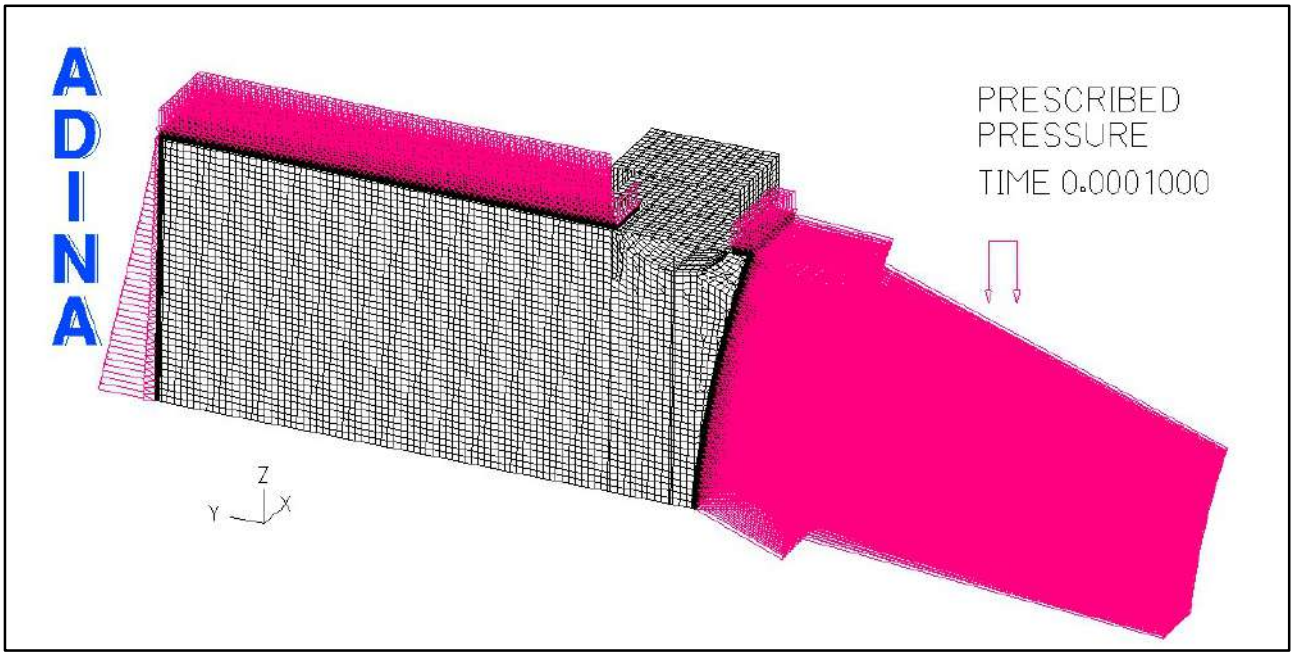

Figure 8.27 Complete fluid-structure model with prescribed pressures

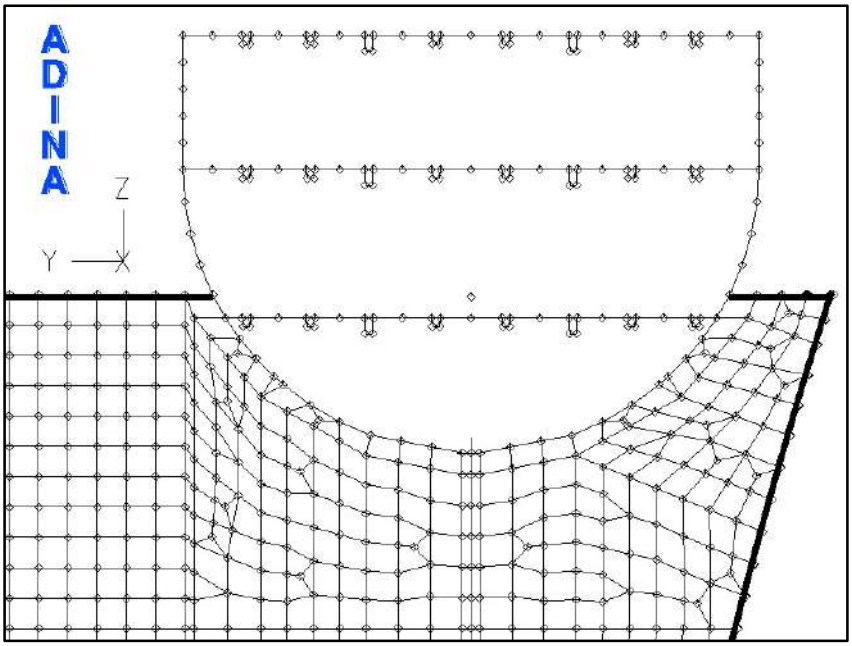

Figure 8.28 Fluid and structural mesh in YZ plane view

8.3.4 Approximate FE and Full FSI approaches: results and comparison

The pressure of the shock wave is moving from the initial surface, where the input loading condition is set, to the section of ship. It affects the ship, deviating its trajectory, until it reaches the free surface where hydrostatic pressure is imposed. Using this setting, problems of wave reflection caused by the opposite wall are avoided. In **Figure 8.29** and **Figure 8.30** the pressure trend along the fluid in the approximate FE and in the CFD environment of the full FSI approach at a significant time step is shown. It can be noted that in structural FE elements the positive peak of pressure is preceded by a negative one of reduced magnitude. A different behaviour is seen in full FSI calculation, where only the positive peak pressure is shown, when the shock wave is moving in the fluid.

In both cases, instead, as expected, this positive pressure is followed by a negative pressure. It depends on the fact that cavitation phenomenon is not modelled. This phenomenon is evident in the time histories comparison of the pressure on the fluid elements below the centre of the panel and close to the wall constraint (respectively position A and B in **Figure 8.31**). It can also be noted that background noise is higher in the approximate FE calculation than in the full FSI one. However, energy of the positive pressure peak of the full FSI calculation is similar to that of the approximate FE method, considering that in this last case a higher positive pressure is preceded by a negative one. In fact, the energetic contribution of these positive and negative peak pressure in approximate FE calculation is close to the positive one obtained by CFD results in full FSI method. In addition, it is

shown that peak pressure is reduced from the wall (position "B") to the centre of the panel (position "A"), caused by the deformation of the structure itself. See **Figure 8.32** and **Figure 8.33**.

A sensitivity analysis has been performed on the approximate FE model to verify if the background noise can be numerically reduced in the pressure signal. However, reducing the mesh size to 50 x 50 x 50 mm and the time step to 10^{-5} seconds does not improve significantly the obtained signal. Same considerations can be done, if the order of integration is increased, passing from eight-nodes to twentyseven-nodes volumetric elements for the fluid. No significant differences in results are shown. In any case, the global effects on structures are less influenced by this phenomenon, as it can be seen in the strain comparison, described in the following.

An example of strain calculation in transversal direction is shown in **Figure 8.34**, where the elements corresponding to the actual position of the strain gauges in the experimental test are highlighted. From **Figure 8.35** to **Figure 8.37**, the complete comparison in the time domain of the experimental and the numerical results obtained by approximate FE model and the full FSI model is reported. It can be noted that the numerical response is slower than the experimental one. In fact, the numerical pressure peak appears after the experimental one, and the decay is slower. It depends by the fact that in real phenomenon cavitation occurs, causing the faster response of the structure. In the numerical models, instead, no water evaporation is represented, slowing down the response of the structure. In addition, in the numerical results the maximum strain values are obtained at the centre of the panel, that is acceptable, considering that the hull keels, and the bilge keels works as constraints for the plating. This behaviour is not shown in the real data, where it seems that all the panel behaves in the same way, as if the whole hull is responding as a single shell. This global behaviour is not represented in the numerical results, where only a block of the hull is modelled. Despite these considerations, the average percentage errors of numerical results referring to experimental data is satisfactory (see **Table 8.8**).

Calculations performed using both the full FSI model and the approximate FE one provide similar results, showing differences lower than 2% in the maximum strain calculation, as reported in **Table 8.8**. In addition, the transversal strains follow the same trend. As it happens in the pressure comparison, the signal of the approximate FE model strain has a higher noise than the full FSI one. However, this phenomenon is negligible in preliminary design phases, considering that both methods provide very close results.

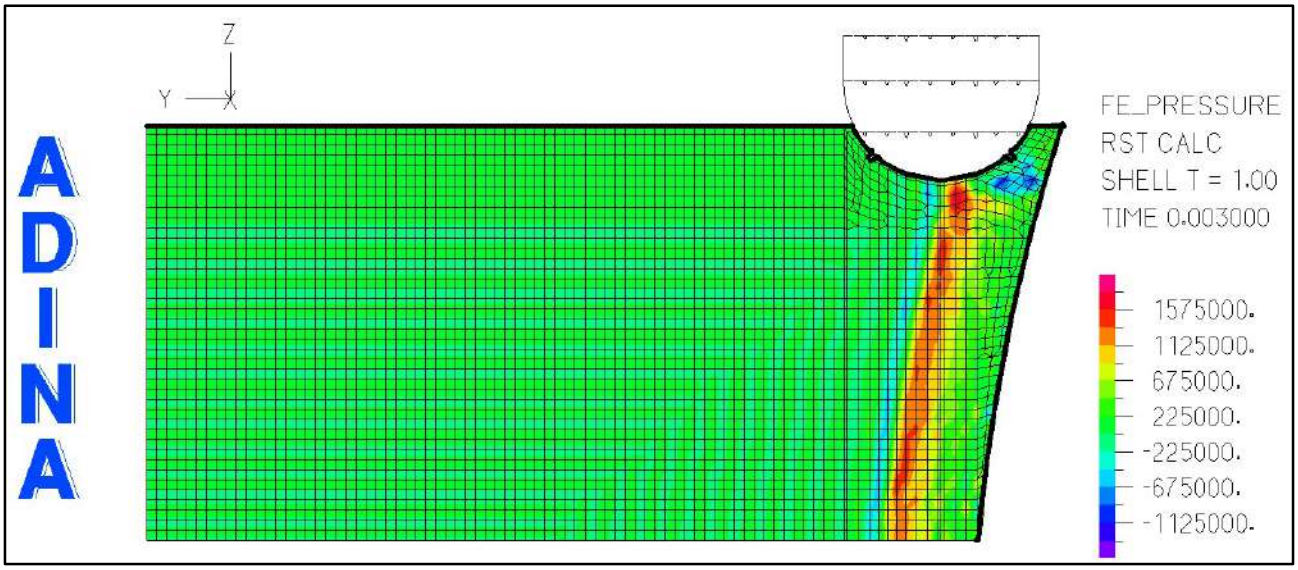

Figure 8.29 Shock wave pressure in approximate FE environment at time step 3 ms

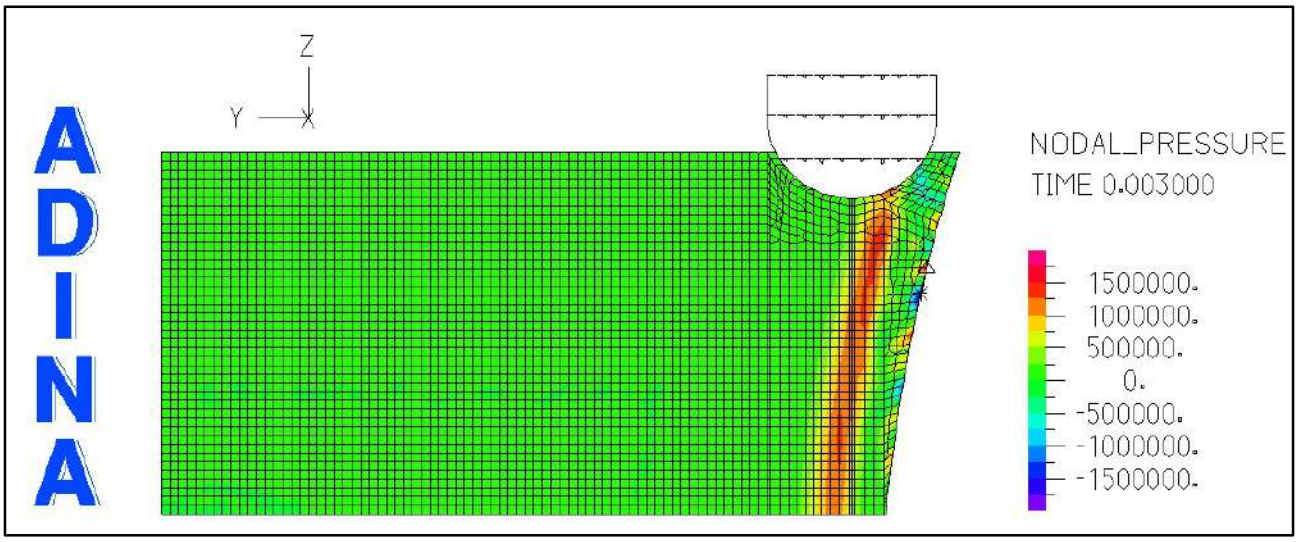

Figure 8.30 Shock wave pressure in CFD environment of the full FSI approach at time step 3 ms

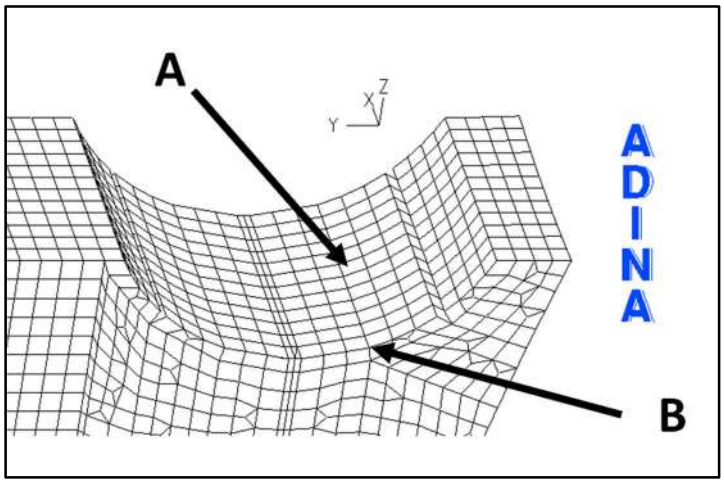

Figure 8.31 Pressure time histories elements in position "A" and "B" for comparison

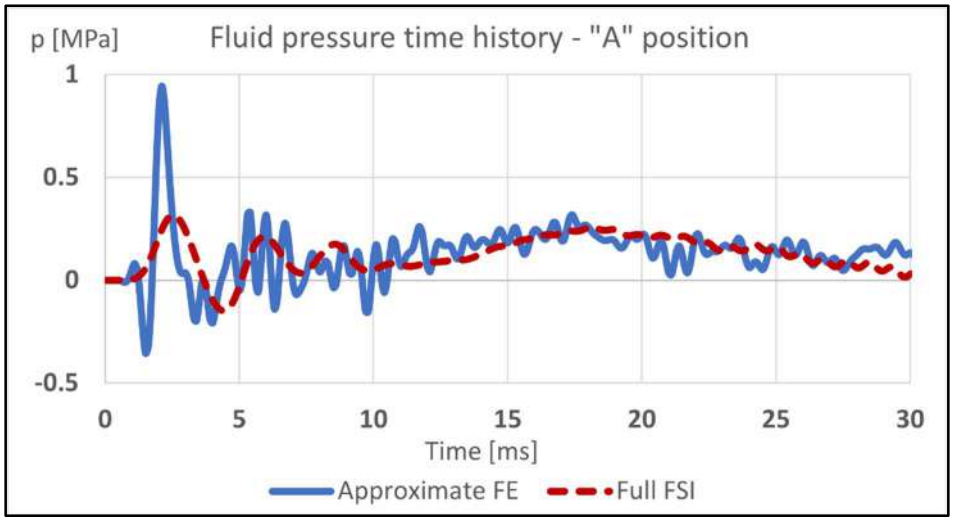

Figure 8.32 Approximate FE and full FSI fluid pressure time history comparison in the fluid element at the centre of the panel – "A" position

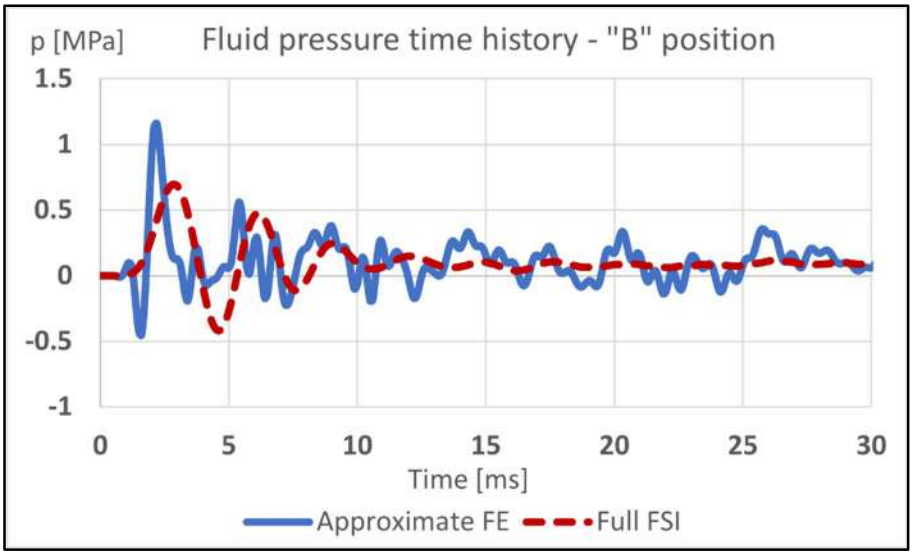

Figure 8.33 Approximate FE and full FSI fluid pressure time history comparison in the fluid element close to the wall constraint – "B" position

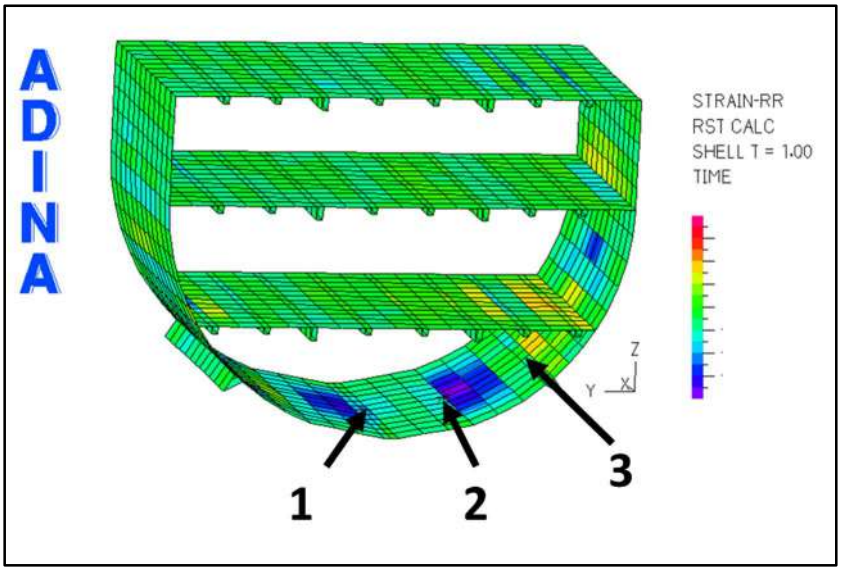

Figure 8.34 Example of transversal strain calculation – Elements corresponding to strain gauges setup

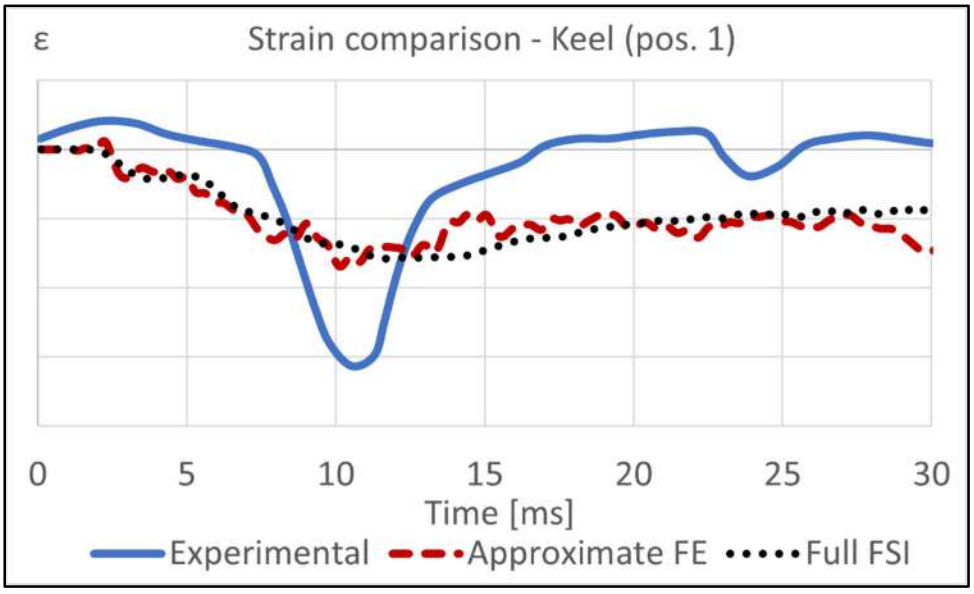

Figure 8.35 Numerical and experimental transversal strain comparison – Strain gauge 1

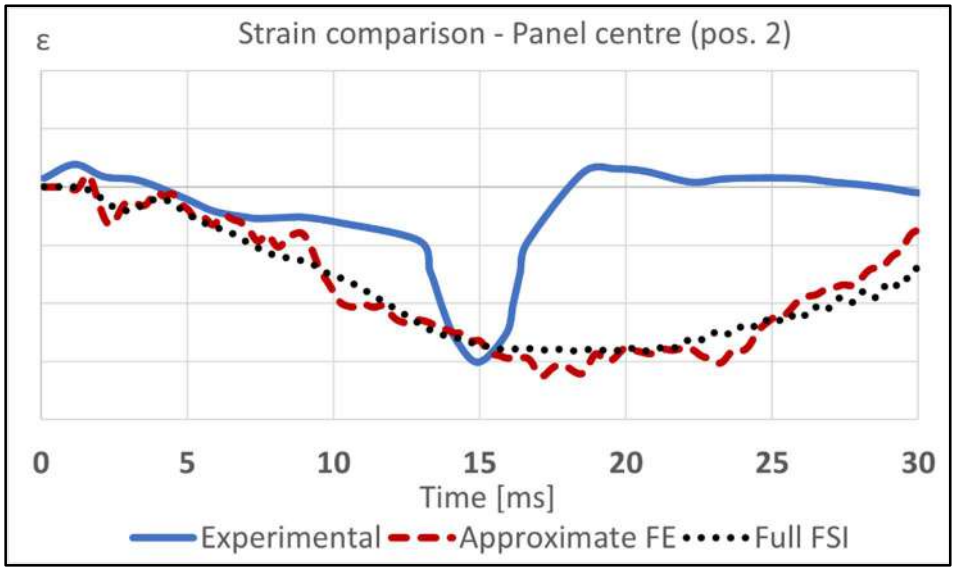

Figure 8.36 Numerical and experimental transversal strain comparison – Strain gauge 2

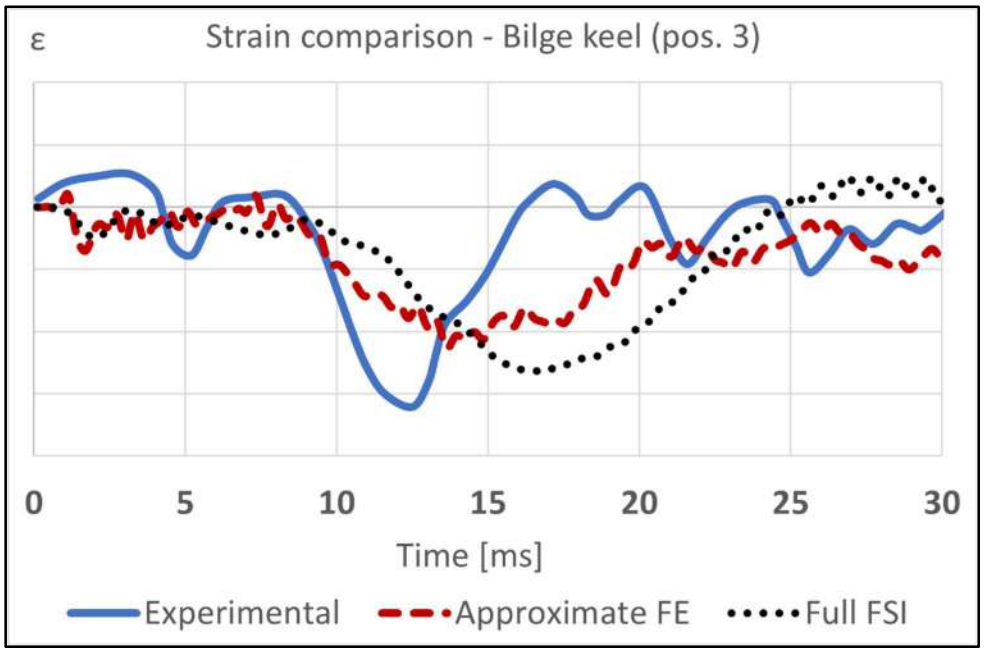

Figure 8.37 Numerical and experimental transversal strain comparison – Strain gauge 3

Table 8.8 Average numerical errors in percentage of approximate FE and full FSI methods

Approximate FE [%]	Full FSI (CFD + FE) [%]
-23.5	-25.4

8.3.5 Volume of Fluid approach: naval ship calibration and results

The same explosion scenario, in which the Approximate FE and the Full FSI approaches were considered, is simulated using the VOF with cavitation method for the fluid. However, considering the features of this approach, some differences in the model strategy occur. In particular, the effects of the free surfaces' boundary conditions request a previous calibration, which was not performed in this thesis. Therefore, instead of the free surface where atmospheric pressure was set in the previous models, a wall boundary condition is applied. As previously done in the parallelepiped benchmark, the nodal pressure is set to the atmospheric pressure ($1 \cdot 10^5$ Pa), and the VOF species is imposed to be 1 (only water) as initial conditions on the fluid volumes. In addition, to obtain more precise results, a more refined mesh is set between the inlet surface, where shock wave pressure is applied, and the ship section (see **Figure 8.38**). This choice is connected to the fact that in the parallelepiped benchmark a refined mesh results in a good spatial representation of the peak pressure in the fluid. In particular, a very refined mesh size (30 x 30 mm in the YZ plane, 500 mm in X direction) is chosen in proximity of the ship block. A particular of the refined mesh is shown in **Figure 8.39**.

ADINA composite integration method is chosen for the transient analysis, considering that is more precise than the Euler scheme. A time step of 10^{-6} seconds is also used.

The FSI pressure, obtained below the centre of the panel by using the VOF method, is compared to the fluid pressures calculated at the same element considering approximate FE and full FSI approach, as shown in **Figure 8.40**. It can be noted that a sharp peak of pressure, more than three times higher than the value obtained using the FSI approach, occurs. Values of pressure never fall below the vapor pressure, as it happens when cavitation phenomenon appears. The same considerations are valid if we compare pressure results obtained close to the wall boundary conditions. However, in this case a further smaller peak, probably caused by the wall constraints, occurs at about 5 ms. See **Figure 8.41**.

After 8 ms, when the shock pressure has already affected the ship and no other interactions with the structures occur, a restart analysis is performed where only structures are involved. This means that the structure, constrained at the edges and preloaded with the FSI pulse, continue its deformation caused by the inertia, as if it was subjected to a zero-pressure load. Adopting this approach, the desired load condition is simulated obtaining reducing the computational efforts.

The comparison of experimental and numerical strains obtained by the different proposed design strategies are shown from **Figure 8.42** to **Figure 8.44**. It can be noted that the strain time histories calculated using the VOF approach follow the experimental peaks in the time domain better than the ones obtained by the other methods. This more realistic results are due to both the better choice in mesh size and the cavitation approach employed. The VOF signal begins to oscillate after the first peak, considering that no damping assumptions have been made. In the experimental results, instead,

effects of damping are shown after the first peak. In addition, VOF results close to the bilge keel seem to be slightly noisy probably for the presence of the constraint itself. However, the minimum values of the peaks for each strain gauge are better caught by the VOF method than the other approaches. The difference between numerical and experimental results in terms of percentage errors are shown in **Figure 8.45**. It can be noted that the error of VOF method is less than the one obtained by the other methods. In particular, in the case of strain gauge 1, it is five time lower than the others.

In **Table 8.9** and **Figure 8.46**, the average error and the scatter of results obtained in the experimental test and by calculations carried out by using all the methods are summarized. In particular, in **Figure 8.46**, each set of data is divided into quartiles, and a box is drawn between the first and third quartiles, with an additional line drawn along the second quartile is used to mark the median. Minimums and maximums outside the first and third quartiles are depicted with lines, while the average value is shown by a crux. It can be noted that the scattering of errors is contained (about 20%) for the VOF method respect to the other methods where scattering can be large (about 60% for the Approximate FE). In addition, as reported in **Table 8.9**, the average percentage error using VOF method substantially decreases.

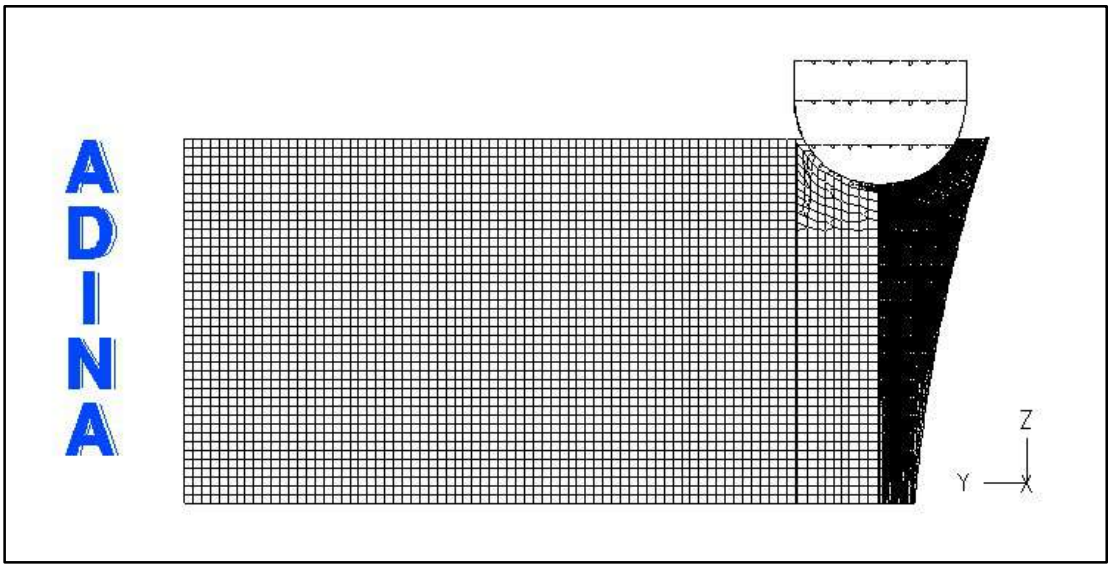

Figure 8.38 VOF – Fluid mesh representation

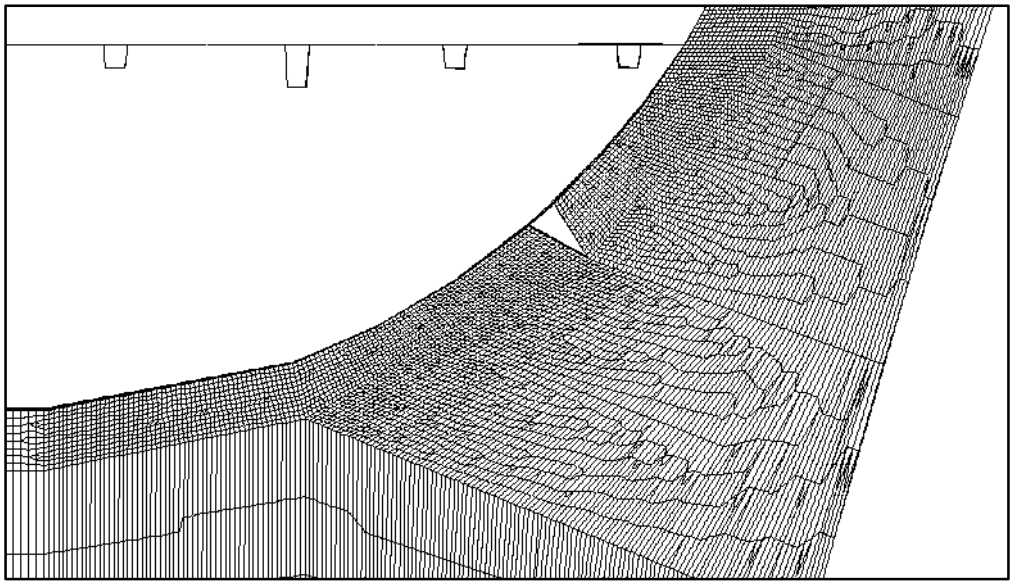

Figure 8.39 Particular of the mesh size close to the ship section

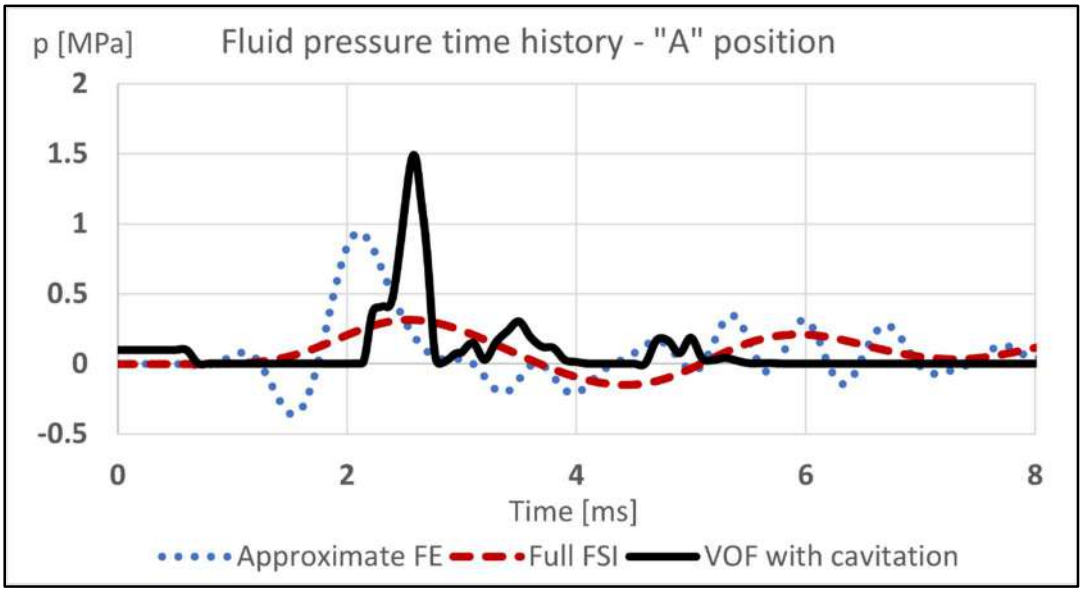

Figure 8.40 VOF with cavitation, approximate FE and full FSI fluid pressure time history comparison in the fluid element at the centre of the panel – "A" position

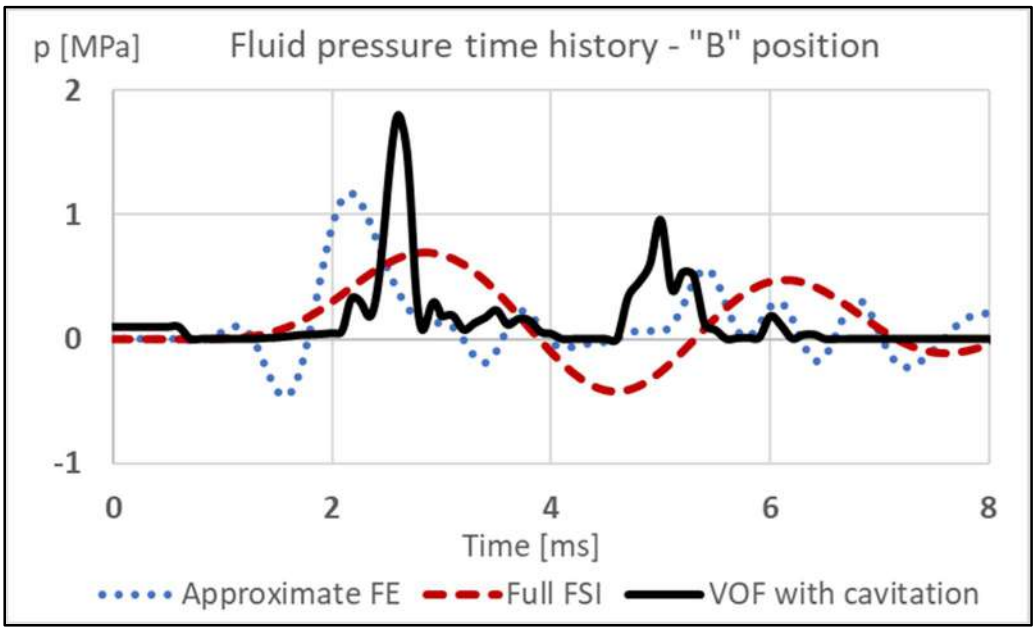

Figure 8.41 VOF with cavitation, approximate FE and full FSI fluid pressure time history comparison in the fluid element close to the wall constraint – "B" position

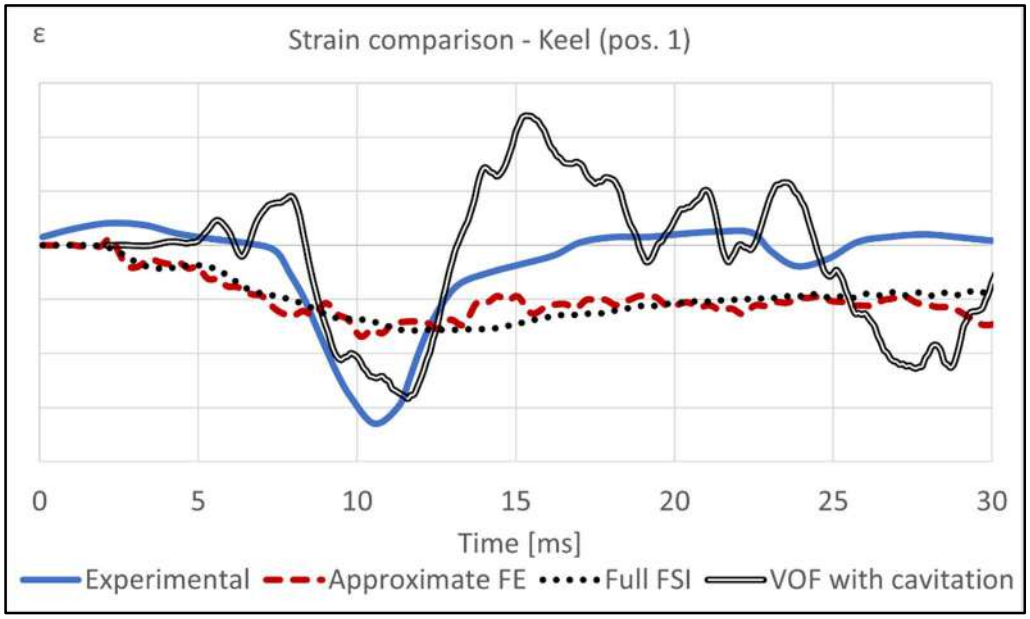

Figure 8.42 Numerical and experimental transversal strain comparison – Strain gauge 1

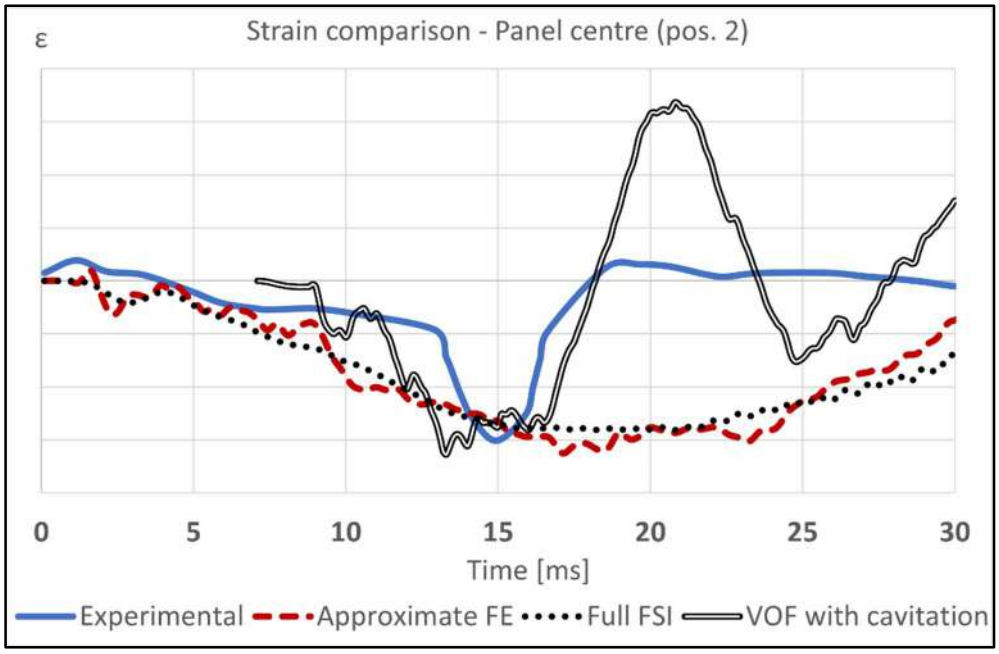

Figure 8.43 Numerical and experimental transversal strain comparison – Strain gauge 2

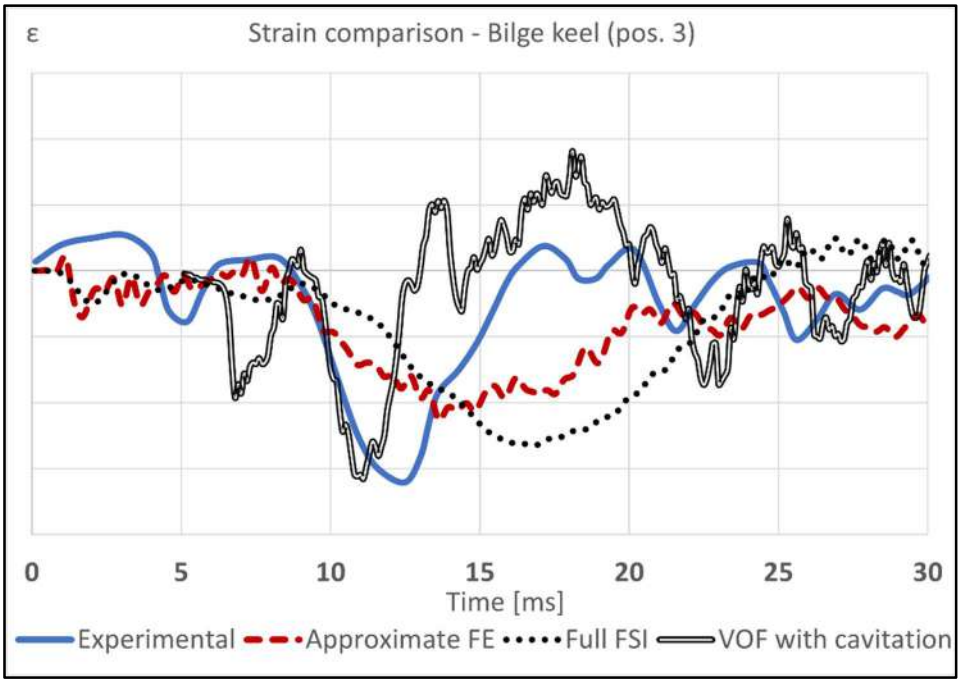

Figure 8.44 Numerical and experimental transversal strain comparison – Strain gauge 3

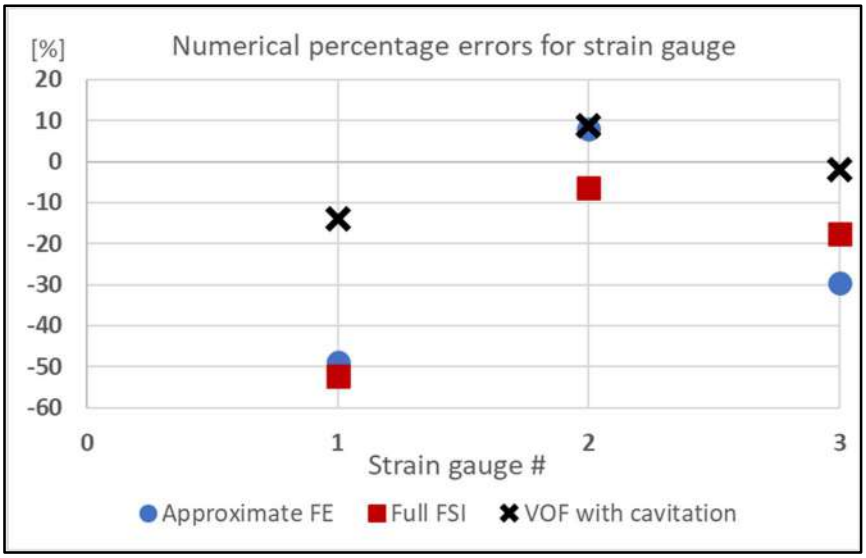

Figure 8.45 Numerical percentage errors in the assessment of the strain peak ordered for strain gauge

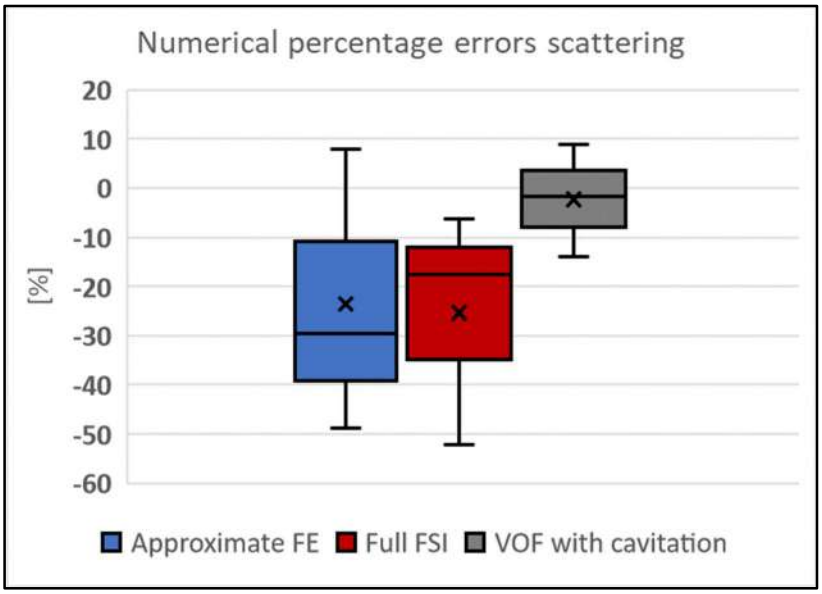

Figure 8.46 Statistics of the percentage errors for each numerical approach

Table 8.9 Average numerical errors in percentage of VOF with cavitation, approximate FE and full FSI methods

VOF with cavitation [%]	Approximate FE [%]	Full FSI [%]
-2.3	-23.5	-25.4

8.4 Considerations

Different numerical strategies (approximate FE, full FSI, VOF) have been adopted to simulate the effects of FSI in the UNDEX scenario. At first, the numerical methods have been calibrated referring to a simple model in which a parallelepiped of fluid have been built. Then, these FSI methods have been used to predict the underwater shock pulse effects on a shell plate of the hull of a naval vessel, comparing numerical results with experimental data obtained by a test in full scale.

A typical section of a minesweeper has been modelled, constrained at its edges, in which the E-glass biaxial polyester resin laminates have been characterized with their orthotropic behaviour. The shock wave pressure, known in position and magnitude from experimental data, has been applied on the hull surface in the FE model. The equivalent explosion scenario of a real test has been FSI simulated, realizing a slice of sea water, and including the free-surface (except in VOF model) and hydrostatic pressure effects. In these simulations, the gas bubble dynamics and the effects of pulses have not been included. However, these last effects provide mainly a global effect, as reported by Keil [8.15], occurring late in time (in terms of seconds), with negligible influence on the panel response. This can be considered true especially for minesweeper referring to the fact that their composite materials should maintain their elastic behaviour, avoiding collapse. No plasticity is shown at all; therefore, the panel must be verified to the first shock peak response. The effects of gas bubble, instead, should be taken into account in case of a whipping analysis or a close-in explosion.

The numerical structural response of a keel panel obtained by using these methods (the approximate FE, full FSI, VOF) has been compared with experimental results. This comparison shows an acceptable result even for the approximate FE model, despite the simplified approach. The choice of using 3-D potential-based fluid involves some approximations, considering the medium as inviscid, irrotational, with no heat transfer, slightly compressible, and relatively small displacements of the fluid boundary. Cavitation is not included in the simulation. In any case, the same calculation is performed, using the full FSI approach, showing a negligible difference in the results. Only a slight increment of numerical noise in the approximate FE signal is reported, while the computational efforts are reduced.

The VOF with cavitation method, instead, provide more realistic results, which are in agreement with the theory and tests, as shown in the parallelepiped benchmark. A more refined mesh, as the one used in the experimental comparison reported in Section 8.2.2, allow the simulation of the vapor effects, including cavitation closure, in the numerical representation. In the full-scale comparison, some approximations have been made, considering that the cavitation is expressed in terms of cut-off pressure, neglecting the possible reloading effects that can be caused by the closure of the cavitation

space outboard the hull. A restart analysis has been performed to save computational time. However, this choice provides suitable results in terms of structural response. In fact, the strain peaks obtained using VOF method are in agreement with the experimental ones. A more refined mesh, of the same size of the one used for the experimental comparison of the parallelepiped benchmark, should be applied to include the vapor effects also in the full-scale comparison, which can be significant in case of explosions which are more severe than the test case studied in this thesis. However, this analysis is time consuming using standard personal computers; the use of more powerful computational devices can lead to a reduction of the computational times. Further studies and calculations are currently running to calibrate the VOF model in order to obtain these results on the minesweeper body block.

In an early phase of design, the relatively straightforward and cost-effective approximate FE model proposed, validated by experimental data, demonstrates to be useful in order to obtain an estimate of the effects of non-contact underwater explosion on board composite minesweepers in a short time. The VOF with cavitation method, if well-calibrated and validated by experimental data, as reported in the text, demonstrates to be useful for the designer in order to obtain a realistic and reliable approximation of the effects of non-contact underwater explosion on board of composite minesweepers.

8.5 Bibliography

[8.1] ADINA, *Theory and Modeling Guide* Volumes I-III, ADINA R & D Inc., Watertown, 2015;

[8.2] Bathe K.J., *Finite element procedures*, Bathe K.J., Watertown, 2014;

[8.3] Bathe K.J., Zhang H., Ji S., *Finite Element Analysis of Fluid Flows fully Coupled with Structural Interactions*, Computers & Structures, Vol. 72, pp. 1-16, 1999;

[8.4] Bryant A. R., Chambers Li. G., *The theoretical shape of the pressure pulse produced by an underwater explosion bubble*, Naval Construction Research Establishment, 1950;

[8.5] Cole R. H., *Underwater explosions*, Woods Hole Oceanographic Institution, 1914;

[8.6] DNVGL-CG-0127, *Finite Element Analysis* in Class Guidelines, DNV GL, February 2016;

[8.7] Dvorkin E. & Bathe K.J., "A Continuum Mechanics Based Four-Node Shell Element for General Nonlinear Analysis", Engineering Computations, Vol. 1, pp. 77-88, 1984;

[8.8] Eymard R., Gallouët T. R., Herbin, R. *The finite volume method* Handbook of Numerical Analysis, Editors: P.G. Ciarlet and J.L. Lions, Vol. VII p. 713–1020, 2000;

[8.9] Gaiotti M. & Rizzo C. M., "Finite element modeling strategies for sandwich composite laminates under compressive loadings", Ocean Engineering 63, 44-51, 2013;

[8.10] Gaiotti M., Rizzo C. M., Branner K., Berring P., "An high order Mixed Interpolation Tensorial Components (MITC) shell element approach for modeling the buckling behavior of delaminated composites", Compos. Struct. 108, 657-666, 2014;

[8.11] Germanischer Lloyds, "Analysis Techniques" in Rules for Classification and Construction, Part 1, Chapter 1, 2011;

[8.12] Green Associates E., *Marine Composites*, Eric Greene Associates, 1999;

[8.13] Halpin J. C., Nicolais L., Materiali compositi: relazioni tra proprietà e struttura, Ingegnere Chimico Italiano 7:173, 1971;

[8.14] Hirt C.W., Nichols, B.D., "Volume of fluid (VOF) method for the dynamics of free boundaries". Journal of Computational Physics 39 (1): 201–225, 1981.

[8.15] Keil A.H., "The Response of Ships to Underwater Explosions", Society of Naval Architects and Marine Engineers, New York, 16-17 Novembre 1961;

[8.16] Mannacio F., Barbato A., Gaiotti M., Rizzo C.M., Venturini M., "Analysis of the underwater explosion shock effects on a typical naval ship foundation structure: experimental and numerical investigation", MARSTRUCT 2021 Congress, Trondheim, 7-9 June 2021;

[8.17] Mannacio F., Barbato A., Di Marzo F., Gaiotti M., Rizzo C.M., Venturini M., "Shock effects of underwater explosion on naval ship foundations: Validation of numerical models by dedicated tests", Ocean Engineering 253 111290, 2022;

[8.18] MARIPERMAN, *Relazione n. 02747*, Commissione Permanente per gli Esperimenti del Materiale da Guerra, 1988;

[8.19] McGoldrick R. T., Gleyzal A. N., Hess R. L ., Gess Jr. G. K., "Recent Developments in the Theory of Ship Vibration", David Taylor Model Basin Report 1451, pp. 2-6 – 2-9, December 1960;

[8.20] Petralia S., *Compendio di esplosivistica*, MARIPERMAN, La Spezia, 2000;

[8.21] Ramajeyathilagama K., Vendhan C.P., “Deformation and rupture of thin rectangular plates subjected to underwater shock”, International Journal of Impact Engineering 30, 699–719, 2004;

[8.22] Smith C. S., *Design of Marine Structures in Composite Materials*, Elsevier, Applied Science, 1990;

[8.23] Sussman T., Sundqvist J., *Fluid-structure interaction analysis with a subsonic potential-based fluid formulation*, Computers & Structures, Vol. 81, pp. 949-962, 2003;

[8.24] Swisdak Jr, M.M., *Explosion effects and properties. Part II. Explosion effects in water*, Naval Surface Weapons Center White Oak Lab Silver Spring Md, 1978;

[8.25] Taylor G.I., “The pressure and Impulse of Submarine Explosion Waves on Plates”, Ministry of Home Security Report, FC 235, 1941;

[8.26] Vedantam K., Bajaj D., Brar N. S., Hill S., “Johnson - Cook strength models for mild and DP 590 steels”, AIP Conference Proceedings, American Institute of Physics, 2006;

[8.27] Zhang H., Bathe K.J., *Direct and Iterative Computing of Fluid Flows fully Coupled with Structures*, Computational Fluid and Solid Mechanics, K.J. Bathe, editor, Elsevier Science, 2001;

[8.28] Zong Z., Zhao Y., Li H., “A numerical study of whole ship structural damage resulting from close-in underwater explosion shock”, Marine Structures 31, 24-43, 2013.

[8.29] Zwart P. J., Gerber A. G., and Belamri T., “A two-phase flow model for predicting cavitation dynamics”, Proceedings of the International Conference on Multiphase Flow (ICMF 04), Yokohama, Japan, 2004.

9 Conclusions

The progressive increase of the threat level in the operational scenario has provided the necessity of designing the new MG – MCMV, and updating the naval fleet, inserting in the design process the concepts of survivability and vulnerability. Reducing the vulnerability of the minesweepers implies the verification of the shock requirements. Performing a correct scantling method is crucial, considering that experimental tests are not always available in an early phase of the design. Numerical methods, such as the finite elements, are surely useful to help designers make the most accurate decisions. However, the prediction of the effects of underwater explosions on composite materials is an extremely complex topic, which requires the definition of some assumptions. The full treatment of the issue is even now a matter of research. Therefore, in this thesis the different aspects of the phenomenon have been analysed, such as the mechanical shock effects on steel and composite materials and the FSI analysis. As a result, different model strategies have been provided to assess the UNDEX effects on minesweepers, evaluating their accuracy referring to experimental data.

As a summary, at first, the bibliographical research, made in collaboration with the Italian shipbuilding industries, has been significant to make a point of the state of the art of the shock design, including traditional and new methodologies, in order to clarify which are the main issues of the UNDEX verification.

Then, the shock phenomenon has been analyzed considering the effects on structures only, as it is required from the standard procedures of verification. Some guidelines on how to perform dynamic calculations using finite elements, which were not clearly defined, have been provided. Dedicated shock tests, performed at CSSN on a typical foundation structure made of mild steel, have been used to verify the procedure, quantifying errors.

The dynamic characterization of the materials, used as input of the calculations, have been particularly important to obtain good results. However, this mechanical behaviour is not known a priori for composite materials, considering that the literature is lacking and sometimes also inconsistent on the topic. An experimental and numerical procedure have been provided to characterize the structural behaviour caused by UNDEX of composite materials, including the dynamic inputs necessary for calculations. Applying this methodology, it is possible to perform calculations also on complex naval structures in order to select of the proper stacking sequences, and, therefore, “designing” the materials.

In the end, different FSI methods, which are necessary to evaluate the effects on naval hulls, have been evaluated, comparing numerical results with theory and tests realized on a minesweeper in full scale. The approximate FE method provides acceptable results: it can be used to obtain an estimate

of the UNDEX effects in a short time. The VOF with cavitation method, instead, is the most realistic, allowing the complete description of the UNDEX phenomenon, as it considers water, vapor and structures effects. It obtains suitable results in comparison with both the parallelepiped benchmark and the full-scale test case. If some assumptions are made, it can be useful also in an early phase of design to predict with a good accuracy the shock effects on naval ships.

In conclusion, the modelling strategies provided and validated, which include the determination of the FE shock guidelines, the dynamic characterization of the composites and the calibration of the FSI numerical models, are powerful instruments which can be used by shock designers to reduce the vulnerability of the mine countermeasures vessels, and consequently to increase their survivability.

9.1 Future developments

During the experiments on composites performed at CSSN, which were necessary to obtain the dynamic characterization of materials performed in this thesis, no failure occurred to the laminates. Further tests are necessary to predict the failure modes of the composites caused by UNDEX in order to obtain a suitable calibration of the relevant numerical methods.

Advanced numerical models, such as VOF with cavitation method, are very promising in predicting the UNDEX effects on naval vessels. This latter approach, calibrated according to theory and experimental data, results to be suitable to predict the complete UNDEX phenomenon, considering that structure, water and vapor are included in the simulation. It can be applied to hull structures, rudders, valves, which cannot be normally verified by test in an early phase of design. However, this approach requests a significant calculation effort. In particular, the phenomenon of the cavitation closure can be deepened, considering that more severe experimental tests are planned in the next future. Therefore, the numerical method can be calibrated refining mesh size and time step with the possibility of running on more powerful computers. In addition, the bulk cavitation caused by the free surface should also be investigated.

For the future, it is believed that the continuous effort of research in calibrating numerical models according to experiments will lead to even more reliable modeling strategies for the shock design of navy ship, reducing the need of tests. The role of CSSN and the cooperation with the national University in this perspective is crucial considering that the expertise of personnel and high-quality instrumentation for tests can be combined with theoretical and numerical assessment in order to provide better understanding of such complex phenomena.